

Lecture Notes in Mechanical Engineering

V. Krishna

K. N. Seetharamu

Yogendra Kumar Joshi *Editors*


Recent Advances in Hybrid and Electric Automotive Technologies

Select Proceedings of HEAT 2021

 Springer

Lecture Notes in Mechanical Engineering

Editorial Board

Francisco Cavas-Martínez , Departamento de Estructuras, Construcción y Expresión Gráfica Universidad Politécnica de Cartagena, Cartagena, Murcia, Spain

Francesca di Mare, Institute of Energy Technology, Ruhr-Universität Bochum, Bochum, Nordrhein-Westfalen, Germany


Mohamed Haddar, National School of Engineers of Sfax (ENIS), Sfax, Tunisia

Young W. Kwon, Department of Manufacturing Engineering and Aerospace Engineering, Graduate School of Engineering and Applied Science, Monterey, CA, USA

Justyna Trojanowska, Poznan University of Technology, Poznan, Poland

Series Editors

Fakher Chaari, National School of Engineers, University of Sfax, Sfax, Tunisia

Francesco Gherardini , Dipartimento di Ingegneria “Enzo Ferrari”, Università di Modena e Reggio Emilia, Modena, Italy

Vitalii Ivanov, Department of Manufacturing Engineering, Machines and Tools, Sumy State University, Sumy, Ukraine

Lecture Notes in Mechanical Engineering (LNME) publishes the latest developments in Mechanical Engineering—quickly, informally and with high quality. Original research reported in proceedings and post-proceedings represents the core of LNME. Volumes published in LNME embrace all aspects, subfields and new challenges of mechanical engineering. Topics in the series include:

- Engineering Design
- Machinery and Machine Elements
- Mechanical Structures and Stress Analysis
- Automotive Engineering
- Engine Technology
- Aerospace Technology and Astronautics
- Nanotechnology and Microengineering
- Control, Robotics, Mechatronics
- MEMS
- Theoretical and Applied Mechanics
- Dynamical Systems, Control
- Fluid Mechanics
- Engineering Thermodynamics, Heat and Mass Transfer
- Manufacturing
- Precision Engineering, Instrumentation, Measurement
- Materials Engineering
- Tribology and Surface Technology

To submit a proposal or request further information, please contact the Springer Editor of your location:

China: Ms. Ella Zhang at ella.zhang@springer.com

India: Priya Vyas at priya.vyas@springer.com

Rest of Asia, Australia, New Zealand: Swati Meherishi at swati.meherishi@springer.com

All other countries: Dr. Leontina Di Cecco at Leontina.dicecco@springer.com

To submit a proposal for a monograph, please check our Springer Tracts in Mechanical Engineering at <https://link.springer.com/bookseries/11693> or contact Leontina.dicecco@springer.com

Indexed by SCOPUS. All books published in the series are submitted for consideration in Web of Science.

V. Krishna · K. N. Seetharamu ·
Yogendra Kumar Joshi
Editors

Recent Advances in Hybrid and Electric Automotive Technologies

Select Proceedings of HEAT 2021

 Springer

Editors

V. Krishna
Department of Mechanical Engineering
PES University
Bengaluru, India

K. N. Seetharamu
IIT Madras
Tamil Nadu, India

Yogendra Kumar Joshi
G. W. Woodruff School of Mechanical
Engineering
Georgia, USA

ISSN 2195-4356

ISSN 2195-4364 (electronic)

Lecture Notes in Mechanical Engineering

ISBN 978-981-19-2093-6

ISBN 978-981-19-2091-2 (eBook)

<https://doi.org/10.1007/978-981-19-2091-2>

© The Editor(s) (if applicable) and The Author(s), under exclusive license to Springer Nature Singapore Pte Ltd. 2022

This work is subject to copyright. All rights are solely and exclusively licensed by the Publisher, whether the whole or part of the material is concerned, specifically the rights of translation, reprinting, reuse of illustrations, recitation, broadcasting, reproduction on microfilms or in any other physical way, and transmission or information storage and retrieval, electronic adaptation, computer software, or by similar or dissimilar methodology now known or hereafter developed.

The use of general descriptive names, registered names, trademarks, service marks, etc. in this publication does not imply, even in the absence of a specific statement, that such names are exempt from the relevant protective laws and regulations and therefore free for general use.

The publisher, the authors, and the editors are safe to assume that the advice and information in this book are believed to be true and accurate at the date of publication. Neither the publisher nor the authors or the editors give a warranty, expressed or implied, with respect to the material contained herein or for any errors or omissions that may have been made. The publisher remains neutral with regard to jurisdictional claims in published maps and institutional affiliations.

This Springer imprint is published by the registered company Springer Nature Singapore Pte Ltd. The registered company address is: 152 Beach Road, #21-01/04 Gateway East, Singapore 189721, Singapore

*Dedicated to
Our Esteemed Professor and Mentor,
Dr. K. N. Seetharamu*

Foreword

Dear Authors, Esteemed Readers,

It is with deep satisfaction that I write this Foreword to the Proceedings of the First Biennial International Conference on Hybrid and Electric Automotive Technologies held at PES University, Bangalore on October 29th and 30th, 2021. In spite of the situation due to pandemic which made organizing a conference, first of its kind a challenging one, the team has put together an intellectually stimulating and thought-provoking platform for all academicians, researchers and industry participants alike.

The conference particularly encourages the interaction of research students with the more established academic community and industry experts in an informal setting to present and to discuss new and current work. Although being in virtual mode has its advantages and disadvantages, I hope all the participants did take advantage of the conference that had eminent keynote addresses delivered by experts in the field of Hybrid and Electric Automotive Technologies. The inaugural keynote was delivered by Dr. Kaushik Basu, Professor, Indian Institute of Science, Bangalore on “Fast Charging of Electric Vehicles: Current Status and Future Prospects”. This was followed by several talks on other important issues and paper presentations.

All these contributions by Authors, Speakers and Participants help to make the conference as outstanding as it has been.

These Proceedings will furnish the researchers in this field with an excellent reference book. I trust also that this will be an impetus to stimulate further study and research in all these areas.

We thank all authors and participants for their contributions.

Bengaluru, India
Heat 2021

T. S. B. Sudarshan
Chair, Steering Committee

Preface

The market and technology for electric drive vehicles is growing rapidly and will soon epitomize the mainstream of new vehicle car sales. As such, it is more important than ever to stay informed on the latest technology, hybridization and electrification solutions, and new emission/energy consumption targets. Hybrid electric vehicles (HEVs) have great potential to save fuel consumption and reduce pollution emissions. The automotive technology that drives hybrid electric vehicles has huge potential for research and development. From efficiency-improving technologies such as regenerative brakes to advanced batteries in plug-in electric vehicles designed for extended life, the scope for enhancing the power available at the wheels is enormous, and as such many researches have focused on the technologies and applications of HEVs both in academia and industry.

The First Biennial International Conference on Hybrid and Electric Automotive Technologies (HEAT 2021) organized by the Department of Mechanical Engineering, PES University, Bangalore, Karnataka, India, in association with Garrett Motion Engineering Solutions Pvt. Ltd. was held from October 29 to 30, 2021. The conference sought to provide a platform for researchers working in this domain with specific topics of discussion which include batteries, battery cooling methodologies, use of nano-coolants, electrified powertrain systems and components, hybridisation infrastructure, energy storage, and many other topics of importance to the industry. The conference also provided an opportunity for national and international experts and industry leaders to share their experiences and success stories. HEAT 2021 played a key role to set up a bridge between academia and industry.

Due to the prevailing COVID-19 pandemic, the conference was organized virtually and hosted around 400 participants from India and across the world to exchange their scientific ideas. During 2 days of the conference, researchers from academia and industries went through various scientific brainstorming technical sessions and presented their most recent cutting-edge discoveries. This conference also provided a scope to establish a network for collaboration between academia and industry.

This book brings together the collection of cutting-edge research articles presented in HEAT 2021. This book, which caters to the aspects related to hybrid and electric automotive technologies, will serve as a reference guide for researchers and

practitioners and is expected to foster better communication and closer cooperation between academia and industry partners. It encompasses the four principal areas of hybrid and electric automotive technologies such as fluid and thermal engineering in EV/HEVS, materials, process and design in EV/HEVS, autonomous vehicles and electrical and electronics in EV/HEVS.

Bengaluru, India
Tamil Nadu, India
Georgia, USA

Dr. V. Krishna
Dr. K. N. Seetharamu
Dr. Yogendra Kumar Joshi

Acknowledgements

We are indebted to our respected Chancellor Dr. M. R. Doreswamy and Pro-Chancellor Prof. D. Jawahar for extending their generous support as without their blessings, and it would not have been possible to complete this task. We sincerely thank the honourable Vice-Chancellor Dr. J. Suryaprasad and respected Registrar Dr. K. S. Sridhar for their wonderful suggestions at all stages. We also thank Dean Research Dr. T. S. B. Sudarshan and Chairperson of the Department of Mechanical Engineering Dr. N. Rajesh Mathivanan for their support at all stages. We thank all faculty, research scholars and staff of the Department of Mechanical Engineering, PES University, who have directly or indirectly helped us to accomplish this goal. We would like to express our gratitude to our platinum sponsors Garrett Motion Engineering Solutions Pvt. Ltd. particularly Mr. John Poomkuzhimannil Zach, Senior Director Breakthrough Initiatives, Garrett Motion Engineering Solutions Pvt Ltd. and Ms. Sampada Patki for their incessant support to the conference. We thank IEEE PELS Bangalore Chapter and SAE India Bengaluru Section for their kind support. We would like to acknowledge all the session chairs, keynote speakers, members of the organising committee and participants who have contributed to the success of the conference.

Last but not least, we thank the staff at Springer, in particular Ms. Priya Vyas and Ms. Silky Abhay Sinha for their help and support.

Though due care has been taken, still, there is always space for improvement. We would appreciate any suggestions from the readers for further improvement of this book.

Bengaluru, India
Tamil Nadu, India
Georgia, USA

Dr. V. Krishna
Dr. K. N. Seetharamu
Dr. Yogendra Kumar Joshi

Contents

Placement Optimization for Field Effect Transistors	1
Dhrupad Vijay, S. V. Amartya, Babu Rao Ponangi, and V. Krishna	
A Simplified Thermal Model to Predict Temperature Profile and Heat Generation of Cylindrical Lithium-Ion Cells	11
Pritam Bhat and Mahesh K. Varpe	
Mathematical Modeling and Parametric FEM Study on the Thermal Management of a Rectangular Microchannel Heat Sink	25
Ria Ann Zachariah, Neelima Kuttappa Mukkatira, M. Sachin Bharadwaj, V. Krishna, and Babu Rao Ponangi	
Production of Cotton Seed Biodiesel and Its Usage in a C I Engine with Methyl Ester and Al₂O₃ Additives	35
Basavaraj Ganiger and B. Yuvaraj	
Tribological and Rheological Studies of Polyolester (POE) Oil and POE + alumina nanolubricant and its effect on the Performance of a Refrigeration System	45
Subramani Narayanasarma and Biju T. Kuzhiveli	
Aerodynamic Effect on Lift Characteristics of a Sedan Car Due to Attached Wing	59
Amrutheswara Krishnamurthy and Suresh Nagesh	
Modelling and Analysis of Brake Disc with Various Profiles for EN31 Material	71
K. Kaviyaran, R. Soundararajan, R. Abhisheak Richter, K. Siva, S. Purusothaman, and S. Shiva Gurunathan	
Production of Biodiesel Using Temple Waste Oil	81
A. Jagadeesh, Basavaraj M. Shrigiri, and Omprakash D. Hebbal	

Experimental Analysis of a Counter Flow Plate Heat Exchanger by Using Nanofluids at Different Concentrations	91
Anil Kumar and Amman Jakhar	
Design Evaluation in Reconfigurable Manufacturing System (RMS): A Multi-Objective Squirrel Search Algorithm	99
N. Swamy, U. M. Daivagna, A. Thimmana Gouda, and R. H. M. Somanath Swamy	
Development of Drive Cycle and Resultant Powertrain Calculations of Electric Bicycle	119
Tejas Savadi, V. N. Abhilash, Kean Fernandes, and Sharanbassappa S. Patil	
Dynamic Analysis of Electric Train Bogie Using MATLAB Simulink ...	125
C. Prithvi, Surajgouda C. Policepatil, and Srinidhi Ramachandracharya	
Design and Development of Electric Powertrain for a Proposed Three-Wheel Personal Mobility Vehicle	137
Arvind Srivatsan Varadharajan, R. Shreekara, Suman Emmanuel Salins, and Sharanabassappa S. Patil	
Artificial Intelligence-Based Trajectory Planning for Driverless Vehicles—A Review	167
Aathira G. Menon and S. Bindu	
An Automatic Indian Traffic Signs Detection and Recognition System Using OpenCV	185
Chinmay Srinivas and Sharanbassappa S. Patil	
A Waypoint Tracking Controller for Autonomous Vehicles Using CARLA Simulator	197
Chinmay Srinivas and Sharanbassappa S. Patil	
An Economic Feasibility Study of Electric Vehicle Charging Stations in India	207
Sajan Jerome and M. Udayakumar	
Liquid Cooled Battery Thermal Management System for 3S2P Li-Ion Battery Configuration	223
Divya D. Shetty, Aditya Nair, Rishab Agarwal, and Kshitij Gupta	
Implementation of Multi-carrier Modulation Techniques to Increase Image Quality for Underwater Sonar Image Transmission	237
Rishav Kumar Kedia, Aditi Goyal, Rohan Vashishtha, and G. Swetha	
Design and Analysis of Skateboard Chassis	263
N. Sharath Chandra and R. Vikas	

Electro-Thermal Model for Field Effective Transistors 277
Allen Denny, Neelkanth Kirloskar, Babu Rao Ponangi, Rex Joseph,
and V. Krishna

**A Parametric CFD Study on the Cooling Capability
of a Rectangular Channel Heat Sink** 285
Akhilesh Danesh Jatti, Mayur Chetan Shanbhag, D. S. Shashwath,
Babu Rao Ponangi, and V. Krishna

**Estimation of Tire Scaling Coefficients and Simulation of On-Road
Vehicle Behaviour** 295
Nandish H S, Prajwal P, and Patil S S

Multivariable Load Prediction Using LSTM 315
G. Satya Rohan, V. Sailaja, K. Deepa, and Abhijith Prakash

About the Editors

Dr. V. Krishna is a Professor in the Department of Mechanical Engineering and Dean, Student Affairs, PES University, Bangalore. He obtained his B.E. (Mechanical) from Bangalore University and Master's degree from Birla Institute of Technology, Mesra, Ranchi. He has received his Ph.D. from Visveswaraya Technological University, Belgaum, India, for his thesis on 'Investigations on Cryogenic Heat Exchangers'. He started his academic career in March 1993 and has over 28 years of experience in teaching, research, consultancy and administration. He is the chief course instructor for courses such as engineering thermodynamics, mechanics of fluids, modelling and analysis of heat exchangers, turbomachines, and heat and mass transfer. He is reviewer for Heat Transfer Engineering published by Taylor and Francis, International Journal of Heat and Mass Transfer published by Elsevier etc. Dr. V. Krishna specializes in the Thermal Engineering Domain and is the Head of the Process Modelling Research Laboratory (PMR Lab) which focusses on cutting edge research in the field of process modelling and its allied areas. He has over 24 publications in peer-reviewed international journals (10) and conferences (14). He has been an invited speaker and chair at numerous national and international conferences. Dr. V. Krishna was invited as Visiting Professor at Technologico de Monterrey, Mexico from 25th to 31st August, 2018. He visited two of its campuses at Toluca and Puebla. During this period, he took a course on 'Automobile Radiators-an Inside Story' and also presented seminars on 'Drivers for Sustainable Energy in the Automobile Industry' and 'Introduction to Internal Combustion Engine'. He has also visited a number of universities in UK in 2013, as part of a tour to look at the best practices and possible collaborations. Dr. V. Krishna is also an accomplished mridangam artiste and has accompanied top musicians across India in numerous Carnatic music concerts.

Prof. K. N. Seetharamu known to his colleagues and students simply as KNS, was a leading computational heat transfer expert. He transformed this area of research in India and elsewhere through his simplified approaches and the use of finite element method. KNS received his undergraduate degree in mechanical engineering from Mysore University in 1960 before earning his Master's degree in power engineering

and Ph.D. in heat transfer, respectively from IISc Bangalore in 1962 and IIT Madras in 1973. After a brief stint in Industry and BIT Ranchi, KNS started his three decades of academic career at IIT Madras until 1998. Between 1999 and until his death in January 2022, he carried out research and taught engineering students in various universities including University Sains Malaysia (1998–2005), MS Ramaiah School of Advanced Studies, Bangalore (2005–2006), Sri Bhagawan Mahaveer Jain College of Engineering Bangalore (2006–2007) and PES University, Bangalore (2007–2022). During his career, KNS formally graduated 57 postgraduate research students and informally helped many others to earn research degrees. He also published 455 articles including 207 journal articles and with total citations exceeding 7000. After a significant contribution to boiling heat transfer in his doctoral work, KNS started working in the area of the finite element method in the early eighties. The finite element research in heat transfer was significantly enhanced by his research visits to Swansea University and fruitful collaboration with senior academics in Swansea. He made the discrete systems approach (a precursor to full finite element method) very popular in heat transfer through his works in heat conduction, flow through pipe networks, heat exchangers and heat transfer enhancement. He continued such a simple but effective approach to energy and momentum balance in various applications throughout his research career. Prof. K. N. Seetharamu passed away on January 16th 2022. His demise is deeply regretted. He leaves behind a legacy on use of FEM for Heat Transfer applications.

Dr. Yogendra Kumar Joshi is Professor and John M. McKenney and Warren D. Shiver Distinguished Chair at the G.W. Woodruff School of Mechanical Engineering at the Georgia Institute of Technology. He obtained his B.Tech. from Indian Institute of Technology Kanpur and M.S. degree from State University of New York, Buffalo. He has received his Ph.D. from University of Pennsylvania in the year 1984. His research areas include heat transfer, combustion, and energy systems; micro and nano engineering; and thermofluidic issues in emerging technologies and microthermal systems. His research interests are in multi-scale thermal management. He is the author or co-author of nearly four hundred publications in this area, including nearly two hundred journal articles. Prior to joining Georgia Institute of Technology in 2001, he held faculty appointments at the University of Maryland at College Park (1993–2001), and Naval Postgraduate School (1986–1993). He has served as the Principal Investigator for multiple Defense Advanced Research Projects Agency (DARPA) programs, and Office of Naval Research Consortium for Resource-Secure Outposts (CORSO). He was Site Director for the National Science Foundation Industry/University Cooperative Research Center on Energy Efficient Electronic Systems. He has held visiting faculty appointments at Stanford University, Katholieke Universiteit Leuven, and Xi'an Jiaotong University. He is an elected Fellow of the ASME, the American Association for the Advancement of Science, and IEEE. He is a recipient of many distinguished awards such as the ASME Electronic and Photonic Packaging Division Outstanding Contribution Award in Thermal Management, ASME J. of Electronics Packaging Best Paper of the Year Award,

IBM Faculty Award, IEEE SemiTherm Significant Contributor Award, ASME Inter-Pack Achievement Award, ITherm Achievement Award, and ASME Heat Transfer Memorial Award.

Placement Optimization for Field Effect Transistors



Dhrupad Vijay, S. V. Amartya, Babu Rao Ponangi, and V. Krishna

Abstract In this fast-paced world where technology has been established in all aspects of human society, there is a constant demand for higher processing capabilities with smaller packaging which leads to increased power dissipation per unit volume. This warrants innovative and more efficient cooling solutions. A Printed circuit board (PCB) is a layered insulating board that mechanically supports the semiconductor chips and facilitates electrical connection between them through an etched metallic coating (usually copper) laminated on its surface. The components are fastened to the PCB by means of solder. Due to the increasing density and number of heat-producing components, it becomes necessary to decrease the overall temperature of the PCB before installing the cooling system, the heat-producing elements must be optimally placed so as to not be too close to the boundary nor be in the range to thermally interfere with other chips, to prevent localized high-temperature regions which could further damage the PCB. This is done through the process of PCB optimization, where prior data from thermal simulations will be used to generate an optimized layout to minimize the board temperature. In the first phase of our project, we worked on modelling the board, chips and enclosure. We made several approximations to start with and slowly refined the model in successive steps. Our goal is to create a model as close to reality as possible and use this to optimize the placement of the chips and various parameters involved.

Keywords Thermal modelling · Simulation · Placement optimization

D. Vijay · S. V. Amartya · B. R. Ponangi (✉) · V. Krishna
Department of Mechanical Engineering, PES University, Bangalore 560085, India
e-mail: baburaoponangi@gmail.com

B. R. Ponangi · V. Krishna
PMR Lab, Department of Mechanical Engineering, PES University, Bangalore 560085, India

© The Author(s), under exclusive license to Springer Nature Singapore Pte Ltd. 2022
V. Krishna et al. (eds.), *Recent Advances in Hybrid and Electric Automotive Technologies*, Lecture Notes in Mechanical Engineering,
https://doi.org/10.1007/978-981-19-2091-2_1

1 Introduction

Thermal management of electronic components is essential in this day and age because of the increasing density of electronic components. Improper placement of the chips has adverse effects on the longevity and efficiency of the chips. It is becoming increasingly important to ensure proper placement of the components. To maintain the operating temperature below the optimum temperature, optimization and various cooling methods are employed.

Suwa et al. [1] talked about the optimization of PCB board layout subject to multiple objectives and pre-defined constraints. The overlap and thermal penalties included made sure the GA is learnt to avoid those in order to minimize the function. Studies were conducted to find the initial population size and number of generations. The methodology was then used on a real-world application and the results were shown.

Ismail et al. [2] present a new type of genetic algorithm to solve the multi-objective function used to optimize the PCB layout. The SOGA approach will ensure an optimal placement of each electronic component on PCB by minimizing the objectives function simultaneously while satisfying a few constraint parameters. In this paper, resistance thermal network is used to predict the junction temperatures.

Jain et al. [3] present an approach to find the optimal design layout of chips on a circuit board in a manner that minimizes the area covered on the board and the connections between the various chips. The authors demonstrate the working with an example. They tweak different parts of the objective function and show the difference in the final output as well.

Tohru et al. [4] introduce a multidisciplinary optimization methodology for the placement of heat-generating semiconductor logic blocks on integrated circuit chips. The thermal and wiring length criteria are simultaneously optimized using a genetic algorithm. The main advantage of the present multidisciplinary design and optimization methodology is its ability to handle multiple design objectives simultaneously for the optimized placement of heat-generating logic blocks.

From the literature reviewed, the main points and methods to best optimize the placement are summarized. The placement of the chips has a major effect on the junction temperatures of the FETs. The other factors affecting the junction temperature are local heat generation through copper traces, copper distribution, placement of vias and thermal resistance of components such as PCB and heat sink. Higher ambient temperature has a negative impact on the performance of the IC. Size reduction and overlapping algorithms can be incorporated to reduce the overall area occupied by the PCB, decreasing the weight of the heat sink to be coupled. The papers reviewed have used approximations for the model, and the trade-off between the decrease in modelling complexity vs the accuracy of the obtained results was not studied.

2 Methodology

2.1 Problem Formulation

FET has a maximum temperature that cannot be exceeded without destroying the device or at least shortening its life. The heat is generated in a bipolar transistor directly under the emitters and very close to the upper surface of the die. For all practical purposes, the heat is considered to be generated throughout the volume of the chip or die. The maximum power rating of the transistor is largely governed by the temperature of the collector/base junction as can be seen from [5]; if too much power is dissipated, this junction gets too hot and the transistor will be destroyed as such, and the performance of a power transistor is closely dependent on its ability to dissipate the heat generated at the junction.

2.2 PCB Modelling

Geometric Modelling. In order to collect data for the ANN, a simple model of the PCB was constructed. 6 FETs were placed vertically upon a three-layered PCB. The PCB contains an alternate layer of copper and FR4, the copper layer being the traces of the PCB. This PCB is then surrounded by an air domain to mimic the effect of an enclosed space. The enclosure is modelled as insulated walls. Convection currents are set up in the air in contact with the PCB. The PCB and enclosure lose heat through the back surface of the PCB as shown in Fig. 1.

The materials used for the model are presented in Table 2.

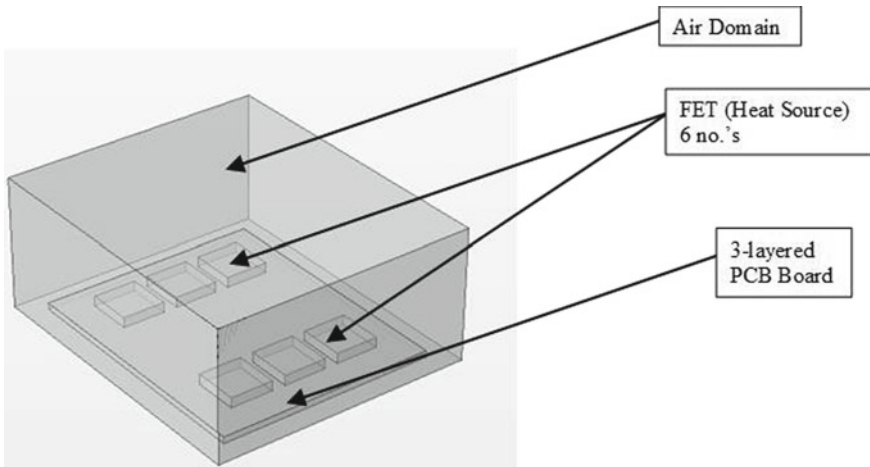


Fig. 1 Geometric model of PCB with FETs surrounded by an air domain

Table 1 Dimensions of the model

Part		Length	Breadth	Height
PCB	Copper layer	50 mm	60 mm	0.035 mm
	FR4 layer	50 mm	60 mm	1.43 mm
FETs		9.9 mm	10.375 mm	2.3 mm
Air Domain		60 mm	70 mm	30 mm

Table 2 Material properties

Part	Materials	Properties	
		Density	Thermal conductivity
FETs	Silicon	2328 kg.m ⁻³	148 Wm ⁻¹ K ⁻¹
PCB	Copper	8950 kg.m ⁻³	401 Wm ⁻¹ K ⁻¹
	FR4	1850 kg.m ⁻³	0.294 Wm ⁻¹ K ⁻¹
Ambient	Air	1.225 kg.m ⁻³	0.024 Wm ⁻¹ K ⁻¹

Table 3 Table of model parameters

Parameter	Value		
Solver	PARDISO solver with Steady-State formulation		
Turbulence model	Laminar flow with standard wall function		
Properties of air (From COMSOL library)	Density	1.184 kg.m ⁻³	Ambient Temp = 25 °C
	Viscosity	1.849 e ⁻⁵ kg.m ⁻¹ . s ⁻¹	
Velocity inlet/outlet	0 m. s ⁻¹ (Enclosed case)		
Pressure outlet	0 Pa (gauge pressure)		
Convergence criteria	Residuals of continuity, e less than 10 ⁻³		

Table 4 Mesh property values for standard mesh sizes

Mesh sizes	Coarser	Normal	Fine	Extra fine
Mesh Properties				
No. of elements	46,395	212,649	560,560	6,155,529
Min. element quality	0.238	0.31	0.33	0.3
Avg. element quality	0.548	0.662	0.678	0.711
Element volume ratio	5.37e-04	3.51e-04	2.12e-04	1.04e-04
Mesh volume (mm ³)	4725	4725	4725	4725
Convergence parameter (Temperature)	84.19 °C	84.15 °C	84.14 °C	84.14 °C

To simulate the heat generated by the FET, a volumetric heat generation function of magnitude 30 W/chip was applied to the blocks. The chips are in contact with the air domain where natural convection occurs. The PCB is connected to a heat sink at

the bottom, which is depicted as a negative boundary heat flux of magnitude $10e8 \text{ W/m}^2$.

The base and wall temperatures are taken to be $25 \text{ }^\circ\text{C}$, and the copper laminated layer covers 25% of the surface, which leads to a net thermal conductivity of $100.12 \text{ Wm}^{-1}\text{K}^{-1}$ by the copper layer. There is a laminar type of flow within the enclosure.

2.3 Optimization Methodology

After going through multiple papers, a common structure for optimization was discerned (Fig. 2).

An ANN [5] was constructed using TensorFlow with the architecture shown in Fig. 3a. Two hidden layers with RELU activation function are used. The two layers have 18 and 10 neurons, respectively. This was then trained with MSE as the cost function and Adam as the optimizer. A train/test split of 0.8/0.2 was used. It was trained for 200 epochs. An R2 value greater than 0.97 was obtained for both train and test set showing that the model generalizes well and the pattern has been recognized. A continuous genetic algorithm was then coded to find the optimal placement. The algorithm generates a random placement and checks for overlap. If the placement is deemed valid, the coordinates are then used as input to the ANN which then gives a temperature prediction. This acts as the fitness value for the chromosome. Figure 3b represents the parameters used for the ANN.

3 Mesh Independence Study

As the number of discrete elements used to approximate the continuous solution increases, the accuracy of the CFD analysis of the actual solution also increases. But

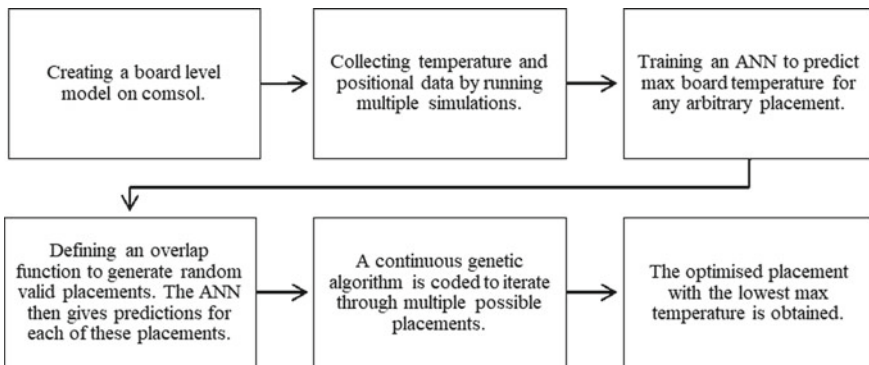


Fig. 2 Optimization methodology

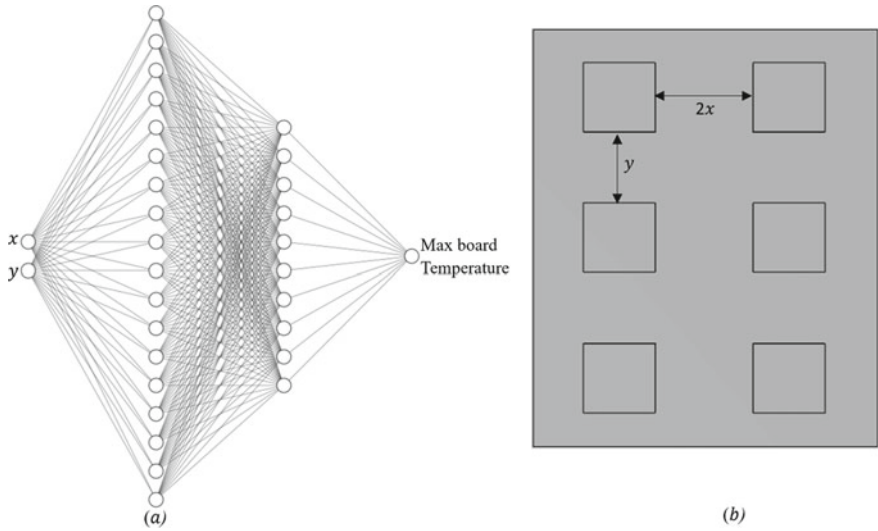
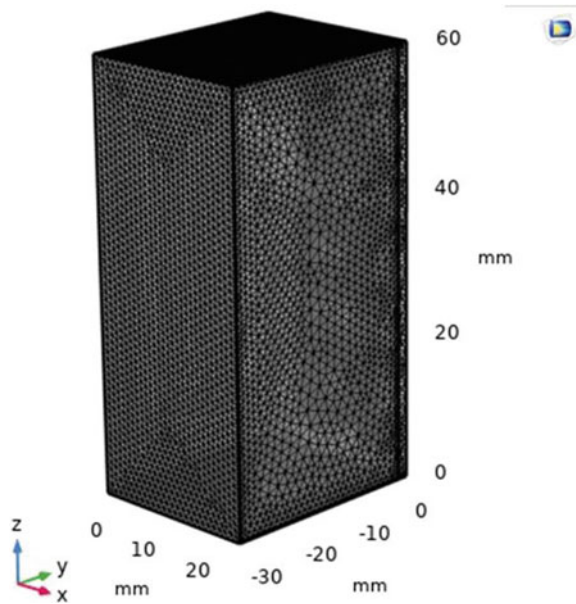


Fig. 3 a Model Architecture; b Input Parameters

Fig. 4 Meshed model of board and air domain



with the increase in the number of elements, the computational cost required to run the simulation also increases. Mesh independence study is carried out to determine the optimal point which gives a compromise between computational time and accuracy, and 'Fine' mesh size was chosen for the simulation. A continuous genetic algorithm

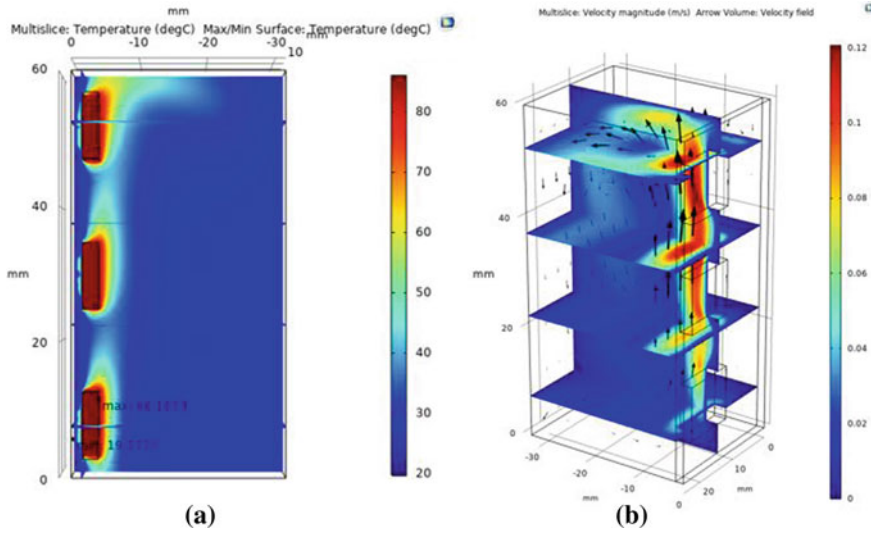


Fig. 5 **a** Temperature Graph for air inside casing; **b** Velocity plot

was then coded to find the optimal placement. The algorithm generates a random placement and checks for overlap. If the placement is deemed valid, the coordinates are then used as input to the ANN which then gives a temperature prediction. This acts as the fitness value for the chromosome.

4 Results and Discussion

4.1 Simulation Results

The effect of heat sources and motion of air in the PCB casing is studied through a temperature plot as shown in Fig. 5a and a velocity graph as shown in Fig. 5b. The changes in junction temperatures are studied by varying the positions of the FETs on the board, and the values are tabulated and used to train the ANN. A laminar flow air current is set up in the enclosure as shown in Fig. 5a.

4.2 Optimization Results

After collecting data by running a parametric sweep, it was observed that symmetric placements had more uniform temperature distribution and lower maximum temperature. This is due to the fact that symmetric placements maximize thermal spread per

chip. Hence to obtain the lowest possible board temperature, it suffices to go through only symmetric placements. Two inputs are sufficient to specify a symmetric placement as shown in Fig. 3b. The optimal placement for our symmetric case was found to be $x = 12.269$ mm and $y = 20.086$ mm, with the maximum board temperature being 86.163 °C. The answer obtained is intuitive as the maximum temperature obtained can be viewed as a trade-off between the chip's proximity to each other and the chip's proximity to the edge of the board. The placement that gives the optimal result is the one that isn't too close to the edge but not too close to the centre either. This behaviour can be observed in the graph. The validity of the optimization method depends on the degree to which the ANN can reproduce this pattern.

5 Conclusion

We have created a methodology to optimize board-level placements based on the placement of heat sources which can be extended to solve more complex problems, which include more parameters. The result obtained from minimizing the curve in Fig. 6 is found to be 86.155 °C. The result obtained from the optimization methodology is 86.163 °C and hence is in good agreement with the theoretical result.

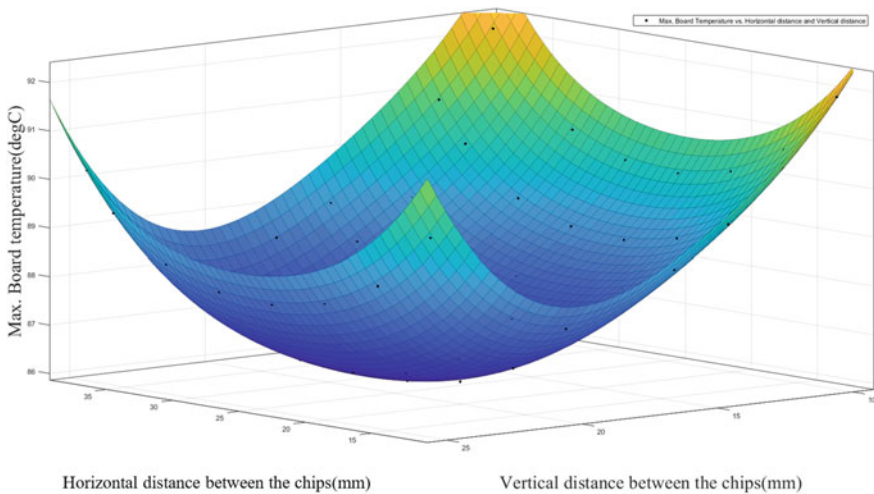


Fig. 6 Maximum board temperature for various placements

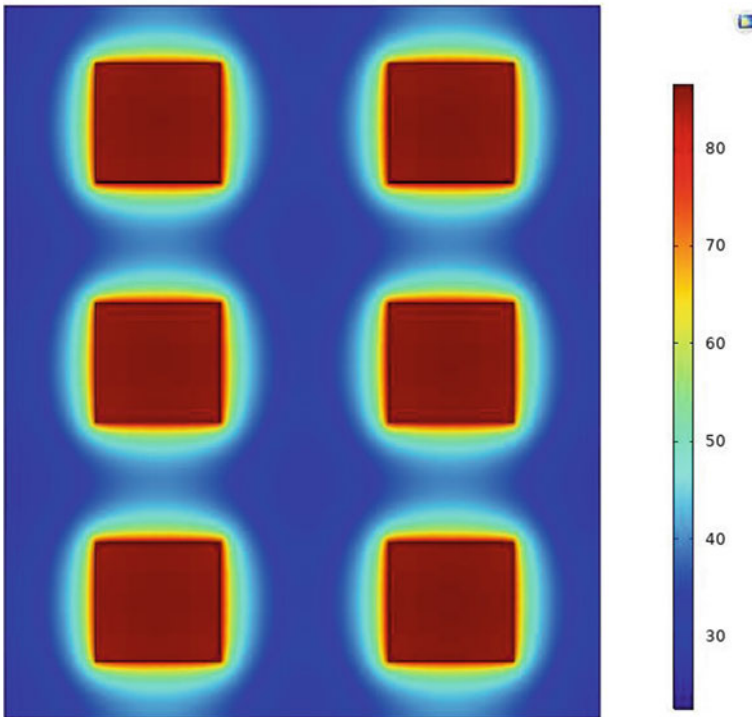


Fig. 7 Temperature distribution for final optimized placement

Acknowledgements The authors acknowledge the financial support from M/s Garrett-Advancing Motion for conducting the present study.

References

1. Suwa T, Hadim H (2007) Multidisciplinary placement optimization of heat generating electronic components on a printed circuit board in an enclosure. *IEEE Trans Compon Packag Technol* 30(3):402–410
2. Ismail FS, Yusof R, Khalid M (2012) Optimization of electronics component placement design on pcb using self organizing genetic algorithm (soga). *J Intel Manufact* 23(3):883–895
3. Jain S, Gea HC (1996) *Pcb layout design using a genetic algorithm*. The American Society of Mechanical Engineers
4. Suwa T, Hadim H (2008) Multidisciplinary heat generating logic block placement optimization using genetic algorithm. *Microelectron J* 39(10):1200–1208
5. SV A (2021) Placement optimisation code. <https://colab.research.google.com/drive/176hPHFfgTUyFUOWZVhiVwMljbdPIW4I>. Accessed 20 March 2022

A Simplified Thermal Model to Predict Temperature Profile and Heat Generation of Cylindrical Lithium-Ion Cells



Pritam Bhat and Mahesh K. Varpe

Abstract The cylindrical lithium-ion cells are being considered as one of the preferred energy storage systems in Electric Vehicles (EV). However, they have operational challenges involving temperature that greatly affects its life and performance. If the cell operating temperature exceeds the threshold limit, decomposition of the battery active material may occur which can trigger thermal runaway leading to the explosion in certain conditions. Therefore, a battery thermal model is essential to analyze the thermal response of the cell to design an efficient and effective battery thermal management system. This paper presents a simplified unsteady one-dimensional radial analytical thermal model to predict the temperature profile and heat generation of an isolated cylindrical cell under natural and forced convection. The model treats the cell as homogeneous body with uniform heat generation throughout the cell and the thermo-physical properties of the cell are assumed to be independent of temperature. The prediction of the model on the effect of forced convection cooling on the surface temperature of the cell for different heat transfer coefficient values is quite interesting. It is seen that surface temperature is under 30 °C for heat transfer co-efficient of 100 W/m² °C. The core and surface temperature non-uniformity across the radius of the cell is nearly 2 °C for different state of charge (SOC).

Keywords Lithium-ion · Heat generation · Battery thermal model

Nomenclature

C_p	specific heat capacity [J kg ⁻¹ K ⁻¹]
D	diameter of cylindrical cell [m]
$\frac{\partial U}{\partial T}$	entropic coefficient [mV K ⁻¹]
h	convective heat transfer coefficient [W m ⁻² K ⁻¹]

P. Bhat (✉) · M. K. Varpe
M. S. Ramaiah University of Applied Sciences, Bengaluru, India
e-mail: pritam.bhat9@gmail.com

H	enthalpy of reaction [kJ kg ⁻¹]
I	cell current [A]
k	thermal conductivity [W m ⁻¹ K ⁻¹]
L	length [m]
Q	heat generation [W]
Q _{gen}	volumetric heat generation [Wm ⁻³]
R	cell radius [mm]
R _e	internal cell resistance [mΩ] radial dimension [mm]
SOC	state of charge [%]
T	temperature [K]
t	time [s]
V	open circuit voltage [V]
U	cell potential [V]

Greek symbols

α	thermal diffusivity [m ² s ⁻¹]
ρ	density [kg m ⁻³]

Subscripts

a	ambient condition
avg	area averaged
c	core
irr	irreversible
o	initial condition
rev	reversible
s	surface condition

1 Introduction

The fast-depleting fossil fuel resources and the environmental concerns has motivated the need to explore environment friendly and viable alternative source of energy for transportation demand and other applications across the world. Also, the pollutants released from Internal Combustion (IC) engines working on fossil fuels is causing severe air pollution resulting in global warming and depletion of ozone layer. Kumar et al. [1] carried out a detail analysis of effects and causes of vehicular emissions and its impact on global climate change and environment. Thus, Electric Vehicles (EV)

are being developed as one of the alternate modes of mobility to IC engine powered vehicles to reduce the vehicular emissions, greenhouse gases and safeguard the environment for future generations. Honda, one of the leading automobile manufacturers claims to electrify two thirds of its global automobile's unit sales in 2030 with zero emission as EV does not have tailpipe emission or fuel evaporation [2]. The EV needs a portable source of energy to drive and power its powertrain. Thus, one of the requirements of EV is the Energy Storage System (ESS). The cost and performance of EV is dependent on the type of onboard ESS. ESS includes batteries, fuel cells and ultra-capacitors which supplies power to drive the EV. The secondary (rechargeable) batteries used to power EV come under the category of Electrochemical Storage Systems (EcSS) which is classified as another type of ESS. In EcSS energy is transformed from electrical to chemical and vice-versa through chemical reactions when connected with external electrical circuit. Rechargeable batteries store energy during charging phase and release energy during discharge phase [3, 4].

Lead-acid, Nickel-Cadmium, Nickel—Metal Hydride, Lithium-Ion, Lithium-Polymer are the different battery technologies available to meet the power requirements of EV. The choice of a battery technology for a given EV depends on number of factors viz. battery chemistry, stability, reliability, and its operating life, besides, performance of EV, range and cost. The different battery technologies and their specifications with potential applications are tabulated in Table 1. Lithium-ion batteries are preferred to power EV as it has high energy density, lower self-discharge rates, higher efficiency, and longer lifespan compared to other types of battery technologies [5]. In Li-ion batteries, the energy release and storage occur, when the lithium ions move from positive to negative electrode, back and forth via the electrolyte. Lithium cell, like general battery, consists of electrodes, electrolyte and separator as shown in Fig. 1. The lithium is initially present in positive electrode (anode) in the form of metal oxides, moves back and forth due to chemical reactions during charging and discharging cycles. Generally, lithiated metal oxides or phosphates are used as anode materials and graphite/silicon or lithiated titanium oxides materials as cathode. The Li-ion batteries can be of various types depending on the chemistry of materials used for electrodes and electrolytes. The performance of li-ion cells is influenced predominantly by different cell chemistries. Apart from the battery chemistries, li-ion batteries also come in various form factor such as prismatic cell, cylindrical, button and pouch cells. Prismatic and cylindrical li-ion cells are preferably used in current EV owing to ease of manufacturing, packaging, and maintenance. A few of the most common li-ion battery chemistry used in EV are listed in Table 1.

The performance of a lithium-ion battery is greatly influenced by operating temperature. The safe operating temperature of a typical li-ion cells/module/packs ranges from 15 °C to 35 °C [7]. Operating the battery outside the permissible range of temperature results in battery degradation, reduced life, low EV range and in extreme cases, can lead to thermal runaway and explosion of battery pack. Thermal modelling of li-ion batteries is essential in the design of battery pack to ensure it is operating in safe working limits. Li-ion cells generate heat due to complex chemical reactions occurring inside the cell during charge and discharge cycles. EV used for transportation necessitates batteries to be charged and discharged at very high C-rates which

Table 1 Different battery technologies and their applications [6]

Battery technology	Energy density [Wh/kg]	Cycle life [cycles]	Applications
Lead-Acid (LA)	35–40	2000	Used in IC engines powered vehicle as a starter, UPS systems and recently valve-regulated LA batteries are being used in low-cost EV
Nickel based	60–120	3000	Used in portable electronics, EV, HEV and starting aircraft engines
Zinc-Halogen	60–85	> 2000	Can be used for EV applications
Metal-air	60–700	> 1000	Al-air is used to power marine and underwater vehicles. Fe-air can be used as a power source for EV but has very low energy density of 60 Wh/kg
Sodium-beta	150–240	10,000	Have been used in older EV
Lithium	100–265	> 2000	Preferred for most of the portable electronic devices and EV because of its high energy density and specific capacity

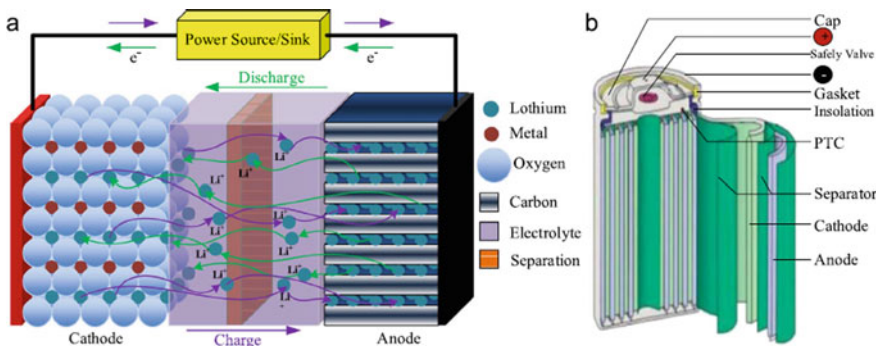


Fig. 1 Lithium-ion battery chemistry: **a** Discharging and charging **b** Sectional view of cylindrical battery [6]

leads to enormous heat generation rate. The generated heat must be dissipated to provide safe working environment for the li-ion cells. Therefore, thermal modelling of li-ion cells is essential to get an insight into the heat generation of the cell at various C-rates which may provide inputs to model the cooling requirements of the battery in thermal management system.

Table 2 Specification of commonly used lithium-ion battery chemistry in EV [10]

Battery chemistry	Specific capacity [mAh/kg]	Energy density [Wh/kg]	Cycle life [cycles]	Properties
LCO	140	110–190	500–1000	Less safe and good life
LMO	146	100–120	1000	Cheaper, safer than LiCoO ₂
NCA	180	100–150	2000–3000	High energy density and expensive
NMC	145	100–170	2000–3000	High cycle life and less safe
LFP	170	90–115	> 3000	Low cost and high stability at high operating temperatures
LTO	170	60–75	> 5000	High specific capacity and thermal stability

Li-ion cells exhibit a large anisotropic behavior in thermal conductivity (k) of the cell. The in-plane thermal conductivity is substantial in magnitude than the through-plane conductivity resulting in increased thermal resistance in the through-plane direction. In cylindrical battery cells (rolled stack layers), thermal conductivity is higher in axial direction (10–50 W/mK) and very low in radial direction (0.3–0.5 W/mK). Thus, the heat dissipation in cylindrical cells along the radial direction is minimal resulting in increased cell temperature [8, 9]. In the present work, a simplified unsteady one-dimensional radial analytical thermal model is developed to predict temperature of the li-ion cell. The battery cell is considered as homogeneous body in the thermal model with uniform heat generation throughout the cell and the thermo-physical properties of the cell are assumed to be independent of temperature. This approach in modelling is adopted to reduce the complexity besides achieving satisfactory prediction (Table 2).

2 Thermal Modeling

2.1 Theoretical Background

Thermal models predict the temperature profile of the cells during charge and discharge cycles. Few of the thermal models reported in the literature are simplified lumped parameter model, pseudo electrochemical-thermal model, equivalent circuit model, one-dimensional (1D), two-dimensional (2D), three-dimensional (3D)

complex numerical (FEA/CFD) models [11]. All these models require heat generation rates and thermo-physical properties of the cells as the input for modeling. A lumped parameter model considers entire cell at uniform temperature with negligible temperature gradient within the cell. The temperature prediction of the cell by the thermal model is sensitive to its complexity involving various heat generation parameters of the cell. The source of heat generation in a li-ion cell is represented by the following equation [12].

$$\dot{Q} = I(V - U^{avg}) + IT \frac{\partial U^{avg}}{\partial T} - \sum_i \Delta H_i^{avg} r_i - \int \sum_j (\bar{H}_j - \bar{H}_j^{avg}) \frac{\partial C_j}{\partial t} dv \quad (1)$$

where \dot{Q} is the heat generated/consumed, I is the current, V voltage, U is equilibrium potential, T is temperature, ΔH the variation of enthalpy of a chemical reaction i , r_i the rate of reaction, \bar{H}_j the partial molar enthalpy of species j , C_j its concentration, t the time and v the volume. The term 'avg' represents properties being evaluated at volume averaged concentration. The first term on the right side of Eq. (1) is the heat generated due to joule heating (irreversible resistive dissipation heat) and is always positive. The second term is reversible entropic potential and can be positive or negative depending on whether the cell is charging or discharging. The third term denotes the heat of chemical reaction of species. The last term of equation represents the heat of mixing occurring due to change in species concentration gradients of the cell. As the contribution of third and fourth term is minimal compared to the first two terms, and can be ignored with minimal errors in the temperature profile [12].

Consequently, the equation (1) reduces to simplest form [13] and is expressed as follows.

$$\dot{Q} = I(V - U) - IT \frac{\partial U}{\partial T} \quad (2)$$

where the term $I(V-U)$ is heat generation due to joule heating and $-IT \frac{\partial U}{\partial T}$ is the entropy change heat source term.

The irreversible heat generation due to joule heating can be expanded as

$$Q_{irr} = I(V - U) = I^2 R \quad (3)$$

Where 'R' is the internal resistance of the cell.

And the reversible heat generation due to entropic coefficient is expressed as

$$Q_{rev} = -IT \frac{\partial U}{\partial T} = -T \Delta S \frac{I}{nF} \quad (4)$$

where ' ΔS ' is the entropy change, n charge number ($n = 1$ for li-ion battery) and 'F' Faraday constant.

2.2 Model Description

The energy balance equation in radial direction is expressed as [11]

$$\frac{1}{r} \frac{\partial}{\partial r} \left(r \frac{\partial T}{\partial r} \right) + \frac{\dot{Q}_{gen}}{k} = \frac{1}{\alpha} \frac{\partial T}{\partial t} \quad (5)$$

The following boundary conditions at the cell centre and cell surface with initial conditions are applied.

$$\frac{dT}{dr} \Big|_{r=0} = 0 \quad \text{and} \quad -k \frac{dT}{dr} \Big|_{r=R} = h(T_s - T_a) \quad (6)$$

$$T = T_a \text{ at } t = t_0 \text{ for all } r \quad (7)$$

Here, \dot{Q}_{gen} is the heat generation per unit volume, α thermal diffusivity, k thermal conductivity, h heat transfer coefficient. Some part of the heat generated remains inside the cell as sensible heat and remaining part gets conducted through the cell layers to the cell surface and then it is dissipated to the surroundings by convective heat transfer. Mahamud and park [9] reported that the heat transfer in spirally wounded cylindrical cells, in the radial direction is very much lower than the axial direction due to the interfaces between the electrode layers. In the present model, 1D heat transfer with internal heat generation in the cylindrical cell is restricted to radial heat transfer only.

3 Results and Discussion

3.1 Validation of One-Dimensional Radial Analytical Model

The simplified one-dimensional radial battery thermal model is simulated using MATLAB[®]. The input parameters used in the model is tabulated in Table 3. The temperature profile of the cylindrical li-ion cell is obtained by simulating the model at constant current discharge rates of 0.5C, 1C and 1.5C. The thermal model solves the energy balance equation (5) for the given ambient conditions and input parameters to obtain temperature points within the cell along the radial direction for different state of charge (SOC). The density of the cell is estimated using the mass and volume data of the cylindrical cell. The heat generated at the battery core is conducted through the spirally wound battery layers to the surface of the cell which is then dissipated to the surroundings by natural convection as depicted in Fig. 2. The validation of model prediction considers both convection and radiation at the battery surface and thus equivalent heat transfer coefficient is utilized in the simulation. The comparison of average volumetric heat generation at 0.5C, 1C and 1.5C with the literature is

Table 3 Specifications and operating conditions of li-ion cells [14]

Battery technology: Li-ion battery (cathode: LiCoO ₂ ; Anode: Graphite)			
Battery specifications		Simulation conditions (validation case)	
Nominal capacity	4 Ah	Current	2 A (0.5C)
Diameter D	26 mm		4 A (1C)
Length L	65 mm		6 A (1.5C)
Nominal voltage	3.7 V	Initial Temperature	24 °C
Cut-off voltage	2.75 V	Heat transfer coefficient	8.4 W/m ² °C (0.5C)
Charge limit voltage	4.2 V		10.2 W/m ² °C (1C)
Density (ρ)	2550 kg/m ³		12.8 W/m ² °C (1.5C)
Specific heat capacity (Cp)	1197 J/kgK	Ambient temperature	24 °C
Thermal conductivity (k)	0.8 W/mk		
Internal resistance	0.5C–57.7 m Ω		
	1C–55.3 m Ω		
	1.5C–53.9 m Ω		
Maximum discharge current	2C		

presented in Table 4. The proposed model presents the temperature distribution in the cell at the battery core and the battery surface. The surface temperature curves are validated with results published in [14]. It is observed in Fig. 3 that the prediction agrees well with the experimental data for 50% of the total time with some deviation thereafter. The deviations observed in the predictions are attributed to the following.

- The experimental data from the referred literature were obtained from three-dimensional model
- The model discussed in present work assumes uniform heat generation which predicts a nearly linear trend of temperature with C-rates.
- Averaged value of reversible heat source is considered due to unavailability of the data in the literature.

Fig. 2 Description of the simplified battery thermal model

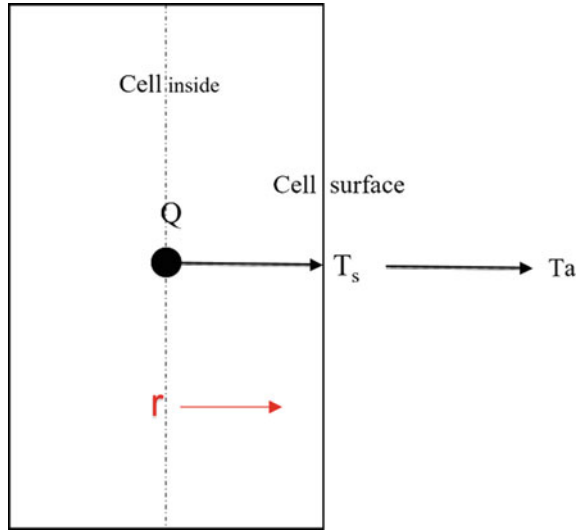


Table 4 Average heat generation of the li-ion cell

Constant current discharge rate	1D radial model (W/m ³)	Literature (W/m ³)	Percentage variation (%)
0.5C	6687	5761	14%
1C	26,751	23,588	12%
1.5C	60,190	52,715	12%

3.2 Effect of Forced Convection on the Temperature Profile

The temperature variation in the li-ion cells depends upon the rate at which the heat is dissipated from the battery to the surroundings. A forced convective heat transfer is effective in dissipating heat compared to natural convection. Most of the battery thermal management systems employ either liquid or air based forced cooling system to dissipate the heat to the surroundings. The cell thermal model is simulated at the maximum discharge current of 2C under the forced convection by using the heat transfer coefficient of 25, 50, 75 and 100 W/m² C. It can be observed from the Fig. 4 that the rise in cell surface temperature saturates quite early for heat transfer coefficient higher than 75 W/m² C. For 100 W/m² C, the cell surface temperature is contained under 30 °C for forced convection cooling. Any further increase in the heat transfer coefficient may not improve the cooling effectively. This is because the heat flow from the core of the cell to the ambient encounters two resistances in series, viz. conduction and convection resistance. Although convection resistance reduces by increasing heat transfer coefficient, conductance resistance is responsible for the thermal response of the cell. Figure 5 shows the temperature variation across

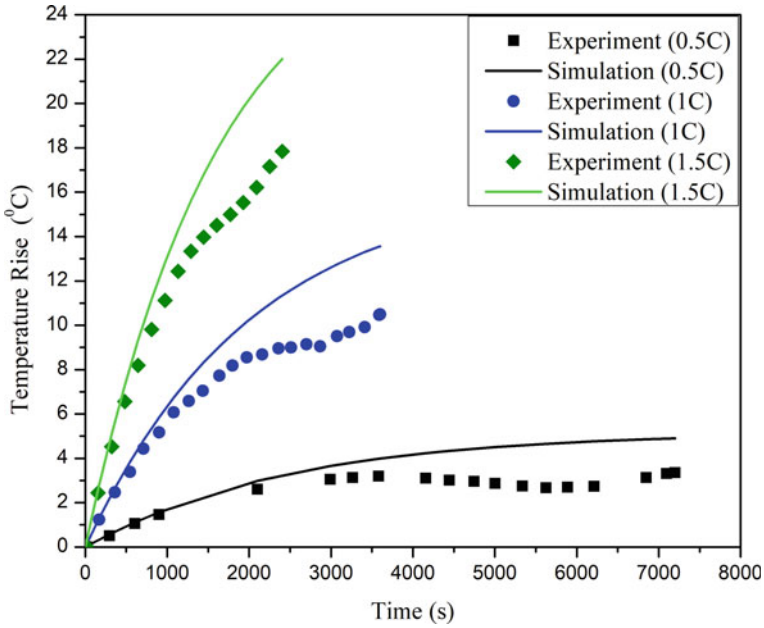


Fig. 3 Comparison of thermal model simulation and experimental data [14] for temperature rise at 0.5C, 1C and 1.5C discharge rates

the radius of the cell from cell center to surface for different state of charge (SOC) at heat transfer coefficient of 75 and 100 W/m² °C. A temperature non-uniformity exists between the cell core and surface with maximum temperature gradient of ~3 °C for a given SOC. It is inferred that decreasing the convection resistance only helps in reducing the cell surface temperature but does not have any effect on temperature gradient inside the cell.

4 Conclusions

This paper presents a one-dimensional radial thermal model to predict the temperature profile and heat generation of the cylindrical lithium-ion cell. The prediction of the model agrees satisfactorily with the experimental data. The model also predicts the effect of forced convection cooling on the surface temperature of the cell for different heat transfer coefficient values. Surface temperature of the cell remains nearly constant after 50% of discharge time for high heat transfer coefficient values attributing to zero heat dissipation from the cell after 50% SOC. It is also observed that the cell surface temperature is contained within the threshold limits for heat transfer co-efficient of 100 W/m² °C. The core and surface temperature non-uniformity across the radius of the cell is found to be around ~3 °C for a given SOC. Temperature

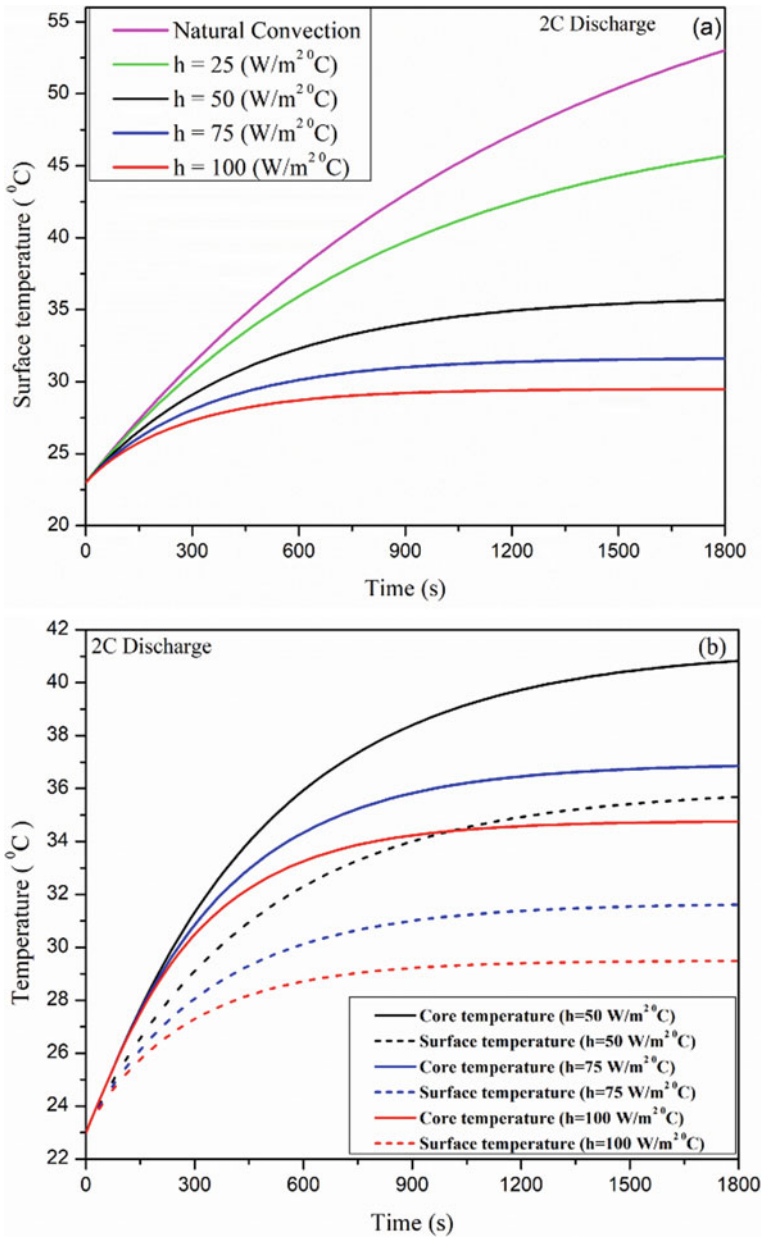


Fig. 4 **a** Surface temperature profile of the cell under natural and forced convection cooling, **b** Core and surface temperature variation of the cell for forced cooling

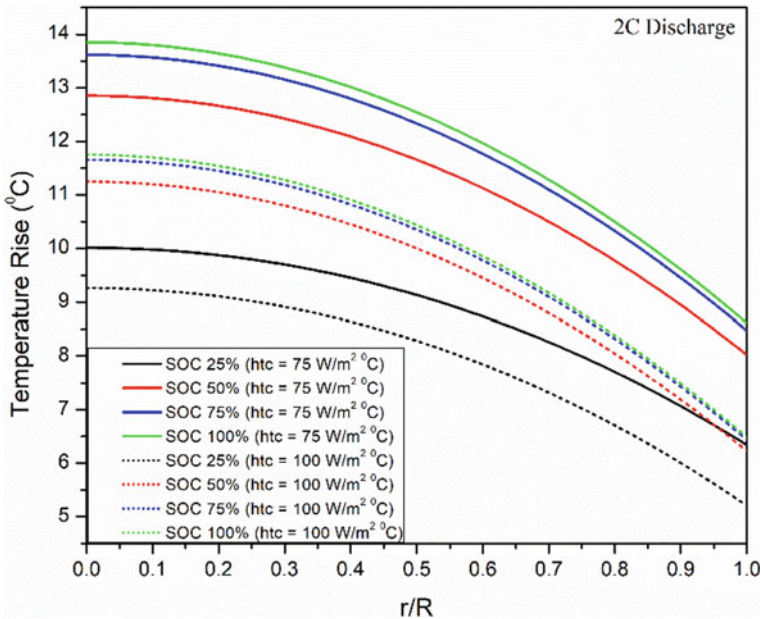


Fig. 5 Temperature variation across the radius of the cell at different SOC

gradient between the core and the surface of the cell remains almost constant with any heat transfer coefficient values higher than $50 \text{ W/m}^2 \text{ }^\circ\text{C}$.

References

1. Gireesh Kumar P, Lekhana P, Tejaswi M, Chandrakala S (2020) Effects of vehicular emissions on the urban environment- a state of the art. *Materials Today Proceedings*
2. Honda Global Homepage (2021). <https://global.honda/innovation/technology/automobile/electric-vehicles.html>. Accessed May 24, 2021
3. Linden, Reddy D (2002) *TB Handbook of Batteries*. 3rd edn. McGraw-Hill: New York, NY, USA
4. Ibrahim H, Ilinca A, Perron J (2008) Energy storage systems—characteristics and comparisons. *Renew Sustain Energy Rev* 12(5):1221–1250
5. Manzetti S, Mariasiu F (2015) Electric vehicle battery technologies: from present state to future systems. *Renew Sustain Energy Rev* 51:1004–1012
6. Hannan MA, Hoque MM, Mohamed A, Ayob A (2017) Review of energy storage systems for electric vehicle applications: issues and challenges. *Renew Sustain Energy Rev* 69:771–789
7. An Z, Jia L, Ding Y, Dang C, Li X (2017) A review on lithium-ion power battery thermal management technologies and thermal safety. *J Therm Sci* 26(5):391–412
8. Drake SJ, Wetz DA, Ostanek JK, Miller SP, Heinzl JM, Jain A (2014) Measurement of anisotropic thermophysical properties of cylindrical Li-ion cells. *J Power Sources* 252:298–304
9. Mahamud R, Park C (2013) Spatial-resolution, lumped-capacitance thermal model for cylindrical Li-ion batteries under high Biot number conditions. *Appl Math Model* 37(5):2787–2801

10. Stan A, Świerczyński M, Stroe D, Teodorescu R, Andreasen SJ (2014) Lithium ion battery chemistries from renewable energy storage to automotive and back-up power applications—an overview. *Int Conf Optim Elect Equip (OPTIM)* 2014:713–720
11. Al Hallaj S, Maleki H, Hong JS, Selman JR (1999) Thermal modeling and design considerations of lithium-ion batteries. *J Power Sourc* 83(1–2):1–8
12. Forgez C, Vinh Do D, Friedrich G, Morcrette M, Delacourt C (2010) Thermal modeling of a cylindrical LiFePO₄/graphite lithium-ion battery. *J Power Sourc*
13. Bernardi D, Pawlikowski E, Newman J (1970) A General Energy Balance for Battery Systems 132(1)
14. Paccha-Herrera E, Calderón-Muñoz WR, Orchard M, Jaramillo F, Medjaher K (2020) Thermal modeling approaches for a LiCoO₂ lithium-ion battery—a comparative study with experimental validation. *Batteries* 6(3):1–23

Mathematical Modeling and Parametric FEM Study on the Thermal Management of a Rectangular Microchannel Heat Sink



Ria Ann Zachariah, Neelima Kuttappa Mukkatira, M. Sachin Bharadwaj, V. Krishna, and Babu Rao Ponangi

Abstract Due to the fast-paced depletion of natural energy resources such as petroleum, more sustainable alternatives, like Electric Vehicles (EVs) are destined to become the new norm. This new demand has increased the amount of research happening in this field, especially with regard to the controllers of the EV, which act as the brain of the operation. Of all the factors that affect the efficiency and functioning of any power electronic system, temperature is the most important. Thermal management should therefore be considered early in the design process. In this discourse, microchannels are considered to be the cooling mechanism applied on a microchannel heat sink system. A mathematical model is proposed based on Finite Element Methods which simplifies the discretization and assembly of parallel and tapered microchannel systems and validates their rates of cooling against similar models constructed using CFD methods. The goal of the study is to obtain a robust mathematical model that can be used to generate data for all attempts at optimizing the cooling rates using combinations of genetic algorithms.

Keywords Mathematical modeling · Microchannel · Finite element · Thermal management

R. A. Zachariah (✉) · N. K. Mukkatira · M. S. Bharadwaj · V. Krishna · B. R. Ponangi
PMR Lab, Department of Mechanical Engineering, PES University, 100 ft Ring Road,
Banashankari Stage 3, Bangalore, India
e-mail: riazach29@gmail.com

N. K. Mukkatira
e-mail: neelimakuttappa@gmail.com

M. S. Bharadwaj
e-mail: sachinbharadwaj98@gmail.com

V. Krishna
e-mail: vkrishna@pes.edu

B. R. Ponangi
e-mail: baburaoponangi@pes.edu

Nomenclature

μ_f	Dynamic viscosity of the fluid (Ns/m ²)
C_p	Specific heat capacity at constant pressure (J/kgK)
D	Hydraulic Diameter of channel (μm , mm)
f	Friction factor
H_c	Height of the channel containing the coolant (μm , mm)
h_c	Overall heat transfer coefficient (W/m ² K)
k	Channel thermal conductivity (W/mK)
k_f	Coolant thermal conductivity (W/mK)
L	Length of the channel containing the coolant (cm)
m	Mass flow rate (Kg/s)
Nu	Nusselt number
Pr	Prandtl number
Re	Reynolds number
T	Average wall temperature (K)
t	Fin half thickness (μm)
T_f	Average fluid temperature (K)
V	Inlet velocity of the coolant (m/s)
w_c	Width of the channel containing the coolant (μm , mm)

1 Introduction

In a sustainable world, innovation revolving around natural resources like petroleum and natural oils cannot survive indefinitely as the core of our industries especially the mobility market. Cleaner alternatives such as Electric Vehicles (EVs) are emerging at the present, to combat the fast depleting petroleum issue. To achieve the best solution for this issue, researchers around the world are working toward optimizing the efficiency and life of EVs. The controller of an EV helps monitoring the overall system and ensure proper flow of energy and balance within the EV and hence its optimal functioning is extremely critical for best vehicle performance. The functioning of the controller is entirely due to power electronics, which are economical, lightweight, compact, integrated, and can operate efficiently at high switching frequencies and operational temperatures [1]. Despite these exceptional qualities, its performance can be sensitive to temperature which can affect the performance of the controller as a whole. For high performance electronics, the heat must be conducted away from the small surface area of the chip to ensure maximum efficiency. The thermal distribution within the substrate can also pose a threat to the overall electronic system [2]. Hence, thermal management of the controller must be considered at an early stage in design. Various techniques have been studied and employed to support the advancing computational power. Passive and active cooling methods were analyzed [3, 4] in 1981, presented a new technique of scaling liquid-cooled heat exchangers down to the

microscopic dimensions. This technique, now referred to as microchannel heat sinks, increased the limit of power density from 20W/sqcm to 1000 W/sqcm. The usage of microchannels resulted in compact configurations enabling it to be integrated with the miniaturized silicon chips. This makes microchannels the most sought-after cooling technique and hence was considered to be the system for our study. The analysis of microchannels can be done using different methods, both numerically and with the help of computer aided simulations [1].

2 Methodology

2.1 Problem Formulation

Microchannel cooling is commonly achieved with the aid of a heat sink that contains a large number of small channels. A suitable coolant is passed through these channels and hence heat is transferred through convection by the fluid, thereby cooling the device. Analysis for these microchannels with their own specific environments can be done using different methods, both numerical and with the help of computer aided simulation. The primary intent in this paper is to create a mathematical FEA model for a microchannel system which can be generalized for any geometric configuration. This model would be further used to determine the maximum wall temperatures and the pressure drop experienced across the channel for a given flow. This model was further used to analyze a parametric sweep study for varying height and width of the channel.

3 Mathematical Model

3.1 Creating a Mathematical Model for Wall Surface Temperature

Quadir et al. [5] were considered as the base study upon which a mathematical FEA model of a microchannel system was built. This would be applicable on any future geometrical configuration.

In Fig. 1, a uniform heat flux from a chip is imposed on the externally exposed face of the base. The other side of the base contains a series of rectangular channels which help in directing the flow of the coolant to enable heat transfer. The first step was to discretize the domain under study, which is described in Fig. 2. Each elemental microchannel wall was further defined using four noded bilinear elements. Conduction heat transfer was considered in two directions in both the vertical walls. The base wall had conduction from the heat sources and convective cooling from

Fig. 1 General structure of the rectangular microchannel arrangement

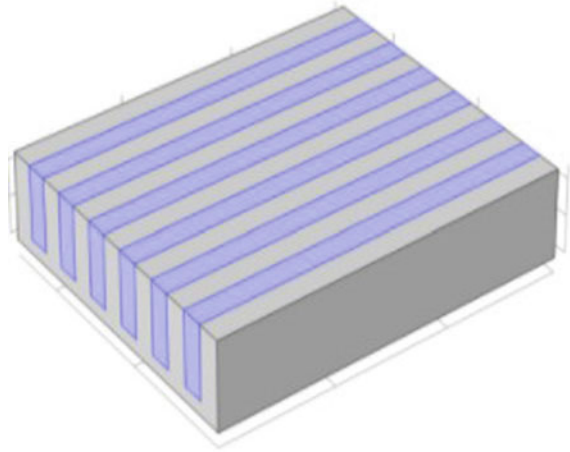
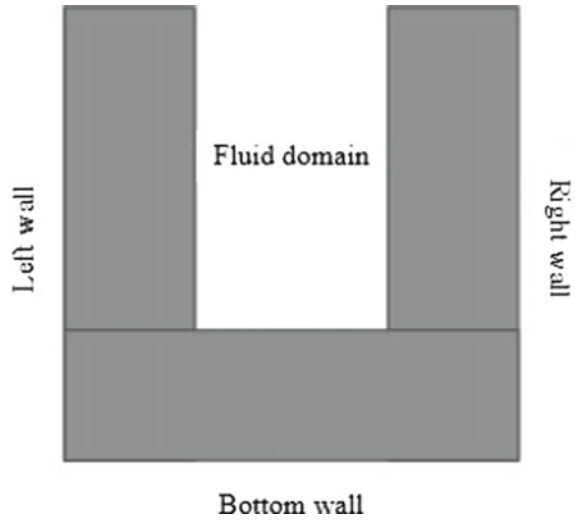


Fig. 2 Discretized domain under study



the coolant flowing above. Once the control volume was defined, energy balance equations for two walls and the coolant were stated.

Left:

$$k \frac{d^2 T}{dx^2} + k \frac{d^2 T}{dz^2} - \frac{h_c}{t} (T - T_f)_{Right} = 0 \tag{1}$$

Right:

$$k \frac{d^2 T}{dx^2} + k \frac{d^2 T}{dz^2} - \frac{h_c}{t} (T - T_f)_{Right} = 0 \tag{2}$$

Table 1 Coolant properties

Properties	Value
Fluid velocity	1.973 m/s
Coolant inlet temperature	10
Coolant thermal conductivity(k_f)	0.609 W/mK
Coolant absolute viscosity(μ_f)	$9.8 \times 10^{-4} \text{Ns/m}^2$
Coolant specific heat capacity(C_{pf})	4180 J/kgK
Coolant density(ρ_f)	1000 kg/m ³

Coolant:

$$mC_p \frac{dT_f}{dx} - h_c H_c (T - T_f)_{Left} - h_c H_c (T - T_f)_{Right} - h_c w_c (T - T_f)_{Bottom} = 0 \tag{3}$$

The finite element formulation of these equations was performed using the Galerkin method [6]. The temperature driving potential for the convective heat transfer was assumed to be the weighted residual integral. These equations were solved on the Maple software simultaneously for each node in the control volume. The coefficients obtained were arranged to attain a global matrix for an elemental microchannel. Subsequently, an algorithm for an assembly of such elemental microchannels was created, which enabled us to get further converging results with [5]. The dimensions used to build the geometry in Fig. 1 are as follows:

- Channel height—200 μm .
- Channel width—56 μm .
- Fin half thickness—12 μm .
- Channel length—0.5 cm.

The channel is made of silicon and its thermal conductivity is 125 W/mK. The coolant considered is water and its general properties are given in Table 1. The overall heat transfer coefficient for this study is 54,290 W/m²K.

3.2 Parametric Study

In parametric studies, the mathematical model formed was further tested by varying channel height and width while keeping the channel length constant which helped analyze the cooling effect of the heat sink using the specific coolant.

Two variations were analyzed as follows:

- Varying height with width constant.
- Varying width with height constant.

The parameter values used are as follows:

Height: 11 mm, 12 mm, 13 mm, 14 mm.

Width: 3.80mm, 3.85mm, 3.90mm, 3.95mm.

The other dimensions and properties of the channel are as follows:

Half fin thickness—2 mm.

Channel length—60 mm.

Channel Thermal Conductivity (Aluminum)—237 W/mK.

The coolant considered in this scenario was water and its properties are given in Table 1.

3.3 Maximum Wall Surface Temperature

To calculate the maximum wall surface temperature, heat transfer coefficient for this was calculated using two different formulas for Nusselt number.

Equation 1:

$$Nu = 0.023 Re^{0.8} Pr^n \quad (4)$$

where $n = 0.4$ for heating of fluids Eq. 2:

$$Nu = \frac{\left(\frac{f}{8}\right) Re Pr}{1.07 + 12.7 \left(\frac{f}{8}\right)^{0.5} [Pr^{0.67} - 1]} \left(\frac{\mu_m}{\mu_w}\right)^n \quad (5)$$

where

$$\frac{\mu_m}{\mu_w} \quad (6)$$

was assumed to be 1. Here, $f = 0.184 Re^{-0.2}$.

3.4 Pressure Drop Across Microchannel

The friction factor was calculated using a generalized formula for smooth tubes

$$f = 0.184 Re^{-0.2}; Re > 10^4 \quad (7)$$

From this the pressure drop was calculated using

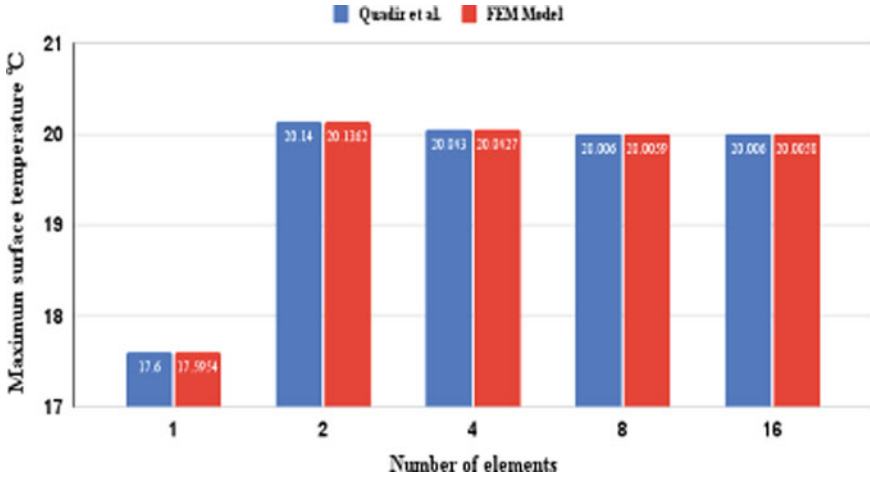


Fig. 3 Maximum surface temperature obtained using the developed mathematical model against the values given in Quadir et al

$$\Delta P = f \frac{L}{D} \left(\frac{V^2}{2} \right) \tag{8}$$

4 Results and Discussions

4.1 Creating a Mathematical Model for Wall Surface Temperature

The maximum surface temperature obtained using the mathematical model mentioned above is plotted in Fig. 3 against the values given in [5]. This also portrays that post eight elements, the maximum surface temperature is independent of the number of elements undertaken for study. With this Quadir et al. were validated and the developed mathematical model is ready to be used for any given configuration.

4.2 Parametric Study: Maximum Wall Surface Temperature

The first variation was done by keeping the width constant and varying the height. The maximum surface temperature obtained for this, with both the heat transfer values have been plotted in Fig. 4. From this it can be concluded that by keeping

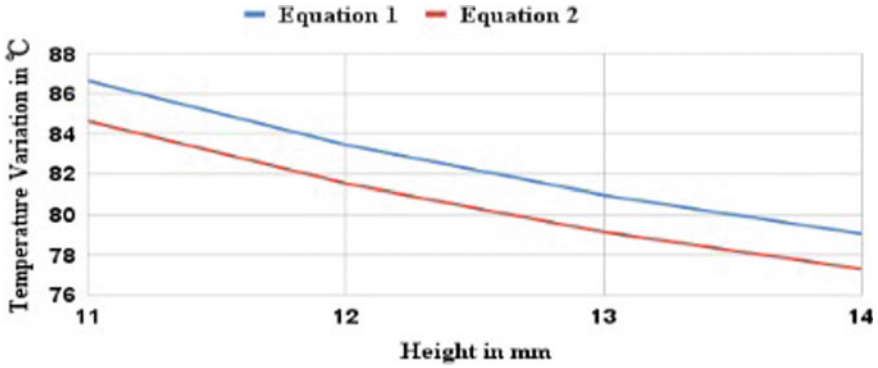


Fig. 4 Maximum surface temperature obtained at constant 3.8 mm width with varying height

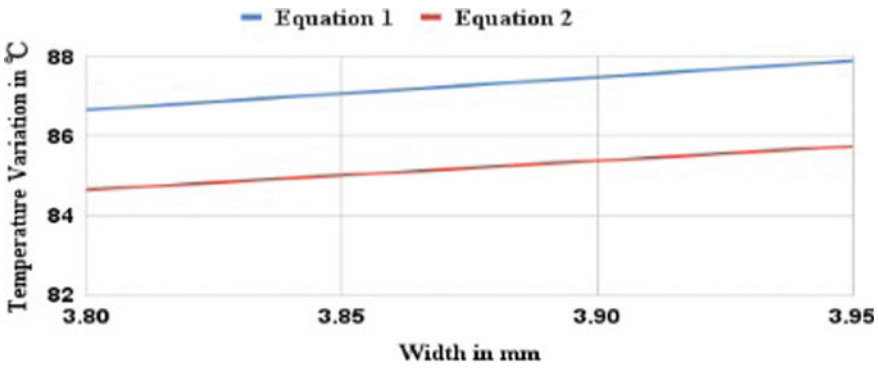


Fig. 5 Maximum surface temperature obtained at constant 11 mm height with varying width

the width constant and increasing the height, maximum surface temperature tends to decrease.

The second variation was done by keeping the height constant and varying the width. The maximum surface temperature obtained for this, with both the heat transfer values have been plotted in Fig. 5. From this it can be concluded that by keeping height constant and increasing the width, maximum surface temperature tends to increase.

Both these trends are consistent with those observed in [7].

4.3 Parametric Study: Pressure Drop Across Microchannel

The first variation was done by keeping the width constant and varying the height. The pressure drop values obtained have been plotted in Fig. 6. From this it can be

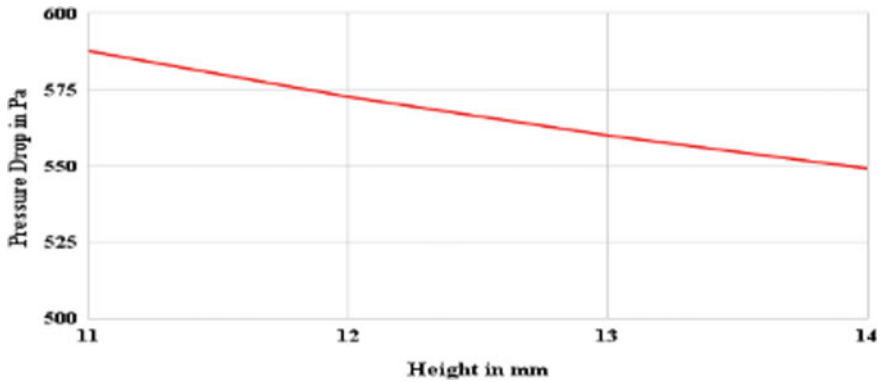


Fig. 6 Pressure drop obtained at constant 3.8 mm width with varying height

concluded that with the increase in height, keeping width constant, the pressure drop value decreases.

The second variation was done by keeping the height constant and varying the width. The pressure drop values obtained have been plotted in Fig. 7. From this it can be concluded that with the increase in width, keeping height constant, the pressure drop value decreases.

These trends are consistent with similar studies that correlate the varying dimensions of the microchannel setup to the pressure drop across the channel. Pressure drop decreases marginally both with the increase in height and width [7].

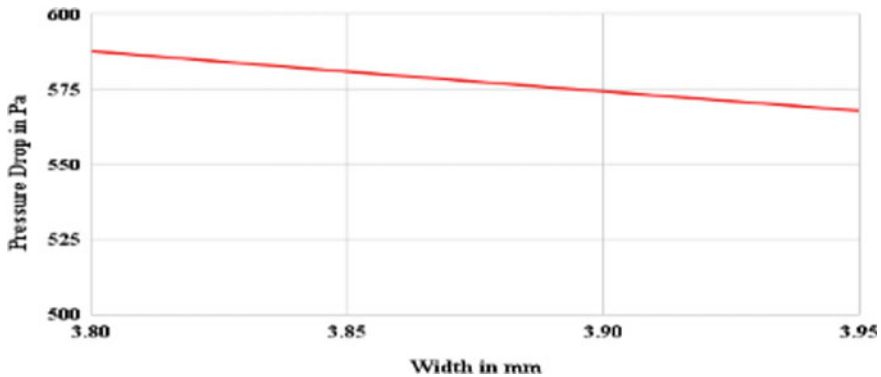


Fig. 7 Pressure drop obtained at constant 11 mm height with varying width

5 Conclusion

Quadir et al. were validated and the maximum wall surface temperature values were attained with no error. The mathematical model generated in this validation was further used in the parametric study of the microchannel for varying values of the height and width to analyze the sensitivity of these parameters and the optimal performance of the heat sink under the specified coolant. Through this it was observed that the maximum surface temperature is directly proportional to the increase in width and inversely proportional to the increase in height. Another conclusion obtained from the parametric study was the variation of pressure drop across the channel with the change in height and width of the microchannel. The pressure drop was found to decrease by 18.28% for 1 mm increase in width compared to 2.56% decrease for 1mm increase in height.

Acknowledgements The authors acknowledge the financial support from M/s Garrett—Advancing Motion for conducting the present study.

References

1. Shahjahanlal M., Lu H., Bailey C (2014) A review of the computer based simulation of electro thermal design of power electronic devices. 20th International Workshop on Thermal Investigations of ICs and Systems
2. Jeevan, Qadir, Seetharamu (2005) Optimization of thermal resistance of stacked micro- channels using genetic algorithms. *Inter J Numer Methods Heat Fluid Flow*
3. Garrett JM, Colin PM, Matthew JR, Steve RD, Nicholas T, Scott MT (2019) Thermal management of vehicle cabins, external surfaces and on board electronics: an overview. *Res Vehic Eng Rev* 5(5):954–969
4. Tuckerman DBW, Pease RF (1981) High performance heat sinking for VLSI. *IEEE Elec t. Dev. Lett.* EDL-2(5)
5. Qadir G, Mydin A, Seetharamu K (2001) Analysis of microchannel heat exchangers using FEM. *Inter J Num Methods Heat Fluid*, 11
6. Lewis RW, Nithiarasu P, Seetharamu K (2004) *Fundamentals of finite element method for heat and fluid flow.* John Wiley & Sons Ltd.
7. Ling Ling (2012) Numerical investigation of the cooling performance of microchannel heat sinks under uniform and non-uniform heating conditions. Diss Concordia University

Production of Cotton Seed Biodiesel and Its Usage in a C I Engine with Methyl Ester and Al₂O₃ Additives



Basavaraj Ganiger and B. Yuvaraj

Abstract In this work, cotton seed crude oil was obtained from the dried seeds using mechanical device called expeller. The free fatty acid (FFA) of cotton seed crude oil was found higher so it was subjected to double stage transesterification process. The maximum yield of cotton seed biodiesel was found with optimized variables; catalytic concentration, molar ratio and reaction time. In addition to pure biodiesel usage the methyl ester (neat diesel) and Al₂O₃ nano particle additives were used to blend the biodiesel in different proportions. The properties of the blend made of 20% cotton seed biodiesel and 80% methyl ester and Al₂O₃ nanoparticles were found close to pure diesel properties. A single cylinder, four strokes diesel engine was tested at different loads by maintaining constant speed with cotton seed biodiesel and its blends with methyl ester and Al₂O₃. It is observed that comparatively higher brake thermal efficiency (BTE), lesser brake specific fuel consumption (BSFC) and higher exhaust gas temperature (EGT) for blend made of 20% cotton seed biodiesel and 80% methyl ester and Al₂O₃ nanoparticles.

Keywords Cotton seed · Mechanical expeller · Trans-esterification process · Methyl ester · Al₂O₃ · BTE · BSFC & EGT

Abbreviations

BSFC	Brake specific fuel consumption
BP	Brake power
BTE	Brake thermal efficiency
B20	20% Biodiesel
B20A30	20% Biodiesel with 30 ppm Nano particles

B. Ganiger
Sapthagiri College of Engineering Bangalore, Bangalore, Karnataka, India

B. Yuvaraj (✉)
Research Scholar, VTU Regional Centre, Mysuru, Karnataka, India
e-mail: yuvarajyuv1030@gmail.com

B20A60	20% Biodiesel with 60 ppm Nano particles
B40A30	40% Biodiesel with 30 ppm Nano particles
B40A60	40% Biodiesel with 60 ppm Nano particles
Al ₂ O ₃	Aluminum Oxide
CO	Carbon monoxide
CO ₂	Carbon dioxide
FFA	Free Fatty Acids
CNG	Compressed Natural gas
EGT	Exhaust gas temperature
RSM	Response Surface Methodology

1 Introduction

The depletion of fossil fuel attached with an increase in fuel charges has been directed the research for other alternatives such as biodiesel, ethyl alcohol and many renewable energies. A Biodiesel is an alkyl ester of fatty acids obtained from plants or animals. These fatty acids can be converted into short chain alcohols such as methanol and ethanol by the trans-esterification process [1]. Biodiesel has numerous advantages over conventional diesel with respect to renewability, nontoxicity, biodegradability etc. Biodiesel contains lesser amount of sulphur compounds and a higher flash point (>1300 °C), lower CO₂ and hydrocarbon emissions and also considerably lesser particulate matter [2].

Higher worth of crude oil and in the view of environmental pollution reduction, the biodiesel as an alternate fuel is extremely concern subject. The biodiesel is the demand of many Asian countries as an alternate fuel to substitute for costly crude oil. The utilization of vegetable oils for cookery purpose raises the matter of their disposal. The correct utilization of these oils is an advantageous by the biodiesel production. The vegetable oil alkyl radical organic compound might be one in all the nice sources for production of biodiesel that is an alternate fuel of diesel [3].

In addition to reduction of dependency on crude oil, biodiesel has a helpful social impact by encouraging farmers to produce oil crops and receive an income [4]. The oils from diverse sources have varying fatty acid compositions. The fatty acids have variations with respect to degree of unsaturation and the chain length. There is a growing interest on non- edible tropical crops such as Honge, *Jatropha curcas* etc. It is found that algae have oil productivities more than any land-based crops and can meet global demand for transport fuels [5, 14].

The biodiesel production process requires either base or acidic materials as catalysts. The Sodium methoxide, Sodium hydroxide and Potassium hydroxide are the most normally used catalysts. Depending on the alcohol triglyceride ratio, concentration, mixing and temperature base catalyzed reactions are quite faster. Compared to base catalysts, acid catalysts (sulfuric and phosphoric acids) reactions have been noticed to be slower [6, 15].

Low-emission fuels like fermentation alcohol, methyl ester and compressed natural gas (CNG) for diesel engines should be developed crucially [7–9]. Cheap oils can be used for C I engine if there is any shortage of crude oils. Biodiesel is popular because of its inexhaustibility, biodegradability and harmlessness. Methyl ester can be manufactured by trans-esterification process. The biodiesels have higher cetane number and free from foul smell [10–13].

2 Methodology

2.1 Biodiesel Production

The process of biodiesel production is having several steps as shown in Fig. 1. The

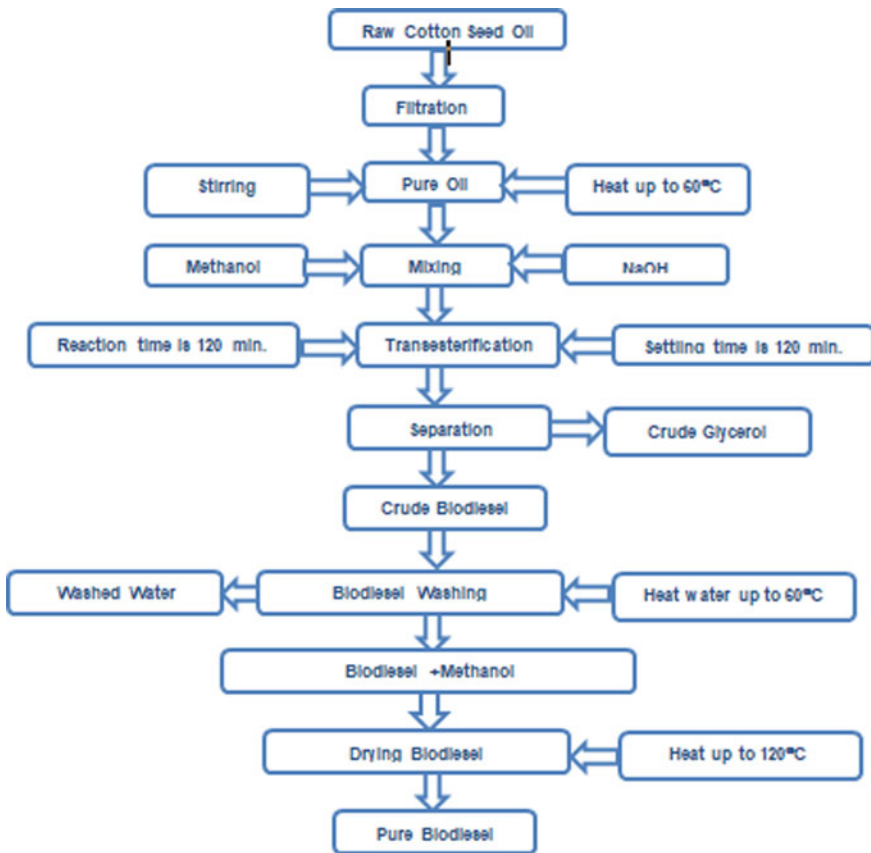


Fig. 1 Production of biodiesel from cotton seed oil

flow chart explains the biodiesel production from cotton seed oil by alkali base trans-esterification process. In this pretreated oil subjected to a trans-esterification process under the suitable alcohol generally methanol and catalyst at given temperature and reaction time. After the process, taken the reaction solution in a separating flask to separate glycerol formation and soap residuals. Based on their densities biodiesel, glycerol and residuals are separated in separating flask two hour later. Separated the glycerol and soap residual from the biodiesel and then carried water wash to the biodiesel and then heated the biodiesel above 100 °C.

50 kg cotton seeds were collected and mechanical expeller was used and got an oil yield of 25 percentages means, 250 ml of oil per kg of cotton seed. In the cotton oil production process it is necessary to remove some impurities by filtration. Since the free fatty acid content was found more, alkali acid trans-esterification was followed. The apparatus used in the biodiesel production has shown in Fig. 2.

The trans-esterification process was carried out by pouring one liter filtered cotton oil into three flasks and fixed a condenser to the flask and mixed 5.5 grams of Sodium Hydroxide (NaOH) and 250 ml methanol, solution was prepared. The solution was heated to 600 °C using heater and simultaneously stirred regularly with magnetic

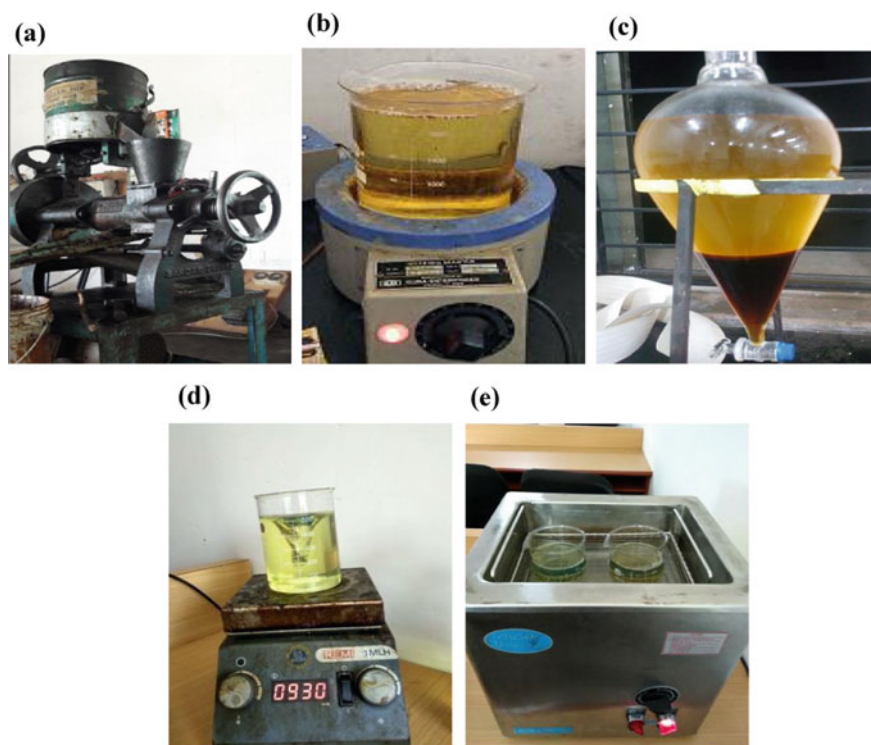


Fig. 2 Apparatus used in the Biodiesel Production; **a** Oil Expeller, **b** Oil Heater, **c** Separation Flask, **d** Magnetic Stirrer and **e** Sonicator

stirrer at speed 600 rpm. The solution was poured into a beaker. The solution was stirred for 2 hours to achieve appropriate reaction. The mixture was transferred into a separate flask and allowed to settle. After the 2 hours settling time in the separation flask two phases were formed; Methyl ester and Glycerol. The glycerol was removed from the separation flask then Poured 1 liter of hot water (600 °C) into the separation flask for water wash. Also to separate soap content 4 to 5 times the water washing was repeated. The methyl ester from the separation flask was transferred to open measuring glass and heated using electrical radiator for around 1200 °C. So methanol vaporized and only methyl ester remained in the flask. It is recorded that from 1 liter of cotton seed oil, 947 ml of biodiesel can be obtained.

2.2 Preparation of Biodiesel Blends with and Without Addition of Aluminum Oxide Nano Particle

Biodiesel extracted from the cotton seed oil is blended with diesel and aluminum oxide nano particles. The B20 (20% Biodiesel and 80% Neat Diesel) taken in a beaker and 0.03 grams of Al_2O_3 per 100 ml blend (30 ppm) was injected. The solution was placed on magnetic stirrer at constant speed and constant temperature of 400 °C for thorough mixing of added nano particles up to 1 hour. This Biodiesel blend with Al_2O_3 was used directly for combustion in diesel engine without any modification. Similarly the Al_2O_3 nano particles added in distinctive proportion of 30 ppm and 60 ppm for B20 (20% Biodiesel and 80% neat diesel), B40 (40% Biodiesel and 60% neat diesel) and B60 (60% Biodiesel ester and 40% neat diesel).

2.3 Experimental Details and Instruments Used

Performance characteristics were studied by using water cooled, single cylinder, 4 strokes diesel engine which had BP of 5.2 kW at 1500 rpm. The experimental set up has shown in Fig. 3. The experimental setup made in such way that by maintaining constant water flow to cool down the engine and heat transfer in the exhaust line. The engine specifications are listed in Table 1. An eddy current dynamometer was used to give load to engine and it was computer interfaced to record the digital data.

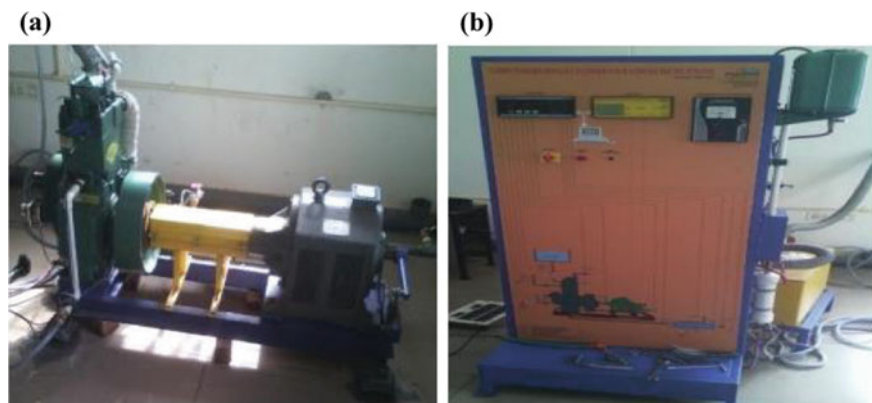


Fig. 3 Experimental set up; **a** Test rig and **b** Control unit

Table 1 Test engine specifications

Particulers	Details
Type of engine	4 stroke diesel engine
Engine make	Kirloskar TV1
Number of cylinder	Single
Engine capacity	661 cm ³
Compression ratio	16.7:1
Bore	87.5 mm
Stroke	110 mm
Brake power	5.2 kW@ 1500 rpm

3 Results and Discussions

3.1 Effect of Al₂O₃ Additive on Cotton Seed Oil Properties

The flashpoint of pure biodiesel is more compared to petro diesel but it is possible to reach the flash point of diesel by adding the aluminum oxide to biodiesel. From Fig. 4a-e, it can be observed that as biodiesel percentage increases in the blends there is an increase in flash point. Among blends B20A60 has flash point nearer to diesel (67 °C). Also the blend B20A60 has fire point nearer to diesel; 700 °C, viscosity nearer to diesel; 3.45 cSt.

Cotton seed biodiesel has maximum density of 900 kg/m³ and Al₂O₃ has a maximum density of 3700 kg/m³. It can be observed from Fig. 4 that addition of Al₂O₃ causes increase in the density of biodiesel. Among blends B20A60 has density close to Diesel; 833.8 kg/m³. It can also be observed that as biodiesel percentage in blends increases there is a decrease in calorific value. It is because of the reason that biodiesel is an oxygenated fuel; its calorific value is less compared to diesel. Diesel

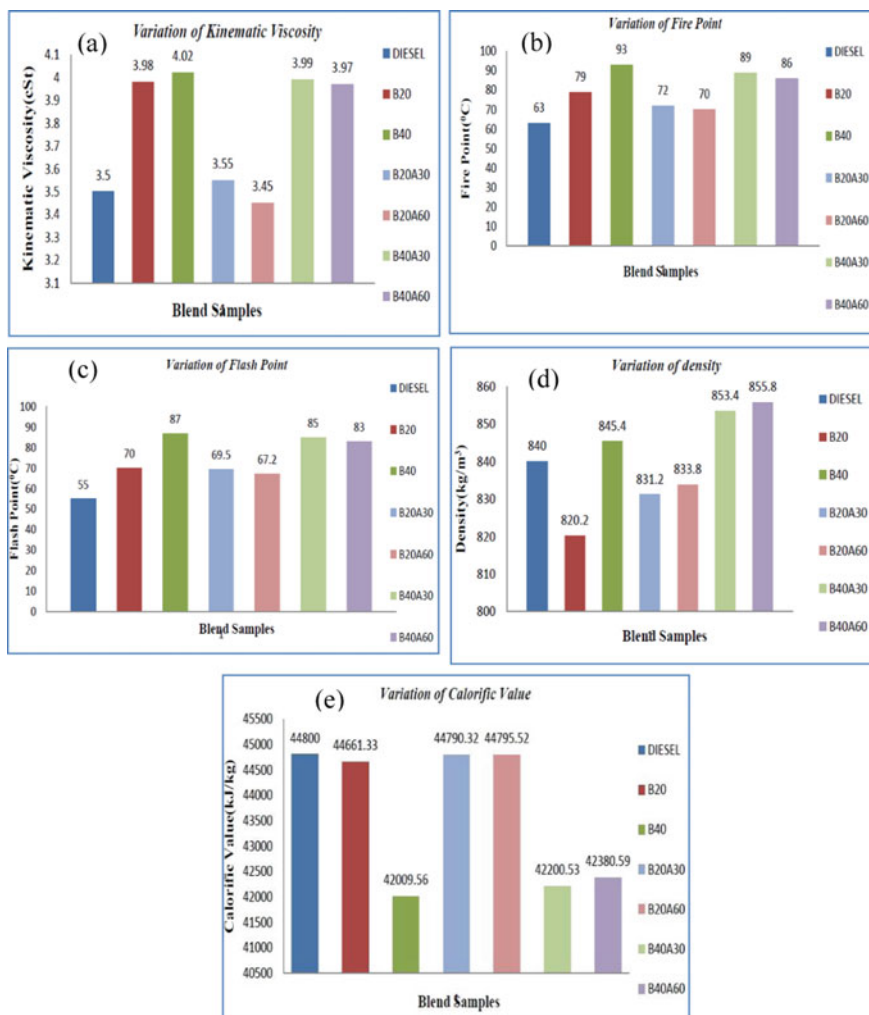


Fig. 4 a–e Comparison of fuel properties; **a** Flash point, **b** Fire point, **c** Viscosity, **d** Density and **e** Calorific value

has a highest calorific value of 44800 kJ/kg and B20A60 has calorific value nearer to diesel; 44795.52 kJ/kg.

3.2 Effect of Al₂O₃ Additive on Engine Performances

The performance parameters such as brake thermal efficiency, specific fuel consumption and exhaust gas temperature have been studied using neat diesel and biodiesel

blends with and without catalysts and results have shown in Fig. 5a-f. Brake Thermal Efficiency (BTE) is a parameter that shows the amount of heat energy of fuel converted into mechanical energy. It can be observed that addition of Al_2O_3 to biodiesel and/or diesel blends resulted in an increase of BTE. Highest BTE was noticed for the blend B40A60 (48.18%). Even though the calorific value of blend B40A60 is less than diesel highest BTE was achieved because of better mixing of fuel and air and good combustion.

Brake specific fuel consumption (BSFC) is another parameter that measures the amount of heat energy of fuel converted into mechanical energy. The Al_2O_3 blended fuels have lower BSFC than blends without Al_2O_3 because at high temperatures it mixes properly with air, resulting in good combustion process, producing higher power output and reduced BSFC. Least BSFC of 0.0029 kg/kW-min noticed with the blend B20A60.

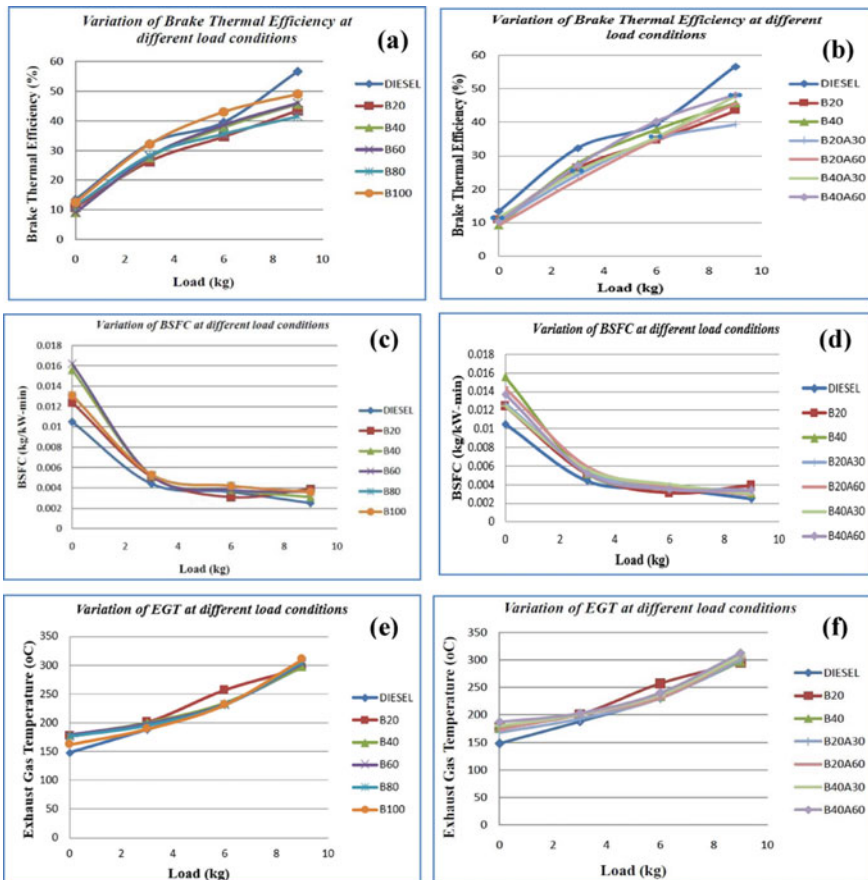


Fig. 5 a–f Variations in performance characteristics; **a** BTE without Al_2O_3 , **b** BTE with Al_2O_3 , **c** BSFC with Al_2O_3 , **d** BSFC without Al_2O_3 , **e** EGT without Al_2O_3 and **f** EGT with Al_2O_3

Exhaust gas temperature (EGT) of a fuel depends on properties like kinematic viscosity, calorific value and cetane number. It can be observed that, with an increase in load EGT also increases since more fuel is injected to maintain same power output. As biodiesel percentage increases in the blends, EGT also increases compared to diesel fuel. It is because biodiesel has more viscosity than diesel which results in poor atomization, because of which proper mixing of fuel and air couldn't happen and hence incomplete combustion occurs during combustion process hence increase in EGT. It can also be observed that addition of Al_2O_3 to blends increases the EGT compared to diesel. This is could be due to lower cetane number leads to longer ignition delay which again causes incomplete combustion of fuel during combustion process and increases the EGT. Highest EGT of 312 °C was observed for the blend B40A60 at high load condition.

4 Conclusions

- The cotton seed biodiesel production is not costly and it uses simple and basic system. Response surface methodology was found good and easy procedure in finding the parameters to expand the biodiesel yield.
- B20 fuel usage shown brake thermal efficiency of 43.83% and when Al_2O_3 was added into blends and compared with B20 and B40 fuel, there was BTE 45.43% in B20A60 and BTE 48.18% in B40A30.
- When diesel and biodiesel blends used for diesel engine, an increase of load showed reduction of brake specific fuel consumption. B40 blend usage resulted in 0.0031 kg/kW-min BSFC at extreme load and it is having lower BSFC next to neat diesel fuel which is 0.0025 kg/kW-min. When Al_2O_3 was added into blends and compared with B20 and B40 fuel, there was BSFC 0.0029 kg/kW-min in B20A60 and 0.003 kg/kW-min B40A30.

References

1. Leenus M, Edwin V (2012) A comparative analysis of different methods to improve the performance of cotton seed oil fuelled diesel engine. *Fuel* 102:372–378
2. Alhassan Y, Kumar N, Bugaje I, Pali H, Kathkar P (2014) Co-solvents trans-esterification of cotton seed oil into biodiesel: effects of reaction conditions on quality of fatty acids methyl esters. *Energy Conv Manag* 84:640–648
3. Hong Li Y, Benxian S (2009) Biofuel potential production from cottonseed oil: a comparison of non-catalytic and catalytic pyrolysis on fixed- fluidized bed reactor. *Fuel Proc Technol* 90:1087–1092
4. Nurun N, Mustafizur M, Shamim A (2009) Biodiesel from cotton seed oil and its result on engine performance and exhaust emissions. *Appl Therm Eng* 29:2265–2270
5. Onukwuli D, Emembolu L, Ude C, Aliozo S, Menkiti M (2016) Optimization of biodiesel production from refined cotton seed oil and its characterization. *Egypt J Petrol* 1–8

6. Royon D, Daz M, Ellenrieder G, Locatelli S (2007) Enzymatic production of biodiesel from cotton seed oil using t-butanol as a solvent. *Bio Res Technol* 98:648–653
7. Senthilraja R, Sivakumar V, Thirugnanasambandham K, Nedunchezian N (2016) Performance, emission and combustion characteristics of a dual fuel engine with Diesel-Ethanol - Cotton seed oil Methyl ester blends and Compressed Natural Gas (CNG) as fuel. *Energy* 112:899–907
8. Pankaj S, Nitin S, Subhash L (2016) Investigation of combustion characteristics of a cotton seed biodiesel fuelled diesel engine. *Proc Technol* 25:1049–1055, Elsevier
9. Duple S, Murugavelh S (2016) Biodiesel production from waste cotton seed oil using low cost catalyst: engine performance and emission characteristics. *Perspec Sci* 8:237–240
10. Basavaraj S, Omprakash H, Hemachandra R (2016) Performance, emission & combustion characteristics of a semi-adiabatic diesel engine using cotton seed & neem kernel oil methyl esters. *Alex Eng J* 55(1):699–706
11. Subbarayan M, Senthil Kumar J, Anantha Padmanabhan M (2016) Experimental investigation of evaporation rate and exhaust emissions of diesel engine fuelled with cotton seed methyl ester and its blend with petro-diesel. *Transp Res Part D* 48:369–377
12. Hariram V, Godwin J, Seralathan S (2017) Cotton seed biodiesel as alternative fuel: production and its characterization analysis using spectroscopic studies. *Der Pharma Chemica* 9(5):1–6
13. Anil S, Shashank K, Deepa M, Rajath P, Jagadish R (2013) Production and characterization of biodiesel from cottonseed oil. *Int J Adv Eng Sci Technol* 2(4):328–334
14. ShyamKumar R, Anil G, Mayur B (2012) Performance evaluation of C.I. engine with cotton seed oil. *Int I J Instrumen Control Autom* 1(4):23–27
15. Siva Kumar A, Maheswar D, Vijaya Kumar R (2009) Comparison of diesel engine performance and emissions from neat and transesterified cotton seed oil. *Jordan J Mech Indl Eng* 3(3):190–197

Tribological and Rheological Studies of Polyolester (POE) Oil and POE + alumina nanolubricant and its effect on the Performance of a Refrigeration System



Subramani Narayanasarma and Biju T. Kuzhiveli

Abstract From the previous few years, diverse studies have been taking place at a faster rate by implementing innovative practices so as to improve the performance of lubricating oils and hence the system in which it is used. Using nanolubricants, bio-lubricants are some of the alternative solutions. In the present study, the various properties viz; rheological, tribological, and performance studies of polyol ester (POE) lubricant, a widely used lubricant in household refrigerator compressor, are evaluated by loading it with alumina nanoparticles and compared the results. The mass percentage of nanoparticles used is from 0.05 to 0.15%. The rheological properties were evaluated for the temperature ranges from 25 to 100 °C. High-Frequency Reciprocating Rig (HFRR) is used to perform tribological studies. The results show that the viscosity, viscosity index, improved with the rise in the proportion of alumina nanoparticles and all the proportions of nanolubricant showed Newtonian behaviour. The POE + 0.125% alumina nanolubricant showcased superior performance in tribological studies, in the energy utilization of the R134a refrigerant compressor and COP. Similar studies can also be conducted in various other mechanical systems that require lubrication, in-view of enhancing its performance and durability.

Keywords Alumina · POE oil · Tribology · COP · Power consumption

1 Introduction

The inclusion of nanoparticles within various heat transfer fluids like water, lubricants, oils, etc. For enhancing its energy transfer capacity has delivered a novel way to significantly improve the thermal efficiency of such systems for the last few years. Primarily in early 1990s Choi S found that the thermal conductivity of a heat transfer fluid gets boosted by the addition of nano-sized particles [1] and also showed a way to quantify the thermal conductivity of such nanofluids [2]. There onwards many researches have been started by utilizing various types of nanoparticles, both oxide

S. Narayanasarma (✉) · B. T. Kuzhiveli
National Institute of Technology Calicut, Kozhikode, Kerala 673601, India
e-mail: npskalyan@gmail.com

© The Author(s), under exclusive license to Springer Nature Singapore Pte Ltd. 2022
V. Krishna et al. (eds.), *Recent Advances in Hybrid and Electric Automotive Technologies*, Lecture Notes in Mechanical Engineering,
https://doi.org/10.1007/978-981-19-2091-2_5

types and metallic types, used alone or as a combination by varying their proportions and sizes in several types of fluids for heat transfer. The nanofluids are made by mixing nanosized particles which are having greater thermal conductivity than the base liquid in the conventional base liquids. The nanofluids have got the succeeding features, (a) greater heat transfer rate amongst the particles and fluid molecules on account of higher heat transfer area (b) superior dispersal stability due to prime Brownian motion (c) reduced particle agglomeration and (d) abridged pumping power when related to the base liquid. Adding the nanoparticles also improves the characteristics of boiling. These nanoparticles can also be made use of in refrigeration systems as a result of its notable enhancement in thermophysical and energy transfer abilities and this can be done by the dispersal of nanoparticles in lubricating oil. As the refrigerant is compressed as it passes over the compressor it transports traces of nanolubricant mixture along with it to the other parts of the system.

Some researches were conducted [3] so as to analyse the influence of nanoparticles dispersed in base fluid and reported that the thermal conductivity and the critical heat flux of the nanofluid enhanced substantially in comparison with the base fluid. Studies were conducted [4] with R134a refrigerant and titanium oxide/mineral oil nanolubricant in a VCRS (vapour compression refrigeration system) and reported that the efficient and normal working of the system and the power utilization of the compressor reduced by 21.2% in comparison with R134a and mineral oil alone. As a continuation of previous studies experimental analysis was carried out [5] and it was identified that as a result of the betterment in the thermo-physical properties of the mineral oil nanolubricant, the freezing capacity improved and the energy consumed by the compressor abridged. Investigation on another VCR system [6] substituting R134a with hydrocarbon refrigerant and alumina mineral oil nanolubricant showed that 60 mass% of R134a and 0.1 mass% of alumina nanoparticles performed better with a reduction of 2.4% in power consumption and the COP enhanced by 4.4%. Experimental studies [7] conducted for studying the tribological performance by adding POE oil with TiO₂ nanoparticles found that the introduction of nanoparticles either improve or worsen the performance. Similarly, in another analysis on a VCRS [8] it was found that the COP (coefficient of performance) enhanced and the power utilization abridged by 10.32% due to the usage of alumina nanolubricant. Experimental studies conducted [9] in similar system with TiO₂ nanolubricant showed substantial enhancement in COP by 20% and fall in power requirement of the compressor by 15.4%. Another correspondingly vital property is the fluid's viscosity as the change in viscosity of the fluid is affected by the heat transfer coefficient of convection [10–12, 22] and the same affects the power required to pump the fluid. Some recent tribological studies using polyolester oil blended with biolubricant showcased encouraging results with reduced CoF and wear rate [23, 24]. Certain studies also conveyed that at small volume concentrations of nanoparticles, at low temperatures and at lower shear rates Newtonian behaviour of the base fluid change to non-Newtonian behaviour [13, 14]. Studies related to tribology, rheology, thermal properties with various types of nanoparticles were conducted by many researchers but validating the same by analysing the performance of the actual systems is very

less. Hence in this contemporary work, the effect of the addition of alumina nanoparticles in the rheological and tribological features of the base POE lubricant and thereby how it influences the working of a simple VCR system is also analysed.

2 Materials and Methods

2.1 Lubricant and Nanoparticles Used

Alumina nanoparticles which are spherically shaped were used to prepare the nanolubricant and are procured from Sigma Aldrich Ltd, USA. The polyolester (ISO VG68) oil, which are widely used and commercially available for the use in compressors using R134a was used for the test. The Scanning Electron Microscope (FESEM-SU6600), Make: HITACHI was utilized for analysing the alumina nanoparticles. To break the agglomeration of alumina nanoparticles, the nanoparticle lubricant mixture is sonicated and magnetically stirred so as to get a uniform suspension.

2.2 Preparation and Stability Analysis of Nanolubricant

With the aim of studying the rheological, tribological, and thereby the performance effects of adding alumina nanoparticles to the POE oil, five different mass proportions (Fig. 1) were made for the analysis (0.05, 0.075, 0.1, 0.125, and 0.15 mass%). The mass of alumina nanoparticles required for each proportion was planned using Eq. 1, where m_p and m_o denote the mass of nanoparticles in grams and quantity of the POE oil in grams and it is measured using a very precise electronic weighing machine. Then by means of a magnetic stirring unit, the nanolubricants are stirred for a duration of 2 h, followed by sonication for seven hours. The sonication is done sporadically in order to offer sufficient cooling time. A UV-Vis (ultraviolet-visible) spectrophotometer was used to examine the dispersion stability of the prepared nanolubricants on the first day till the 6th day of preparation, and surfactants were not used while preparing the nanolubricants. The 0.2 mass% of alumina was unstable and hence the

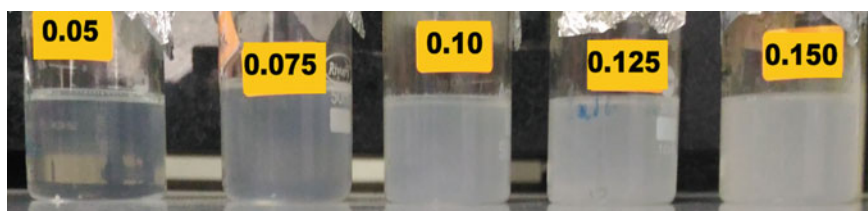
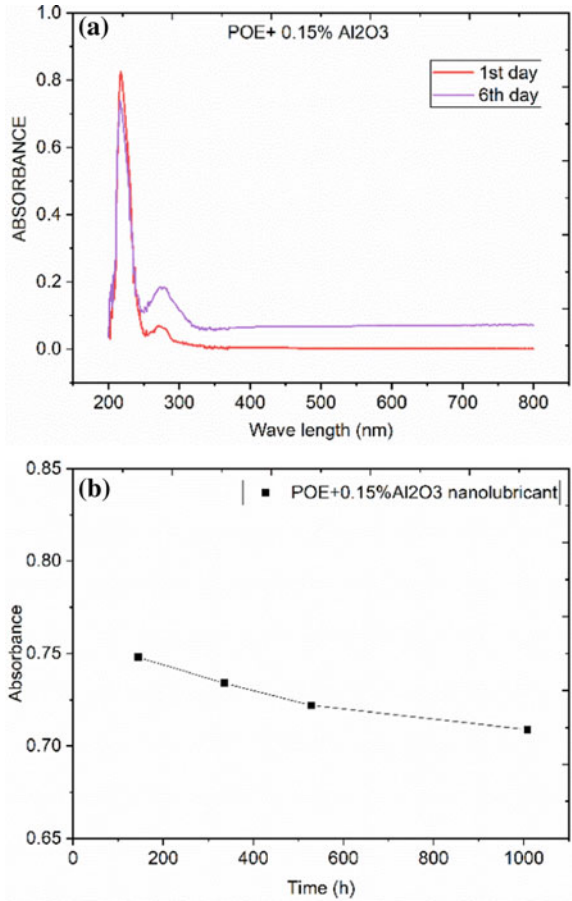


Fig. 1 Synthesized POE+alumina nanolubricants

Fig. 2 a UV-Vis spectrum of POE + 0.15%alumina on the 1st and 6th day **b** absorbance rate of POE + 0.15%alumina till 42 days



study was limited to 0.15% mass proportion and its stability was examined till 42 days (Fig. 2).

$$\text{mass\%} = \frac{m_p}{m_p + m_o} \times 100 \tag{1}$$

2.3 Assessment of Rheological Properties

The viscosity of all the synthesized POE+alumina nanolubricants was valued using a Rheometer (Anton Paar 102) and is consistent with the standard ASTM 4473. The viscosity values were measured for temperatures varied from 25 to 100 °C and for a shear rate of 1–1500 (1/s). A redwood viscometer was used for evaluating the

kinematic viscosities of all the lubricants at temperatures 40 and 100 °C. From the attained results, the viscosity index (V.I) was intended using the ASTM standard D220.

2.4 Assessment of Tribological Properties

The tribological properties viz; coefficient of friction (CoF) of the synthesized nanolubricants were evaluated using a HFRR, high-frequency reciprocating rig (Make: DUCOM)) and the surface roughness and the wear scar diameter were tested utilizing the Alicona 3D optical profilometer, Make: Bruker, USA. The CoF test was at par with the ASTM 6079-18 standard. In this test, a 10 mm diameter and 3 mm thick SS discs were used as the lower specimen upon which a 6 mm SS ball (upper specimen) reciprocates. These discs were polished using 600, 800, 1000 and 1500 silicon carbide papers fitted in a rotary polishing machine which is followed by a 1 and 3- μ m diamond paste. The discs were kept in a disc holder in HFRR and 2 ± 0.2 ml of the lubricant is poured, and a stroke length of 2 ± 0.02 mm, a frequency of 50 Hz, a load of 200 ± 1 g is applied and the lubricant is heated to a constant temperature of 60 ± 2 °C and the test is carried out for a duration of 75 min, maintaining a 55% relative humidity.

2.5 Experimental Setup and Instrumentation for the Performance Study

For conducting refrigeration performance test, a test rig was developed. The rig comprises of a compressor, a condenser (forced air-circulated), a capillary tube (expansion device) and an evaporator, (a copper spiral coil, kept fully dipped in water and that act as a refrigerating load). The pressure gauges (Bourdon type) were used to quantify the pressures at the outlet of all the components. Thermocouples Type-T (SWG 36), calibrated with a constant temperature source, were used to quantify the temperature at above-mentioned points with the help of a temperature scanner. The single phase digital power meter was utilized to measure the energy consumption of the compressor. In advance of filling the system with R134a refrigerant, it was thoroughly tested for leaks by pressurizing the system with Nitrogen at 200psi followed by evacuation using vacuum pump. Thereafter, the POE oil was filled in the compressor and after conducting all the performance studies the POE oil in the compressor was drained and refilled with the POE+alumina nanolubricant for further performance studies and all the tests were conducted 3 to 4 times in order to ensure the repeatability. The performance parameters viz; pull-down test, power consumption of the compressor, cooling capacity, and COP were estimated.

3 Results and Discussion

3.1 *Dispersal Stability of POE+alumina Nanolubricant*

The dispersal stability of nanolubricants is evaluated at ambient conditions by measuring the UV-Vis spectrum absorbance rate on the 1st and 6th day following the synthesis (Fig. 2a). The peak value of absorbance obtained for the POE + 0.15% alumina on the first day was 0.8258 at a wavelength of 216.999 nm, and keeping the sample idle, the absorbance rate was measured again on the sixth day and was found to be 0.748 on the same wavelength, which indicates its short-term stability. In order to know the long-term stability, the absorbance rate was tested after 42 days, and, it was found that (Fig. 2b) the absorbance rate was 0.709 and this minimal reduction in absorbance with time may be due to the strong Vander Waals force of attraction and aggregation effects [15, 16].

3.2 *Rheological Physiognomies of POE+alumina Nanolubricant*

The absolute viscosity of all the synthesized nanolubricants (0.05–0.15 mass%) was measured at shear change rates from 1 to 1500 s⁻¹ and temperatures from 25 to 100 °C.

Influence of temperature on absolute viscosity

The absolute viscosity may be defined as the internal forces of friction developed amongst different layers of liquids as they move relative to one other. It can be seen from Fig. 3 that the value of viscosity decreases for all mass fractions of nanolubricant as the temperature of the nanolubricant increases. The reason for the increase in viscosity at low-temperature conditions may be due to the development of nano-racemes which obstruct the movement of layers of lubricating oil on each other and as the temperature increases, it causes weakening of the intermolecular interactions and thereby the clustering of nanoparticles to disintegrate due to the remarkable Vander Waals forces of attraction and which in due course leads to the decrease in viscosity of the nanolubricant [17].

Influence of nanoparticles mass proportion on absolute viscosity

It is obvious from Fig. 3 that as the mass percentage of the alumina nanoparticles upsurges, the corresponding values of viscosity of the nanolubricant rises. The enhancement of the viscosity of the nanolubricant is because of the collisions amongst the suspended nanoparticles and the molecules of the base POE oil. More and more nano-racemes develop due to Vander Waal forces or the nanoparticles agglomerate within the suspension as the mass proportion of alumina nanoparticles in the same

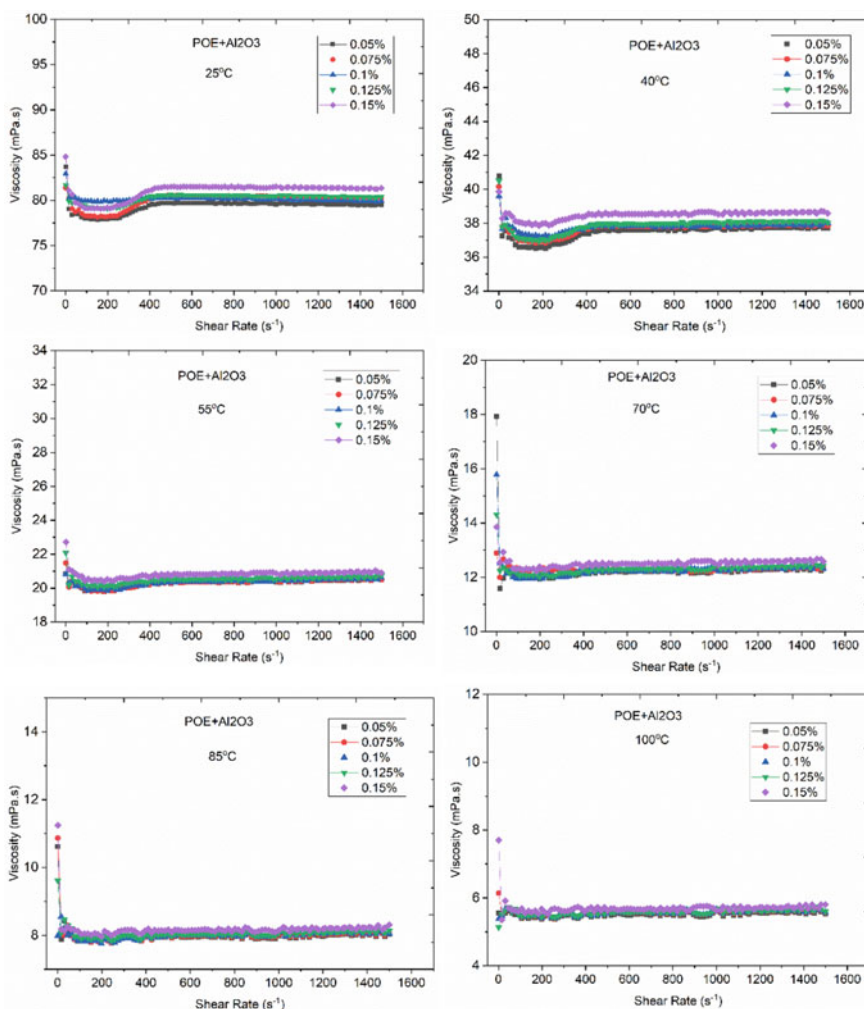


Fig. 3 Variation of viscosity at different temperatures and mass proportions of POE+alumina nanolubricant

volume or mass of POE oil increases which effects in the intensification of inner shear stress and thereby the rise in the viscosity of the lubricant.

Kinematic viscosity and viscosity index

The viscidness of a liquid falls with a rise in its temperature and the viscosity index quantifies this change in viscosity with temperature. The value of the viscosity index of a liquid shows its ability to retain its viscosity even if its temperature changes and if a liquid is having a high value of viscosity index it implies that it has high ability to retain its viscosity than the liquid which is having lower viscosity index. Table

Table. 1 Kinematic viscosity and viscosity index (V.I) of synthesized nanolubricants

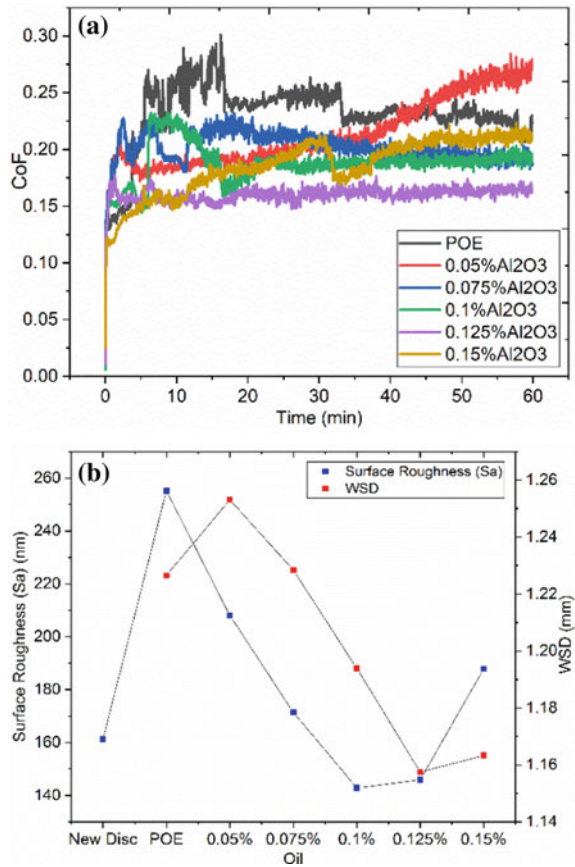
Oil	Kinematic viscosity (mm ² /s)		V.I
	40 °C	100 °C	
Pure POE	42.66 ± 1.96	6.35 ± 0.92	95.47
+0.05% alumina	42.94 ± 1.65	6.42 ± 1.09	97.58
+0.075% alumina	43.25 ± 0.33	6.55 ± 1.17	101.81
+0.1% alumina	43.40 ± 1.23	6.67 ± 1.37	106.29
+0.125% alumina	43.62 ± 1.86	6.73 ± 1.25	107.94
+0.15% alumina	44.23 ± 1.06	6.83 ± 1.45	109.65

1 exhibits the viscosity index and kinematic viscosity of POE and POE+alumina nanolubricant and it can be noted that the kinematic viscosity falls with an increase in temperature and escalates with the nanoparticles quantity. As the viscosity gets lowered at high temperatures, it assists in the reduction of viscous friction and it endorses the effect of the nanoparticles in subsiding the asperity friction and thenceforth reduces the power loss due to friction/pumping power loss [15, 20]. The maximum value of kinematic viscosity and viscosity index was shown by POE + 0.15%alumina nanolubricant and the percentage rise in the viscosity index was about 46%. The result also confirms the fact that the degree of fall in the kinematic viscosity with a rise in temperature of the base oil is suppressed by the addition of the alumina nanoparticles.

3.3 Tribological Characteristics of POE+alumina Nanolubricant

Tribological properties like wear scar diameter (WSD), CoF (Friction coefficient) and surface roughness were evaluated using a high-frequency reciprocating rig (HFRR) of the base POE oil, POE+alumina nanolubricants. Figure 4a shows the variation of CoF with the time and Fig. 4b shows the surface roughness and wear scar diameter values of the tested specimen on all the synthesized lubricants. From Fig. 4a, it is also to be noted that as the alumina mass proportion in the POE+alumina nanolubricant rises, the CoF drops and the least value of CoF was recorded by the POE+ 0.125% alumina nanolubricant and it was about 30.91% lesser than the base POE oil and this reduction in CoF may be as a result of the rotund shape of the alumina nanoparticles with the help of which the sliding friction is transformed to rolling friction and/or establishing a tribological layer on the area of contact [19]. The least minimum value of surface roughness was shown by POE + 0.1%alumina nanolubricant followed by POE + 0.125% alumina nanolubricant whereas the least minimum value of wear scar diameter was recorded by the POE + 0.125% alumina nanolubricant. The drop of CoF and surface roughness may also contribute to the increase in the life and

Fig. 4 a CoF versus time **b** surface roughness and wear scar diameter (WSD)



efficiency of the compressor [15, 20] as the power loss due to friction reduces which in turn reduces the power consumption of the compressor [18].

3.4 Influence of POE+alumina Nanolubricant on the Pull-Down Time and Cooling Capacity

The pull-down time illustrates the time essential for plummeting the cooling load (water) temperature which was initially at ambient temperature to the required temperature (here it is 1 °C) and cooling capacity shows the amount of thermal energy absorbed from the evaporator (water load) while cooling it to the specified temperature. From the experimental study, it was seen that the pull-down time significantly reduces with the addition of alumina nanoparticles and the lowest value of pull-down temperature (Fig. 5) and higher value of cooling capacity (Fig. 6) was

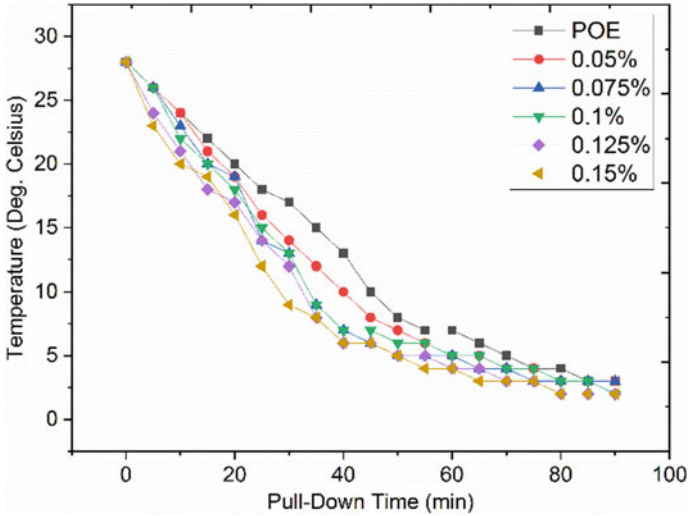


Fig. 5 Pull-down time of POE and all the synthesized nanolubricants

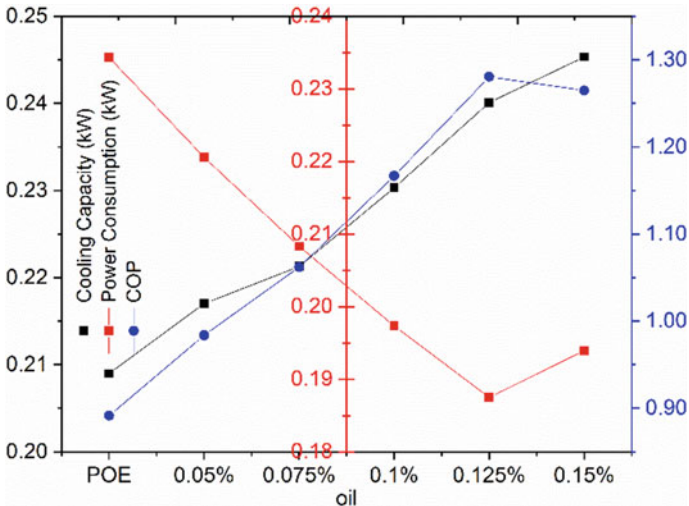


Fig. 6 Cooling capacity, power consumption and COP of POE and all the synthesized nanolubricants

demonstrated by the POE + 0.15% alumina nanolubricant and the enhancement in cooling capacity was about 17.39% higher than that of base POE oil.

3.5 Influence of POE+alumina Nanolubricant on the Compressor Energy Consumption

Figure 6 shows the influence of using POE lubricant alone and with POE+alumina nanolubricants on the power consumed by the compressor using R134a refrigerant and it can be seen that adding nanoparticles in the base lubricant, significantly reduces the energy consumption of the compressor. The maximum value of energy consumption was shown by POE oil and as the mass proportion of alumina nanoparticle in the base POE lubricant increased, the energy consumption reduced. The minimum value of power consumption was recorded by POE + 0.125%alumina followed by POE + 0.15%alumina nanolubricant which clearly substantiates the tribological results. It was also found that the energy consumption slashed by 5.73%, 10.97%, 15.65%, 19.87% and 17.11%, respectively for the 0.05, 0.075, 0.1, 0.125 and 0.15 mass% alumina+POE nanolubricant.

3.6 Influence of POE+alumina Nanolubricant on the COP of the System

The influence of POE+alumina nanolubricant on the COP is illustrated in Fig. 6 and it can be ascertained that the COP value gets enhanced as the proportion by mass of the alumina nanoparticle rises in the base POE lubricant. The augmentation in COP of the system may be due to the fact like decrease in energy consumption of the refrigerant compressor and/or due to the subcooling effect of the refrigerant in the condenser and/or due to the enhanced cooling capacity. The enhancement of COP of the system may also be due to the formation of porous layers of nanoparticles in the refrigerant-lubricant mixture which in turn reduces the thermal resistance of the mixture [21]. It can be seen that the maximum value of COP was given by the POE + 0.125%alumina nanolubricant and it was about 43.62% enhancement which reestablishes the rheological and tribological results.

4 Conclusions

To analyse the performance of alumina-based POE lubricant in a simple vapour compression refrigeration system, an extensive experimental assessment has been carried out by evaluating the rheological properties (at various temperatures viz; 25–100 °C), tribological performance (CoF, Surface roughness and wear scar diameter), and performance studies with all the synthesized POE+alumina nanolubricants. The range of proportions of alumina nanoparticles utilized for the work was from 0.05 to 0.15 mass%. The performance parameters like pull-down time, cooling capacity,

energy consumption and COP were estimated. The important inferences from the study are:

- All the proportions of POE+alumina nanolubricant worked safely and efficiently in the developed vapour compression refrigeration system.
- The viscosity and viscosity index of the base POE lubricant increased with increase in the mass proportion of alumina nanoparticles and decreased with increase in temperature and the higher value of viscosity was shown by the 0.15% POE+alumina nanolubricant.
- The coefficient of friction, surface roughness and the wear scar diameter of the specimen tested in HFRR decreased with increase in the mass proportion of alumina nanoparticles and the minimum value of CoF was obtained for 0.125 mass% alumina+POE nanolubricant and it was about 30.91% lesser than the base POE oil.
- The pull-down time, and power requirement of the compressor decreased whereas the cooling capacity and COP augmented with the rise in the mass proportion of alumina nanoparticles.
- However, the cooling capacity of the system increased with increase in the alumina nanoparticles proportion in the POE oil, the highest value of COP and lowest value of pull-down time and power requirement was shown by POE + 0.125% alumina nanolubricant followed by POE + 0.15% alumina nanolubricant.

Hence it can be concluded that with the absence of any surfactants, a 0.125 mass% of alumina in POE lubricant is capable enough and shall reflect in the longevity of moving parts in refrigerant compressors along with better tribological, rheological properties and performance characteristics.

Acknowledgements I would like to thank The Mechanical Engineering department and the School of Material Science and Engineering, National Institute of Technology Calicut, for aiding me during my project work.

I too thank, The Department of Science and Technology (DST), Govt. of India and Centre for Precision Measurements and Nano-Mechanical Testing, Department of Mechanical Engineering, National Institute of Technology Calicut, for providing me with the facility purchased under the scheme 'Fund for Improvement of Science and Technology' (FIST—No. SR/FST/ETI-388/2015) during the period of my project work.

References


1. Choi SUS, Eastman JA (1995) Enhancing thermal conductivity of fluids with nanoparticles. In: International mechanical engineering congress and exposition. ASME, San Fransisco. <https://www.osti.gov/biblio/196525-enhancingthermal-conductivity-fluids-nanoparticles>
2. Lee S, Choi US, Li S, Eastman JA (1999) Measuring thermal conductivity of fluids containing oxide nanoparticles. *J Heat Transf* 121(2):280–289. <http://doi.org/https://doi.org/10.1115/1.2825978>
3. Keblinski P, Eastman JA, Cahill DG (2005) Nanofluids for thermal transport. *Mater Today* 8(6):36–44. [http://doi.org/https://doi.org/10.1016/S1369-7021\(05\)70936-6](http://doi.org/https://doi.org/10.1016/S1369-7021(05)70936-6)

4. Bi S, Shi L, Zhang L (2007) Performance study of a domestic refrigerator using R134a/mineral oil/nano-TiO₂ as working fluid. ICR 2007. Refrigeration creates the future. In: Proceedings of the 22nd IIR international congress of refrigeration. ICR07-B2–346
5. Bi S-S, Shi L, Zhang L-I (2008) Application of nanoparticles in domestic refrigerators. *Appl Therm Eng* 28:10
6. Jwo C-S, Jeng L-Y, Teng T-P, Chang H (2009) Effects of nanolubricant on performance of hydrocarbon refrigerant system. *J Vac Sci Technol B* 27(3):1473. <https://doi.org/10.1116/1.3089373>
7. Bobbo S, Fedele L, Fabrizio M, Barison S, Battiston S, Pagura C (2010) Influence of nanoparticles dispersion in POE oils on lubricity and R134a solubility. *Int J Refrig* 33(6):1180–1186. <https://doi.org/10.1016/j.ijrefrig.2010.04.009>
8. Kumar DS, Elansehian DR (2012) Experimental study on Al₂O₃-R134a Nano refrigerant in refrigeration system. 2(5):3
9. Subramani N, Mohan A, Prakash JM (2013) Performance studies on a vapour compression refrigeration system using nano-lubricant. *Int J Innov Res Sci Eng Technol* 2(1):552–530
10. Murshed SMS, Leong KC, Yang C (2008) Thermophysical and electrokinetic properties of nanofluids—a critical review. *Appl Therm Eng* 28:2109–2125. <https://doi.org/10.1016/j.applthermaleng.2008.01.005>
11. Eastman JA, Phillpot SR, Choi SUS, Keblinski P (2004) Thermal transport in nanofluids. *Annu Rev Mater Res* 34:219–246. <https://doi.org/10.1146/annurev.matsci.34.052803.090621>
12. Wang X-Q, Mujumdar AS (2007) Heat transfer characteristics of nanofluids: a review. *Int J Therm Sci* 46:1–19. <https://doi.org/10.1016/j.ijthermalsci.2006.06.010>
13. Aberoumand S, Jafarimoghaddam A, Moravej M, Aberoumand H, Javaherdeh K (2016) Experimental study on the rheological behavior of silver-heat transfer oil nanofluid and suggesting two empirical based correlations for thermal conductivity and viscosity of oil based nanofluids. *Appl Therm Eng* 101:362–372. <https://doi.org/10.1016/j.applthermaleng.2016.01.148>
14. Sanukrishna SS, Jose Prakash M (2018) Experimental studies on thermal and rheological behaviour of TiO₂-PAG nanolubricant for refrigeration system. *Int J Refrig* 86:356–372. <https://doi.org/10.1016/j.ijrefrig.2017.11.014>
15. Ali MKA, Xianjun H, Mai L, Qingping C, Turkson RF, Bicheng C (2016) Improving the tribological characteristics of piston ring assembly in automotive engines using Al₂O₃ and TiO₂ nanomaterials as nano-lubricant additives. *Tribol Int* 103:540–554. <https://doi.org/10.1016/j.triboint.2016.08.011>
16. Narayanasarma S, Kuzhiveli BT (2020) The effect of silica nanoparticle on thermal, chemical, corrosive, and the nature-friendly properties of refrigerant compressor lubricants—a comparative study. *Asia-Pac J Chem Eng* 15. <https://doi.org/10.1002/apj.2551>
17. Afrand M, Toghraie D, Ruhani B (2016) Effects of temperature and nanoparticles concentration on rheological behavior of Fe₃O₄-Ag/EG hybrid nanofluid: an experimental study. *Exp Thermal Fluid Sci* 77:38–44. <https://doi.org/10.1016/j.exptthermflusci.2016.04.007>
18. Subramani N, Prakash M (2012) Experimental studies on a vapour compression system using nanorefrigerants. *Int J Eng Sci Tech* 3:95–102. <https://doi.org/10.4314/ijest.v3i9.8>
19. Khatai S, Kumar R, Sahoo AK, Panda A, Das D (2020) Metal-oxide based nanofluid application in turning and grinding processes: a comprehensive review. *Mater Today Proc* 26:1707–1713. <https://doi.org/10.1016/j.matpr.2020.02.360>
20. Narayanasarma S, Kuzhiveli BT (2019) Evaluation of the properties of POE/SiO₂ nanolubricant for an energy-efficient refrigeration system—an experimental assessment. *Powder Technol* 356:1029–1044. <https://doi.org/10.1016/j.powtec.2019.09.024>
21. Ahmed F, Khan WA (2021) Efficiency enhancement of an air-conditioner utilizing nanofluids: an experimental study. *Energy Rep* 7:575–583. <https://doi.org/10.1016/j.egy.2021.01.023>
22. Babarinde TO, Akinlabi SA, Madyira DM (2018) Enhancing the performance of vapour compression refrigeration system using nano refrigerants: a review. *IOP Conf Ser Mater Sci Eng* 413:012068. <https://doi.org/10.1088/1757-899X/413/1/012068>
23. Vithya P, Sriram G, Arumugam S (2021) Vegetable oil based biodegradable refrigeration oil—an optimization of tribological characteristics using d-optimal design. *Tribol Ind* 43:397–412. <https://doi.org/10.24874/ti.1014.11.20.02>

24. Narayanasarma S, Kuzhiveli BT (2021) Evaluation of lubricant properties of polyolester oil blended with sesame oil-an experimental investigation. *J Clean Prod* 281:125347. <https://doi.org/10.1016/j.jclepro.2020.125347>

Aerodynamic Effect on Lift Characteristics of a Sedan Car Due to Attached Wing



Amrutheswara Krishnamurthy  and Suresh Nagesh

Abstract The aerodynamic effect plays a major role in the fuel efficiency and stability of the vehicle. The contact patch loads between the tire and road also play a vital role in the stability and fuel efficiency and are directly related to the vehicle load. In this research, lift force generated because of an additional wing attached to the car is studied. While the vehicle moves around 40–130 kmph. Upward vertical lift force produced from aerodynamics reduces the weight of the car virtually. The wing or airfoil is attached to use the gap between the car's top surfaces to the lower surface of the wing to cause a Venturi-like effect. Lightweight car will be able to make more efficient use of its tires than a heavier car. Computational fluid dynamics (CFD) analyses are done with ANSYS Fluent. The validation of airflow characteristics, lift and drag forces from simulations, is done with data from wind tunnel testing. The study was carried out by varying parameters such as height between the upper surface of the car and the lower surface of the wing, and wingspan. The result obtained shows that the weight of the car can be reduced by 11% virtually with the wing forces, and the payload could increase by 11% or improve the fuel efficiency by 10–15%.

Keywords Aerodynamics · Tire/road · Car-wing · Drag · Lift · Nozzle effect

1 Introduction

The aerodynamics changes the fuel efficiency. The airfoil is used in the race cars to create a sufficient downforce at high speed with the negative angle of attack, which increases the stability, but the fuel efficiency decreases, and it is very much required to steer the vehicle at high-speed stability due to downward force. While the vehicle is moving with constant velocity, the aerodynamic forces, the tire contact patch, and

A. Krishnamurthy (✉)
Research Scholar PES University, Bangalore 560085, India
e-mail: amruthisac@gmail.com

S. Nagesh
CORI-Lab- PES University, Bangalore 560085, India

longitudinal forces almost remain constant. More the contact patch, more stability and less fuel efficiency, and vice versa. The entire vehicle load is transferred to the road via the contact patch between the road and the tire [27]. The vertical load including the lift forces and downward forces on each tire is directly proportional and has a significant contribution to the longitudinal [2, 3, 6] and lateral forces. The study done by Ahmed et al. [1] used wind tunnel test to measure the force and pressure measurements of a basic ground vehicle type of bluff body [5], a generic shape of the car. The model was studied with varied parameters as base slant angle from 0 to 40 degrees in steps of 5 degrees. The rear slant angle has been studied by Guilmineau [7, 8] and Tunay [24]. The underbody of the car studied by Huminic et al. [11] shows the effect of the nozzle due to the diffuser. The influence of the underbody was studied by Zhang et al. [28] shows the aerodynamic ground effect to reduce the upward lift forces due to the gap between ground and wing. The magic formula [21] of the tire model shows that the contact patch loads depend on the vertical load and the stiffness. Aerodynamic drag forces [12, 13] reduce due to the usage of a spoiler [14]; in this study, the wing acts as a spoiler structure but besides generates lift force. The study done by engineers on realistic car model DrivAer [16, 22, 25] is numerically analyzed and the results are compared with experiments for better aerodynamic performance.

Being a continuous subject of research, the authors in the current paper propose a new aspect of attaching a wing at the top surface of the car, which creates the nozzle effect on the top surface of the car to reduce the drag and utilize the lift forces to reduce the payload virtually. The wing is attached so that the coefficient of pressure is passing through the CG of the vehicle. The CFD study shows that the lift forces generated by a car attached with the wing are slightly more than the lift forces generated by the wing alone.

2 Tire Loads and Nozzle Effect

The venturi nozzle effect is a jet effect. Figure 1 shows the geometry of the scaled model attached with the wing and nozzle effect. The inlet is having a higher area due to the windshield and the airfoil shape. In the middle region, the gap between the upper surface of the car top and the lower surface of the airfoil makes the nozzle.

In this zone, the pressure is greater than the air at the inlet. The mass flow rate of air through the nozzle depends on the density of air, area of the flow, and velocity. The relative velocity of the air on the top surface is higher than that on the lower surface, and pressure is increased in the nozzle zone.

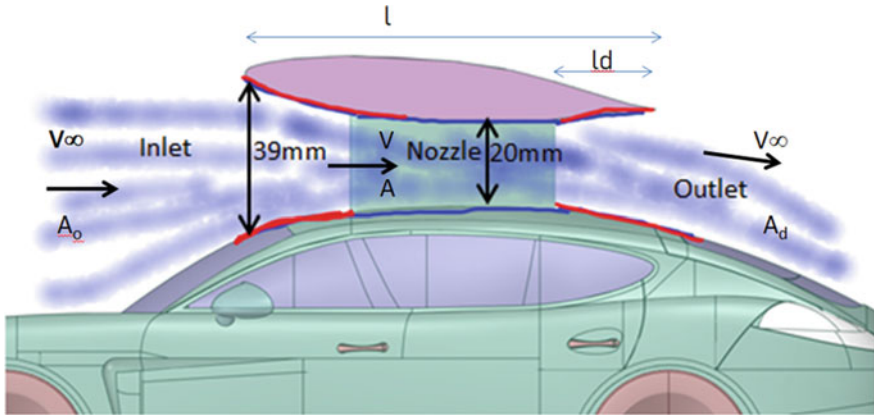
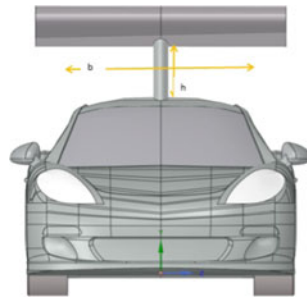


Fig. 1 The nozzle effect due to the wing attached to the car. Volumetric airflow rate Q is given by velocity multiplied by area.

- A area
- b breadth
- h height
- β coefficient of the aerodynamic resistance of the nozzle
- ρ_{air} density of air
- D_u drag at the upper body



$$Q = v1A1 = v2A2 \tag{1}$$

where A is the area of cross-section of venturi at any point and v is the velocity of air at that point.

Considering that the resultant fluid is homogeneous in the entire cross-section of the nozzle $b \cdot h$, for the component of the drag of vehicles, D_u , determine analytically the following equation [11]:

$$D_u = \frac{\beta * b * h * \rho_{air} * v^3}{2 * v_{\infty}} \tag{2}$$

where β : coefficient of the aerodynamic resistance of the nozzle (top surface of car geometry). v : average velocity of the air through the constant section of the nozzle.

As the vehicle speed increases, the force required to overcome the rolling resistance of friction and the drag forces also increase.

The total load acting on the wheels is given by

$$F_{\text{wheels}} = \frac{T_{\text{Engine torque}} * i_{\text{Gear ratio}} * \eta_{\text{efficiency}}}{r r_{\text{dynamic}}} = F_{\text{Total Force}}$$

$$= F_{\text{Air drag}} + F_{\text{Rolling resistance}} + F_{\text{Inertia}} + F_{\text{Slope}} \quad (3)$$

The aerodynamic lift force generated due to the airfoil attached is given by

$$F_{\text{lift}} = \frac{C_{l_{\text{coefficient lift}}} * S * \rho_{\text{air}} * v^2}{2} \quad (4)$$

The contact patch load for the front wheel is given by

$$F_{\text{ContactPatch_load}} = \frac{m * g * (1 - \frac{CG}{WB})}{2} + F_S - \frac{F_{\text{lift}}}{4} + \frac{F_{\text{Air drag*COG}}}{4} \quad (5)$$

The lift force is due to the pressure difference between the upper and lower surface of the airfoil, which reduces the total load on the wheels without adding much of the drag component. This is because of the nozzle effect, the drag remains the same but only lift forces increase.

3 Test Model

The 1:18 scaled [9, 20] car model [29, 30] used in this analysis is replicated using the CATIA for the CFD analysis [17]. The model is attached with the airfoil NACA 660,215 with a different wingspan. Starting with a 100 mm wingspan is then increased up to 300 mm in steps of 50 mm. The gap between the car surface from the top surface of the car and the wing's lower surface is maintained as 25 mm and the gap is varied as a parameter to check the venturi nozzle effect and aerodynamic forces. Figure 2 shows the test facility and model fixed at the wind tunnel lab.

The automotive industry widely uses the two-equation model for the CFD analysis [17] that is the standard $k - \omega$ SST model [18], which is reliable and converges quickly. Boundary conditions used in the CFD analysis are given in Table 1. The Geometry used in the analysis is shown in Fig. 3. The CFD mesh is generated with fine resolution meshes around the vehicle, a body of influence is created around the vehicle, and a finer mesh size of 4 mm is used. Similarly, one more body of influence is created around the airfoil with a small mesh to capture the flow separation and study the lift forces.

The air flows from the inlet at the vehicle's speed and the car with the wing is fixed stationary. Assuming the car runs in a straight line with the maximum speed,



Fig. 2 The car body with the airfoil attached in the wind tunnel test

a velocity from 1 to 40 m/s is given to the airflow. Wall boundary conditions are given to the solid surfaces of the car model and the airfoil. Pressure outlet boundary conditions are given at the domain outlet.

4 Results and Discussion

To clearly show the relationship between the nozzle effect, due to the wing attached to the car and the aerodynamic forces, graphs are presented as shown in Fig. 7. It can be observed that when the angle of attack is less, upward force increases.

Figure 4 shows the CFD model of the car used in this analysis. The velocity plot indicates the airflow in the nozzle area and the top surface of the wing (Fig. 5).

The pressure plot from the CFD analysis results is shown in Fig. 6.

Table 1 Boundary conditions used in the CFD analysis

Boundary conditions	
Velocity inlet	
Velocity specification method	Magnitude and direction
Velocity magnitude	30 m/s
X-component of flow direction	1
Specification method	Intensity and viscosity Ratio
Backflow turbulent intensity (%)	5
Backflow turbulent viscosity ratio	10
Reference values	
Compute from	Inlet
Area (m ²)	0.25617 m ²
Density (kg/m ³)	1.225
Viscosity (kg/m-s)	179E-05
Reference zone	
Solution methods	
Scheme	Coupled
Gradient	Least square cell based
Pressure	Second-order
Momentum	Second-order upwind
Turbulent kinetic energy	Second-order upwind
Specific dissipation rate	Second-order upwind

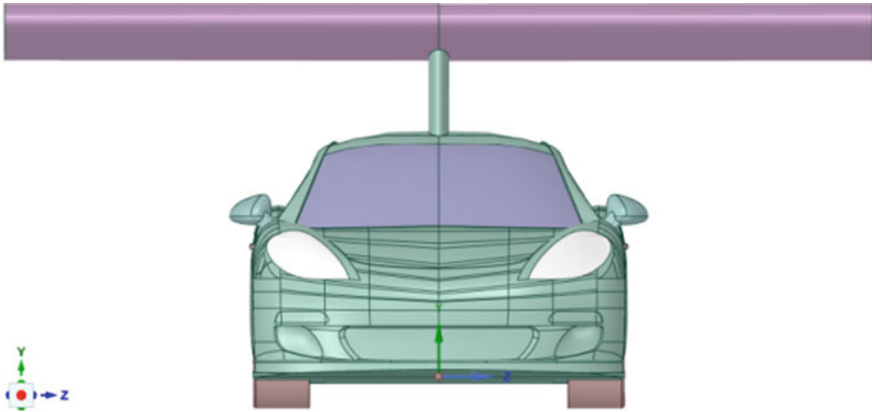


Fig. 3 The geometrical model used for the CFD analysis

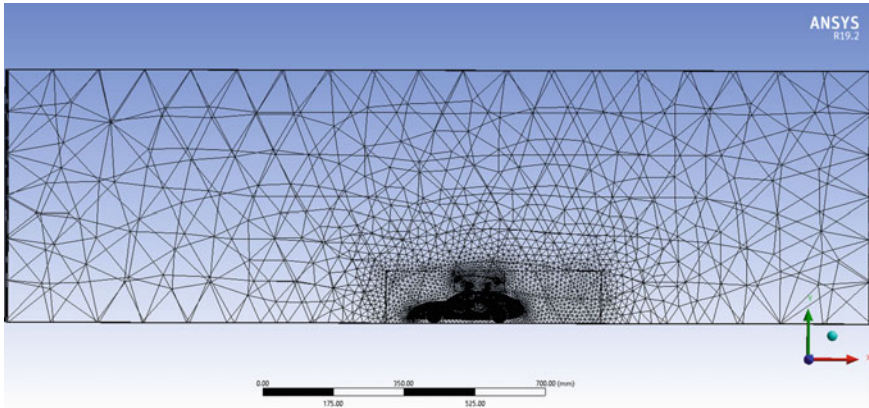


Fig. 4 CFD mesh of full car body and airfoil

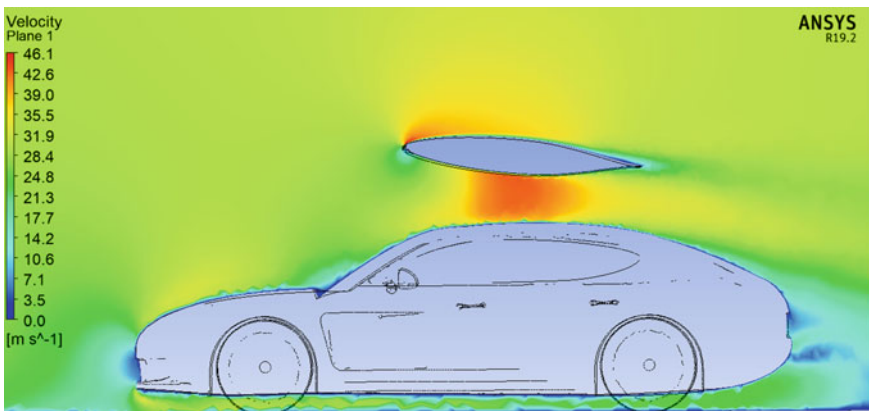


Fig. 5 Velocity plot of CFD model, car attached with wing



Fig. 6 Pressure plot of CFD model, car attached with wing

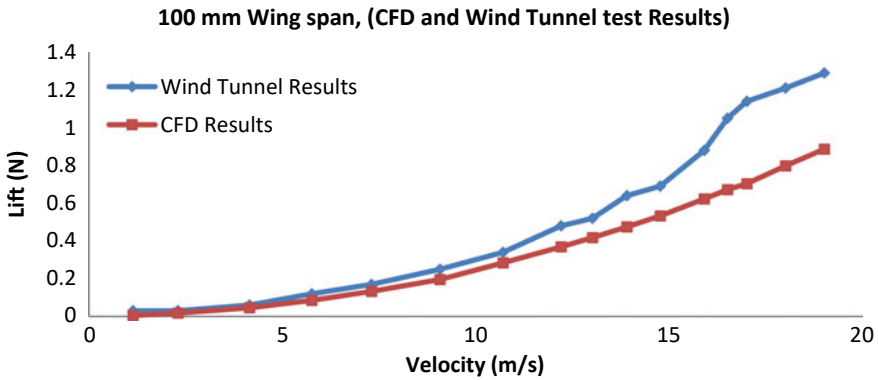


Fig. 7 Wind tunnel results versus CFD results for 100 mm wingspan attached to the car

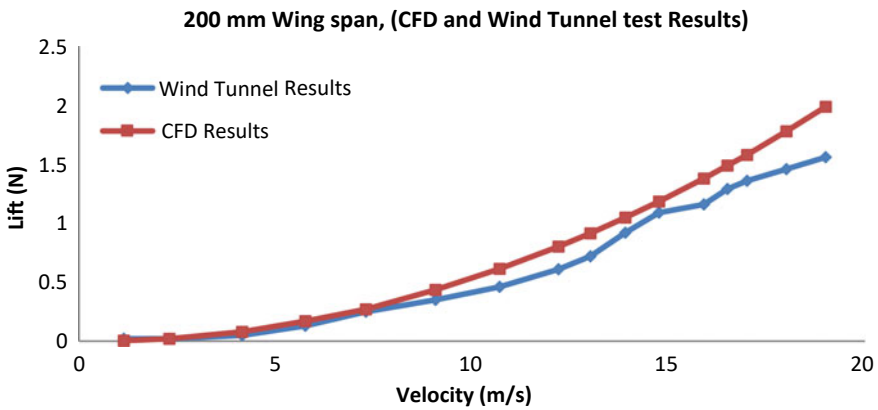


Fig. 8 Wind Tunnel Results versus CFD Results for 200 mm wingspan attached to the car

Figure 7 shows that results obtained from the wind tunnel test using the 100 mm wingspan attached to the car produce more lift force than the wing alone. The NACA 662,015 airfoil with a 100 mm wingspan is analyzed with 3D CFD mesh and the results are compared. The graph shows that the forces are increased in the wind tunnel due to the nozzle effect.

Figure 8 shows that as the wingspan increased, the lift forces generated also increased. The lift forces in the 100 mm wingspan and the 200 mm wingspan depict the same.

Figure 9 shows that when the height between the wing's lower surface and the car body is increased, the lift forces generated decrease. Due to the reduction in nozzle effect, the lift generated reduces as the gap increases; in this experiment, height is varied from 25 to 50 mm. and velocity is increased from 1 to 40 m/s. The graph

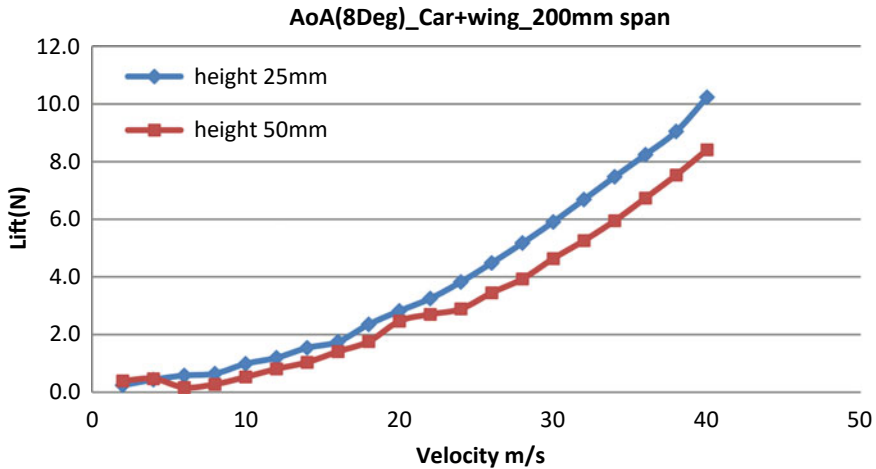


Fig. 9 Lift versus velocities for symmetric airfoil attached to CAR with a different height between car and the airfoil

shows that though the wingspan and the angle of attack are the same, the lift force decreases.

To show the lift force in the actual model, the NACA 660215 airfoil with the 3.6 m wingspan is analyzed and generates 2775 N lift force at 36 m/s airspeed and 5° of AOA. By converting this lift force into kg, it is almost 282 kg, which virtually reduces the weight of the car. This much weight reduction adds to fuel consumption per 100 km = $282 \times (0.4/100) = 1.1$ L/100 km. This is around 11% fuel efficiency depending on the weight of the car and driving conditions.

5 Summary/Conclusions

In this paper, the authors present a new aspect of the airflow of a car fitted with a simple wing with different wingspans. The influence of the top car body geometry shaped as a venturi nozzle on the main aerodynamic characteristics, lift and drag, is revealed. The wingspan is varied, and the results are compared with the CFD results. Venturi nozzle effect generates lift at zero degrees of angle of attack and no drag. This approach can help to evaluate the contribution of the lift and drag forces on the car body and loads on the tires, even in an early stage of the design process.

Firstly, it is shown that due to the nozzle effect, the lift force is generated. Secondly, the height of the wing shows the ground effect, and the lift generated decreases as the height of the wing increases from the top surface of the car. The fuel efficiency improves due to the wing attached due to virtual load reduction.

References

1. Ahmed S, Ramm G, Faltin G (1984) Some salient features of the time-averaged ground vehicle wake. SAE Technical Paper Series, pp 473–503. <https://doi.org/10.4271/840300>
2. Baffet G, Charara A, Lechner D (2009) Estimation of vehicle sideslip, tire force and wheel cornering stiffness. Control Eng Pract 17(11):1255–1264. <https://doi.org/10.1016/j.conengprac.2009.05.005>
3. Department of Automatic Control Lund Institute of Technology, Gerard M (2006) Tire-road friction estimation using slip-based observers (ISRN LUTFD2/TFRT--5771--SE). <http://lup.lub.lu.se/luur/download?func=downloadFile&recordOid=8847816&fileOid=8859385>
4. Dominy RG (1992) Aerodynamics of grand prix cars. Proc Inst Mech Eng Part D J Automob Eng 206(4):267–274. https://doi.org/10.1243/pime_proc_1992_206_187_02
5. Gaylard A, Kabanovs A, Jilesen J, Kirwan K, Lockerby D (2017) Simulation of rear surface contamination for a simple bluff body. J Wind Eng Ind Aerodyn 165:13–22. <https://doi.org/10.1016/j.jweia.2017.02.019>
6. Gillespie TD (1992) Fundamentals of vehicle dynamics. SAE International
7. Guilmineau E (2014) Numerical simulations of flow around a realistic generic car model. SAE Int J Passeng Cars Mech Syst 7(2):646–653. <https://doi.org/10.4271/2014-01-0607>
8. Guilmineau E (2018) Effects of rear slant angles on the flow characteristics of the Ahmed body by IDDES simulations. SAE Technical Paper Series, pp 001–0010. <https://doi.org/10.4271/2018-01-0720>
9. Heinemann T, Springer M, Lienhart H, Kniesburges S, Othmer C, Becker S (2014) Active flow control on a 1:4 car model. Exp Fluids 55(5):75–81. <https://doi.org/10.1007/s00348-014-1738-0>
10. Hucho W, Sovran G (1993) Aerodynamics of road vehicles. Annu Rev Fluid Mech 25(1):485–537. <https://doi.org/10.1146/annurev.fl.25.010193.002413>
11. Huminic A, Huminic G, Soica A (2012) Study of aerodynamics for a simplified car model with the underbody shaped as a Venturi nozzle. Int J Veh Des 58(1):15. <https://doi.org/10.1504/ijvd.2012.045927>
12. Katz J (2006) Aerodynamics of race cars. Annu Rev Fluid Mech 38(1):27–63. <https://doi.org/10.1146/annurev.fluid.38.050304.092016>
13. Kim I, Chen H (2010) Reduction of aerodynamic forces on a minivan by a pair of vortex generators of a pocket type. Int J Veh Des 53(4):300. <https://doi.org/10.1504/ijvd.2010.034103>
14. Kim I, Geng X, Chen H (2008) Development of a rear spoiler of a new type for mini-vans. Int J Veh Des 48(1/2):114. <https://doi.org/10.1504/ijvd.2008.021155>
15. Mansour H, Afify R, Kassem O (2020) Three-dimensional simulation of new car profile. Fluids 6(1):8. <https://doi.org/10.3390/fluids6010008>
16. Matsumoto D, Kiewat M, Haag L, Indinger T (2018) Online dynamic mode decomposition methods for the investigation of unsteady aerodynamics of the DrivAer model (first report). Int J Automot Eng 9(2):64–71. https://doi.org/10.20485/jsaeijae.9.2_64
17. Nabil T, Helmy Omar AB, Mohamed Mansour T (2020) Experimental approach and CFD simulation of battery electric vehicle body. Int J Fluid Mech Therm Sci 6(2):36. <https://doi.org/10.11648/j.ijfmts.20200602.11>
18. Menter FR (1994) Two-equation eddy-viscosity turbulence models for engineering applications. AIAA J 32:1598–1605
19. Olson B, Shaw S, Stepan, G (2003) Nonlinear dynamics of vehicle traction. Veh Syst Dyn 40(6):377–399. <https://doi.org/10.1076/vesd.40.6.377.17905>
20. Romijn T, Hendrix W, Donkers M (2017) Modeling and control of a radio-controlled model racing car. IFAC-PapersOnLine 50(1):9162–9167. <https://doi.org/10.1016/j.ifacol.2017.08.1726>
21. Ružinskas A, Sivilevičius H (2017) Magic formula Tyre model application for a Tyre-Ice interaction. Procedia Eng 187:335–341. <https://doi.org/10.1016/j.proeng.2017.04.383>

22. Strangfeld C, Wieser D, Schmidt HJ, Woszilko R, Nayeri C, Paschereit C (2013) Experimental study of baseline flow characteristics for the realistic car model DrivAer. SAE Technical Paper Series, pp 2342–2350. <https://doi.org/10.4271/2013-01-1251>
23. Targosz M, Skarka W, Przystała P (2018) Model-based optimization of velocity strategy for lightweight electric racing cars. J Adv Transp 2018:1–20. <https://doi.org/10.1155/2018/3614025>
24. Tunay T, Sahin B, Ozbolat V (2014) Effects of rear slant angles on the flow characteristics of Ahmed body. Exp Thermal Fluid Sci 57:165–176. <https://doi.org/10.1016/j.expthermflusci.2014.04.016>
25. Varney M, Passmore M, Wittmeier F, Kuthada T (2020) Experimental data for the validation of numerical methods: DrivAer model. Fluids 5(4):236. <https://doi.org/10.3390/fluids5040236>
26. Varshney H (2017) Aerodynamic drag reduction of tractor-trailer using wishbone type vortex generators. Int J Res Appl Sci Eng Technol V(IX):1833–1846. <https://doi.org/10.22214/ijraset.2017.9266>
27. Wang R, Wang J (2013) Tire–road friction coefficient and tire cornering stiffness estimation based on longitudinal tire force difference generation. Control Eng Pract 21(1):65–75. <https://doi.org/10.1016/j.conengprac.2012.09.009>
28. Zhang X, Toet W, Zerihan J (2006) Ground effect aerodynamics of race cars. Appl Mech Rev 59(1):33–49. <https://doi.org/10.1115/1.2110263>
29. Techart for the Panamera models. (n.d.). Techart. <https://www.techart.de/en/models/panamera/techart-for-970/>
30. Porsche Panamera 4S. (n.d.). Porsche AG Dr. Ing. h.c. F. Porsche AG. <https://www.porsche.com/international/models/panamera/panamera-models/panamera-4s/>

Modelling and Analysis of Brake Disc with Various Profiles for EN31 Material



K. Kaviyarasan, R. Soundararajan , R. Abhisheak Richter, K. Siva, S. Purusothaman, and S. Shiva Gurunathan

Abstract Disc brakes are the existing brake system in automobiles. The disk plays a vital role in slowing down as well as to stop the vehicle. When brake is applied, at the juncture, friction will be developed between brake pad and disk. Because of this braking effect, there generates a large quantity of heat on the contact area. Different sandwich structures may be designed with the aim that the generated heat can be ventilated during the braking action. The primary objective of this article is to study the thermal characteristics of the sandwich ventilated structures of three different profiles of the brake disc and valuate the obtained results and recommend a better profile. EN31 is chosen as the brake disc material since it has low density and good mechanical and thermal properties. X-core, Corrugated and Round O-core were chosen as the various profiles to be analysed. For the sandwich structures, the heat and the pressure output parameters were found with a condition that one face of a sheet is subjected to heating (constant heat flux) while the other face was cooled (forced air convection). From the analysis, it was found that heat dissipation of the profile depends upon the property (density and the thermal conductivity) of the material utilized. Also, O-core sandwich structure offers comparatively better performance than the other three profiles.

Keywords Disc brake · Thermal analysis · Von mises stress · Deformation

1 Introduction

Disc brake is a vital component in vehicles in order to reduce the speed or stop the vehicle and it was developed by many researchers from early as 1900s [1, 2]. One

K. Kaviyarasan (✉) · R. Abhisheak Richter · K. Siva · S. Purusothaman · S. Shiva Gurunathan
Department of Mechanical Engineering, Sri Krishna College of Technology, Coimbatore 641042,
Tamil Nadu, India
e-mail: kkaviyarasan92@gmail.com

R. Soundararajan
Sri Krishna College of Engineering and Technology, Coimbatore 641008, Tamil Nadu, India
e-mail: soundararajan.mtech@gmail.com

© The Author(s), under exclusive license to Springer Nature Singapore Pte Ltd. 2022
V. Krishna et al. (eds.), *Recent Advances in Hybrid and Electric Automotive Technologies*, Lecture Notes in Mechanical Engineering,
https://doi.org/10.1007/978-981-19-2091-2_7

of the most common brake disc defects is overheating. In case of overheating, the disc temperature reaches critical values, causing the brake pad to slip on the disc and reducing the efficiency of the brake system to a minimum. A brake disc is a rotating part of wheel's disc brake and it operates by the principle of friction [3]. Due to the continuous application of braking action, enormous amount of heat is generated and it is dispersed based on the profile design [4–6]. In few profiles, the heat energy leads to the expansion of the rotor [7]. It also leads to brake liquid, seals and other segments to overheat [8, 9]. Sandwich panels offer a wide scope of benefits over customary solid materials and their utilization is persistently expanding in applications in the aviation, car, maritime and development ventures [10] and the main objective of the research is to study the thermal characteristics so, diverse sandwich structure is designed so that generated heat can be ventilated during the slowing down activity. Four different profiles such as X-core, Corrugated and Round O-core were chosen and compared so that suitable ventilation construction is identified. EN31 is taken as the brake disc material since EN31 is a high strength steel material that has low density, low coefficient of thermal expansion and good wear resistance. The corrugated sandwich panel have numerous distinctive features like high flexural solidness to-weight attribute, its capability to have brilliant ventilation characteristics [10] than conventional structures X-core have high energy absorption [11]. All of the three different profiles were analysed at the same operating conditions and their results were noted [12–18]. Out of the different brake profiles, O-core structure offers better properties than the other profiles. After conducting analysis, the design which offers optimum properties can be utilized in automobiles (Figs. 1 (a) and (b)).

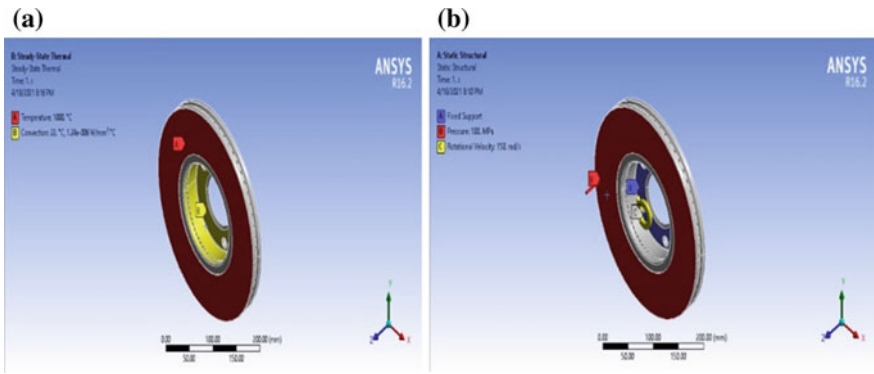


Fig. 1 a Boundary conditions (thermal). b Boundary conditions (static structural)

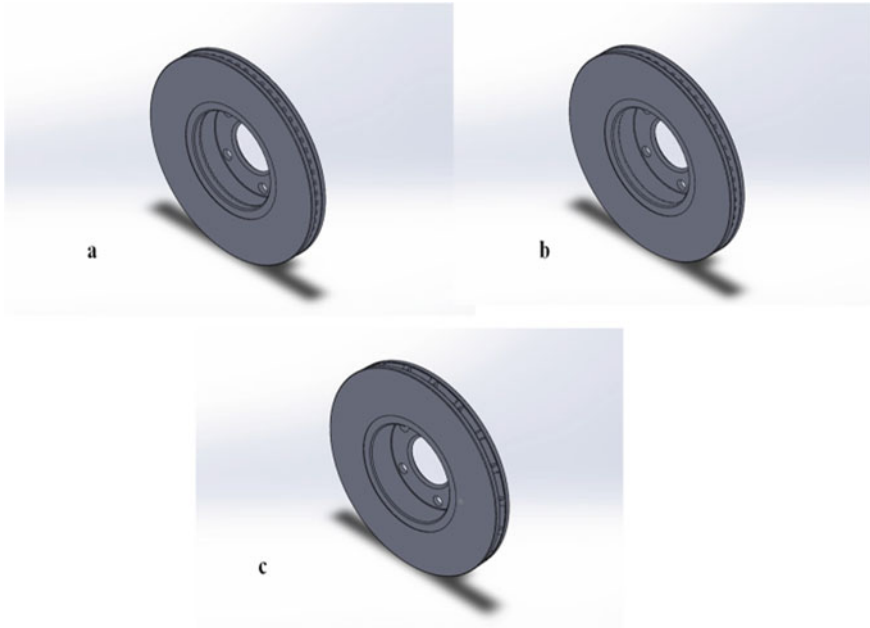


Fig. 2 3D model of the rotor profiles

2 Methodology

2.1 Software Used

Solid works 2018 is utilized to model the disc brake. Solid Works is modelling software that allows the user to design and develop products in 3D. The user should first sketch in 2D and then use the given features and develop it into a 3D model and is shown in Fig. 2. In order to analyse the designed profile ANSYS 16 software is used. ANSYS is a software package that lets the user to analyse the real-world circumstances and various testing conditions and the meshed component is shown in Fig. 3. The types of elements used are tetrahedral and the maximum skewness for tetrahedral cells are less than 0.95. The maximum cell squish index for all types of cells is less than 0.99. The mesh is very fine and accurate.

2.2 Material Selection

Two types of analysis were made on the disc brake system, they were static structural and transient thermal. The profiles that were compared are X-core, Corrugated and Round O-core. The properties are shown in Table 1. The design was done using

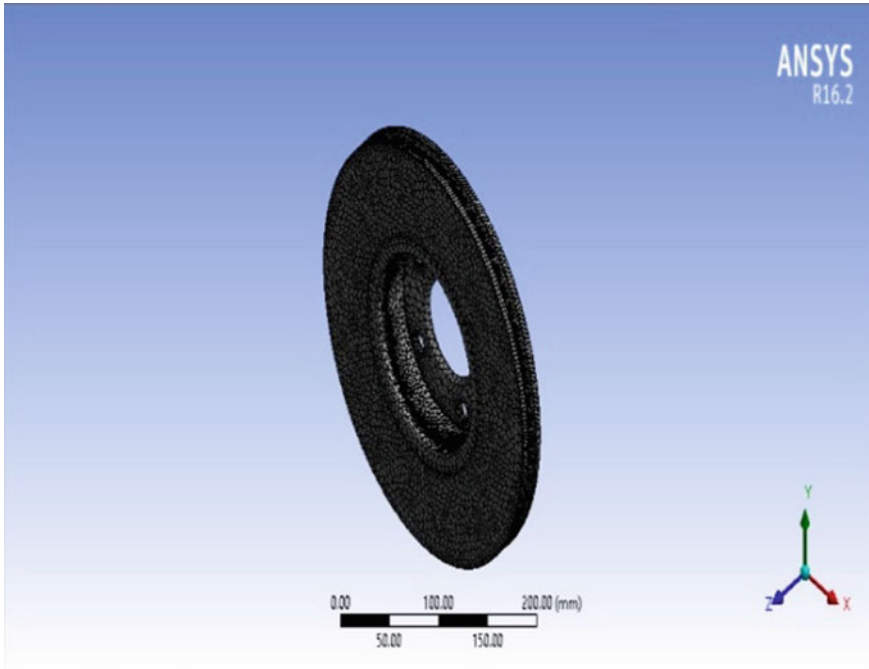


Fig. 3 Meshing

Table 1 Results of various materials

Profile	Temperature (°C)	Von Mises stress (MPa)	Deformation (mm)	Heat flux (W/mm ²)
X-core	1000	992.65	0.13468	0.24977
Round O-core	1000	961.95	0.091777	2.8499
Corrugated	1000	337.99	0.074692	0.9732

Solidworks 2018 and the analysis study was completed successfully with ANSYS 16 workbench suite. The profiles that are selected offer remarkable ratio of strength to weight and high corrosion resistance, and biocompatible. EN31 is a high quality alloy steel with carbon that offers high hardness values with supreme compressive strength and high abrasion resistance compared to the other steel alloys.

3 Results and Discussion

The Finite Element analysis was completed on the disc brake rotor model using the ANSYS 16 software. To substantiate the Disc, a static structural and transient state

thermal analysis study of the rotor was executed for working conditions with fixed hydraulic pressure and continual angular velocity, and a temperature of 1000 °C is applied to all the materials. The stress and the total deformation of the disc brake rotor with the various materials with similar boundary conditions were fed to the ANSYS program and the outcomes were presented in Table 1. The values for each of analysis are shown in Table 1. Using these outcomes, the strength and toughness of the disc brake rotor can be established. The von mises stress and total deformation outcomes reveal the stiffness, strength and toughness of the disc material, respectively. The thermal characteristic for the rotor depends on various criteria such as the application of the disc, the structure of the disc, the type of cooling and the materials used in the disc. The transient state is used to present the thermal results for the disc in this particular study. ANSYS aided to give deeper perspective in thermal behaviour of all the three different profiles like X-Core, Rounded O-core and corrugated and the output results were shown in the Figs. 4, 5 and 6 respectively. After analysing the three profiles, Round O-core has better thermal performance. It is clearly seen that the magnitude of temperature developed and the deformation are comparatively lesser than the other two profile. The stress and temperature outcomes are tabulated in Table 1. The extreme or the highest stress value is found in X-core and the minimum occurs in Corrugated although the difference is noticeable. A temperature of 1000 °C was applied to all three profiles. The maximum deformation occurs in X-core and the least occurs in Corrugated. The heat flux attains highest in Round O-core and least in the X-core disc brake rotor.

4 Conclusion

From the above analysis of the various profiles, if the brake has been designed where the main priority is strength, the corrugated profile can be favoured. Since, it is exposed to a lower quantity of stress and deformation when associated with the other profiles. Corrugated profile offers 98.39% and 95.99% lesser amount of stress when compared with X-Core and Round O-Core, respectively. Similarly with respect to deformation, corrugated profile is 57.30% and 20.52% lesser deformation with X-Core and Round O-Core, respectively. Likewise, if it required to be thermal grounded design Rounded O-core profile may be preferred. Subsequently, the total heat flux and 167.76% and 98.17% are higher when compared to X-Core and corrugated rotor profiles, respectively.

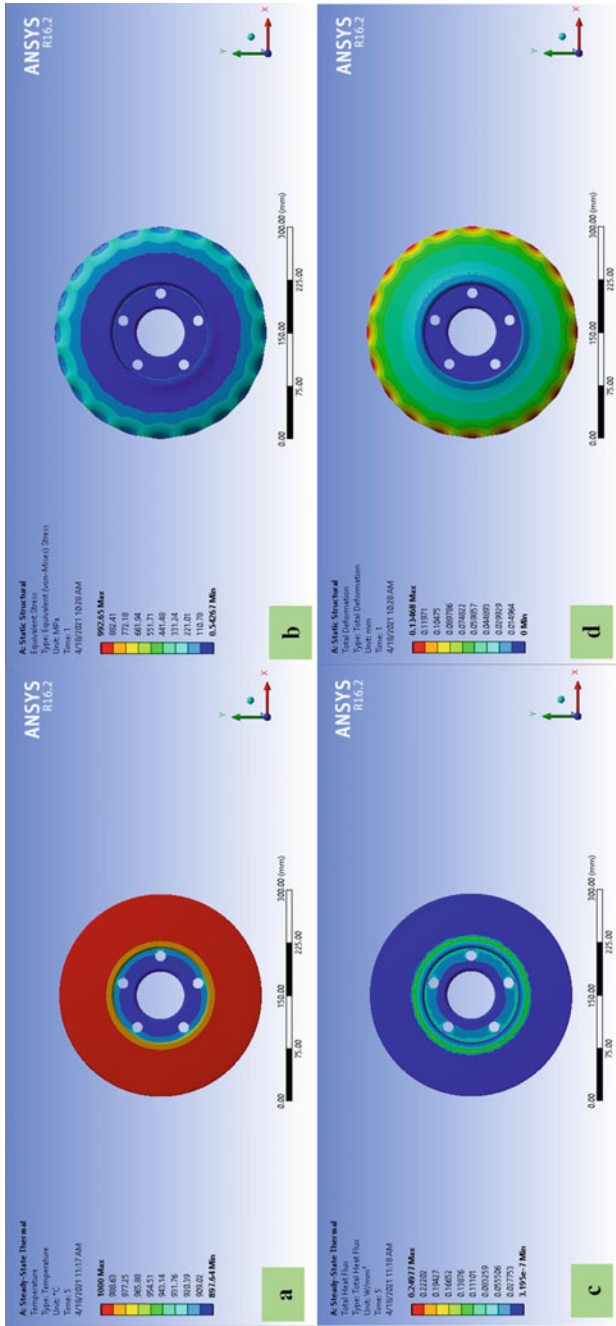


Fig. 4 Outcomes of X-core (a) Temperature (°C), (b) Equivalent stress, (c) Total deformation and (d) Total heat flux (W/mm²)

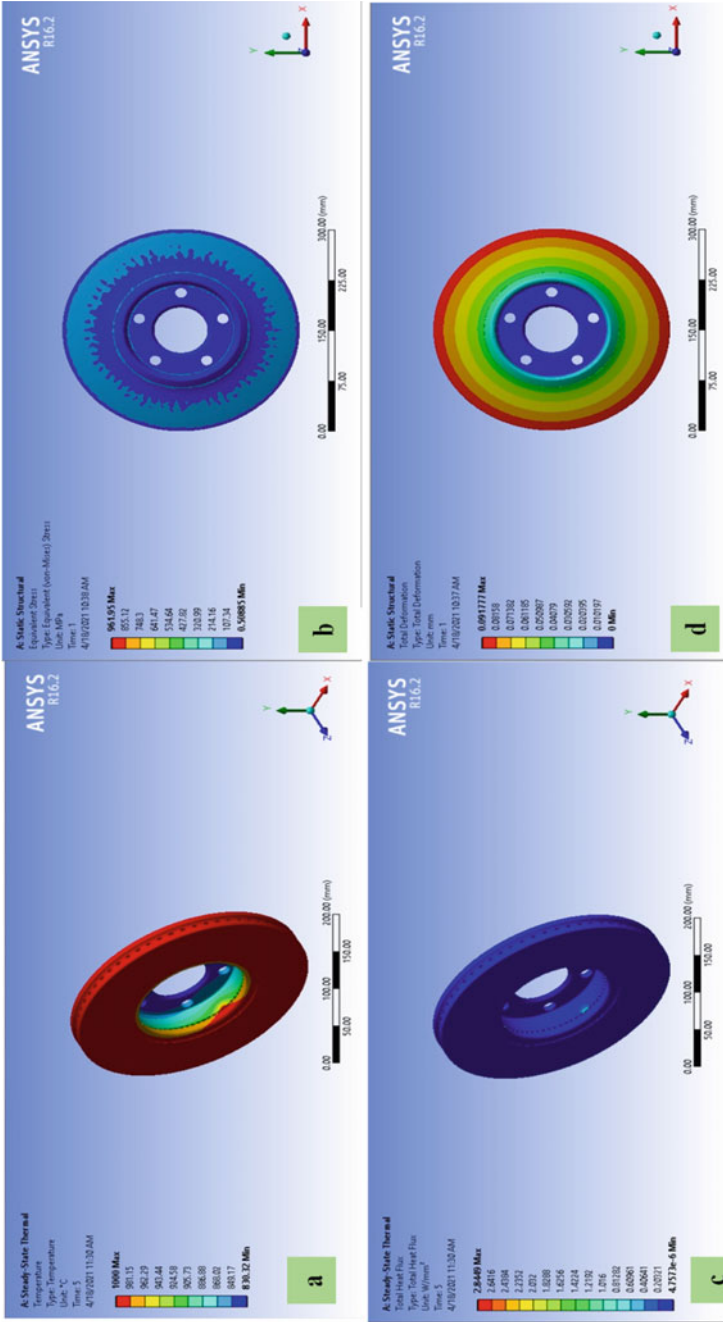


Fig. 5 Outcomes of rounded O-core (a) Temperature (°C), (b) Equivalent stress, (c) Total deformation and (d) Total heat flux (W/mm²)

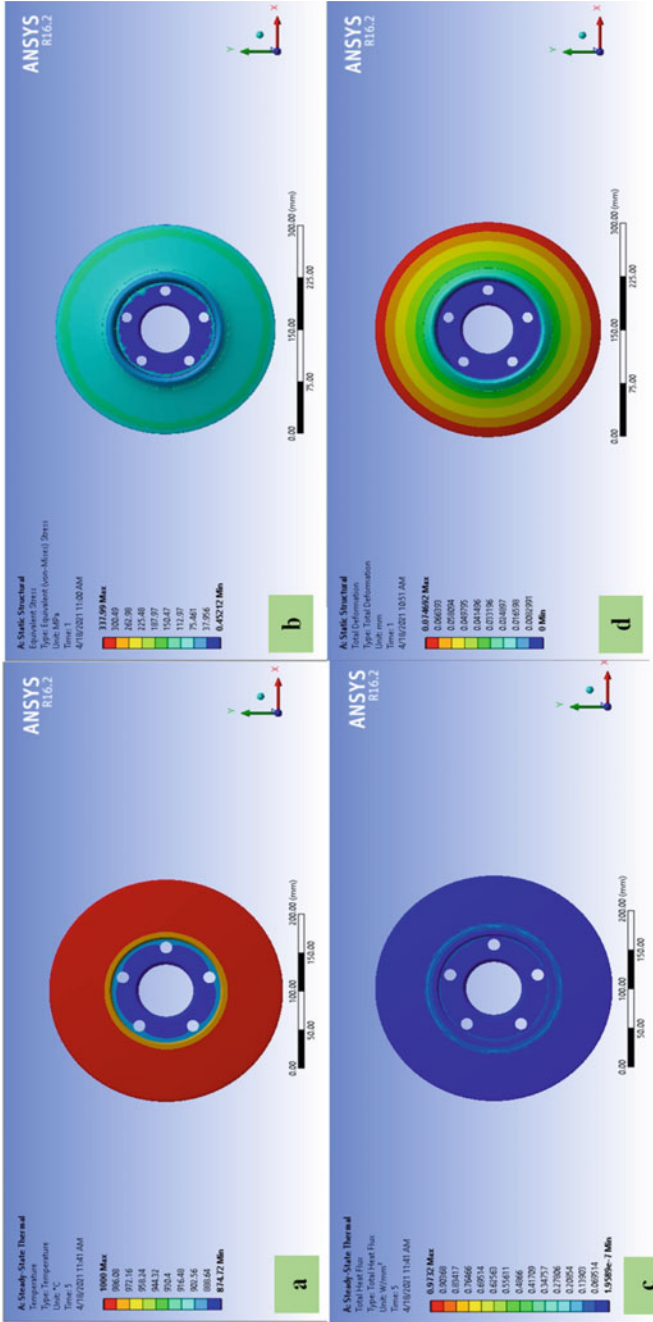


Fig. 6 Outcomes of corrugated (a) Temperature (°C), (b) Equivalent stress, (c) Total deformation and (d) Total heat flux (W/mm²)

References

1. Chengal Reddy V, Gunasekhar Reddy M, Harinath Gowd G (2013) Modeling and analysis of FSAE car disc brake using FEM. *Int J Emerg Technol Adv Eng* 3(9):383–389
2. Dhir DK (2018) Thermo-mechanical performance of automotive disc brakes. *Mater Today Proc* 5(1):1864–1871. <https://doi.org/10.1016/j.matpr.2017.11.287>
3. Tirovic M, Day AJ (1991) Disc brake interface pressure distributions. *Proc Inst Mech Eng Part D J Automob Eng* 205(2):137–146
4. Adamowicz A, Grzes P (2011) Analysis of disc brake temperature distribution during single braking under non-axisymmetric load. *Appl Therm Eng* 31(6–7):1003–1012. <https://doi.org/10.1016/j.applthermaleng.2010.12.016>
5. Belhocine A, Bouchetara M (2012) Thermal analysis of a solid brake disc. *Appl Therm Eng* 32:59–67. <https://doi.org/10.1016/j.applthermaleng.2011.08.029>
6. Chan DSEA, Stachowiak GW (2004) Review of automotive brake friction materials. *Proc Inst Mech Eng Part D J Automob Eng* 218(9):953–966. <https://doi.org/10.1243/0954407041856773>
7. Belhocine A (2017) FE prediction of thermal performance and stresses in an automotive disc brake system. *Int J Adv Manuf Technol* 89(9–12):3563–3578. <https://doi.org/10.1007/s00170-016-9357-y>
8. Voller GP, Tirovic M, Morris R, Gibbens P (2003) Analysis of automotive disc brake cooling characteristics. *Proc Inst Mech Eng Part D J Automob Eng* 217(8):657–666. <https://doi.org/10.1243/09544070360692050>
9. Jacobsson H (2003) Aspects of disc brake judder. *Proc Inst Mech Eng Part D J Automob Eng* 217(6):419–430. <https://doi.org/10.1243/095440703766518069>
10. Maleque MA, Dyuti S, Rahman MM (2010) Material selection method in design of automotive brake disc. In: *Proceedings of the world congress on engineering*, vol 3
11. Zhang J, Perez RJ, Lavernia EJ (1993) Documentation of damping capacity of metallic, ceramic and metal-matrix composite materials. *J Mater Sci* 28(9):2395–2404. <https://doi.org/10.1007/BF01151671>
12. Shunyu L, Shin YC (2019) Additive manufacturing of Ti6Al4V alloy: a review. *Mater Des* 164:107552. <https://doi.org/10.1016/j.matdes.2018.107552>
13. Dai N, Zhang L-C, Zhang J, Chen Q, Wu M (2016) Corrosion behaviour of selective laser melted Ti-6Al-4 V alloy in NaCl solution. *Corros Sci* 102:484–489. <https://doi.org/10.1016/j.corsci.2015.10.041>
14. Lee, D-G, Lee S, Lee Y (2008) Effect of precipitates on damping capacity and mechanical properties of Ti-6Al-4V alloy. *Mater Sci Eng A* 486(1–2):19–26. <https://doi.org/10.1016/j.msea.2007.08.053>
15. Kaviyaranan K, Ranganathan S, Guruswamy S, Kathiresan S, Nagarajan B Computation design and analysis of brake disc with various profiles No. 2020-28-0350. SAE Technical Paper, 202. <https://doi.org/10.4271/2020-28-0350>
16. Molinari A, Straffelini G, Tesi B, Bacci T (1997) Dry sliding wear mechanisms of the Ti6Al4V alloy. *Wear* 208(1–2):105–112. <https://doi.org/10.1007/s40544-019-0338-7>
17. Arrazola P-J, Garay A, Iriarte L-M, Armendia M, Marya S, Le Maître F (2009) Machinability of titanium alloys (Ti6Al4V and Ti555. 3). *J Mater Process Technol* 209(5):223–2230. <http://dx.doi.org/https://doi.org/10.1016/j.jmatprotec.2008.06.020>
18. He L, Cheng Y-S, Liu J (2012) Precise bending stress analysis of corrugated-core, honeycomb-core and X-core sandwich panels. *Compos Struct* 94(5):1656–1668. <http://dx.doi.org/https://doi.org/10.1016/j.compstruct.2011.12.033>

Production of Biodiesel Using Temple Waste Oil



A. Jagadeesh , Basavaraj M. Shrigiri , and Omprakash D. Hebbal

Abstract Energy need is the main focused area for the overall development of a country; the world's most widely used fuel is petroleum fuels. Diesel is the primary fuel for transportation and commercial usage, as the days passes the fossil fuel are depleting at alarming range. So in India most of the oils are poured on Hanuman and Shani god idols, based on mythological and religious belief, the oil poured on idols are considered not usable for any other purposes. This oil is called as temple waste oil and same can be used as best source of biodiesel, which is available cheaply at low cost. Temple waste oil biodiesel gives similar physical characteristics as that of diesel. Temple waste oil biodiesel blended with diesel can be used as alternative automobile fuel. In this paper, various blend characteristics are experimented and out of all the blends T25 will give similar properties as that of diesel, the viscosity of T25 is 8.25 cSt at 40 °C, density 830 kg/m³ and Calorific value is 41.6 MJ/kg and can be used in an existing engine. So temple waste oil can be a potential alternative source for diesel engine.

Keywords Viscosity · Density · Biodiesel · Calorific value · Combustion

1 Introduction

The world is moving on the wheels and at the same time wheels are driven by the engine. So there is a need for an efficient engine, which gives optimized performance by consuming a minimal amount of fuel. The resources of fossil fuel are depleting at a faster rate and even the dependencies on electric vehicles (EV) need up-gradation of material and technology [1]. As of now, electric vehicles are not replacing the diesel engine but they act as a substitute for diesel engines. The present world is in

A. Jagadeesh (✉) · O. D. Hebbal
PDA College of Engineering, Kalaburagi, Karnataka 585102, India
e-mail: jagadeeshalkur@gmail.com

B. M. Shrigiri
Sharnbasva University, Kalaburagi, Karnataka 585102, India

© The Author(s), under exclusive license to Springer Nature Singapore Pte Ltd. 2022
V. Krishna et al. (eds.), *Recent Advances in Hybrid and Electric Automotive Technologies*, Lecture Notes in Mechanical Engineering,
https://doi.org/10.1007/978-981-19-2091-2_8

demand of alternative energy sources to reduce the greenhouse effect and to enhance performance at a lower cost [2]. There are various forms of alternative energy are available like solar, wind, hydel, tidal, geothermal energy, etc [3]. Apart from all sources of energy, the most dependable energy source is a fossil fuel, which is harmful to the environment [4–6]. So there is a need for an affordable, accessible, and available energy source. Though any fuel can't replace diesel surely it will contribute lesser pollution to the environment there by global temperature can be controlled.

1.1 Alternative Fuels

Fossil fuels are depleting at a rapid rate, so there is a need for alternative fuel for diesel fuel. The alternative fuel must fulfill the properties of diesel to give the same or nearer performance given by that of diesel. The fuels chosen must meet the following criteria.

- i. Local availability
- ii. Higher calorific value
- iii. Better combustion parameters
- iv. Higher safety features
- v. Affordability
- vi. Accessibility.

The best alternative fuels are alcohol and biodiesel, as alcohol requires additional fuel handling arrangements. The only fuel with no or minor arrangements is biodiesel.

1.2 Biodiesel

The eco-friendly, low cost and locally available fuels are known as biodiesel. As the name indicated it is drawn from sources like vegetable oils and algae. Out of all these, biodiesel is generally drawn from non-consumable oils like jatropha, honge, cottonseed, neem oil, etc.

In this, the biodiesel is drawn from the temple waste oil. In our country oil is poured on Hanuman and Shani god idols. This is followed from ancient days as in our mythological and religious beliefs. The temple waste oil is one of the abundantly available sources of biodiesel. The temple waste oil is not used for any other applications. It is available cheaply, near temples. Biodiesel is derived from vegetable oils through the process called transesterification process. In this process, the vegetable oil is treated with alcohol and a catalyst to perform the chemical reaction. Generally, methanol/ethanol is used as alcohol and sodium hydroxide/potassium hydroxide is used as a catalyst.

2 Literature Survey

In this section, the productions of biodiesel from various sources are discussed. Table 1 gives details of various properties of biodiesel compared with diesel. Shrigiri et al. [7] experimented on Sugar apple seed oil biodiesel and found a greater calorific value of about 15 MJ/kg compared to diesel, with other properties similar to diesel. Abhishek Sharma et al. [8] used tyre pyrolysis oil biodiesel as a primary fuel and 0.81 unit higher viscosity, 78 kg/m³ of density higher than diesel; this is due to the chemical nature of the TPO. B. Dhinesh et al. [9] worked on *Cymbopogon flexuosus* biodiesel, with 2.06 units of viscosity and 70 kg/m³ of higher density compared to diesel; these can be minimized with preheating. Further works of many authors [10–14] concerning castor oil biodiesel, cottonseed oil biodiesel, Neem kernel oil biodiesel, Pongamia oil biodiesel, Simarouba oil biodiesel, Mahua oil biodiesel, and waste cooking biodiesel oil are got similar properties with that of diesel with slight variations in viscosity and density. The other biodiesels are, Tobacco seed oil biodiesel, *Thevetia peruviana* oil biodiesel, Polanga (*Calophyllum inophyllum*) oil biodiesel, Fish oil biodiesel (FOME), *Pithecellobium dulce* biodiesel, and Linseed oil biodiesel [15–20], experimented with higher flash and fire point with nearer calorific values (CV) compared to diesel. Higher flash and point assures safety operation with the use of biodiesel and other properties are a comfort to conduct testing on the given engine without any minor modifications. From the above literature survey, no or less work has been carried out on temple waste oil (TWO) as a source of biodiesel. In our country one can locate at least one of Lord Hanuman, Lord Shiva temple, and other temples [21, 22]; these temples are the sources of TWO, the TWO can easily convert to TWOB and it's sufficient to fulfill the local transportation needs. So this paper fills the gap and proposes the use of temple waste biodiesel (TWOB) as an alternative fuel for IC engines.

3 Materials and Methods

This section discusses detailed work on sources of biodiesel and the production of biodiesel.

3.1 Collection of Temple Waste Oil

The temple waste oil was collected in a clean bottle from Hanuman temple, Toor-nahalli, Belagavi, India. It is a mixture of various unknown quantities of edible oils and ghee.

Table. 1 Physical properties of diesel and other biodiesels

Sl.No	Ref. No	Authors/ref	Fuel	Flash point (°C)	Fire point (°C)	Kinematic viscosity cSt at 40 °C	Density (kg/m ³)	CV (MJ/kg)
			Diesel	54	63	2.54	835	42.5
1	[7]	Shrigiri	Sugar apple seed oil biodiesel	138	167	5.7	875	57.5
2	[8]	Sharma and Murugan	Tyre pyrolysis oil biodiesel (TPO)	49	58	3.35	913	38.1
			Jatropha biodiesel (JME)	156	171	5.6	881	39.4
3	[9]	Dhinesh et al.	Cymbopogon flexuosus biofuel	55	–	4.6	905	37
4	[10]	Arunkumar et al.	castor oil methyl ester	168	178	9.86	888	34.4
5	[11]	Shrigiri	Cotton seed oil biodiesel (CSOME)	165	175	4.02	878	39.029
			Neem kernel oil biodiesel (NOME)	160	175	4.08	896	41.53
6	[12]	Jagadeesh et al.	Pongamia oil biodiesel (POME)	144	155	12.5	900	40.273
7	[13]	Siddalingappa et al.	Karanja Oil	>200	–	54.14	930	36.48
8	[14]	Manjunath et al.	Simarouba oil biodiesel	152	–	5.09	878	40.62
			Mahua oil biodiesel	150	–	5.45	874	38.21
			Waste cooking oil biodiesel	150	–	4.72	882	38.91
9	[15]	Shrigiri	Tobacco seed oil biodiesel	145	162	4.69	887	38.9
10	[16]	Harari et al.	Thevetia peruviana oil biodiesel (TPME)	177	–	5.75	892	39.45

(continued)

Table. 1 (continued)

Sl.No	Ref. No	Authors/ref	Fuel	Flash point (°C)	Fire point (°C)	Kinematic viscosity cSt at 40 °C	Density (kg/m ³)	CV (MJ/kg)
11	[17]	Sahoo and Das	Polanga (Calophyllum inophyllum) oil biodiesel	140	–	3.99	869	41.4
12	[18]	Kattimani et al.	Fish oil biodiesel (FOME)	172	185	4.18	898.3	39.5
13	[19]	Sekhar et al.	Pithecellobium dulce biodiesel (PDBD)	158	165	3.54	870	39.51
14	[20]	Uyumaz	Linseed oil biodiesel	108	–	16.23	924	39.75

3.2 Biodiesel Preparation

The titration method is used to find the free fatty acid content of temple waste oil (TWO). Titration is performed in a conical flask as shown in Fig. 1, collection of 1 ml TWO in micropipette, 10 ml isopropyl methanol, and 2–4 drops of phenolphthalein indicator with continuous shaking. Once the solution turns to faint pink conclude the reaction. Note down the burette readings. FFA was known to be 1.17%. The mean

Fig. 1 Titration

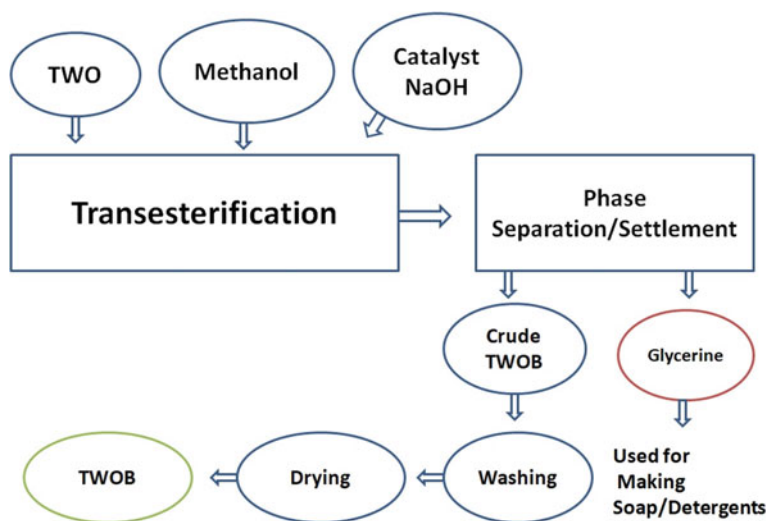


Fig. 2 Biodiesel production workflow

burette measurement was divided by 10 and 3.5 were added to get the FFA, which provides the grams of sodium hydroxide necessary for the transfer of 1 l of TWO into biodiesel.

The workflow is shown in Fig. 2 which gives detailed biodiesel production [22]. The TWO is filtered to remove dust and dirt. Oil is pre-heated up to 60–70 °C to reduce the viscosity. The oil was additionally heated up to 100 °C for about 30 min to eliminate moisture. The basic catalyst (NaOH, 6 g/l of oil) was dissolved in methanol (200 ml, density 0.792 g/cm³) in a different container and was transferred into a three-neck flask containing pre-heated oil and continuously stir the mixture for 2 h with the help of a magnetic stirrer at 600 RPM to mix the oil with the solution. After completion of the reaction, the entire mixture is transferred to a separating funnel. The mixture was allotted to settle for 1 day in a separating funnel. After 1 day one can easily differentiate the temple waste oil biodiesel (TWOB) in the upper portion with amber color and in lower part glycerine, excess alcohol, traces of untreated oil, and catalyst impurities as shown in Fig. 3. At this point, the glycerine was removed and used to make detergent. The remaining TWOB is washed with water to remove soap contents.

Transfer TWOB into a heating funnel and heating is done above 100 °C to eliminate traces of moisture present in TWOB as shown in Fig. 4. Now TWOB was used for characterization.

Fig. 3 Phase separation/settling tank



Fig. 4 Temple waste oil biodiesel (TWOB)



4 Results and Discussions

This chapter gives insights into TWOB properties and their comparison with diesel and other biodiesels. As the TWO is collected from the Tooranahalli Hanuman temple and converted to TWOB through the transesterification process as mentioned in the above chapter. Physical characteristics of TWOB are measured at the Government recognized state-of-the-art laboratory in Gandhi Krishi Vigyana Kendra (GKVK) at

Table 2 Physical properties of temple waste oil biodiesel, its blends and diesel

Properties	Diesel	T25	T50	T 75	T 100	TWO
Density (kg/m ³)	835	830	845	858	868	910
Kinematic viscosity @ 40 °C cSt	2.54	2.85	3.5	4.3	5	27.02
Flash point (°C)	54	56	78	121	164	202
Fire point (°C)	63	58	82	125	167	209
Calorific value (MJ/kg)	42.5	41.6	39.35	39.17	39.0	38.52

Table 3 Physical properties of TWOB and some other non-edible oil biodiesels

Properties	Temple waste oil biodiesel	Jatropha oil biodiesel	Pongamia oil biodiesel	Waste cooking oil biodiesel	Fish oil methyl ester
Density (kg/m ³)	868	881	900	882	900
Kinematic viscosity @ 40 °C cSt	5	5.6	12.5	4.72	4.18
Flash point (°C)	164	156	144	150	172
Fire point (°C)	167	171	155	170	185
Calorific value (MJ/kg)	39.0	39.4	40.2	38.9	39.5

the University of Agricultural Science, Bengaluru according to IS 1448 (P6, P25, P32, and, P66) and were compared with diesel as listed in the Tables 2 and 3.

4.1 Physical Characteristics of TWOB and Its Blends

The properties of TWOB, its blends are compared with diesel, are mentioned in Table 2. From the given Table 2 it is clear pure biodiesel (B100–100% TWOB) has similar physical characteristics as that of diesel. T25 (25% of TWOB and 75% of diesel) blend has 5 kg/m³ less density compared to diesel, 38 kg/m³ are lesser than of B100. Viscosity also plays a crucial role in combustion. So T25 has a difference of 0.31 cSt at 40 0C with diesel, 2.15 cSt lower compared to B100. Flashpoint of T25 is almost the same as diesel with only 20C difference, further other blends and TWO have shown an increasing trend in the flashpoint. This is due to the rise in oxygen content in the respective blends. The fire point of diesel 5 0C larger compared to T25 and B100 has 1040C differences. From the table, fire point increases as blend percentage increases and is higher for TWO. A larger fire point makes the fuel operating in safer conditions with lower emissions. Calorific value (CV) decides the fuel economy and

combustion performance of an engine. Higher the biodiesel proportion lower will be the CV. Diesel having a maximum CV compared to all other blends and TWO. This is due to the chemical nature of biodiesel. Table 2 gives T25 nearer physical characteristics compared to diesel

Further Table 3 explains the TWOB properties compared with known non-edible oil biodiesels, the density of TWOB is least as compared to all other biodiesels, this is due to the chemical nature of the TWO, as it is a mixture of many edible and non-edible oils. The viscosity is the deciding factor in combustion, larger viscosity fuels require additional equipment to handle the high viscous fuel, TWOB was 0.6 cSt lower than jatropha biodiesel, 7.5 cSt lesser than Pongamia biodiesel, whereas it is higher compared to waste cooking oil and fish oil biodiesel. The TWOB has higher flash and fire points compared to other biodiesels, and it is an added advantage. As higher the fire point safer will be the engine operation with controlled combustion. Calorific values of all biodiesel are nearer to 40 MJ/kg, but Pongamia biodiesel shows better results compared to TWOB and remaining biodiesels.

5 Conclusion

The main aim of the article is to prove that temple waste oil is a potential fuel for an engine. Physical characteristics of temple oil were enhanced through the transesterification process, and the subsequent conclusions were listed.

1. The waste temple oil is transferred into temple waste oil biodiesel (TWOB) by the simple transesterification and found that free fatty acid content is below 2% (1.17% FFA).
2. T25 properties are superior related to diesel, but they are within the standards.
3. T25 has a lesser density (830 kg/m^3) compared to conventional fuel (835 kg/m^3), which makes it easy handling of fuel.
4. Calorific value of T25 is found to be 41.6 MJ/kg, it is neared to diesel (42.5 MK/kg), So temple waste oil biodiesel is a promising substitute fuel for diesel; this biodiesel is locally available at a low cost compared to other non-edible vegetable oil biodiesels.
5. The main limitation of temple waste oil biodiesel is that the collected oil sample contains many other components like ghee, vegetable oil, and other particles, so there is a need for cleaning and drying before converting TWO to TWOB.

References

1. Barbir F, Veziroğlu TN, Plass HJ Jr (1990) Environmental damage due to fossil fuels use. *Int J Hydrogen Energy* 15(10):739–749
2. York R (2012) Do alternative energy sources displace fossil fuels? *Nat Clim Chang* 2(6):441–443

3. Lee S (1996) *Alternative fuels*. CRC press
4. Withagen C (1994) Pollution and exhaustibility of fossil fuels. *Resour Energy Econ* 16(3):235–242
5. Lvovsky K (2000) Environmental costs of fossil fuels: a rapid assessment method with application to six cities
6. Joensuu OI (1971) Fossil fuels as a source of mercury pollution. *Science* 172(3987):1027–1028
7. Shrigiri BM (2021) Combustion characteristics of sugar apple seed (*Annona squamosa*) oil methyl ester and its blends on compression ignition engine. *Int J Ambient Energy* 1–10
8. Sharma A, Murugan S (2015) Potential for using a tyre pyrolysis oil-biodiesel blend in a diesel engine at different compression ratios. *Energy Convers Manag* 93:289–297
9. Dhinesh B, Lalvani JIJ, Parthasarathy M, Annamalai K (2016) An assessment on performance, emission and combustion characteristics of single cylinder diesel engine powered by cymbopogon flexuosus biofuel. *Energy Convers Manag* 117:466–474
10. Arunkumar M, Kannan M, Murali G (2019) Experimental studies on engine performance and emission characteristics using castor biodiesel as fuel in CI engine. *Renew Energy* 131:737–744
11. Shrigiri BM, Hebbal OD, Reddy KH (2016) Performance, emission and combustion characteristics of a semi-adiabatic diesel engine using cotton seed and neem kernel oil methyl esters. *Alex Eng J* 55(1):699–706
12. Alku J, Patil PS, Hebbal O (2013) Experimental investigation of performance and combustion characteristics of pongamia biodiesel and its blends on diesel engine and IHR engine
13. Siddalingappa RH, Omprakash H (2011) Performance and combustion characteristics of single cylinder diesel engine running on karanja oil/diesel fuel blends. *Engineering*
14. Manjunath H, Omprakash H, Reddy KH (2015) Process optimization for biodiesel production from simarouba, mahua, and waste cooking oils. *Int J Green Energy* 12(4):424–430
15. Shrigiri BM (2020) Performance of a low heat rejection engine fuelled with tobacco seed oil and its methyl ester (TSOME). *Int J Ambient Energy*:1–9
16. Harari PA, Banapurmath NR, Yaliwal VS, Soudagar M, Khan TY, Mujtaba MA, Safaei MR, Akram N, Goodarzi M, Elfasakhany A, EL-Seesy AI (2021) Experimental investigation on compression ignition engine powered with pentanol and thevetia peruviana methyl ester under reactivity controlled compression ignition mode of operation. *Case Stud Therm Eng* 25:100921
17. Sahoo PK, Das LM (2009) Combustion analysis of *Jatropha*, *Karanja* and *Polanga* based biodiesel as fuel in a diesel engine. *Fuel* 88(6):994–999
18. Kattimani SS, Topannavar SN, Shivashimpi MM, Dodamani BM (2020) Experimental investigation to optimize fuel injection strategies and compression ratio on single cylinder DI diesel engine operated with FOME biodiesel. *Energy* 200:117336
19. Sekhar SC, Karuppusamy K, Sathyamurthy R, Elkelawy M, Bastawissi H, Paramasivan P, Sathiyamoorthy K, Edison P (2019) Emission analysis on compression ignition engine fuelled with lower concentrations of *Pithecellobium dulce* biodiesel-diesel blends. *Heat Transfer—Asian Res* 48(1):254–269
20. Uyumaz A (2020) Experimental evaluation of linseed oil biodiesel/diesel fuel blends on combustion, performance and emission characteristics in a DI diesel engine. *Fuel* 267:117150
21. Saddu S, Kivade SB, Ramana P (2020) Used temple oil, a source for biodiesel production. In: *Advances in energy research, vol 2: selected papers from ICAER 2017*, vol 405
22. Saddu S, Kivade SB, Ramana P (2019) The synthesis of biodiesel from used temple oil. *J Inst Eng (India): Ser C* 100.4:701–706

Experimental Analysis of a Counter Flow Plate Heat Exchanger by Using Nanofluids at Different Concentrations



Anil Kumar and Amman Jakhar

Abstract Heat transfer characteristics of nanofluids are improved by increasing the mass flow and inlet temperature. This article is intended to study the rate of transfer heat of nanofluids by counter flow conditions using forced convection mode. A two-step method was used to finalise the alumina nanoparticles. In this experimental analysis as the size of the particle decreases, the rate of heat transfer increases. In this experimental analysis, nanoparticles with a diameter size of 30 nm were used. Distilled water was used as the base fluid to prepare the nanofluids of alumina with different volume concentrations (0.14, 0.28, 0.4 and 0.52%). The experimental results show better thermophysical properties of nanofluid, and also Reynolds number and Prandtl number have been calculated.

Keywords Plate heat exchanger · Nanofluids · Base fluid

1 Introduction

The heat exchanger is a component that uses thermal energy to control the temperature of a substance or system. It can be classified as either a direct contact or indirect contact device. Pandey et al. [1] have studied that the Reynolds number for a hydraulic diameter of 750–3200 is varied by the flow rates of air and water. The data are presented in an experimental analysis. Singh and Ghosh et al. [2]. In experimental analysis numerical and experimentation results were analysed and got that the two results are in good agreement. And the results showed an improvement of approximately 13% in thermal conductivity and 14% in heat transfer rate, and 9% in efficiency in total heat transfer coefficient at the expense of heat loss and pump power when using nanofluids. “The exergy rate were also reduced by using a nanofluid with an optimal concentration of 1 vol%” Khanlari et al. [3]. The experiments were performed under different positions to establish the influence of the use of nanofluid. Mansoury [4] has studied the double HE tube that showed the best

A. Kumar (✉) · A. Jakhar

Department of Mechanical Engineering, OM Sterling Global University, Hisar 125001, India
e-mail: anilmec191@osgu.ac.in

rate of heat transfer coefficient result with a maximum improvement of 60%. The use of the nanofluid denoted the lowest penalty at pressure losses with a maximum improvement of 27% for the HE plate, while the highest penalty was observed at pressure losses with a maximum improvement of 85% in HE with double tube and calendar. Barzegarian et al. [5]. The heat transfer assessment revealed that the addition of nanofluids to the mix increases the Nusselt numbers by almost 30%. It also showed a significant increase in heat transfer coefficient due to the volume fraction. The heat transfer result demonstrates the application of nanofluids as compared to base fluids which leads to an increase in Nusselt numbers up to “9.7, 20.9 and 29.8% at 0.03, respectively, 14 and 0.3% by volume, respectively”. Since it was found that the volume fraction of said nanoparticles, the total heat transfer coefficient of the heat exchanger increased by about “5.4, 10.3 and 19.1%, respectively”. Choi et al. [6] have found a new class of fluid that can be designed using the principle of suspending metal nanoparticles in a conventional heat transfer fluid. Pak et al. [7]. In this experiment, a circular tube has been studied. Measurements of viscosity were also carried out by using a viscometer of Brookfield rotary. The viscosity of liquids dispersed with particles of Al_2O_3 and TiO_2 at a concentration of 10% by volume is about 200 and 3 times that of water. Xuan et al. [8]. It is observed that the heat transfer rate enhance by nanoparticles which increases nanofluid increases the thermal conductivity and induces heat dispersion of the flow, it is an new way to improve heat transfer. Passman et al. [9]. “In this study, an attempt was made for a nanofluid consisting of water and a volume concentration of 1% Al_2O_3 /water. Al_2O_3 nanoparticle with a diameter size of 50 nm was used, and it was found that the rate of heat transfer coefficient and the heat transfer coefficient of the nanofluid were slightly higher than that of the base liquid at the same mass velocity and at the same inner temperature”.

2 Word Methodology

The experimental study proposes nanofluid’s heat transfer rate in plate-type heat exchanger (PHE). A sequence of steps for this work is shown below (Fig. 1).

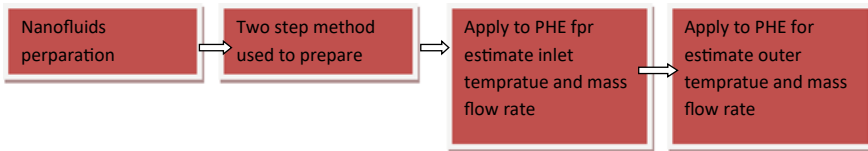


Fig. 1 .



Fig. 2 Ultrasonic cleaner

Table 1 Properties of basic liquids and nanoparticles at atmospheric temperature 27 °C

	(ρ) (kg/m ³)	C_p (J/kg K)	K (W/m K)	Viscosity μ (kg/m s)	A (m ² /s)	Prandtl no. (Pr)
Water	1000	4200	0.65	838.2×10^{-6}	0.147×10^{-6}	5.8
Al ₂ O ₃	2925	745	45			

2.1 Preparation of Nanofluids

Alumina is a mixture of aluminium and oxygen. Preparation of nanofluid plays a very important role. Nanofluids were prepared by using commercially available alumina of approximate 30 nm diameter with the base fluid being distilled water. The Nano alumina powder is dispersed in 1,000 common basic liquids such as water at different volume concentrations of 2, 3, 4 and 5% using an ultrasonicator that is available in the nanotechnology lab (Fig. 2 and Table 1).

2.2 Experimental Setup

The counter flow heat exchangers are made up of mild steel. In this work is included a photograph of the experimental setup fabricated to find out the characteristics of different flow rates at different fluid volume concentrations. It includes a hot water and coolant loop and measuring system. The main components of the setup are



Fig. 3 Setup

numbered in schematics. It includes a water tank containing a heater, pump and the flow rate and temperature measuring instruments. Pump flow rate is 0.4 kg/s and surface area (A) of the heat exchanger is 0.3 m² (Fig. 3).

Nanofluids thermophysical properties

Experimentally, thermophysical properties of nanofluids were measured. The viscosity of nanofluid is measured by viscometer at room temperature and thermal conductivity by K-type thermocouple, and specific heat by measuring thermal instruments.

3 Heat Transfer Rate and Nanofluid Properties’ Evaluation

3.1 Heat Transfer Rate

Nanofluid density by Pak and Cho [9] relations is

$$\rho_{nf} = (1 - \varphi)\rho_{bf} + \varphi\rho_p \tag{1}$$

where Nanofluid density is ρ_{nf} , φ is the nanoparticle volume concentration, and base liquid ρ_p is nanoparticles density.

Specific heat of nanofluid from Xuan [10] is

$$(\rho C_p)_{nf} = (1 - \varphi)(\rho C_p)_f + \varphi(\rho C_p)_p \tag{2}$$

where Nanofluid specific heat is $(C_p)_{nf}$ and $(C_p)_p$ is Nanoparticle specific heat and (C_{pf}) is heat capacity of the base fluid.

The heat transfer rate is

$$Q = m(C_p)_{nf}\Delta T \quad (3)$$

where heat transfer rate is Q and m is the mass flow rate of nanofluid flow, temperature difference of cooling fluid is ΔT .

The logarithmic mean temperature difference (LMTD) is determined according to the following relationship:

$$\Delta T_{lm} = [(T_{bi} - T_{no}) - (T_{bo} - T_{ni})/\ln(T_{bi} - T_{no}/T_{bo} - T_{ni})] \quad (4)$$

When the logarithmic mean temperature difference (LMTD) is ΔT_{lm} , T_{bi} and T_{bo} are inlet and outlet temperatures of the base liquid, where T_{ni} , T_{no} are nanofluid inlet temperature and outlet temperature.

The heat transfer coefficient is determined according to the relation given below.

$$Q = U A_s \Delta T_{lm} \quad (5)$$

In this relationship, the total heat transfer coefficient is U and the surface area of the heat exchanger is A_s .

Nanofluids thermal conductivity from Choi and Yu [8] relation is

$$K_{nf} = K_{bf} * (K_p + 2K_{bf}) - 2\varphi(K_{bf} - K_p)/K_p + 2K_{bf} + \varphi(K_{bf} + K_p) \quad (6)$$

where the thermal conductivity of the nanofluid is K_{nf} , and thermal conductivity of the nanoparticle is K_p and thermal conductivity of the base fluid is K_{bf} .

Drew and Passman [11] proposed an equation to calculate nanofluid viscosity as follows:

$$\mu_{nf} = (1 + 2.5)\mu_{bf} \quad (7)$$

where μ_{nf} is the viscosity of the nanofluid and μ_{bf} is for base fluid.

To assess the accuracy of the measurement, the test was performed on distilled water, before checking the characteristics of heat transfer of different volume concentrations of Al_2O_3 /water. From the experimental system, the measured values are the inner and outer temperatures of the inlet of distilled water and the different concentrations of the nanofluid as well as for hot water at different flow rates.

“Friction factor (f) calculated by using the Gnielinski equation for base fluid and Duangthongsuk and Wongwises relation for nanofluid is as follows”:

$$f = [1.58 \ln Re - 3.82]^{-2} \quad (8)$$

Table 2 The result for base fluid and nanofluids in counter flow conditions

Counter flow condition			
	LMTD	U	Q
Water	52.5	247.23	3761.12
0.14%	45	423.12	6104
0.28%	47	468.24	6427.98
0.4%	42	678.18	8121
0.52%	38	895.00	8665.89

This equation indicates to find out the friction factor, where f denotes the friction factor and Re denotes the Reynolds number.

Find the Reynolds number and Prandtl number by using the relation

$$Re = \rho V D / \mu \tag{9}$$

$$Pr = \mu / \rho \alpha \tag{10}$$

In this relation, velocity is V , diameter is D and viscosity is μ of the nanofluid and α denotes thermal diffusivity of fluid.

And we calculated thermal diffusivity and the Peclet number by using the equation

$$\alpha = [K / \rho C_p] \tag{11}$$

and

$$\text{Peclet number (Pe)} = [V D / \alpha] \tag{12}$$

For finding the Nusselt number (Table 2),

$$Nu = [(0.125 f)(Re - 1000)Pr / 1 + 12.7(0.125 f)^{0.5}(Pr^{2/3} - 1)] \text{ for base fluid} \tag{13}$$

$$Nu = [0.074 Re^{0.707} Pr^{0.385} \varphi^{0.074}] \text{ for nanofluid.} \tag{14}$$

4 Result and Discussion

Heat was measured from the experimental analysis. In this experiment, first we calculated the values of heat transfer characteristics for pure water and then calculated the values of Al_2O_3 /water at the same mass flow rate and inlet and outlet temperatures at the same values. In this experiment, the nanofluid concentrations are 0.14, 0.28, 0.4

and 0.52% and then applied for the heat exchanger and calculated the heat transfer characteristics for counter flow conditions. In the counter flow conditions, the highest rate observed for 0.52% volume percentage is 8665.89 W. And as the Nusselt number increases, the Prandtl number also increases (Figs. 4 and 5).

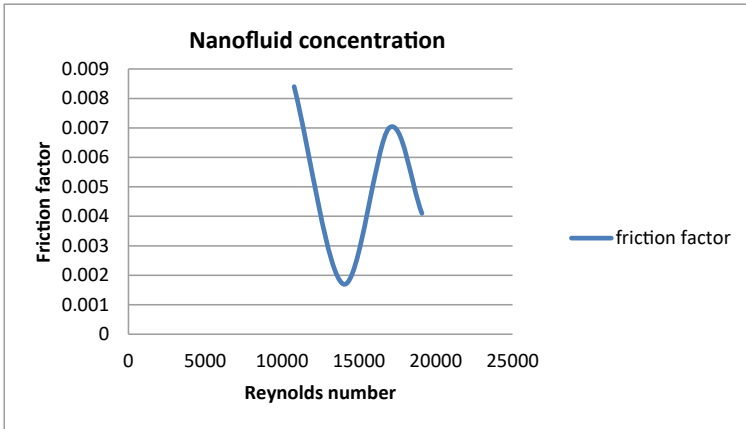


Fig. 4 The relation between friction factor and Reynolds number

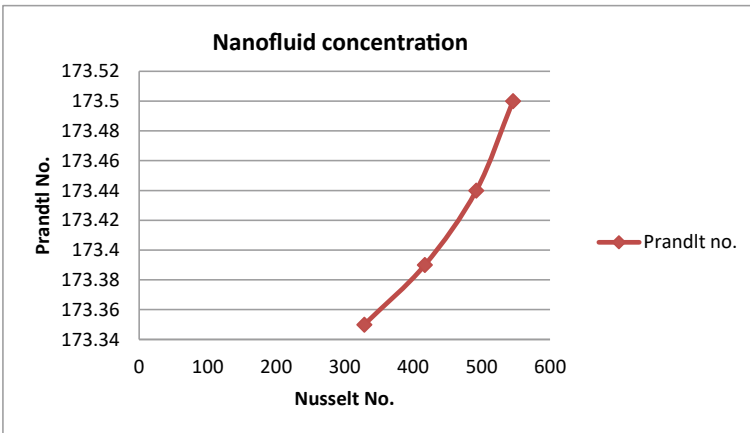


Fig. 5 Relation between Prandtl and Nusselt numbers

5 Conclusion

The rate of heat transfer on counter flow plate-type heat exchanger by using Al_2O_3 nanofluid has been investigated experimentally. And heat transfer rate, Reynolds number, Prandtl number, friction factor and overall heat transfer coefficient were measured for counter flow conditions. Important results were measured in this experiment as follows:

1. The heat transfer rate of the nanofluid increases as the volumetric concentration of the nanofluid increases.
2. Reynolds number increases with decreasing friction factor for nanofluid.
3. In counter flow conditions, the rate of heat transfer is more for 0.52%, and volume concentrations of nanofluids is 8665.89 W. The total heat transfer rate of nanofluids is more than 2 times that of the base liquid.
4. The stability of nanofluid for 30 nm size is incipient.

References

1. Pandey SD, Nema VK (2011) Investigation of the performance parameters of an experimental plate heat exchanger in single phase flow. *Energy Eng* 1(1):19–24
2. Singh S, Verma P, Ghosh SK (2021) Numerical and experimental analysis of performance in a compact plate heat exchanger using graphene oxide/water nanofluid. *Int J Numer Methods Heat Fluid Flow*
3. Khanlari A, et al (2020) Investigation of the influences of kaolin-deionized water nanofluid on the thermal behavior of concentric type heat exchanger. *Heat and Mass Transf* 56(5):1453–1462
4. Mansoury D, et al (2019) Heat transfer and flow characteristics of Al_2O_3 /water nanofluid in various heat exchangers: experiments on counter flow. *Heat Transf Eng*
5. Barzegarian R, Aloueyan A, Yousefi T (2017) Thermal performance augmentation using water based Al_2O_3 -gamma nanofluid in a horizontal shell and tube heat exchanger under forced circulation. *Int Commun Heat Mass Transf* 86:52–59
6. Choi SU, Eastman JA (1995) Enhancing thermal conductivity of fluids with nanoparticles (No. ANL/MSD/CP-84938; CONF-951135-29). Argonne National Lab., IL
7. Pak BC, Cho YI (1998) Hydrodynamic and heat transfer study of dispersed fluids with submicron metallic oxide particles. *Exp Heat Transf Int J* 11(2):151–170
8. Xuan Y, Roetzel W (1998) Conceptions for heat transfer correlation of nanofluids. *Int J Heat Mass Transf* 43(19):3701–3707
9. Drew DA, Passman SL (1998) Theory of multicomponent fluids. *Appl Math Sci* 135:105–120. 185 https://doi.org/10.1007/0-387-22637-0_11

Design Evaluation in Reconfigurable Manufacturing System (RMS): A Multi-Objective Squirrel Search Algorithm



N. Swamy, U. M. Daivagna, A. Thimmana Gouda,
and R. H. M. Somanath Swamy

Abstract In recent years, the manufacturing situation is considered through the requirement of cost-effectively, coping speedily, in addition customized flexibility toward manage market requirements. These issues should be satisfied by minimizing time, cost, and modularity index. This paper has proposed a Multi-Objective Squirrel Search Algorithm (MOSSA) to optimize the Reconfigurable Manufacturing System (RMS) design. To empower the RMS performance, three different objectives are considered such as system cost minimization, system completion time minimization, and system modularity maximization. The main objective of the research is the optimization of RMS machine selection. The optimal selection of machines is modular and observed as solitary of the most essential machineries of RMS. The optimal selection of machines is to generate at a high volume though consuming the capability to process operations otherwise parts within the invention family. The proposed methodology is utilized to select a set of modular machines from a machine and the required set of design that consist these machines. This projected methodology is validated by numerical analysis.

Keywords Reconfigurable manufacturing system · Squirrel search algorithm · Reconfigurable machine tool · Cost · Time · And modularity index

1 Introduction

The intensity of market formation these days goes hand in hand with cost and time productivity as it is naturally harmless [1]. The distribution of the report Our Common Future through the United Nations in 1987 recognized the most usually utilized meaning of fair progress, “the ability of people to solve their problems in the future

N. Swamy (✉) · A. T. Gouda · R. H. M. S. Swamy
Department of Mechanical Engineering, RYMEC, Ballari, India
e-mail: swamyrockers@gmail.com

U. M. Daivagna
Department of Mechanical Engineering, BITM, Ballari, India

without compromising the problems of the present.” Maintenance potential applies to many locations including design, assembling, and planning. RMS is a most recent assembly models that consider a few perspectives, for example, the standards of the two assembly structures, separately, dedicated to the transitional market variations, financial globalization, form customization, speedy mechanical development changes, in addition of late friendly and natural variations. Flexible Manufacturing system (FMS) and Dedicated Manufacturing System (DMS) are brilliant improvements. “RMS aims to integrate FMS’s high adaptability capability with DMS’s high build rate,” due to its adaptive design and graph center [2]. Modular product design (MPD) is the best strategy to produce a large product variety. MPD’s configuration phase represents a key step for mass customization because it allows customers to be integrated into the value creation process [3]. A reconfigurable manufacturing system (RMS) is a manufacturing paradigm that is proven to be time and cost-effectively adaptable to a wide range of market changes due to its customizable capacity and functionality [4].

Of late, RMS is believed to be the most relevant standard with prerequisites for support. RMS is also known as ‘reconfiguration’, which has various properties such as modularity: a measured design for equipment components and programming, integration: a custom interface that helps to effectively integrate modules and machines, customization: basic adaptation around an item family, adaptability: improving usability over the long-term capacity, each of these attributes provides the required amount of response to an RMS according to different levels [5]. In this way, the idea of RMS has received extensive consideration among established researchers, with some 60% of logical documents being distributed somewhere between 2010 and 2017. Including the course of operation of RMS design inquiry machines, hardware selection, and operational tasks affecting the exhibition of assembly companies. RMS configuration analysis is important for the assembly business for two reasons [3]. The six characteristics, modularity, Integrability, and Diagnosability are essential characteristics that allow rapid reconfiguration [6]. First and foremost, RMS configuration analysis is fundamental to achieving high adaptation, dynamic market interest, expanding customization, better products, interchangeable clusters, and extended item life cycles critical to expanded assembling intensity. Besides, studies suggest that RMS setup triggers more advanced execution when varied with conventional generating framework arrangements, including performance, responsiveness, and cost. Previous attempts at multi-target explanation for RMS system investigation have zero and dominate genetic algorithms (GA) [7]. Similarly, it reads the GAs applied to review how tasks are assigned to machines/stages, while at the same time, restricting the size of the machines used to come to a certain limit or increasing the configuration limit for a convinced number of machines. Similarly, the usage aimed at RMS-CA is random, and does not include multi-objective development, in addition, requires substantial computational exertions toward show up in arrangements in this manner. As a result, new efficient technology is needed to improve RMS performance with productivity. Researchers have investigated various RMS existing literature in order to get an idea of the present amount of research in this domain. We will try to do our best to showcase the most important research publications related

to RMS in this section, with a priority on the problem at hand and the proposed algorithm to tackle it.

The remaining section of the article is pre-arranged as surveys, Sect. 2 provides the literature review of the related papers. The problem formulation of the RMS configuration is presented in Sect. 3. A detailed description of the objective function and the proposed method is given in Sect. 4. The arithmetical analysis of the paper is given in Sect. 5. The conclusion of the paper is presented in Sect. 5.

2 Literature Review

Different kinds of methods are developed by the researcher to reconfigure the RMS system efficiently. Some of the methods are reviewed in this section.

Massim et al. [8] have presented a heuristic-based nonlinear mixed-integer method to optimize modularity and integrability in a sustainable RMS environment. This approach was selected to optimize the energy consumption in an RMS with the consideration of integrability and modularity, this objective function was used to reduce the energy issue. Dou et al. [9] have introduced, a multi-objective particle swarm optimization (MoPSO) case that shows the adequacy of MoPSO. The similar outcomes among MoPSO and non-dominated sorting genetic algorithm II (NSGA-II) against eight issues show that the MoPSO outflanks the NSGA-II in both arrangement quality and calculation effectiveness for the coordinated advancement issue. Battaia et al. [10] have introduced a cost optimization issue for streamlines outfitted with reconfigurable machines which convey turrets, machining modules, and single shafts. The objective has to limit hardware cost while arriving at a given yield and fulfilling everyone's requirements. A Mixed Integer Program (MIP) was created for the thought about improvement issues. Khettabi et al. [11] have introduced nonlinear multi-objective integer program (NL-MOIP), where four destinations were limited separately, the all-out creation cost, the absolute creation time, the measure of the ozone harming substances discharged by machines, and the unsafe fluid squanders. Second, to tackle the issue, introduced four adjusted adaptations of developmental methodologies, specifically two forms of the notable random weighted genetic algorithms (RWGA), weighted genetic algorithms (WGA) and non-dominated sorting genetic algorithm (NSGA-II and NSGA-III). Pal Singh et al. [12] have introduced another measurement for item stream setup choice for RMS that thinks about nine modernly applicable significant elements. The created strategy of CPM gives the client to select either an abstract or a targeted way to deal with allotting reasonable loads for every one of the nine-execution measurements. Created CPM has been applied in a mechanical climate with the help of an assembling organization by taking two contextual investigation parts and substitute arrangements to lead the review.

3 Problem Formulation

Mainly, RMS is designed to improve responsiveness to customer variations and markets through customized flexibility in the manufacturing system design. To empower higher production rates and provide faster throughput, the improvement of flexibility in RMS is essential. This kind of alteration is described as a key behavior of a reconfigurable system emphasis. The flexibility improvement should be considered different types of products such as tools, configurations, tasks, modules, and different machines. Additionally, the main process of the system strategy is to choose a set of machines that are combined in the production procedure. This research develops a multi-objective SSA method for the optimal RMS machine selection. In the RMS, RMT is an essential machine that is modular. The different parts of the reconfigurable machine are illustrated in Fig. 1.

In Fig. 1, two types of modules are considered such as auxiliary module and basic module. An auxiliary module can be removed or added and it is called a reconfigurable component in the RMT. Normally, this module is defined as motion-providing modules and kinematic modules like spindle heads, angle structures, tool changers, and adapter plates. In basic modules, it can be a fixed component in the RMT and it is normally structural like columns, bases, and slideways. The RMT aims to generate at a high volume and it can produce parts or operations within an RMS system [13]. The RMT can be changed by required hardware and software module variations to various positions. Hence, the proposed methodology is utilized to select a set of segmental machines after the incline of identified additional candidate machines for designing

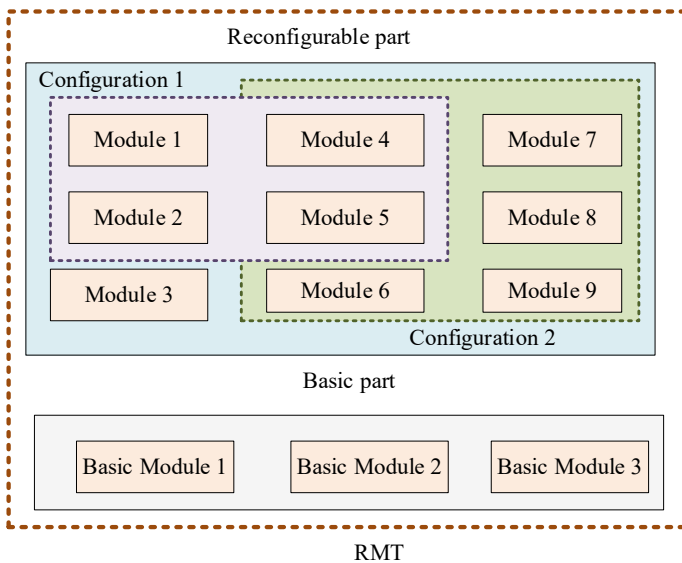


Fig. 1 Reconfigurable machine with various parts

a new configurable system. A detailed description of the proposed methodology is presented in the below section.

4 Proposed System Module

This research proposed a multi-objective SSA method for machine chosen issue in the RMS design with the consideration of the single-product case. To analyze the proposed methodology, the product is considered which contains N features. Every feature is containing different operations which are formulated as follows:

$$K = (K = 1, \dots, N)NOPF^K \tag{1}$$

where K can be described as features and $NOPF^K$ can be described as a number of operations of the feature F^K . The operations consisting of common operation (COP^s) in the RMS structure. The issue of the proposed methodology can be formulated as follows:

$$Op_U^K (K = 1, \dots NOPF^K, U = 1, \dots, N) \tag{2}$$

Set of machines

$$M^J = (J = 1, \dots, N^M) \tag{3}$$

Constraint to

$$(N^{Mod} \leq N^{um}) \tag{4}$$

where M^J can be considered as a set of machines, Op_U^K can be described as operations of features, N^{um} can be described as a limited number of modules, and N^{Mod} can be described as a total number of distinct auxiliary modules. Every machine has a different configuration and it contains different functionalities. Hence, the optimal set of machines is selected based on their process. Initially, detection of the machine operation associated with that process can be achieved in the RMS system. After that, recognize the presence of every auxiliary unit required for the scheme. Additionally, the sequence and order of operations are computed. The above mentioned problems are the minimization of completion time, maximization of the system modularity, and total cost of the production process.

4.1 Objective Function

To design an optimal RMS structure, three different types of objective functions are considered such as system cost minimization, system completion time minimization, and system modularity maximization. The detailed formulation of the objective functions is presented in this section.

4.1.1 System Cost Minimization

The system cost minimization is considered as a first objective function which consists of three cost functions such as configuration changing cost, auxiliary module use cost, basic module cost, and machine exploitation cost [14].

Configuration changing cost

The configuration changing cost is defined as the generator cost for changing configuration from one to another, which is formulated as follows:

$$CCC = \sum_{U=0}^{OPT^N} \sum_{I=0}^{N^{um}} \left| mcModR[M_J][C_1(U)][aMod_I] - mcModr[M'_J]C'_1(U')[aMod'_J] \right| \times \alpha \quad (5)$$

where $aMod'_J$ can be described as an auxiliary unit for the machine J which equals 1 if the machine J required unit 0, otherwise, C_1 can be described as the configuration of the machine, OPT^N can be considered as the total number of operations for complete operations, cost of machines is described as mc and a is computed as follows:

$$\alpha = NMod_I \times ModhC_I \quad (6)$$

where $ModhC_I$ is described as the modeling cost of the machines.

Auxiliary module use cost

The auxiliary module use cost can be a cost incurred if utilizing a specified design for a single time unit. It is formulated as follows:

$$AMC = \sum_{U=0}^{OPT^N} \sum_{I=0}^{N^{um}} \left| ModOp[Op_U][aMod_I] - AMC[aMod'_J] \right| \times P(time)M_J(Op_U^K)[C_1^J(Op_U^K)] \quad (7)$$

Basic module cost

$$BMC = \sum_{U=0}^{OPT^N} \sum_{I=0}^{N^{um}} BMC_J^R \times \sigma \times P(time)M_J(Op_U^K)[C_1^J(Op_U^K)] \quad (8)$$

where BMC can be described as the cost of utilizing a basic module R of machine j intended for a single time unit and $\sigma = 1$ can be described as the machine J to the processing operation U .

Machine exploitation cost

It is defined as the cost that happened when using any specified machine for a given operation. This cost is formulated as follows:

$$MEC = \sum_{U=0}^{OPT^N} muC[M_J(Op_U^K) + mcC[M_J(Op_U)]][M'_J Op'_U] \quad (9)$$

where $muC[M_J(Op_U^K)]$ can be described as machine use cost and mcC can be described as machine changing cost. From the formulations, the first objective function is formulated as follows:

$$FF1 = Min((Cost)) \quad (10)$$

$$= CCC + AMC + BMC + MEC \quad (11)$$

4.1.2 System Completion Time Minimization

System completion time is considered as the second objective function which contains operation processing time, tool changeover time, configuration change time, and machine change time.

Operation processing time

$$PT = \sum_{K=1}^N \sum_{U=1}^{NF_K} P(time)M_J(Op_U^K)[C_1^J(Op_U^K)] \quad (12)$$

Tool changeover time

$$TCT = \sum_{U=0}^{OPT^N} T(Time)[[T_R(Op_U)]][T'_R Op'_U] \quad (13)$$

Configuration change time

$$CCT = \sum_{U=0}^{OPT^N} \sum_{I=0}^{N^{um}} \left| mcModR[M_J][C_1(U)][aMod_I] \right. \\ \left. - mcModr[M'_J]C'_1(U')[aMod'_J] \right| \times ModHT_I \quad (14)$$

where $ModR[M_J]$ can be described as a three-dimensional matrix which is a relationship among a machine in the auxiliary module, $ModHT_I$ can be described as module handling time.

Machine change time

$$MCT = \sum_{K=1}^N \sum_{U=1}^{NF_K} MC(time)M_J(Op_U^K)[M_1^J(Op_U^K)] \quad (15)$$

From the formulations, the second objective function is formulated as follows:

$$FF2 = Min(F(Time)) \quad (16)$$

$$= PT + TCT + CCT + MCT \quad (17)$$

4.1.3 System Modularity Maximization

The system modularity index is considered as the third objective function which consists of Machine–module relationship, Number of shared modules, Product–module relationship, Process plan–machine relationship, and Product family–module relationship. This objective function is presented in this section.

Machine–module relationship

$$CMod = \sum_{I=0}^{N^{um}} \sum_{I=0}^{N^{sm}} \frac{aMod'_J}{NSM} \quad (18)$$

where NSM can be described as a RMS design selected machines.

Number of shared modules

$$SMod = \sum_{I=0}^{N^{um}} \frac{NMod_I}{\sum_{U=0}^{OPT^N} \sum_{I=0}^{TNC} |mcModR[M_J][C_1][aMod_I]|} \quad (19)$$

where $NMod_I$ can be described as a number of obtainable incidences of a specified auxiliary design I and TNC can be described as a total number of configurations.

Product–module relationship

$$PMod = \sum_{U=0}^{OPT^N} \frac{\sum_{U=0}^{Num} (NMod_I \times aMod_I^U)}{NModOp_U \times Num} \quad (20)$$

Process plan–machine relationship

$$DF = \frac{1}{\sum_{J=0}^{NSM} \frac{\sum_{U=0}^{OPT^N} (M_J(OP_U^k))}{NSM}} \quad (21)$$

Product family–module relationship

$$FMod = \sum_{I=0}^{Num} \sum_{Cop=0}^{Ncop} \frac{aMod_I^{cop}}{Ncop \times Num} \quad (22)$$

where $Ncop$ can be described as the number of common operations. From the formulations, the third objective function is formulated as follows:

$$FF3 = Max(F(Modularity)) \quad (23)$$

$$= DF \times (SMod + PMod) + CMod + FMod \quad (24)$$

4.2 Squirrel Search Algorithm

In the SSA, the search procedure starts when foraging characteristics are started in flying squirrels. In the warm weather (autumn) condition, the squirrel searches for food resources with the consideration of the gliding process from one tree to another tree. In hot weather conditions, the flying squirrel search to achieve daily energy requirements very fast. Once completing daily energy needs, they start to collect optimal food sources for warm weather conditions. In the weather condition, the hickory nut helps to maintain their daily energy requirements which decreases the foraging costs and improves the survival probability condition. In the winter condition, leaf covers loss is an augmented danger of predation, henceforth, flying squirrels are less active but do not overwinter. Once the midwinter season is completed, the flying squirrels change to inactive condition. This is defined as the repetitive process

and lifecycle of the flying squirrels [15]. In the SSA, some of the assumptions should be considered for developing a mathematical model which is presented as follows:

A flying squirrels are considered in a forest in addition each squirrel can be presented in each tree.

Each and every flying squirrel is searching intended for food separately in addition optimally used obtainable food capitals through processing a lively foraging characteristic.

In the SSA, the three types of trees are considered such as a normal tree, oak tree, and hickory tree.

The considered forest area is assumed to contain one hickory tree and three oak trees.

Step by step procedure of SSA

In the SSA, the random location initialization of flying squirrel is an initial step. The flying squirrel location is denoted as a vector and dimensional search space.

Step 1: Random initialization

The location of the flying squirrels in the forest is mentioned by the vector. The flying squirrels can be formulated as follows:

$$S = \begin{bmatrix} S_{1,1} & S_{1,2} & \dots & S_{1,D} \\ S_{2,1} & S_{2,2} & \dots & S_{2,D} \\ \dots & \dots & \dots & \dots \\ \dots & \dots & \dots & \dots \\ S_{N,1} & S_{N,2} & \dots & S_{N,D} \end{bmatrix} \tag{25}$$

where flying squirrel location is mentioned as $S_{I,J}$, J th dimension of I th. The initial location of the squirrel is formulated as follows:

$$S_I = S_L + U(0, 1) \times (S_U - S_L) \tag{26}$$

where the S_U can be represented as upper bounds, S_L can be represented as lower bound of squirrels in the J th dimension, random number is denoted as $U(0, 1)$ which is in the range of $[0,1]$.

Step 2: Fitness Evaluation

In the flying squirrel, fitness is considered as the location of each squirrel which is computed by putting the parameters of the solution vector (RMS design parameter) into a fitness function. The fitness function is formulated as follows:

$$FF = A.Min(F(Cost)) + B.Min(F(Time)) + C.Max(F(Modularity)) \tag{27}$$

The fitness function-based parameters are stored in the array which is formulated as follows:

$$FF(S) = \begin{bmatrix} F1([S_{1,1}, S_{1,2}, \dots, S_{1,D}]) \\ F2([S_{1,1}, S_{1,2}, \dots, S_{2,D}]) \\ \dots \\ \dots \\ FN([S_{N,1}, S_{N,2}, \dots, S_{N,D}]) \end{bmatrix} \quad (28)$$

Based on the foraging behavior, the fitness parameter of every squirrel is computed. Additionally, the fitness value is dependent on the squirrel's location which is computed from the best food source. Three kinds of food sources are obtainable, such as normal tree (squirrel is on the normal tree), acorn tree (normal food source), and in addition, hickory tree (optimal food source). The optimal location also depends on their probability function [16].

Step 3: Random selection, declaration, and sorting

The optimal location of the squirrels is stored in the array. After that, it is sorted in ascending order. The best fitness value of SSA is described as a hickory nut tree. The following best fitness value of SSA is described as acorn nuts, it tries to change to hickory nut tree. The extra squirrels can be considered as the final fitness value which is taken as normal trees. By adding the random selection, approximately squirrels are change to hickory nut trees which assumes that they have satisfied their day-to-day dynamism needs. This foraging characteristic of squirrels is continuously pretentious with the consideration of marauders. These normal characteristics are designed by considering the location updating technique with the probability function of the predator [17].

Step 4: Generate new locations

The generating of the new location depends on the three different situations in the dynamic foraging behavior such as the presence of predators which creates cautions and is forced to utilize minor random walks, squirrel gliders, and hunts professionally through the forest and the absence of predator.

Scenario 1: In the present scenario, the squirrels are presented in acorn nut trees which move to the hickory tree. In this condition, the squirrel's new location is computed by the following equation:

$$S_{AT}^{T+1} = \begin{cases} S_{AT}^T + d_g \times g_c \times (S_{HT}^T - S_{AT}^T) & r_1 \geq P_{DP} \\ \text{Random location} & \text{otherwise} \end{cases} \quad (29)$$

where S_{HT}^T can be described as a location of a flying squirrel in a hickory nut tree, r_1 can be described as a random number, d_g can be described as the gliding distance, and T can be described as the current iteration. The balance between exploitation and exploration is computed with the consideration of the constant value of gliding (g_c).

The gliding constant value has affected the performance of the proposed technique. This constant value is taken as 1.9 which is computed with the consideration of rigorous analysis.

Scenario 2: In this scenario, the flying squirrels are moved to the acorn nut trees to achieve the required food. In this condition, the new location is computed based on the below conditions

$$S_{NT}^{T+1} = \begin{cases} S_{NT}^T + d_g \times g_C \times (S_{AT}^T - S_{NT}^T) & r_2 \geq P_{DP} \\ \text{Random location} & \text{otherwise} \end{cases} \quad (30)$$

Here, the r_2 can be described as a random parameter in the variety [0,1].

Scenario 3: In this situation, the squirrels are on normal trees which previously spent acorn nuts may change near hickory nut trees to store hickory nuts that can be considered at the period of food shortage. The new site of squirrels is achieved follows:

$$S_{NT}^{T+1} = \begin{cases} S_{NT}^T + d_g \times g_C \times (S_{HT}^T - S_{NT}^T) & r_3 \geq P_{DP} \\ \text{Random location} & \text{otherwise} \end{cases} \quad (31)$$

Here, the r_3 can be described as an arbitrary parameter in the period [0,1]. P_{DP} can be described as a probability function taken as 0.1 for three scenarios.

4.2.1 Aerodynamics of Gliding

The slithering process of squirrels can be presented with the consideration of equilibrium glide. It is the summation of drag (D) and Lift (L) force and it makes the resultant force (R) whose magnitude is opposite and equal to the way which depends on squirrel weight. The lift to drag ratio is presented as follows:

$$\frac{L}{D} = \frac{1}{\tan \theta} \quad (32)$$

where θ can be described as glide angle. The flying squirrels can improve their slither way distance which increases the drag ratio. The lift outcomes from downward deflection are presented as follows:

$$L = \frac{1}{2\rho c_l v^2 s} \quad (33)$$

where s can be described as the surface area of the body (i.e., 154 cm²), speed is denoted by $v = 5.25 \text{ ms}^{-1}$, lift coefficient can be denoted as c_l , and density of air is denoted as $\rho = 1.204 \text{ kg m}^{-3}$. The frictional drag can be presented as follows:

$$D = \frac{1}{2\rho c_l v^2 s c_d} \quad (34)$$

where c_d can be represented as frictional drag coefficient. At sluggish speed, the drag parameter can be high. Similarly, at a huge speed, it develops smaller. The glide angle at a steady state can be computed as follows:

$$\emptyset = \arctan\left(\frac{D}{L}\right) \quad (35)$$

The gliding distance is computed based on the below equation,

$$d_g = \left(\frac{H_g}{\tan \theta}\right) \quad (36)$$

where H_g can be considered as a loss in height which is taken as 8 m.

4.2.2 Seasonal Monitoring Scenario

In the SSA, seasonal variations meaningfully touch the scavenging action of squirrels. They affect heat loss at very low temperatures. The seasonal constant value should be considered to enhance the performance which is presented as follows:

$$S_C^T = \sqrt{\sum_{K=1}^D (S_{AT,K}^T - S_{HT,K}^T)^2} \quad (37)$$

where $T = 1, 2, 3$.

4.2.3 Random Rearrangement at the End of the Winter Period

The relocation of the flying squirrels is designed with the below equation

$$S_{NT}^{new} = S_L + Levy(N) \times (S_U - S_L) \quad (38)$$

where the levy can be described as a levy distribution function that empowers the best and well-organized search space exploration. Levy distribution function can be presented as follows:

$$L(S, \gamma, \mu) = \begin{cases} \sqrt{\frac{\gamma}{2\pi}} \exp\left[-\frac{\gamma}{2(s-\mu)}\right] \frac{1}{(s-\mu)^{3/2}} & 0 < \mu < s < \infty \\ 0 & otherwise \end{cases} \quad (39)$$

where $\mu, \gamma > 0$, μ can be described shift parameter, γ can be described as the scale parameter. The levy flight can be computed as follows:

$$Levy(x) = 0.01 \times \frac{r^a \times \sigma}{|r^b|^{\frac{1}{\beta}}} \quad (40)$$

where β can be considered as constant (i.e. 1.5), r^b and r^a can be described as two usually dispersed arbitrary statistics in $[0,1]$.

$$\sigma = \left[\frac{\Gamma(1 + \beta) \times \sin\left(\frac{\pi\beta}{2}\right)}{\Gamma\left(\frac{1+\beta}{2}\right) \times \beta \times 2^{\left(\frac{\beta-1}{2}\right)}} \right]^{\frac{1}{\beta}} \quad (41)$$

where $\Gamma(x) = (x - 1)!$

4.2.4 Stopping Condition

Broadmindness is a usually utilized convergence condition in which allowable but small threshold parameter can be defined among the last two upcoming outcomes. In this condition, maximum iteration is checked. Based on the algorithm, the optimal RMS design parameters are selected. Once complete, the MOSSA algorithm organizes a set of explanations that are given to the decision-maker in the manufacturing industry.

5 Result and Discussion

In this section, the performance of the proposed methodology is evaluated and compared. The simulation is carried out with MATLAB 2021a on an i5 machine with 4 GB of RAM. To evaluate the proposed methodology, an RMS module library with six auxiliary modules and four basic modules are considered. The product consists of four important features that are required to do five, four, three, and two operations. Every operation required the tools which are presented in Table 1. The proposed implementation parameters are presented in Table 2. The candidate machine configuration is presented in Table 3. The three objective function parameters are evaluated in Table 4 (Fig. 2).

The objective functions are achieved and reconfigured with the RMS design with the help of a multi-objective SSA algorithm. The RMS system is reconfigured by considering three objective functions such as time, cost, and modularity index. With the help of the proposed methodology, the optimal parameters are selected and the

Table 1 Tool Requirements for every operation

S. No.	Operations	Features	$NMod_I$	Required Tool
1	Operation 1	Feature 4	2	Tool 3
2	Operation 2		3	Tool 4
3	Operation 3		1	Tool 1
4	Operation 1	Feature 3	3	Tool 1
5	Operation 2		2	Tool 5
6	Operation 3		1	Tool 1
7	Operation 4		1	Tool 5
8	Operation 5		2	Tool 2
9	Operation 1	Feature 2	3	Tool 1
10	Operation 2		3	Tool 5
11	Operation 3		2	Tool 4
12	Operation 4		2	Tool 1
13	Operation 5		3	Tool 4
14	Operation 1	Feature 1	2	Tool 1
15	Operation 2		3	Tool 5

Table 2 Implementation parameters of the proposed method

S. No.	Description	Parameters
1	Number of iterations	1000
2	Hard limit	10
3	Soft limit	20
4	Minimum temperature	1
5	Maximum temperature	5000
6	Cooling rate	95%
7	Perturbation rate	45%

RMS system is reconfigured. This proposed methodology is validated by numerical analysis. The best solution in terms of the cost function is with the machines (M1 M2 M3 M4 M7 M8 M10) with the less value of 56,601.95. The best modularity index is obtained with the machines (M1 M2 M3 M4 M7 M8 M10) with the high value of 20.1, and in terms of time, the function is obtained with the machines (M1 M2 M3 M4 M7 M8 M10) with the less value of 4837. In the future, an efficient method will be developed to reduce the cost and time compared with the proposed methodology.

Table 3 Machine specifications

Machines	Auxiliary modules	Basic modules	Using cost	Tools	Configuration
Machine 1	A1, A2, A5	B1, B2	50	T1, T2, T3, T4, T5	C1
	A1, A2, A3				C2
	A1, A2, A4				C3
Machine 2	A3, A4	B1, B4	20	T3, T5	C1
	A1, A4				C2
	A1, A4, A5				C3
	A2, A3, A4				C4
Machine 3	A1, A3, A4, A5	B1, B3	25	T4	C1
	A1, A2, A3, A6				C2
Machine 4	A1, A3, A4	B1	22	T3	C1
Machine 5	A3, A5, A6	B3	30	T2	C1
Machine 6	A2, A3, A4, A5	B2, B3	19	T3	C1
	A2, A3, A1, A6				C2
Machine 7	A2, A3, A5	B2	26	T2	C1
Machine 8	A4, A5, A6	B4	39	T3, T4	C1
	A3, A4, A5				C2
	A3, A4, A6				C3
Machine 9	A1, A3	B1, B3	36	T2, T3	C1
	A1, A3, A6				C2
Machine 10	A1, A2	B2	24	T3, T4	C1
	A2, A5, A6				C2

Table 4 Proposed selected values based on objective functions

S. No.	Objective 1 (cost function)	Objective 2 (time function)	Objective 3 (modularity index)	Solution	Chosen machine sets
1	66,189.85	4886	18.99	A	M1 M2 M3 M4 M7 M8 M10
2	64,936.05	4865	15.29	B	M1 M2 M4 M5 M8 M10
3	64,775.25	4884	11.69	C	M1 M2 M4 M5 M8 M10
4	64,861.35	4948	12.32	D	M1 M2 M4 M5 M8 M10
5	64,881.85	4886	14.10	E	M1 M2 M4 M5 M8 M10
6	77,170.85	5558	19.22	F	M1 M2 M3 M4 M7 M8 M10
7	65,491.25	4905	16.39	G	M1 M2 M3 M4 M7 M8 M10
8	66,345.45	4852	13.72	H	M1 M2 M3 M4 M7 M8 M10
9	67,072.05	4885	15.78	I	M1 M2 M3 M4 M7 M8 M10
10	67,088.65	4885	17.53	J	M1 M2 M3 M4 M7 M8 M10
11	64,927.85	4865	14.14	K	M1 M2 M4 M5 M8 M10
12	64,425.45	4837	14.98	L	M1 M2 M3 M4 M7 M8 M10
13	64,880.05	4857	9.51	M	M1 M2 M4 M5 M8 M10
14	66,182.65	4926	18.10	N	M1 M2 M3 M4 M7 M8 M10
15	58,097.05	5113	14.59	O	M1 M2 M4 M8 M9 M10
16	61,411.35	5231	15.23	P	M1 M2 M3 M4 M7 M8
17	56,881.25	5023	13.35	Q	M1 M2 M3 M5 M8 M10
18	56,601.95	4926	12.81	R	M1 M2 M3 M4 M7 M8 M10
19	58,094.65	4985	14.31	S	M1 M2 M3 M7 M8 M10
20	72,470.55	5119	20.01	T	M1 M2 M3 M4 M7 M8 M10

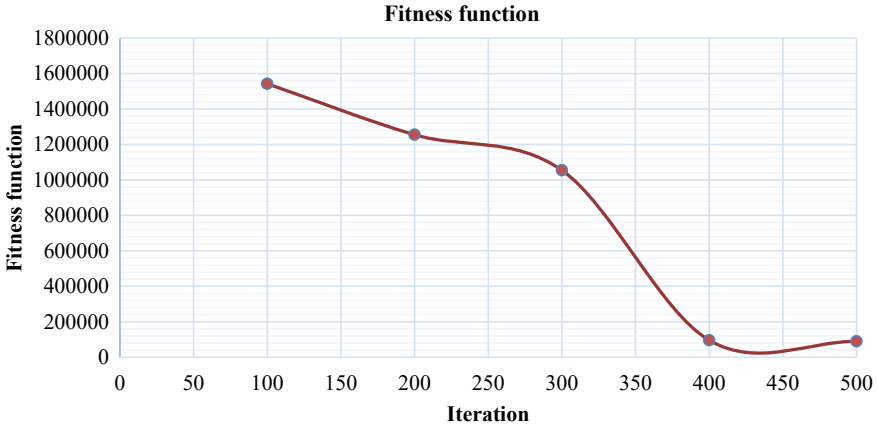


Fig. 2 Convergence analysis of the proposed method

6 Conclusions

This paper has proposed a MOSSA to optimize the RMS design. To empower the RMS performance, three different objectives are considered, such as system cost minimization, system completion time minimization, and system modularity maximization. The main objective of the research is the optimization of RMS machine selection. The optimal selection of machines is modular and observed as unique of the most essential mechanisms of RMS. The optimal selection of machines can be to produce at a high volume though consuming the capability to generate operations or parts within the product family. The proposed methodology has been utilized to select a set of modular machines from a machine and, the required set of components that comprise these machineries. This proposed methodology is validated by numerical analysis. The best solution in terms of the cost function is obtained with the machines (M1 M2 M3 M4 M7 M8 M10) with the less value of 56,601.95. The best modularity index is obtained with the machines (M1 M2 M3 M4 M7 M8 M10) with the high value of 20.1, and in terms of time, the function is obtained with the machines (M1 M2 M3 M4 M7 M8 M10) with the less value of 4837. In the future, an efficient method will be developed to reduce the cost and time compared with the proposed methodology.

References

1. Moghaddam SK, Houshmand M, Fatahi Valilai O (2018) Configuration design in scalable reconfigurable manufacturing systems (RMS); a case of single-product flow line (SPFL). *Int J Prod Res* 56(11):3932–3954
2. Ehsan Hashemi Petroodi E, Beauville Dit Eynaud A, Klement N, Tavakkoli-Moghaddam R (2019) Simulation-based optimization approach with scenario-based product sequence in a reconfigurable manufacturing system (RMS): a case study. *IFAC-PapersOnLine* 52(13):2638–2643
3. Sabioni RC, Daaboul J, Le Duigou J (2021) An integrated approach to optimize the configuration of mass-customized products and reconfigurable manufacturing systems. *Int J Adv Manuf Technol* 1–23
4. Kazemisaboer A, Aghaie A, Salmanzadeh H (2021) A simulation-based optimisation framework for process plan generation in reconfigurable manufacturing systems (RMSs) in an uncertain environment. *Int J Prod Res* 1–19
5. Moghaddam SK, Houshmand M, Saitou K, Fatahi Valilai O (2020) Configuration design of scalable reconfigurable manufacturing systems for part family. *Int J Prod Res* 58(10):2974–2996
6. Kurniadi KA, Ryu K (2021) Development of multi-disciplinary green-BOM to maintain sustainability in reconfigurable manufacturing systems. *Sustainability* 13(17):9533
7. Bortolini M, Ferrari E, Galizia FG, Regattieri A (2021) An optimisation model for the dynamic management of cellular reconfigurable manufacturing systems under auxiliary module availability constraints. *J Manuf Syst* 58:442–451
8. Massimi E, Khezri A, Benderbal HH, Benyoucef L (2020) A heuristic-based non-linear mixed integer approach for optimizing modularity and integrability in a sustainable reconfigurable manufacturing environment. *Int J Adv Manuf Technol* 108:1997–2020
9. Dou J, Li J, Xia D, Zhao X (2020) A multi-objective particle swarm optimisation for integrated configuration design and scheduling in reconfigurable manufacturing system. *Int J Prod Res* 1–21
10. Battaia O, Dolgui A, Guschinsky N (2020) Optimal cost design of flow lines with reconfigurable machines for batch production. *Int J Prod Res* 58(10):2937–2952
11. Khettabi I, Benyoucef L, Boutiche MA (2021) Sustainable reconfigurable manufacturing system design using adapted multi-objective evolutionary-based approaches. *Int J Adv Manuf Technol* 1–19
12. Pal Singh P, Madan J, Singh H (2021) Composite performance metric for product flow configuration selection of reconfigurable manufacturing system (RMS). *Int J Prod Res* 59(13):3996–4016
13. Benderbal HH, Benyoucef L (2019) Machine layout design problem under product family evolution in reconfigurable manufacturing environment: a two-phase-based AMOSA approach. *Int J Adv Manuf Technol* 104(1):375–389
14. Benderbal HH, Dahane M, Benyoucef L (2018) Modularity assessment in reconfigurable manufacturing system (RMS) design: an archived multi-objective simulated annealing-based approach. *Int J Adv Manuf Technol* 94(1):729–749
15. Jain M, Singh V, Rani A (2019) A novel nature-inspired algorithm for optimization: squirrel search algorithm. *Swarm Evol Comput* 44:148–175
16. Basu M (2019) Squirrel search algorithm for multi-region combined heat and power economic dispatch incorporating renewable energy sources. *Energy* 182:296–305
17. Hu H, Zhang L, Bai Y, Wang P, Tan X (2019) A hybrid algorithm based on squirrel search algorithm and invasive weed optimization for optimization. *IEEE Access* 7:105652–105668

Development of Drive Cycle and Resultant Powertrain Calculations of Electric Bicycle



Tejas Savadi, V. N. Abhilash, Kean Fernandes, and Sharanbassappa S. Patil

Abstract To model the powertrain for an electric bicycle, it was observed that the drive cycle was a critical input required to get accurate results. While trying to find a priorly available drive cycle in the past literature, it was observed that there were no good reference points for powertrain calculations of an electric bicycle and the corresponding drive cycle used. Hence, this paper demonstrates the process of creating a drive cycle that is used to then obtain the powertrain requirements of an electric bicycle. The process of creating a drive cycle consists of data collection, analysis, and generation of the final drive cycle. The features of the drive cycle are compared with standard drive cycles like World Motorcycle Drive Cycle (WMTC). This drive cycle is then used as input to a powertrain model which was built. The powertrain model consists of 4 components, namely the chassis, transmission, motor, and battery. The salient features of each individual component are explained briefly. The battery and motor requirements pertaining to our unique inputs are shown and the variation of battery power with respect to bicycle speed is explained graphically.

Keywords Drive cycle · Powertrain · Electric bicycle · Micro-trips · Motor power

1 Introduction

Drive cycle is a critical component of the vehicle representing the traffic behavior. To obtain, the driving cycle is a representative plot of the driving behavior of a given city or a region and is characterized by speed and acceleration versus time.

As part of our project, we need to obtain the powertrain parameters like wheel speed, motor torque, motor speed, motor power, and battery capacity for our electric bike. A drive cycle is needed as input for our powertrain model. Online resources and

T. Savadi (✉) · V. N. Abhilash · K. Fernandes · S. S. Patil
Department of Mechanical Engineering, PES University, Bengaluru, India
e-mail: tejas.savadi@gmail.com

S. S. Patil
e-mail: sspatil@pes.edu

papers yielded drive cycles that did not fit our requirements in speed and acceleration pertaining to an e-bike [1]. All of the online resources and paper had redundancies when it came to velocity and acceleration generally, the velocity being too high as they were done with motor cars and bikes in mind while also not having a realistic portrayal of acceleration changes in real-time traffic. For example, the Indian Drive Cycle (IDC) assumes all vehicle activities to be homogeneous irrespective of variations in traffic and driving characteristics. Since the driving pattern varies from region to region and vehicle to vehicle and the data pertaining to this is not available readily, the most accurate results would be obtained with a custom drive cycle which can then be used to model the powertrain.

2 Methodology

The most common characteristic related to methodology to develop the cycle as seen in Kamble and Mathew [2] is by taking into account various parameters like average speed, percentage time spent accelerating, percentage time spent idle, etc. The steps involved in this methodology are a collection of driving data (speed–time), generation of micro-trips, data analysis, and construction of the driving cycle.

Data is collected using a mounted sensor on an electric bike which is taken by an operator for repeated trips on selected routes. The data is collected at varying times to get a good distribution of traffic conditions during peak and non-peak hours. From this data, speed, time, and distance values are obtained.

Further on, another facet shown in [1] is that the development of a drive cycle is dependent on micro-trips which are representative of the existing traffic conditions. To generate these micro-trips, the period in between two periods of rest is considered as one micro-trip. Taking this into account, all the data collected is split into micro-trips with their individual speed–time data. Analysis of the data is then done in two parts, first on the base data which is the total data collected, and second on each individual micro-trip generated.

For analysis, acceleration frequency matrices need to be made which requires us to calculate acceleration at each interval from the speed–time data. Next, data analysis of our obtained acceleration values needed to be carried out to see whether the data obtained was valid and usable for our purposes. This means checking for anomalies in any of the acceleration values exceeding sensible values. On doing a basic analysis of these acceleration values, multiple intervals had acceleration greater than 4 m/s^2 . Also, maximum acceleration was in values greater than 9.8 m/s^2 which is physically impossible. To offset this issue, the abnormal data was removed and replaced with values obtained through interpolation. Once the validation of obtained data was completed, next, analysis of the base data collected and micro-trips needed to be done.

To obtain parameters, an acceleration frequency matrix is made for the base data and then normalized so that they can be compared later. From the normalized matrix,

Table 1 Drive cycle parameters of base data

Percentage acceleration	40.00761
Percentage deceleration	35.64055
Percentage cruise	24.35184

parameters like percentage acceleration, percentage deceleration, and percentage cruise are calculated as shown (Table 1).

Subsequently, similar parameter values are calculated for each individual micro-trip and tabulated. Out of 51 micro-trips, 8 micro-trips with parameters similar to the base data parameters were chosen and combined to generate the drive cycle (Fig. 1 and Table 2).

Characteristics of the generated drive cycle:

Percentage acceleration: 41.69014, Duration: 2130 s

Percentage deceleration: 35.77465, Total Distance: 9.6 km

Percentage idle: 22.53521

Using SCILAB-XCOs, we made a powertrain model to get values like wheel speed, motor torque, battery capacity, etc.

To calculate battery power required, the energy flow from chassis to the battery as shown in the figure is used. The chassis model consists of two components, wheel torque and wheel speed, with the input as our custom drive cycle mentioned earlier. To calculate the wheel torque, we take the product of the sum of the resistance forces

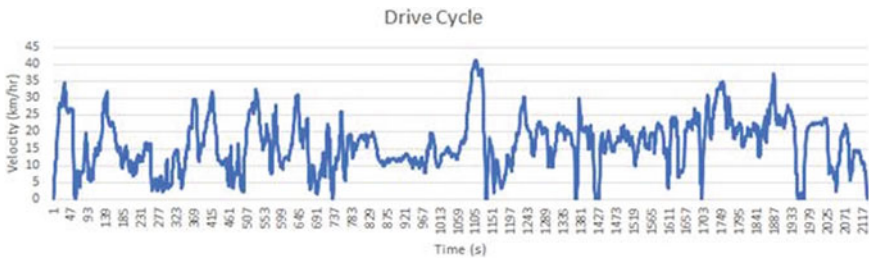


Fig. 1 User-generated drive cycle

Table 2 Comparison of drive cycle parameters with WMTC drive cycle [3]

	Custom drive cycle	WMTC drive cycle
Percentage acceleration	41.69014	30.22
Percentage deceleration	35.77465	33.22
Percentage cruise or idle	22.53521	36.72
Total time	2130 s	1800 s
Total distance	9.6 km	28.8 km

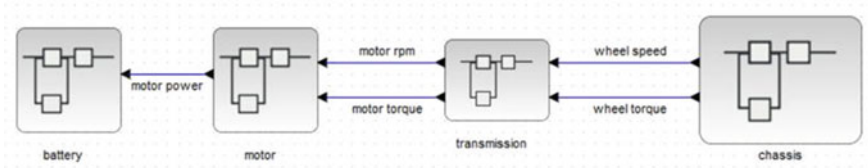


Fig. 2 Energy flow diagram of power train model

acting on the bike and wheel radius, and to obtain wheel speed, we convert bike speed from kmph to rpm (Fig. 2).

For the transmission model, taking the wheel torque and wheel speed as inputs, we obtain motor torque and motor speed with the help of gear ratio and transmission efficiency using the following formulas:

$$\text{Motor Torque (Nm)} = \text{Wheel Torque} / (\text{Gear Ratio} \times \text{Transmission Efficiency})$$

$$\text{Motor Speed (RPM)} = \text{Wheel Speed} \times \text{Gear Ratio}$$

In the motor component, we calculate the output motor power by taking the product of motor rpm in the form of radians/s and motor torque.

In the battery component, we integrate the motor power to get the battery capacity which we divide with cell capacity to get the number of cells in parallel and divide battery voltage by cell voltage to get the number of cells in series (Table 3).

The outputs generated by the steps described previously are tabulated and displayed above.

Table 3 Motor and battery requirements between different drive cycles

Sl. No.	Parameters	WMTC	Custom drive cycle
1	Motor		
	Peak torque (Nm)	22	20
	Nominal torque (Nm)	10	8
	Peak power (W)	2100	1200
	Nominal power (W)	800	260
	Max speed (rpm)	820	820
	Nominal speed (rpm)	400	500
2	Battery		
	No of cell (S,P)	10,4	10,4
	Capacity (Ah)	12.5	11.3
3	Force acting on the wheel (N)	280	220

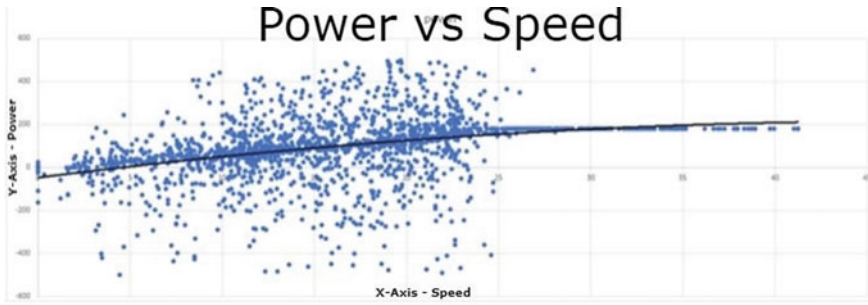


Fig. 3 Behavior of nominal power requirement at various speeds

Table 4 Nominal power values at different speeds

Speeds (km/h)	Power (Watts)
5	4.914
10	50.939
15	91.334
20	126.099
25	155.234

To show the behavior of power requirement at different speeds, we make a cluster graph between speed and power values obtained from the powertrain after which a rough best fit line is drawn to get a rough estimation of nominal power (Fig. 3).

Equation of the best fit line where y is power and x is the corresponding speed is given by

$$y = -0.1126 * x^2 + 10.894 * x - 46.741 \tag{1}$$

Subsequently, the nominal power requirements for our motor at various speeds up to our maximum speed of 25 km/h are calculated (Table 4).

We know empirically that power varies with the square of the speed, hence that's why we get quadratically increasing power values at increasing speeds according to Eq. (1).

3 Conclusion

Here, we can see that the nominal power required by the motor at different speeds is well within the 250 W limit given by the guidelines with a reasonable variance, hence we can assume that the drive cycle we use is suitable for our purposes. As observed in Table 3, the motor peak and nominal power of our drive cycle are considerably lesser owing to the fact that acceleration slopes are much steeper in the WMTC drive

cycle which is not realistic for an E-Bike. Therefore, the values in the second column are a much more accurate representation of our powertrain requirements.

References

1. Parekh V, Shah V. Measurement and analysis of indian road drive cycles for efficient and economic design of HEV component. *World Electr Veh J* 7. ISSN 2032-6653. ©2015 WEVA
2. Kamble SH, Mathew TV, Sharma GK (2009) Development of real-world driving cycle: case study of Pune, India. ISSN 1396-9209. Elsevier Science
3. Barlow TJ, Latham S, McCrae IS, Boulter PG. A reference book of driving cycles for use in measurement of road vehicles, Published Project Report for Department for Transport, Cleaner fuels and vehicles

Dynamic Analysis of Electric Train Bogie Using MATLAB Simulink



C. Prithvi, Surajgouda C. Policepatil, and Srinidhi Ramachandracharya

Abstract The dynamic analysis of Railway Bogies is an important field of research in the design of Railcar to improve the ride comfort of the passengers. The Bogie used in this research is Fabric Italiana de Automobil Torino, Switzerland (FIAT) Bogie used by Indian Railways. The paper aims at dynamic analysis of the FIAT Bogie under step input condition which simulates the repeated disturbances caused by wheel wear due to fretting. The quarter suspension of the Bogie is modeled as a spring, mass, and damper system with 3 degrees of freedom. The equations of motion are derived for the model, and it is built accordingly in MATLAB Simulink. The parameters and specifications of the FIAT Bogie obtained from the Indian Railway Manual are assigned to the spring, mass and damper system, and it is simulated for a step input. The displacement, velocity, and acceleration of the coach, Bogie frame, and wheel-sets are obtained in time domain. The results show that majority of the vibrations occur in the wheel-sets and the Bogie frame. The suggestion for redesigning of wheel-sets and suspension system is suggested. Suspension system can be redesigned for better ride comfort by the use of hydraulic actuator controlled by PID controller.

Keywords Electric train · FIAT bogie · LHB coach · Quarter suspension · Dynamic analysis

1 Introduction

The Indian Railways have been transporting passengers mainly through the coaches of Integral Coach Factory (ICF) design since the beginning of the Railway era. But the ICF coaches have limitations in terms of speed potential, poor riding comfort, heavy corrosion, and frequent wearing of parts. To overcome these limitations the

C. Prithvi · S. C. Policepatil (✉)
Department of Mechanical Engineering, The National Institute of Engineering, Mysore, India
e-mail: surajgoudacp@gmail.com

S. Ramachandracharya
Department of Mechanical Engineering, Sri Jayachamarajendra College of Engineering, Mysore, India

Indian Railways have introduced Linke Hofmann Busch (LHB) coaches which are capable of overcoming the limitations of ICF coaches especially in terms of speed potential and superior ride comfort.

The Indian Railways joined hands with M/s. ALSTOM LHB/Germany for design and manufacturing of the LHB Coaches. In the year 2001, 24 coaches were supplied which consisted of 19 AC chair cars, 2 AC executive class chair cars, and 3 generators cum brake vans. The Bogies used in these coaches are Fabric Italina de Automobil Torino, Switzerland (FIAT) Bogies. The Bogies are manufactured by M/s. FIAT/SIG Switzerland [1].

1.1 Need of This Research in Railways

The development in the field of Railways has been very slow, especially in India. The world has come a long way in the field of automotive sector in terms of design and technology, but no significant improvements have been done in the field of Railways. Since Railway being one of the major mode of transport, there is a need for further improvement in the design of the coaches.

Bogies are the important part of the coach because they carry the whole weight of the Car body and are also responsible for transferring the disturbances from track to the Car body which are in turn transferred to the passengers. The generation of vibration is primarily due to irregularities in the track and excitation of the wheel when running on the track. The irregularities may be in the form of defects in track or the wheels and also due to presence of foreign substances on the track. Also due to the long run, the surfaces of the wheel and track surfaces are not smooth, hence the vibration occurs due to series of peaks and troughs. Vehicle suspension is the other source of vibration in the train. The vibrations caused due to the above mentioned factors affect the ride comfort of the passengers. Hence there is a need for analysis and improvement of the Bogie for their advancement. In this work, FIAT Bogie is used for analysis.

2 Structure of a Railway Coach

For effective modeling of any physical system, its structure should be studied properly. A Railway coach consists of 1 Car body and 2 Bogies. The Car body carries the passengers or goods and the Bogie acts as the chassis of the coach. Figure 1 shows a side view of a coach consisting of a Car body and a Bogie attached with two axle wheel-sets, connected by primary and secondary suspension elements.

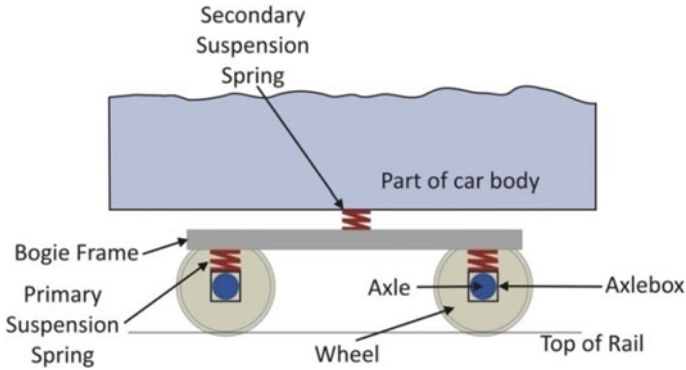


Fig. 1 Structure of a railway coach [2]

2.1 Degrees of Freedom of a Coach

The types of motions occurring in a structure determine the transmission of forces to its various parts. A rail coach has 6 Degrees of freedom, 3 linear, and 3 rotational movements. Figure 2 represents the 6 degrees of freedom of the Car body in the spatial views and shows the difference between 3 Linear and 3 rotational movements.

The longitudinal and pitching motions occur during acceleration and braking. The lateral, yawing, and rolling motions occur while the train is taking a turn. The vertical motion takes place when the Bogie passes through the disturbances on the track or due to wheel wear. Sometimes these motions can occur simultaneously due to a combination of the above-mentioned situations.

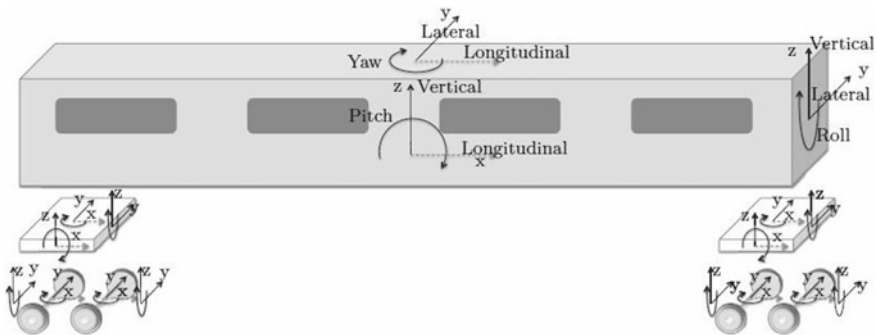


Fig. 2 Degrees of freedom (DoF) of a rail vehicle [3]

2.2 Principles of Force Transmissions

Force transmission in the Bogie is as follows:

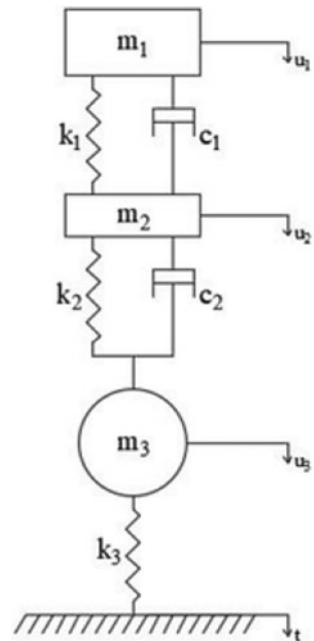
- Vertical forces: Body—bolster beam—secondary suspension—Bogie frame—primary suspension—axles
- Lateral forces: Body—bolster beam—lateral damper—secondary springs—Bogie frame—primary suspension—axles
- Longitudinal traction efforts and braking powers: Body—bolster beam—traction center—traction rods—traction lever—Bogie frame—primary suspension—axles.

3 Analytical Modelling of the Quarter Suspension System

Any mechanical system can be modelled as a spring, mass, and damper system. The accuracy of the results obtained from the model depends on how close the model represents the physical system. The quarter suspension system of the FIAT Bogie is modelled as a linear spring, mass, and damper system having 3 degrees of freedom. Figure 3 represents the quarter suspension model of FIAT Bogie.

The mass of Car body is represented by m_1 . The equivalent secondary spring stiffness is represented by k_1 and its damping coefficient is represented by c_1 . The

Fig. 3 Quarter suspension model of FIAT bogie [4]



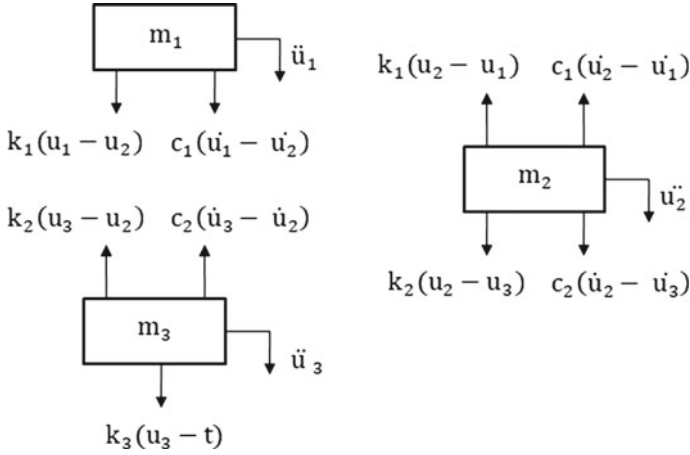


Fig. 4 Free body diagrams of the masses

mass of the Bogie frame is represented by m_2 . The equivalent primary spring stiffness is represented by k_2 , and its damping coefficient is represented by c_2 . The mass of the wheel-set is represented by m_3 , and its stiffness is represented by k_3 . The displacements of masses m_1, m_2 , and m_3 are represented by u_1, u_2 , and u_3 respectively. The track input is represented by t .

3.1 Free Body Diagrams

Free body diagrams help to analyze the various forces acting on the individual bodies by freeing them by adjacent elements and replacing the elements with the forces. Figure 4 represents the free body diagrams of masses m_1, m_2 , and m_3 .

3.2 Equations of Motion

The equations of motion are derived using Newton’s second law of motion, i.e., sum of all forces is equal to inertia force. The forces in the direction of motion are taken as positive, and the forces opposite to the direction of motion are taken as negative.

The derived equations of motion are as follows:

$$m_1 \ddot{u}_1 = -c_1(\dot{u}_1 - \dot{u}_2) - k_1(u_1 - u_2) \tag{1}$$

$$m_2 \ddot{u}_2 = -c_1(\dot{u}_2 - \dot{u}_1) - c_2(\dot{u}_2 - \dot{u}_3) - k_1(u_2 - u_1) - k_2(u_2 - u_3) \tag{2}$$

$$m_3\ddot{u}_3 = -c_2(\dot{u}_3 - \dot{u}_2) - k_2(u_3 - u_2) - k_3(u_3 - t) \quad (3)$$

The derived equations of motions are modelled using MATLAB Simulink.

4 Equivalent Simulink Model of the Quarter Suspension System

To study the dynamic response of the quarter suspension system, it needs to be simulated. MATLAB Simulink is used for the simulation. Figure 5 represents the equivalent Simulink model of the quarter suspension system.

The parameters and specifications for the spring, mass, and damper are obtained from Indian Railway Manual for LHB Coaches. Since this is a simulation of a quarter suspension system, the masses are divided accordingly. Table 1 shows the values of the parameters used for simulation. The system is simulated for the fixed parameters of the system.

4.1 Step Input

The track or wheel disturbances are given as a step input for 0.2 s with amplitude of 1 unit. The displacement, velocity, and acceleration of the system are obtained in time domain. Figure 6 shows the type of input signal.

5 Results

5.1 Displacements of Masses m_1 , m_2 , and m_3

Displacement results help to understand the motion of the masses about their mean position. A maximum displacement of 1.6, 1.25, and 1.75 units is observed for the Car body, Bogie frame, and the wheel-set respectively.

5.2 Velocities of Masses m_1 , m_2 , and m_3

Velocity results give an idea of, with what velocity the masses are moving about their mean position. The Car body displays a maximum velocity of 10 units for the

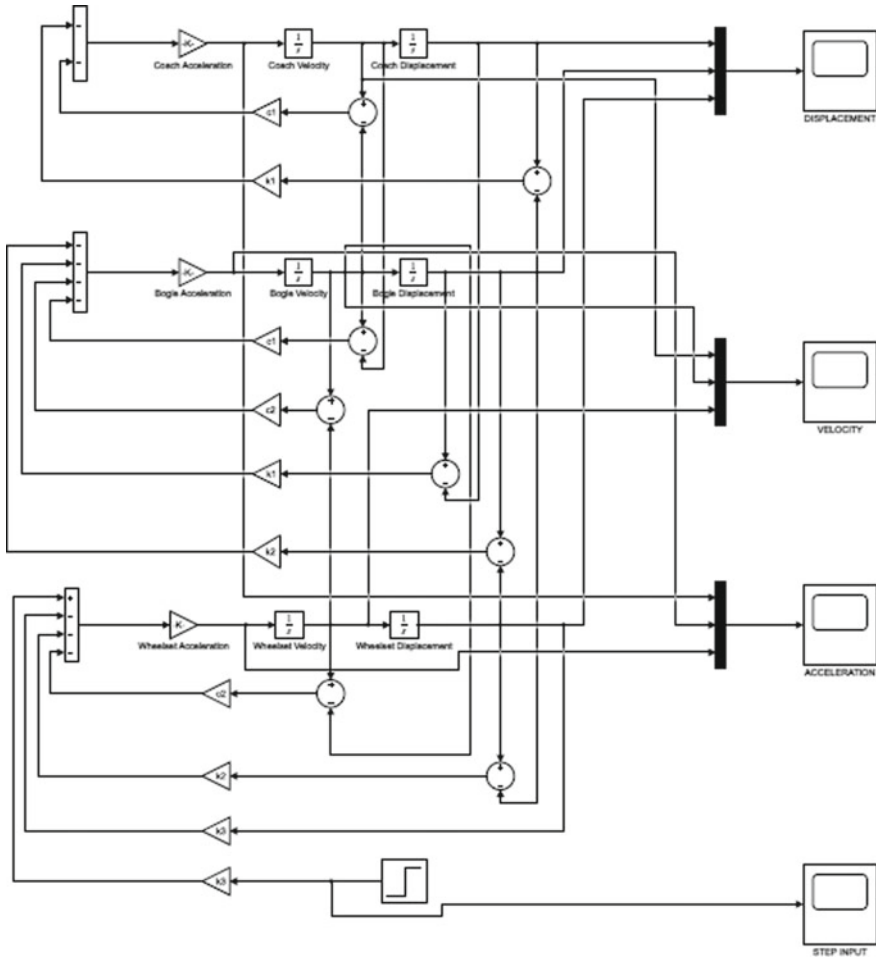


Fig. 5 Equivalent Simulink model of quarter suspension

Table 1 Parameters and specifications used for simulation [5, 6]

Parameters	Symbol	Values
Mass of the car body	m_1	5200 kg
Mass of bogie frame	m_2	650 kg
Mass of the wheel-set	m_3	800 kg
Secondary spring stiffness	k_1	6.1×10^5 N/m
Primary spring stiffness	k_2	11×10^5 N/m
Stiffness of wheel-set	k_3	100×10^6 N/m
Secondary damping coefficient	c_1	40.2×10^3 N s/m
Primary damping coefficient	c_2	32.6×10^3 N s/m

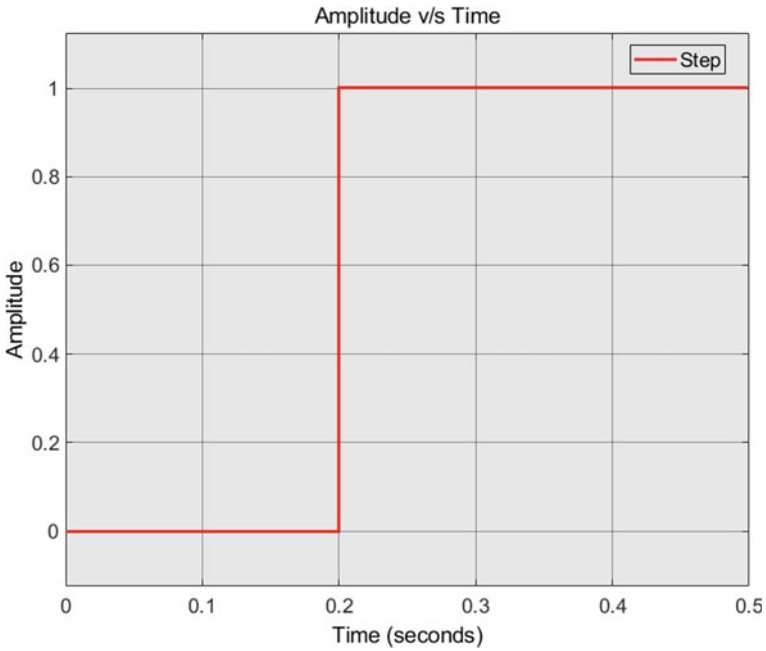


Fig. 6 Step input signal

excitation at the wheel. The Bogie frame and the wheel-set have maximum velocities of 70 and 310 units respectively.

5.3 Accelerations of Masses m_1 , m_2 , and m_3

Acceleration analysis of the masses gives an idea about the amount of jerk undergone by the masses. The Car body experiences almost no jerk. A sudden jerk of 10,000 units is observed at the Bogie frame when the wheels are excited. The jerk is experienced just for a fraction of seconds.

5.4 Summary of Simulation Results

The results of the simulation are summarized in Table 2.

Table 2 Results table

Part	Parameter	Value
Car body	Displacement	1.6 units
	Velocity	10 units
	Acceleration	0 units
Bogie frame	Displacement	1.25 units
	Velocity	70 units
	Acceleration	10,000 units
Wheel-set	Displacement	1.75 units
	Velocity	310 units
	Acceleration	125,000 units

6 Inference

From Fig. 7, the results show that major displacement takes place in the wheel sets with the highest frequency but has a less settling time. The Car body has more displacement compared to the Bogie frame which may affect the ride comfort.

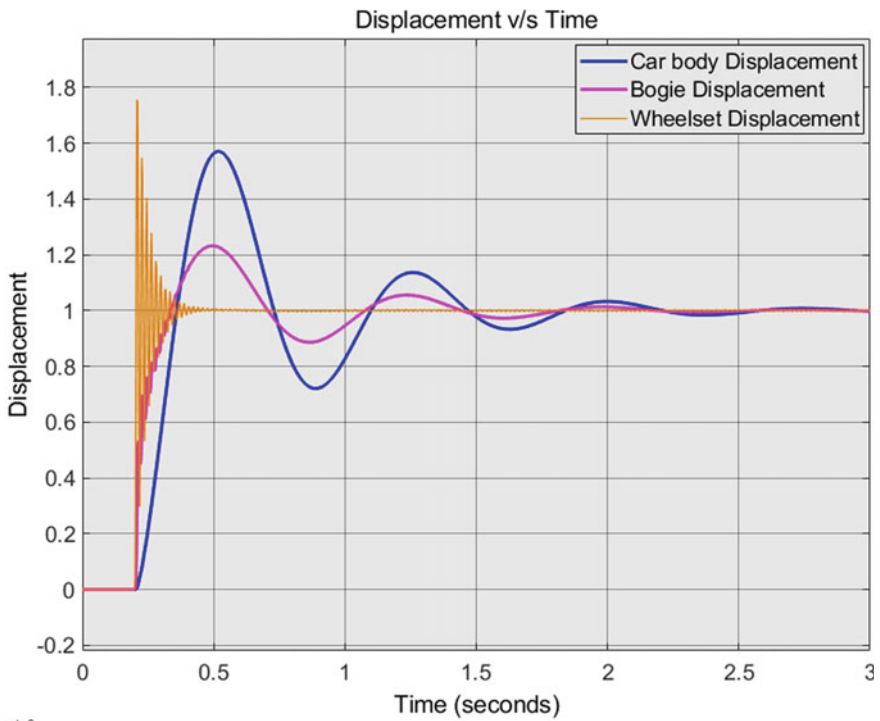


Fig. 7 Displacement versus time plot

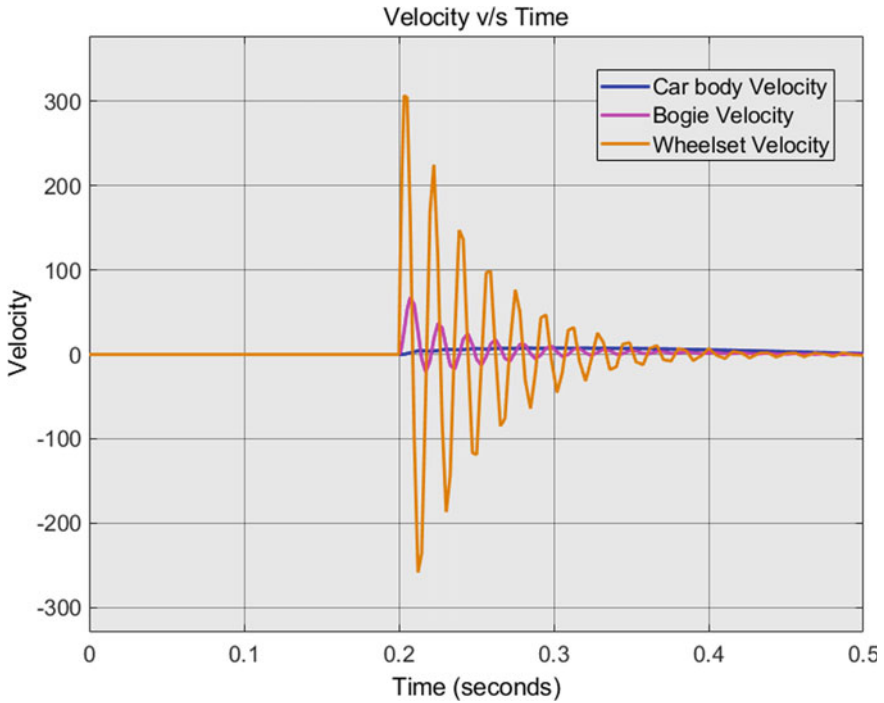


Fig. 8 Velocity versus time plot

From Fig. 8, there is maximum velocity recorded for the wheel-sets with highest settling time. The Car body has lowest velocity compared to the Bogie frame and wheel-sets.

From Fig. 9, we can observe maximum acceleration in wheel-sets, which may lead to jerk in the system. The Bogie frame also shows a minimum amount of acceleration with lesser settling time. The Car body shows almost negligible amount of acceleration, which indicates that the passengers do not feel jerk.

7 Conclusion

The results for simulation of quarter suspension of the FIAT Bogie show that the wheel-sets have higher amplitudes of vibrations compared to the Car body and Bogie frame. Therefore the wheel-sets can be redesigned to have better damping properties. The web can be redesigned or the rim of the wheels can be reinforced with materials having good damping properties.

Since the world is moving toward electric vehicles, which demand lightweight structure, the Bogie frame can also be further optimized for weight and damping

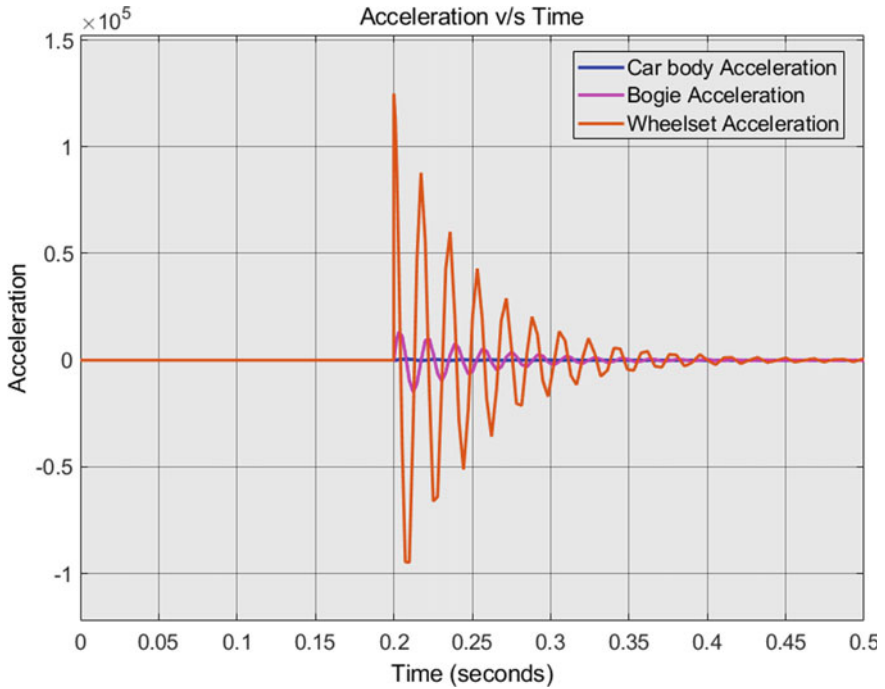


Fig. 9 Acceleration versus time plot

properties. Currently steel is being used whose composition is not disclosed by the Railways. For reducing the weight aluminum alloy can be used and composite structures can be used for the parts on which heavy forces are not acting.

The Car body is observed to have minimum vibration compared to its counterparts, but it can be further optimized for better ride comfort by using an active suspension system or different damping techniques. Hydraulic actuator connected in parallel with secondary dampers controlled by PID is suggested as the active suspension system. The hydraulic actuator will control the damping force on the connected parts by the actuation of the piston, and this force will be regulated by the PID controller by its tuned set points.

Therefore, there is a scope of work to improve the vibration characteristics of the LHB Coach or designing of a new coach for improving ride comfort. In this work the system is simulated only for step input, thus there is also scope for simulation of the system for different types of inputs.

References

1. IRCAMTECH/M/12-13/FIAT Bogie/1.0 (Indian Railways Centre for Advanced Maintenance Technology) (2012) Introduction handbook on FIAT bogie, Maharajpur, Gwalior
2. <http://www.Railway-technical.com/trains/rolling-stock-index-1/Bogies.html>
3. Matamoros-Sanchez AZ (2013) The use of novel mechanical devices for enhancing the performance of railway vehicles. PhD thesis, Loughborough, University
4. Hebbar K, Prithvi C, Ramachandracharya S (2019) Analytical modeling of Railway suspension system using MATLAB Simulink. Department of Mechanical Engineering, The National Institute of Engineering, Mysuru
5. Suresh BS, Prithvi C, Ramachandracharya S (2020) Modal analysis of FIAT bogie of LHB railway coach. Department of Mechanical Engineering, The National Institute of Engineering, Mysuru, India
6. Singh SD, Mathur R, Srivastava RK (2017) Dynamic response of Linke Hofmann Busch (LHB) rail coach considering suspended equipments. Department of Applied Mechanics, Motilal Nehru National Institute of Technology Allahabad

Design and Development of Electric Powertrain for a Proposed Three-Wheel Personal Mobility Vehicle



Arvind Srivatsan Varadharajan, R. Shreekara, Suman Emmanuel Salins, and Sharanabassappa S. Patil

Abstract This paper presents the design and development of the powertrain for a three-wheeled electric vehicle having a tadpole configuration with rear wheel drive. This three-wheeler, aimed at personal mobility, is designed for a top speed of 50 kmph with a range of 20–25 km per charge fueled by highly efficient Lithium-ion batteries with a reduction ratio of 6.2:1 split into two stages and powered by a 6 kW electric motor. Tractive force simulations for the prescribed vehicle parameters were carried out using the QSS toolbox of MATLAB-Simulink by choosing the appropriate drive cycle post the drive cycle analysis. Motor Sizing and Battery Sizing procedures along with suitable reduction ratio ensured the perfect selection of motor and battery pack combination for the required performance parameters and efficient output of the system. Following sizing procedures, the various components of the drivetrain were checked for interference and finally integrated on the swing-arm of the vehicle post analysis of all the components involved.

Keywords Electric vehicle · Tadpole design · Range · Tractive force simulations · QSS toolbox · Drive cycle analysis · Reduction ratio · Motor sizing · Battery sizing · Drivetrain integration

1 Introduction

In the present scenario, transportation accounts for one-fourth of all carbon emissions. The transport sector is witnessing rapid growth and is expected to reach one-third of the overall carbon emissions. Although developing countries have the fastest growing fleets, the majority of them have no vehicle emissions standards, programs and incentives in place to promote zero emission vehicles. Introduction of electric

A. S. Varadharajan (✉) · R. Shreekara · S. S. Patil
Bangalore, India
e-mail: vsarvind97@gmail.com

S. E. Salins
Udupi, India

vehicles especially three wheelers for congested city traffic serves to be an excellent alternative to combat the pollution caused by ICE vehicles. In order to achieve a cleaner transport sector, a combination of measures such as well-designed cities, increased usage of public transport and cleaner on-road fleets like electric vehicles have to be implemented. Of the above-suggested measures, the introduction of Electric Buses, Electric Light duty Vehicles and Electric Two and Three Wheelers offers a higher impact towards green mobility solutions. Thus, the first priority in moving towards electric mobility is by replacing the present conventional two and three wheelers with electric ones.

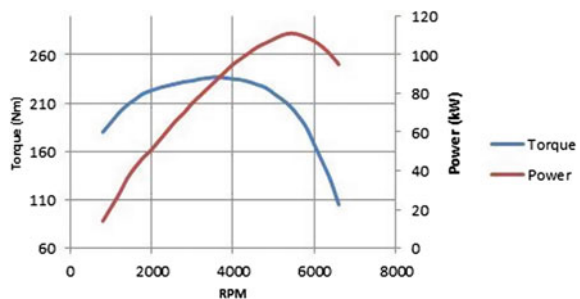
1.1 Electric Motor Versus IC Engine

The electric motor or an IC Engine are designed to convert one form of energy into useful mechanical work to propel a vehicle.

The IC Engine: An IC engine, by design, must rotate to generate torque. It must suck in air, compress it and remove it. This cannot be achieved at low RPM. A piston makes power only 25% of the time and it has to pay for the remainder of the strokes. So, it must rotate at a modest speed to generate ample power. ICEs convert linear motion from pistons into rotational motion and hence have to overcome a lot of internal friction. For this reason, ICE's do not operate much below 700 RPM and do not establish any serious torque until at least 1000 RPM and max torque around 3500 RPM.

The Electric Motor: Electric motors, on the other hand, include just wires and magnets. When current is passed through the wire, it becomes a magnet, this pushes against another magnet and develops force. More the current supply, more the force. The greatest current usually runs at 0 RPM, as there's practically zero resistance in the wires. Compared to an ICE, they have very few components and very low internal friction. Electric motors can also operate at any speed from 0 RPM up to their maximum RPM. They have an almost constant torque profile from 0 RPM up to their highest rated power (Figs. 1 and 2).

Fig. 1 A typical IC engine performance curve



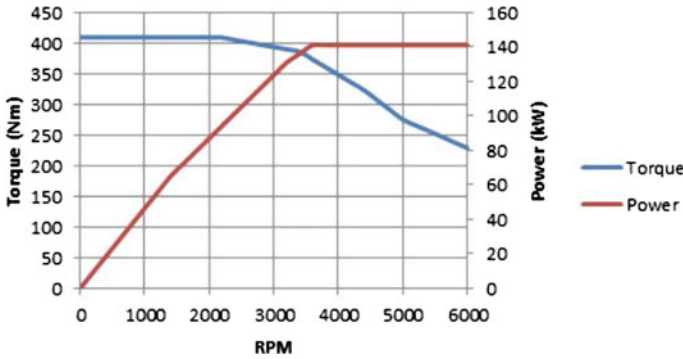


Fig. 2 A typical electric motor performance curve

1.2 Electric Powertrain

The powertrain of any vehicle includes the components which generate the required power and transmit the same to the wheels in order to propel the vehicle. In an electric powertrain, the source of the propulsive energy arises from an electric motor. The other major components in an electric powertrain include the battery pack, transmission system and controllers.

1.3 Challenges in City Mobility—Last Mile Connectivity

Last Mile connectivity often describes the means of transport which is responsible for getting people from various transportation hubs to their final destination. Environmentalists are facing a lot of challenges as people often revert back to conventional combustion vehicles. Electric vehicles, when used for this specific purpose, need not worry about the range, charging facilities etc. while providing pollution-free rides. Personalizing mobility by the introduction of electric two and three wheelers will help in achieving a greener last mile connectivity.

1.4 Three Wheelers

Three wheelers have two different orientations namely:

- **Tadpole:** This orientation consists of two wheels in the front and a single wheel in the rear.
- **Delta:** This orientation consists of two wheels in the rear and a single wheel in the front (Figs. 3 and 4).

Fig. 3 Delta and Tadpole configuration

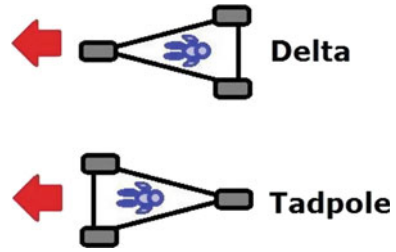
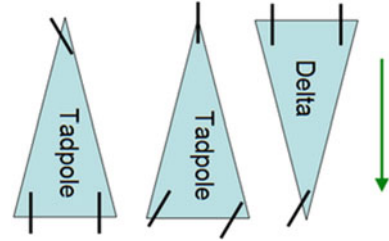


Fig. 4 The steering wheels in Delta and Tadpole



Tadpole Design: The Tadpole design as mentioned above, has higher stability during hard braking, also the two wheels in the front provide greater support while taking sharp turns and handling lateral acceleration loads. This configuration has improved aerodynamics and it also facilitates the usage of small lightweight motors in the rear. Furthermore, the usage of a front wheel drive vehicle will increase the transversal stability and the rear wheel-driven tadpole design ensures the complete transfer of drive to surface. Hence, this configuration is more advantageous than Delta type and is subsequently used for the construction of this mobility vehicle.

2 Literature Review

Łebkowski [1], in his work on electric vehicles mentions that electric vehicles can substantially reduce the local emission of noxious gasses into the environment. He also mentions the decreased energy consumption and efficiency of electric vehicles during their operation. Choi and Jahns [3] have worked on a specialized design evaluation tool for electric machines intended for use in electric vehicles that seek to maximize the machine's efficiency in the operating regions that most closely correspond to the vehicle's driving schedules and influences of different designs on a production battery-electric vehicle based on different driving cycles for optimization of EV range are studied. Karamuk [4] has extended the study on operation modes of an electric vehicle on the torque-speed curve of an electric motor for different driving scenarios. He has conducted a survey to review the essential components of an electric powertrain and based on simulations in Matlab-Simulink for sizing of electric motors considering the vehicle performance. Balamurugan and Manoharan

[5] have stressed on the selection of PMDC motor over a commercially available induction motor and suggested that the increased number of bushes would apparently improve the overall motor efficiency. Butler et al. [6] have mentioned that computer modelling and simulation, if done, lead to reduction in the expense and the length of design cycle of electric vehicles before the prototype construction begins. They have also carried out various simulations implementing drive cycles and compared the energy consumption between them. Andres et al. [7] suggested that the utilization of a reduction gearbox in an electric vehicle results in an improvement of overall energy consumption along with the required torque for a defined acceleration performance. The investigation also proved that the efficiency increase is achieved by selecting appropriate gear ratios thereby reducing machine losses and energy demands. Lee and Ahmed [9] mentioned during their work on development of electric powertrain that the battery package can be used as a rechargeable energy source. They also suggested the use of LiFePO₄ as battery cells for a better life and compact packaging. Their experiments proved that properly designed battery packs provide the required energy to the motor successfully. Park et al. [11], mentioned in their work related to dynamics of EV that Integrated modelling considering both the mechanical and electrical systems is essential. They acknowledged that integrated modelling is necessary in order to assess ultimate kinetic and dynamic characteristics of an Electric Vehicle.

2.1 Problem Statement

One of the major causes for the constant degradation of the air quality especially in urban areas is the emissions from combustion vehicles. With the reference to the above-stated text along with the literature survey carried out, it is the need of the hour to find a replacement for the conventional IC engine run vehicles. With this as background, we came up with the idea of designing a pure electric powertrain for a three-wheel vehicle which would be used within city limits as a personal mobility vehicle aiming to solve the above stated challenges.

2.2 Vehicle Parameters

Since the Electric Powertrain is specifically designed for a vehicle which is targeting the urban transport sector, it aims to solve trivial problems like last mile connectivity and the most important being to cut down harmful emissions. With this as foundation we will have to design a Powertrain which meets the above standards while most of the parameters of the proposed vehicle will be defined only after a thorough investigation. The proposed vehicle parameters are as—Top Speed: 50 kmph; Acceleration: 2.2 m/s²; Max Gradient: 14°.

2.3 Methodology

The work is split into three phases consisting of literature survey, design and development and finally integration and optimization of the electric powertrain for improved performance. The initial phase of the literature survey involves the understanding of the electric powertrain and the challenges faced in the current scenario. In further stages, studies on different driving cycles are carried out. After the selection of a suitable driving cycle, motor and wheel selection is done, wherein the appropriate motor and wheel dimensions as per power requirements are chosen in coordination with the suspension and brakes team. Simulations are performed on the QSS Module of MATLAB-Simulink, to cross verify the different parameters for the considered vehicle performance. Post selection of motor and wheels, the required size of the battery and the reduction ratios are calculated. Battery sizing is also done on the QSS module of MATLAB-Simulink to cross verify the results after which the drive is selected. Post battery sizing and drive selection, final drive components are designed on SOLIDWORKS. Modal and structural analysis are performed on the designed components on ANSYS. The components are then assembled in SOLIDWORKS for efficient packaging.

3 Driving Cycle

Driving Cycle is a series of data points representing the speed of a vehicle with respect to time developed by various countries and organizations. There are two major types of driving cycles:

- Transient—Involves many changes that represent the continuous change in speed of a vehicle as seen in typical on-road vehicles.
- Modal—Represents protracted periods at constant speeds.

The transient kind of driving cycle is the most preferred kind as it gives us a continuous change in vehicle parameters with respect to time unlike the modal driving cycle, which gives changes in parameters only after a certain fixed time. Knowledge of driving cycles in various regions is important for comparative testing and vehicle design purposes. The various uses of driving cycles are:

- Analyze powertrain operation and resulting fuel consumption
- Variation of road gradients and its effect on performance parameters.
- Performance variation by considering various conditions like traffic density, environmental effects etc.

3.1 Available Driving Cycles

Most of the currently used driving cycles originated in Europe. Further, the United States, China and India have played a significant role in adding new driving cycles. Some of the commonly used driving cycles are NEDC—New European Drive Cycle, FTP—Federal Test Procedure and WLTC—Worldwide Harmonized Light vehicle Test Cycle.

The following observations are noted from the above-listed drive cycles:

- FTP—75 cycle does not take into consideration the road gradient and this scenario does not hold good for Indian roads.
- The New York City cycle was developed with the aim to represent driving in highly congested urban traffic, typical for a city with frequent stops and idling.
- The NEDC driving cycle was the most widely followed drive cycle in the automotive industry before the introduction of the WLTP cycle as it includes both urban and highway driving regimes.
- WLTP has been in use since September 2017 and is a global standard driving cycle as it has data from all major countries and all types of road conditions. WLTP Class 01 is used specifically for low-speed vehicles.

Based on the above study, it was decided that NYCC and WLTP Class 3–2 low were the most suitable cycles, which can be considered for the design of our proposed personal mobility vehicle.

The consolidated data collected from various standard driving cycles is mentioned in Table 1 (Fig. 5).

4 Motor Sizing

Motor sizing refers to the process of selecting the correct motor for a given load. The sizing method enables the usage of the maximum machine speed to reduce the torque requirement on the electric machine which in turn minimizes its size, cost and power.

Table 1 Consolidated drive cycle data

Cycle name	Run time (s)	Distance (km)	Avg. speed (km/h)	Top speed (km/h)	Max acceleration (m/s ²)
FTP – 75	1372	11.9	38.3	91.2	1.48
NYCC	598	2.0	16.8	44.6	2.68
NEDC	1180	10.65	32.5	90	1.04
WLTP	589	3.09	18.9	56.5	1.60

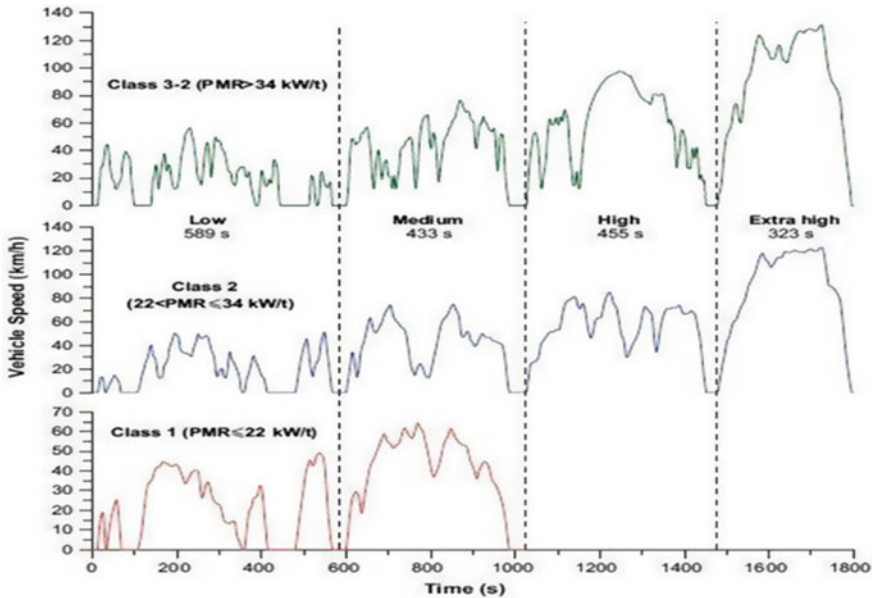


Fig. 5 Image comparing WLTC Class 2 and 3 Cycle

4.1 Procedure

The steps to determine the size of the motor suitable for our application is as follows:

1. Determine the traction forces of the vehicle, based on its performance requirements.
2. Select the speed and operating range of the motor required, through market research and survey.
3. Determine the required gear reduction ratio, based on the maximum required vehicle speed and the maximum motor speed.
4. Determine the maximum required torque to overcome the maximum traction force.
5. Determine the power required based on the maximum required torque, which is the required motor power.

4.2 Quasi-Static Simulation (QSS) Approach

QSS toolbox is a MATLAB-Simulink toolbox developed by the University of Zurich. It follows a backward simulation approach that is quasi-stationary simulation of Hybrid and Electrical powertrain mainly directed towards their correct sizing, optimization and energy flow in them. This tool consists of several blocks representing

Fig. 6 An overview of the QSS toolbox

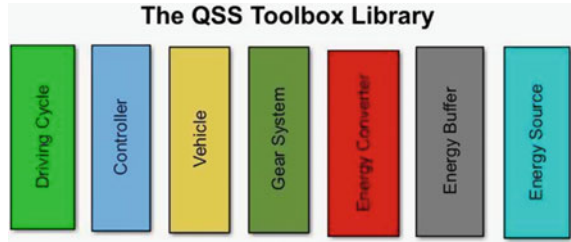
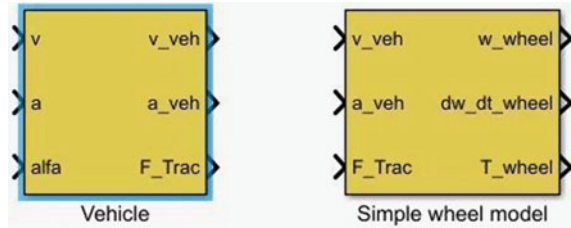


Fig. 7 The vehicle model in QSS toolbox library



the main components of a powertrain like the engines, electrical motors, electrical storage devices, transmissions and other mechanical coupling equipment. The above-mentioned toolbox is implemented for the calculation of the tractive force required to overcome the various resistances that the vehicle is expected to encounter by the utilization of the vehicle model (Figs. 6 and 7).

4.3 Vehicle Driving Forces

The major resistive forces experienced by a vehicle are rolling resistance of tires, aerodynamic drag, gradient and acceleration forces.

The above-mentioned forces on the car are given by the following mathematical equations:

- Rolling resistance,

$$F_{roll} = \mu_r * m * g \tag{1}$$

- Aerodynamic drag,

$$F_{aero} = 0.5 * \rho * C_d * A * v^2 \tag{2}$$

- Gradient force,

$$F_{grade} = m * g * \sin \alpha \tag{3}$$

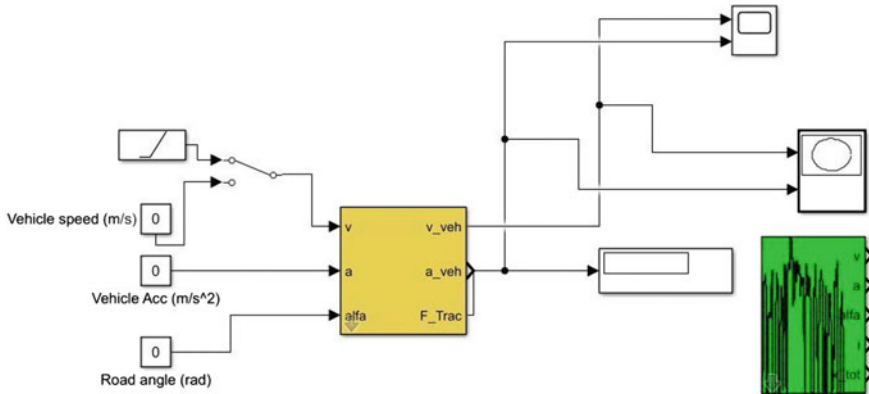


Fig. 8 The various elements of the vehicle block

- Acceleration force,

$$F_{\text{Net}} = m * a \quad (4)$$

- Traction force,

$$F_{\text{Trac}} = F_{\text{Net}} + F_{\text{grade}} + F_{\text{aero}} + F_{\text{roll}} \quad (5)$$

These forces add up to make the tractive force required by the vehicle to meet the desired performance parameters. The force from the vehicle powertrain should exceed the tractive force of the vehicle for the vehicle to move from rest.

A simulator model is then built in MATLAB-Simulink to determine the tractive force of the vehicle under different conditions. The model is as shown (Fig. 8).

This model contains a vehicle block, which requires a ramp generator function for providing the time varying velocity input to the vehicle block and also requires scope and an XY—Plot for viewing the output in the required graphical format. The addition of the appropriate driving cycle block to the module is necessary for obtaining accurate values of the simulation. City-2 driving cycle was chosen for this iteration. The vehicle block requires various input parameters which are further explained.

4.4 Vehicle Parameters

- Considered Mass of the Vehicle – 270 kg (Driver and Pillion)
- Frontal Area of the Vehicle – 0.6 m²
- Drag coefficient – 0.5 [13]
- Rolling resistance coefficient – 0.02 [14]

Table 2 The results of the traction force iterations

Inputs				Outputs
Case	Speed, v(m/s)	Acceleration, a(m/s ²)	Road inclination, α (rad)	Traction force, F _{trac} (N)
1	0 – 13.89	2.2	0.052	847.7
2	13.89	0	0.052	226.6
3	9.722	0	0.122	391.7
4	6.95	0	0.122	383.5
5	9.72	0	0.244	708
6	6.95	0	0.244	698.8

- Mass increase due to Rotating inertia – 5%
- Top Speed to be achieved – 50 kmph/ 13.88 m/s
- Assumed gradients are - 3° (0.052 rad), 7° (0.122 rad) & 14° (0.244 rad)

Input parameters: *Vehicle speed, Vehicle acceleration, Road inclination angle.*

Output parameter: *Traction force of the vehicle.*

The vehicle performance requirements for different conditions are shown in Table 2.

After obtaining the traction forces (F_{Trac}) for different driving conditions, we move onto the subsequent steps, taking the highest possible value of traction force (F_{Trac}) for further calculations. The obtained values were validated by hand calculations using:

$$F_{Trac} = F_{Net} + F_{Roll} + F_{Aero} + F_{Grade} \tag{6}$$

The values obtained were found to have a deviation of 3.8%, 0.37% and 0.14% respectively, hence validating our results.

4.5 Gear Reduction

If the electric machine is at its maximum speed when the vehicle runs at its top speed, the highest possible gear ratio is achieved. The highest gear ratio minimizes the required torque of the electric machine. As cost is roughly proportional to the torque of the machine, it is clear that using the highest possible gear ratio reduces the machine cost. The required gear ratio is calculated from the equation:

$$\text{Gear ratio, } i = \frac{\omega_{EM} * r_{wheel}}{V_{vehicle}} \tag{7}$$

The vehicle has a wheel radius of, $r_{wheel} = 0.203$ m and is required to travel at a speed of, $V_{vehicle} = 50$ kmph at a motor speed of, $\omega_{EM} = 428.4$ rad/s. Substituting these values in the above equation results in the gear ratio, **$i = 6.2$** .

4.6 Torque Requirements

The torque required from the motor is given by,

$$T_{EM} = \frac{F_{Trac} * r_{wheel}}{i} \quad (8)$$

We have already calculated the values of parameters required to calculate the torque. The vehicle experiences a traction force of, $F_{Trac} = 848$ N with a wheel radius of, $r_{wheel} = 0.203$ m and a gear reduction value of, $i = 6.2$.

Substituting these values in the above equation results in a torque value of, $T_{EM} = 27.7$ Nm, which is the maximum required torque from the electric motor.

4.7 Power Requirements

The power output required from the motor is given by:

$$P_{EM} = \omega_{EM} * T_{EM} \quad (9)$$

Torque required from the electric motor as per the previous calculation is, $T_{EM} = 27.7$ Nm at a motor speed of, $\omega_{EM} = 428.4$ rad/s.

Substituting these values in the above equation results in a power output of, $P_{EM} = 11.86$ kW, which is the required power from the electric motor for the necessary vehicle performance.

4.8 Motor Availability

Based on the above calculations, an electric motor having a power rating of 11.86 kW and torque in the range of 27.7 Nm is to be used, if the vehicle is to reach the performance levels previously mentioned. A motor having the above specifications is not readily available in the University. So, a 6 kW motor with a peak power of 8.6 kW is used in this case. By using a lower power motor, we will be compromising our acceleration, against the desired value.

5 Reduction Ratio

When it comes to electric vehicles, multi-speed gearboxes are not necessary. As a single reduction ratio is sufficient for operation, the ratio must be chosen to support both acceleration and top speed. A very low ratio might prove good for high speeds but will fall back in acceleration and vice versa. The gear ratio of transmission is selected to make the vehicle meet the desired dynamic performance. Three indexes will be used to indicate the vehicle dynamic performance namely grade ability, top speed and acceleration.

5.1 Torque and Speed Requirements of the Vehicle

The maximum required traction is 848 N and the max rated speed is 50 kmph. Based on this, the reduction ratio is then calculated.

- Reduction ratio for max speed: To calculate the reduction ratio for max speed, we need to consider the max rated RPM of the motor that is 4091 RPM. Considering a wheel of 0.406 m (16 inches) diameter. Therefore, for $V_{\text{vehicle}} = 50 \text{ kmph} = 13.88 \text{ m/s}$, $\omega_{\text{wheel}} = 68.37 \text{ rad/s}$, $N_{\text{wheel}} = 652.84 \text{ RPM}$. Thus:

$$\text{Reduction ratio (i)} = \frac{N_{\text{motor}}}{N_{\text{wheel}}} = \frac{4091}{652.84} = 6.266 \quad (10)$$

- Reduction ratio for max traction: Max traction demanded by the vehicle is during the maximum acceleration that is 848 N. The torque required at the wheels during the maximum acceleration is $848 \times 0.203 = 172.144 \text{ Nm}$.

Max torque produced by motor = 28.2 Nm

$$\text{Reduction ratio (i)} = \frac{T_{\text{wheel}}}{T_{\text{motor}}} = \frac{172.144}{28.2} = 6.10 \quad (11)$$

5.2 Ratio Finalization

Based on the above two calculations a ratio of 6.26:1 was selected giving importance to limiting the vehicle's top speed to only 50 kmph as the EV is specially designed for the purpose of urban transportation. Using the above ratio also gives the EV a slightly better acceleration at higher gradients due to the availability of higher torque at the wheels (Fig. 9).

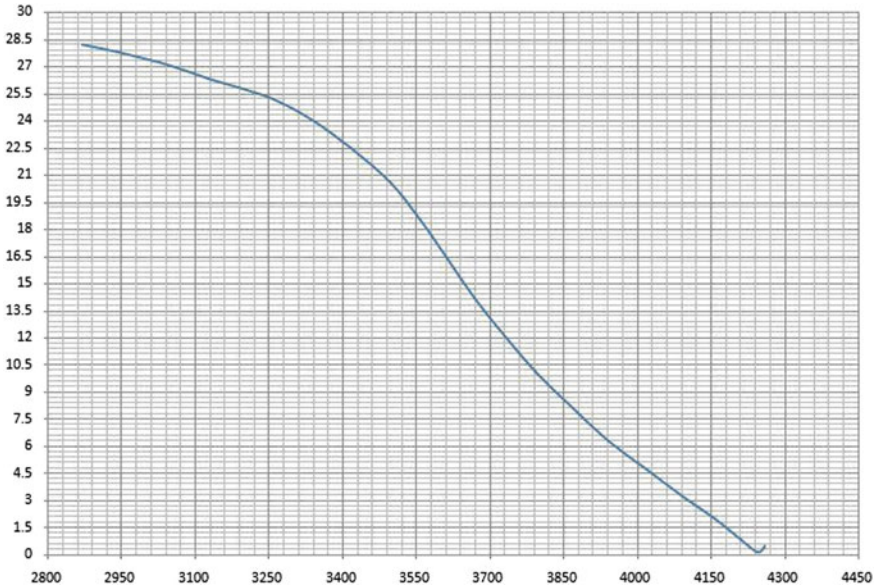


Fig. 9 Torque versus RPM—6 kW Motor

6 Battery Sizing

The primary source of propulsive energy for the electric vehicles is provided by the batteries. This battery is a collection of one or more cells which are stacked together into modules. Furthermore, the battery cells inside modules are connected in series and parallel to provide the required amount of voltage for the vehicle. Cells connected in series create a higher voltage potential for the battery pack which in turn provides higher efficiency and lower losses over its usage. The cells connected in parallel are predominantly used to support the main pack and power up the auxiliaries.

6.1 Why is Sizing Required?

The main function of the battery is to meet the energy demands of the powertrain, to generate the required tractive force to propel the vehicle at the desired speeds and acceleration. The inputs for the desired battery characteristics will be the power demand and the driven distance requirements from the powertrain to which the battery has to provide the energy consumption in kWh per 100 kms as a standard for comparison. The sizing of the battery is also vital to determine the range of the electric vehicle per charge.

6.2 Preliminary Battery Calculations

Since it is a pure electric vehicle, the usage of energy-optimized batteries over power-optimized batteries is recommended.

Motor Requirements to be satisfied by the battery—Rated power: 6 kW; Peak power: 8.6 kW; Operating Voltage: 72 V;

Peak current: 157 Amperes.

Input Parameters – Distance per charge: 20 km; Speed at Max power: 37.3 kmph; Max Power: 8.6 kW

$$\text{Energy consumption/km} = \frac{\text{Power}}{\text{Speed}} = 230.56 \text{ Wh/km} \quad (12)$$

Motor operating voltage = 72 V

$$\text{Ampere hour used/km} = \frac{\text{Wh/km}}{\text{V}} = 3.22 \text{ Ah/km} \quad (13)$$

$$\text{Capacity of battery} = 3.22 \times 20 \times 1.20 = 80.5 \text{ Ah} \quad (14)$$

For lithium-ion batteries we take into consideration *Peukert's constant* of 1.05.

$$\text{Therefore, total capacity} = 80.5 \times 1.05 = 84.525 \text{ Ah} \quad (15)$$

The consolidated capacity required for the battery, with respect to the motor testing data is as listed in the data below (Figs. 10 and 11).

From the above table, we get an average capacity rating of 59.6 Ah and the C rating will be decided based on the loading scenarios.

6.3 Battery Sizing Using QSS

The battery model in QSS is a continuation of the vehicle model with addition of the simple transmission block, electric motor block and the battery with SOC block. The input to this battery model consists of the gear ratio, efficiency of the transmission, idling losses, power of electric motor (kW), capacity of the battery (Ah) and initial charge of the battery while maintaining the same inputs provided for the vehicle model during tractive force calculations. There is also an inclusion of the integrator block into the model, which receives the power demand from the electric motor block as its input and provides the energy consumed in kWh as the output.

This battery model along with the implementation of the '**To workspace**' block will provide time series values of the power generated from the electric motor, which when passed through an integrator block will give the curve of Energy (kWh) v/s Driven Distance (km), the slope of which will provide the average energy requirement

Voltage (V)	Current (A)	P in (Watt)	Torque	RPM	P out
71.59	157.123	11249.19	28.175	2871	8470
71.61	157.035	11244.88	27.972	2907	8514.77
71.6	157.178	11253.91	27.75	2944	8554.55
71.59	157.158	11250.51	27.502	2984	8593.45
71.59	156.947	11236.66	27.183	3026	8613.01
71.6	156.905	11235.18	26.812	3074	8630.54
71.6	156.93	11236.19	26.335	3127	8622.99
71.61	156.92	11236.26	25.787	3187	8605.73
71.61	156.79	11227.73	25.172	3258	8587.64
71.68	150.492	10786.93	24.072	3335	8406.47
71.71	138.223	9911.24	22.452	3416	8031.18
71.75	125.233	8984.81	20.57	3496	7530.13
71.72	111.64	8007.1	18.515	3558	6898.05
71.73	97.979	7028.03	16.367	3611	6188.8
71.78	84.862	6091.78	14.19	3668	5450.15
71.85	72.398	5201.81	12.067	3730	4713.27
71.91	60.615	4358.98	10.032	3795	3986.74
71.97	49.601	3569.91	8.097	3867	3278.85
72.03	39.489	2844.37	6.3	3941	2599.82
72.09	30.384	2190.32	4.682	4019	1970.57
72.14	22.5	1623.07	3.242	4091	1389.01

Fig. 10 Consolidated motor test data

in Wh/km for the required driving range. Hence for the required distance the vehicle is expected to travel for a given charge we can determine accurately the exact amount of energy required in kWh for the specified driving cycle. The energy curve obtained from this model will also be helpful in deciding the max discharge current limit for the battery operating region. The battery operating region in the Power versus Energy curve consists of only the discharge limits, as there is no regenerative braking. This region is formed by the minimum and maximum SOC limits which are derived from the battery model above, along with the under voltage limit which ensures that the battery will not be exhausted (Figs. 12 and 13).

7 Final Drive Integration

The drive train in an electric vehicle consists of numerous components similar to a conventional vehicle Powertrain. The vehicle will be able to deliver the desired performance only if these components function in perfect harmony when integrated efficiently.

Max Speed	Dist. Per Charge	Power	RPM	Voltage	Wh/km	Ah/km	Capacity (Ah)
35.44	20.00	8470.00	2871.00	71.59	238.98	3.34	83.45
35.89	20.00	8514.77	2907.00	71.61	237.27	3.31	82.83
36.34	20.00	8554.55	2944.00	71.60	235.38	3.29	82.19
36.84	20.00	8593.45	2984.00	71.59	233.28	3.26	81.46
37.36	20.00	8613.01	3026.00	71.59	230.57	3.22	80.52
37.95	20.00	8630.54	3074.00	71.60	227.43	3.18	79.41
38.60	20.00	8622.99	3127.00	71.60	223.38	3.12	77.99
39.34	20.00	8605.73	3187.00	71.61	218.73	3.05	76.36
40.22	20.00	8587.64	3258.00	71.61	213.52	2.98	74.54
41.17	20.00	8406.47	3335.00	71.68	204.19	2.85	71.21
42.17	20.00	8031.18	3416.00	71.71	190.45	2.66	66.39
43.16	20.00	7530.13	3496.00	71.75	174.48	2.43	60.79
43.92	20.00	6898.05	3558.00	71.72	157.05	2.19	54.74
44.58	20.00	6188.80	3611.00	71.73	138.83	1.94	48.39
45.28	20.00	5450.15	3668.00	71.78	120.36	1.68	41.92
46.05	20.00	4713.27	3730.00	71.85	102.36	1.42	35.62
46.85	20.00	3986.74	3795.00	71.91	85.10	1.18	29.58
47.74	20.00	3278.85	3867.00	71.97	68.68	0.95	23.86
48.65	20.00	2599.82	3941.00	72.03	53.44	0.74	18.55
49.61	20.00	1970.57	4019.00	72.09	39.72	0.55	13.77
50.50	20.00	1389.01	4091.00	72.14	27.50	0.38	9.53

Fig. 11 Consolidated capacity of battery from motor test data

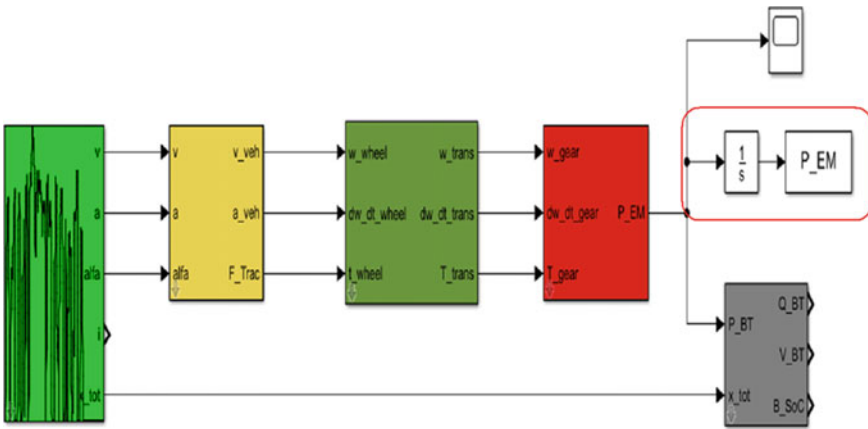


Fig. 12 To workspace model in QSS module

7.1 Drive Selection

Following the process of sizing the motor and the battery, the required reduction ratio of 6.2:1 (Motor to Wheel) has to be achieved and we proceeded to design this reduction with two approaches.

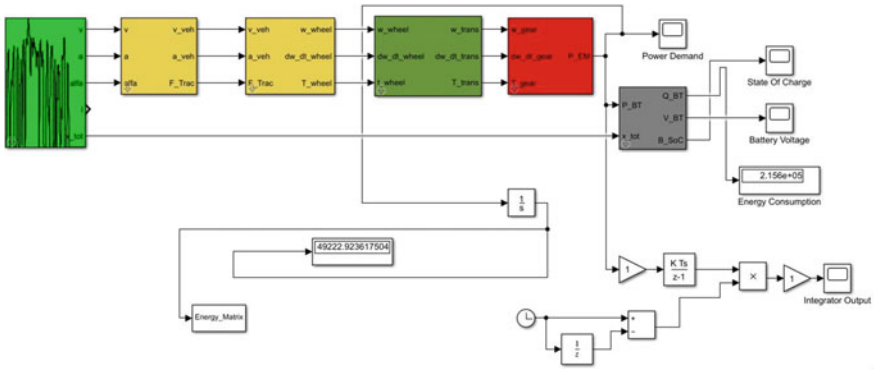


Fig. 13 Battery model layout in QSS module

Single Stage reduction using roller chain and sprocket—Preliminary Design:

In this case, the entire reduction ratio of 6.2:1 was achieved using a single roller chain and sprocket setup having the above-mentioned ratio. For this purpose, a chain and sprocket with the following parameters were chosen: ANSI Chain Number: 41; Pitch: 12.70 mm; Roller Diameter: 7.77 mm.

Based on the above parameters we achieved a roller chain setup with the following values: C to C distance: 323.23 mm; No of Links: 109; No of teeth on driving sprocket: 15; No of teeth on driven sprocket: 90.

As it can be seen from the assembly, the size of the driven sprocket and the wheel are not in perfect proportion. As the diameter of the driven sprocket is very close to the diameter of the wheel the clearance between the sprocket and the ground would cause a problem even in case of a slightest undulation in the road surface.

Two-stage reduction using gearbox and roller chain and sprocket—Final Design:

The total reduction ratio of 6.266:1 was suitably split into two stages consisting of a custom gearbox followed by a chain and sprocket setup. The gearbox carried a ratio of 2.2:1 and the remaining ratio of 2.84:1 was provided by the chain and sprocket. The following are the parameters considered for the gearbox: Gear module: 2; No Teeth on Pinion: 15; No of Teeth on Gear: 33.

For the chain and sprocket setup an OEM product was used after modifying the links as per our C to C distances. As it can be observed in the model, the drive train looks more compact and better integrated compared to the preliminary design. In this case, the dimensions of the driven sprocket are reduced and have a safe clearance to the ground (Figs. 14 and 15).

Fig. 14 Preliminary design—single roller chain

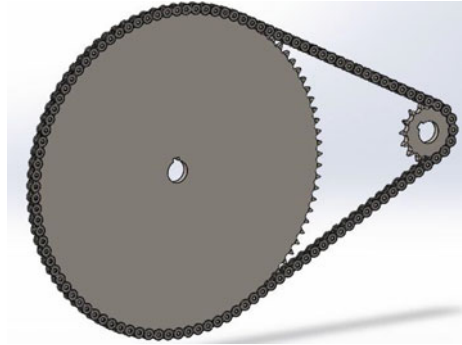
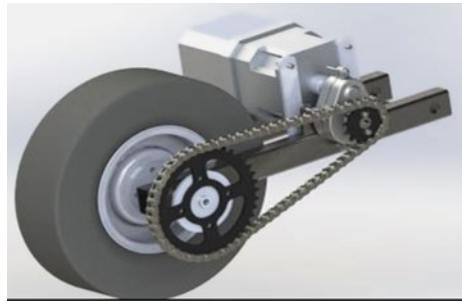


Fig. 15 Final design—gearbox and roller chain



7.2 First Stage Reduction—Gearbox

The first step reduction consists of a single-stage gearbox having a reduction ratio of 2.2:1. This was achieved by a pair of shaft integrated spur gears with a module of 2 and a face width of 38 mm. The implementation of the shaft integrated gears enabled the design of a very compact and robust gearbox, thus providing a perfect fit of this gearbox into the current swing-arm assembly. The gears will be fabricated using EN36C, a very high yield material which withstands the high bending loads of the teeth and provides the perfect wear resistance to the gears during its service. The mounting brackets of the gearbox have been ergonomically placed on the swing-arm for better access and higher serviceability of the gearbox at all times. The shafts on the gearbox have been adequately supported by the bearings on either sides of the shaft hence ensuring a smooth transmission of the drive power from the motor to chain sprocket (Figs. 16 and 17).

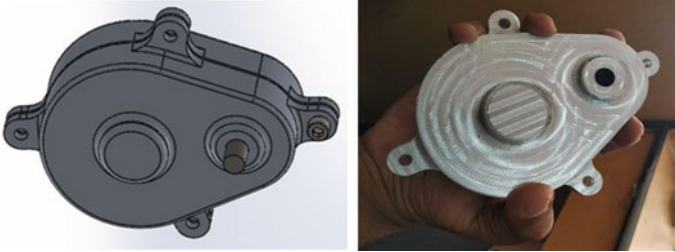
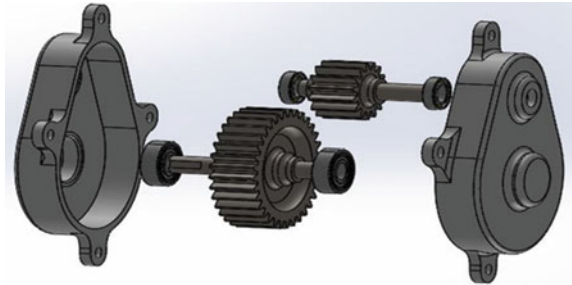


Fig. 16 Model and prototype—gearbox

Fig. 17 Exploded view of the gearbox



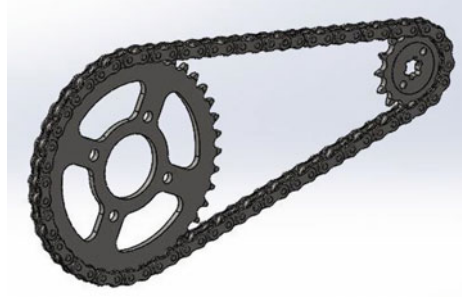
7.3 Second Stage Reduction—Chain and Sprocket

The second stage reduction consists of the chain and sprocket setup which connects the output of the gearbox to the wheels with a reduction of 2.8:1. An OEM chain and sprocket setup was selected for this purpose. The setup consists of a 14-teeth driving sprocket and 39 teeth driven sprocket. The reduction ratio of the above-mentioned gearbox was finalized by obtaining the ratio of the OEM setup and back calculating to the required overall ratio. Based on the position of the gearbox output shaft, where the driving sprocket is placed and the location of the drive axle, where the driven sprocket is placed, the center-to-center distance of the second stage reduction is determined to be 314 mm.

The selected chain sprocket setup belongs to a motorcycle grade with the following dimensions as per the standard charts as follows (Fig. 18):

- Chain Grade No—520
- Pitch—15.875 mm
- Width—6.35 mm
- Roller Diameter—10.16 mm
- Pin Diameter—5.06 mm
- Pin Length—8.50 mm
- Inner Link Diameter—13 mm

Fig. 18 Driven and driving sprocket



- Outer Link Diameter—14.80 mm
- Link Thickness—2 mm
- Average Strength—3100 kg

7.4 Drivetrain Integration

- Entire powertrain setup is assembled on the trailing arm after considering Bump and Rebound limits.
- The drive is transmitted to the wheel with the help of couplers fastened to the driveshaft.
- The driveshaft is supported by roller bearings for smooth rotation (Figs. 19 and 20).

8 Analysis

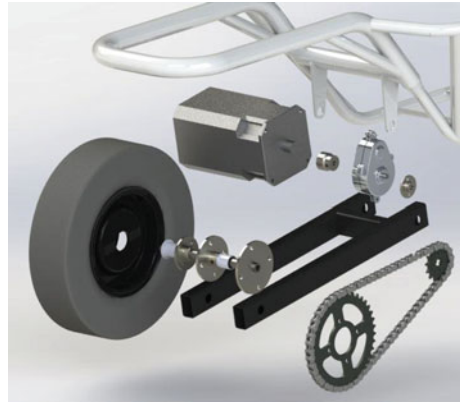
8.1 Modal Analysis

Modal analysis involves the study of dynamic properties of systems in the frequency domain and includes measuring and analyzing the dynamic response of structures

Fig. 19 Chain sprocket setup after assembly



Fig. 20 Exploded view of final assembly



during excitation. It also involves the determination of natural frequencies and associated mode shapes of a component or structure under free vibration. The procedure of computerized modal analysis involves:

- Building the model of the component to be analyzed.
- Defining the frequency range followed by meshing.
- Expanding the modes to obtain mode shapes.
- Evaluating the mode shapes and identifying the natural frequency.

8.2 *Motor Operating Range*

- Minimum speed of motor—0 rpm
- Maximum speed of motor—5000 rpm
- Converting the above into frequency domain, we obtain the motor frequency range to be 0–84 Hz.

8.3 *Modal Analysis of Various Components*

See Tables 3 and 4, Figs. 21, 22, 23 and 24.

Results:

1. Six rigid modes are obtained for all the components analyzed.
2. Mode frequencies of the components lie outside the range of motor, gears and gearbox frequencies. This ensures resonance-free operation during its service.

Table 3 Mode frequencies—left and right casing

Gearbox left casing		Gearbox right casing	
Modes	Frequency (Hz)	Modes	Frequency (Hz)
Rigid	0	Rigid	0
	0		0
	0		1.80E-03
	2.50E-03		4.03E-03
	4.47E-03		5.05E-03
	5.76E-03		6.46E-03
1	2102.5	1	2102.7
2	2969.5	2	2976.9

Table 4 Mode frequencies-driving and driven sprocket

Driving sprocket		Driven sprocket	
Modes	Frequency (Hz)	Modes	Frequency (Hz)
Rigid	0	Rigid	0
	0		0
	0		1.70E-03
	2.39E-03		3.89E-03
	1.15E-02		5.03E-03
	1.29E-02		9.16E-03
1	6138.7	1	559.58
2	6144	2	615.92

Fig. 21 Modal analysis of left casing

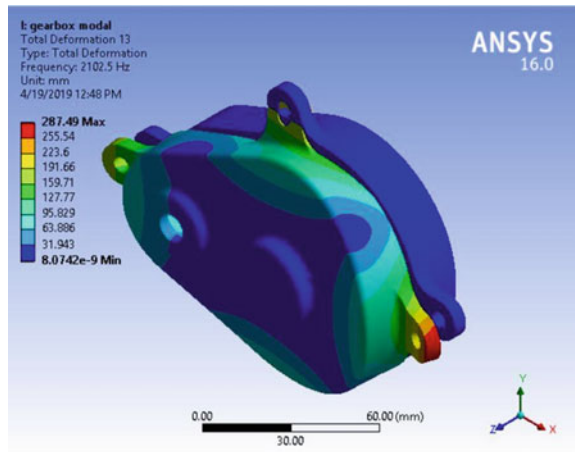


Fig. 22 Modal analysis of right casing

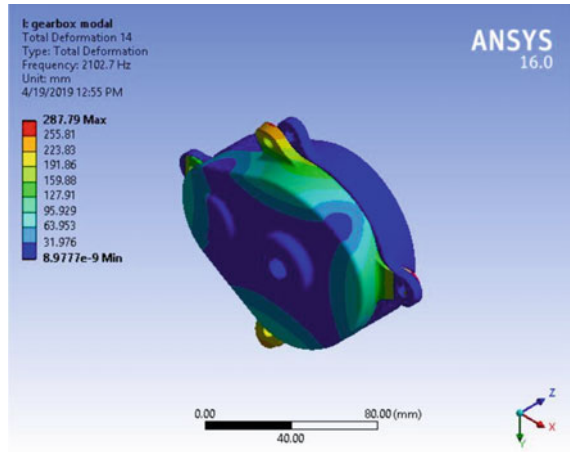
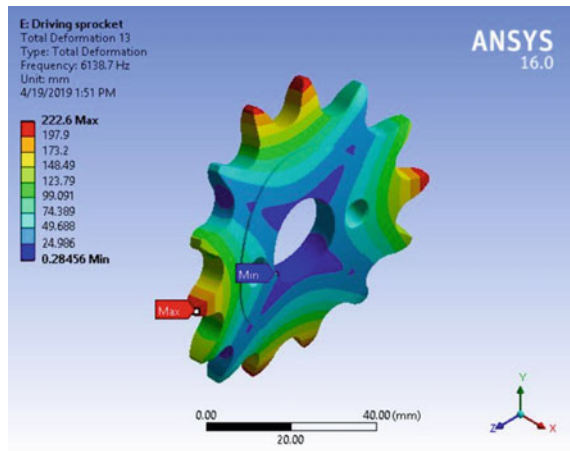


Fig. 23 Modal analysis of the driving sprocket



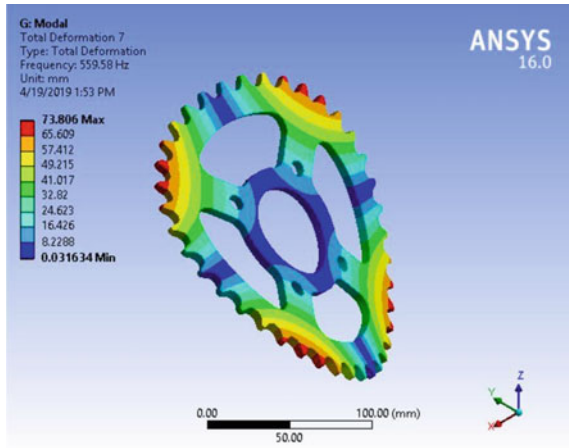
8.4 Static Structural Analysis

A static structural analysis determines the stresses, strains, displacements and forces in components primarily caused by loads that do not induce significant inertia and associated damping effects on the component.

8.5 Structural Analysis of Gears

Material properties of EN36C are applied to the gears. The gears are then assembled such that there is contact between the teeth of both gears. It is followed by meshing

Fig. 24 Modal analysis of the driven sprocket



the gears to an element size of 1 mm. Cylindrical supports are provided for shafts on which bearings are placed. A torque of 28.8 Nm is applied to the shaft connected to the motor shaft.

8.6 Structural Analysis of Gearbox Casing

The major loads acting on the gearbox is through the faces of the bearing pocket. As the current gearbox encloses only spur gears, the axial loads are totally neglected. The radial loads are the ones that are predominant and hence are considered for analysis. The radial load of the gears is taken by the bearings, which in turn transfer these loads to the gearbox casing through the bearing pocket faces. Along with the radial loads, the Chain pull acting through the output shaft is also applied through remote force acting via remote point. These loads are resolved using moment balance equations to find out the respective bearing reaction force and the source of these forces being the gears they act through the center of the shaft (Figs. 25, 26 and 27).

8.7 Structural Analysis of Sprockets and Couplings

Material properties of AISI 1045 are applied to both the sprockets and coupling. They are then meshed to an element size of 1 mm. Fixed supports are provided to the mounting points of the sprocket while cylindrical supports are provided to the portion in contact with the shafts for the couplings. In case of sprockets, torques of 63.6 Nm and 177.6 Nm are applied to the driving and driven sprockets to the portion of the sprocket which is in contact with the chain during its operation. On the other

Fig. 25 Stress distribution on the gears

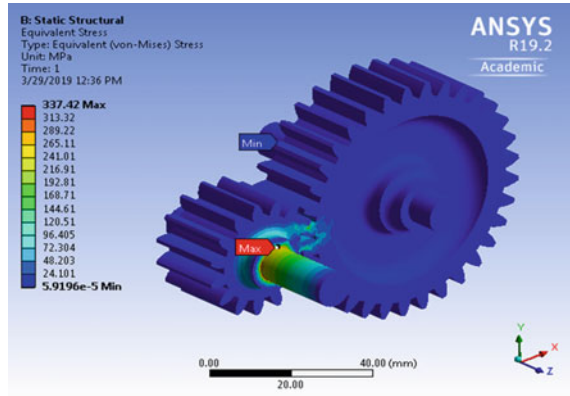
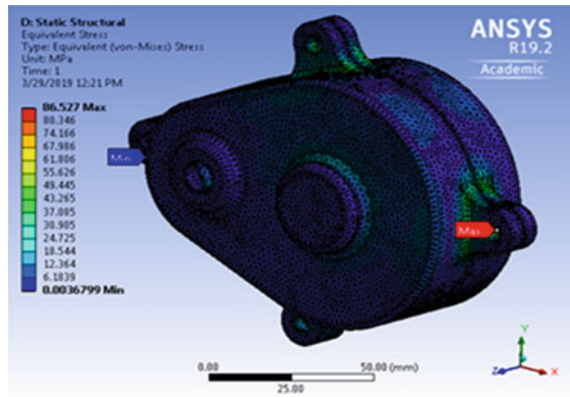


Fig. 26 Stress distribution on gear box



hand, torque is applied on the mounting points of the coupling through which it is connected to the respective sprockets and based on the torque experienced by the respective sprockets, torque values are applied (Figs. 28 and 29).

8.8 Results

Post analysis, it has been observed that all the custom-designed components including gears, couplings, gearbox exhibit safe operating stresses with satisfactory FOS values. The results of the analysis have been mentioned in Table 5.

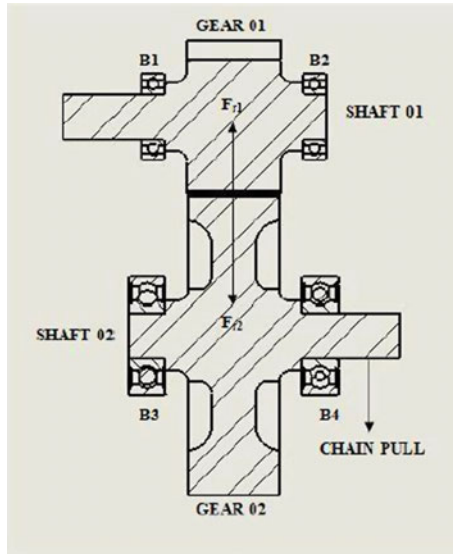


Fig. 27 Loads acting on the bearings

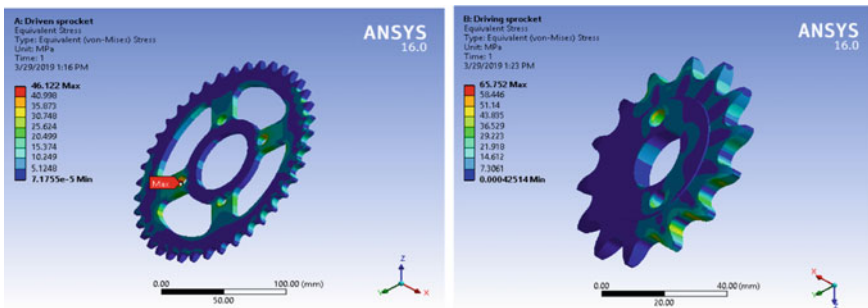


Fig. 28 Stress distribution on the driven and driving sprockets

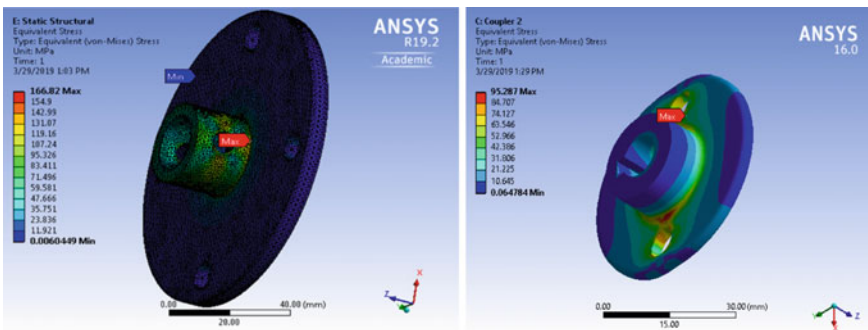


Fig. 29 Stress distribution on the sprocket couplings

Table 5 Results of static structural analysis

Components	Material	Yield strength (MPa)	Max stress (MPa)	FOS
GEARTRAIN	EN36C	737.9	337.42	2.18
GEARBOX	ALUMINIUM (6S)	276	86.527	3.18
DRIVING COUPLER	AISI 1045 (MS)	310	95.287	3.25
DRIVEN COUPLER	AISI 1045 (MS)	310	166.82	1.85

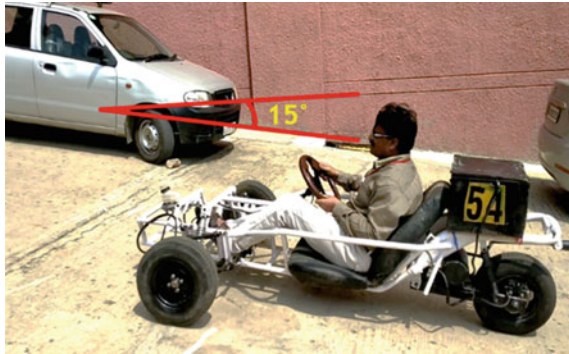
9 Results and Conclusions

The final outcome was a working prototype of our designed powertrain, which was installed in a tadpole configuration three-wheel vehicle as seen in the images below. When tested, the vehicle was able to achieve speeds of 25–30 kmph and was able to successfully scale a gradient of 15°. There were no issues concerning the power transmission from the motor to the wheels. The prototype is powered by a lead acid battery pack against the desired lithium-ion cells due to the unavailability of the same. For this reason, in the prototype the position of the pillion rider is compromised to accommodate the battery pack. Conclusively it can be said that the vehicle was completed successfully along with the fabrication of a running prototype (Figs. 30 and 31).

Fig. 30 Powertrain assembly with the battery pack



Fig. 31 Prototype testing on campus



References

1. Lebkowski A (2017) Light electric vehicle powertrain analysis. *Sci J Silesian Univ Technol* 94:124–137
2. Lei A et al (2019) A novel approach for electric powertrain optimization considering vehicle power performance, energy consumption and ride comfort. *Energy* 167:1040–1050
3. Choi G, Jahns TM (2013) Design of electric machines for electric vehicles based on driving schedules. In: *Wisconsin Electric Machines and Power Electronics Consortium (WEMPEC)*. Madison, Wisconsin, USA
4. Karamuk M (2011) A survey on electric vehicle powertrain systems. In: *International Aegean conference on electrical machines and power electronics and electromotion (ACEMP-Electromotion)*. Istanbul, Turkey
5. Balamurugan T, Manoharan S (2014) Design of solar/electric powered hybrid vehicle (SEPHV) system with charge pattern optimization for energy cost. *Int J Eng Technol* 5(6):4543–4555
6. Butler KL et al (1999) A Matlab-based modeling and simulation package for electric and hybrid electric vehicle design. *Trans Vehicular Technol* 48(6):1770–1778
7. Schönknecht A et al (2016) Electric powertrain system design of BEV and HEV applying a multi objective optimization methodology. In: *6th Transport Research Arena (TRA-2016)*, vol 14. Warsaw, Poland, pp 3611–3620
8. Walker PD et al (2013) Modelling, simulations, and optimization of electric vehicles for analysis of transmission ratio selection. *Adv Mech Eng* 340435
9. Lee J et al. Development of electric vehicle powertrain: experimental implementation and performance assessment. In: *Eighteenth international middle east power systems conference (MEPCON)*. Cairo, Egypt
10. Zou Y et al (2012) Optimal energy management strategy for hybrid electric tracked vehicles. *Int J Veh Des* 58:307–324
11. Park G et al (2013) Integrated modeling and analysis of dynamics for electric vehicle powertrains. *Expert Syst Appl* 41(5):2595–2607
12. Walker P et al (2017) Powertrain dynamics and control of a two speed dual clutch transmission for electric vehicles. *Mech Syst Signal Process* 85:1–15
13. Wong JY (2001) *Theory of ground vehicles*, 3rd edn. Wiley, New York, USA
14. Jazar RN (2008) *Vehicle dynamics: theory and applications*. 1 edn. Springer Science + Business Media, LLC – NY, USA

Artificial Intelligence-Based Trajectory Planning for Driverless Vehicles—A Review



Aathira G. Menon  and S. Bindu 

Abstract One of the hurdles in implementing self-driving automobiles is their precise decision-making in uncertain traffic conditions. The paper reviews various Artificial Intelligence-based trajectory planning algorithms addressing this issue. The review focuses on lane changing, trajectory selection, and safety to model a Level-5 autonomous vehicle. The prominent algorithms are discussed in terms of their features, status, and scope. The algorithms are analysed in the increasing order of levels of automation. As the trajectory planning algorithm mimics human intelligence, it is more probable to develop the characteristics of a trustworthy self-driving vehicle capable of making accurate decisions in extreme road or traffic circumstances. In addition to the major traffic elements, pedestrian interaction, vehicle dynamics, and the usage of an adaptive controller can ensure more promising results to achieve safe lane changing/selection.

Keywords Autonomous vehicles · Lane changing algorithms · Artificial Intelligence

1 Introduction

Autonomous Vehicles (AVs) have been tipped as the answer to road safety-related concerns by taking humans out of the equation. While still in its infancy, self-driving technology is increasingly becoming mainstream and could drastically change our transport system, our economy, and society. An AV can sense and operate in its environment without human interference, thus avoiding road traffic collision fatalities due to human mistakes like drink and drive, drowsy or distracted driving, and illegal manoeuvres. AVs with advanced sensing and control capabilities can also reduce the

A. G. Menon (✉) · S. Bindu
Manipal Institute of Technology, Manipal, Karnataka 576104, India
e-mail: aathiragm7@gmail.com

S. Bindu
e-mail: bindu.s@manipal.edu

possibility of accidents due to bad conditions or topology of the roads or lack of visibility. Self-driven vehicles depend on sensors, actuators, and complex Machine Learning (ML) systems. Advancements in Artificial Intelligence (AI) technologies have made self-driving vehicles a reality sooner than expected. Self-driving systems use large quantities of data from image recognition systems and various sensors. This data is fed into AI models, which identify the data patterns to classify drivable paths and obstruction detection such as pedestrians and other road users in each driving environment. To make AV mimic human intelligence, it is crucial to use sophisticated lane changing algorithms that can tackle any emergency or unpredictable situations that are obvious to occur during driving.

This paper reviews some prominent motion planning algorithms based on AI and ML. This paper aims to highlight different AI-based algorithms to develop suitable motion strategies for autonomous driving by targeting the algorithms' effectiveness in real-time scenarios. No effort is put to rank the methods; instead, various algorithms that would drive the self-driving system to the level-5 types of AVs are analysed. An analysis is laid down regarding the constraints considered for modelling the algorithms, their advantages, and drawbacks. The objective is to ensure a continuous path for the ego vehicle following the ego lane and adapting its longitudinal states. Section-2 traverses through several prominent AI-ML-based trajectory planning algorithms to achieve a smooth, reliable, and quick navigation, with minimal to no human intervention required. The paper is concluded with future scope for research in the field of AVs.

2 AI-Based Safe Lane Changing Algorithms

A review on prominent AI-ML-based trajectory planning algorithms to achieve a dependable and fast navigation, with minimal to no human intervention required, is presented in this section. The algorithms are divided into various categories based on their nature of functioning [1].

2.1 *AI Logic-Based Algorithms*

AI Logic-based algorithms can be classified as rule-based, decision tree-based, and Markov Decision Process (MDP)-based algorithms.

Rule-Based Algorithms

These algorithms are one of the purest forms of AI-based models. They are based on expert systems, which mimic the human brain's reasoning in analysing and solving a complex problem. A simple rule-based model is built-in [2, 3] to provide an optimised decision on lane changing. Depending on whether the system wants to turn left or right, a relation is drawn between the ego vehicle's velocity and position. If the AV

intends to turn left or right, it must readjust the velocity to its preceding vehicle in the same lane and the vehicle in the adjacent lane (to which manoeuvre is desired). Two broad classifications of manoeuvre cues are longitudinal intention cues and lateral intention cues. The former considers the lateral velocity and position relative to the lane boundaries. The latter considers the relative velocity, time gap, and time-to-collision to the preceding vehicle in the current lane. Based on the longitudinal and lateral intention cues, a confusion matrix is created, using which the direction of the lane changing can be predicted. A variety of error and accuracy measures are deduced to evaluate the model precisely from the confusion matrix.

Decision Tree-Based Algorithm

The work presented in [4] aims to choose the desired trajectory from a set of parameterised candidate trajectories to optimise the required criteria. This choice is complex in keeping off collisions and eliciting natural behaviour for passenger consolation. Under the shape of a selection tree, a finite set of deterministic candidate paths is considered. To ensure continuous driving, specific regulations are imposed on these paths. Hence, it forms to be a minor subset of all the possible paths [4]. Algorithms using motion primitives [5] or probabilistic procedures [6] optimise the model described. The decision tree branches are snipped if the paths depicted by the decision trees are hazardous to the automobile or ask for any compromise for the passenger's comfort factor. This strategy helps in restricting the growth of the decision tree. Hence, a limited number of optimal paths are deduced with the aid of the decision tree. These paths are chosen to satisfy all the constraints imposed on the model to ensure a few requisites such as maximising travelled distance, reducing journey time or gas consumption, and providing a smooth journey.

The binary decision diagrams (BDD) are incorporated as a framework for the suggested method of trajectory planning. BDD is an intuitive approach that seeks to imitate humans' decision-making skills to achieve optimal lane change and velocity adaptation. The methodology used in [4] is novel because it is predicated on the critical assumption that an intelligent controller for trajectory planning is self-predictive and capable of avoiding collisions. Hence, it rules out the possibility of having a highly predictable route planner and a quick response system for risky situations. The required intelligent route tracker is carried out using Model Predictive Control (MPC). Because of (i) the non-linearity of automobile dynamics and (ii) the inclusion of state and input constraints to prevent collisions which directs the AV to follow a preferred path, a Markov planner proves as an effective manipulation method for self-driving vehicles because of its potential to systematically deal with nonlinearities and constraints at the design level [7, 8]. Depending upon the need for the change of path, several candidate rules are defined based on certain assumptions. These candidate rules are evaluated based on the following constraints.

- (i) The major and minor axis of the ellipsoidal region around the ego vehicle.
- (ii) Longitudinal distance to the fictional collision point, L_d .
- (iii) Sum of the distance of the ego vehicle and the imaginary collision point about the corresponding obstacle, S_d .

Table 1 The truth table for the first criteria (L_d _Straight = ' L_d _S', L_d _Left = ' L_d _L', L_d _Right = ' L_d _R')

Is it the highest value?			
L_d _S	L_d _L	L_d _R	Decision
No	No	No	Impossible
No	No	Yes	Turn right
No	Yes	No	Turn left
No	Yes	Yes	Table 2
Yes	No	No	Continue straight
Yes	No	Yes	Table 2
Yes	Yes	No	Table 2
Yes	Yes	Yes	Table 2

Table 2 The truth table for the second criteria

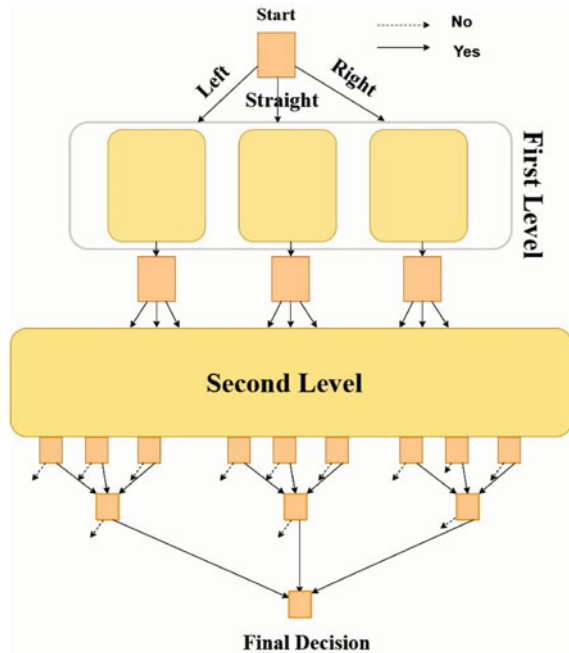
Is it the highest value?		
S_d _Left	S_d _Right	Decision
No	No	Turn left
No	Yes	Turn right
Yes	No	Turn left
Yes	Yes	Turn left

In [3], the optimal trajectory is determined by considering the value of the parameters such as L_d and S_d . The path is said to be optimal if it has a large value of L_d .

In case of a tie between two or more paths, the decision is made by considering the S_d value. If a second tie occurs, the route with the highest quality position within the first-order profile matrix is selected. Tables 1 and 2 present the first and second tie criteria [4].

The first stage of the decision tree consists of a maximum of three candidate paths and wards off the combined outbreak of the decision tree. A similar approach is laid for each of the three branches from the first level, forming the decision tree's second level [4]. Hence, a maximum of nine candidate paths is generated at the end of the second level. A pictorial representation of the BDD is depicted in Fig. 1. The algorithm works faster even in a complex environment and predicts the safe path during the manoeuvre. This approach uses an MPC-based manipulation to evaluate a route planner corresponding to a defined reward function. Each branch of a decision tree corresponds to a chain of motions over a predicted horizon, apply the first action of sequence with the greatest cumulative reward, and repeat this process at each updating step. Even though this method is evident in the structure and can be implemented without difficulty, it requires multiple simulations to evaluate the action sequences. The depth of the tree (the number of layers) for onboard implementation

Fig. 1 A decision tree with nine candidate rules



is limited by the computational effort needed to run these simulations. State transition models must represent the state’s evolution due to actions; deterministic state transition models are widely used.

Thus, in [9], a specific decision tree technique is proposed to successfully address the above demanding situations. An AV’s decision-making process is modelled as a Partially Observable Markov Decision Process (POMDP), with traffic represented as a Markov chain with only partially observable states. This work’s dynamic traffic model comprises more than one automobile as a discrete-time Markov chain, with the state partially observable via the ego vehicle. The state space is supposed to be continuous and bounded. A message is a piece of fixed data about the state space that the AV may examine. To reflect the quantisation of sensor signals, the messages will be pairwise disjoint units. A one-step reward function is used to determine monitored coverage for AVs. The objective is to maximise the cumulative reward over a specified horizon. Due to the most cumulative reward value, given the current message, a Q-value for the message-motion pair is defined as the immediate response over all possible mixtures of subsequent actions.

MDP-Based Algorithm

A vital aspect of lane changing is to choose between lane-staying and lane navigation while avoiding collisions. To attain this objective, a sophisticated MDP planner is formulated in [10, 11] to generate the decisions robotically without degrading the benefits, desirability, and opportunity. A few of the constraints are passed to the lower

lever controls as the actions' choice is streamlined. Hence, the latency and execution errors are eliminated. The chances of collision include unexpected braking or speed reduction of the preceding vehicle. As these cases have quick response times, they cause a mismatch with the actual execution time. Therefore, it is challenging for the excessive level planner to make an appropriate choice.

As a result, with a constant velocity profile, a low degree longitudinal control is proposed to change vehicle navigation, following, and collision avoidance all at once. By making acceleration decisions through a high-level planner and designing a simple planner with a sophisticated controller, control discontinuity and execution errors are minimised. A non-linear dynamic vehicle model is incorporated into this work. Two vehicle control inputs, namely acceleration command and Front wheel steering angle command, are introduced in [10, 11] for the steering command.

A reference trajectory with continuous curvature is to be determined in real time. The lane changing decision is made with respect to two general highway actions:

- i. Lane-staying: Maintaining a favoured velocity and a safe distance from a preceding automobile even when staying on a lane.
- ii. Lane-converting: Equipped for lane navigation because of various purposes like collision avoidance, passing a gradual speed automobile, and getting ready for merging ahead or to exit.

The proposed Markov planner aims to determine if the lane change is consistent with necessity, desirability, and possibility. The lane change necessity is described as that the automobile will continuously choose to continue within the original lane until there are unavoidable situations in advance that compel the AV to the alternate road. Various benefits describe the desirability of the vehicle to initiate a lane change. The benefits include a speed boom, sidestepping a halted obstacle, or approaching a smaller road curvature for the vehicle's higher manoeuvrability. The probability is determined by whether the ego vehicle is much more stable and physically capable of carrying out the expected motion and fully executing it as deliberate.

For the planner's formulation, a reward function is designed to address layout problems such as riding as quickly as possible without exceeding the speed limit, driving precisely and avoiding excessive lane navigation, and decelerating for balance during intense flips.

Hence, one can conclude that by directly coupling sensing to actuation, an uncomplicated environmental hazard can be treated quickly without the aid of any high-level models. Near the surrounding obstacles and control command delay, the automobile could efficiently navigate its deduced trajectory and maintain a smooth velocity profile.

2.2 AI-Heuristics

When traditional approaches are too gradual, the heuristic method is used to solve a problem quicker or find an estimated solution when traditional methods fail to

determine an exact solution. Execution is done with the aid of trading optimality, completeness, accuracy, or precision for velocity. Two of the well-known methods that fall under heuristics are discussed below.

Support Vector Machine

One of the crucial parts of modelling a self-driving system is to make its lane changing behaviour highly efficient by choosing an appropriate collision-free and safe path. It is observed that ten per cent of all parkway crashes occur at some stage in alternate lane manoeuvres. The authors in [12] have put forth a Support Vector Machine (SVM) model for deciding a suitable route during the lane change. SVM is a supervised algorithm that can be used for each category or regression challenge.

Several SVMs have been trained on the demonstrations given by the human drivers by using real-time lane navigation and lane statistics. The SVM decides whether to remain on track or begin lane navigation based solely on the individual driver's verified opportunity. The output of the classifier is then used to determine a trajectory. A predictive control structure optimises the control inputs to follow the reference trajectory while remaining within safe and convenient limits. It is possible to capture and reflect natural human driving through experimental lane change training data. The focus of the work implemented in [12] is to enhance the confidence of the passenger, which leads to fewer human interventions and more secure self-sustaining automobile operations.

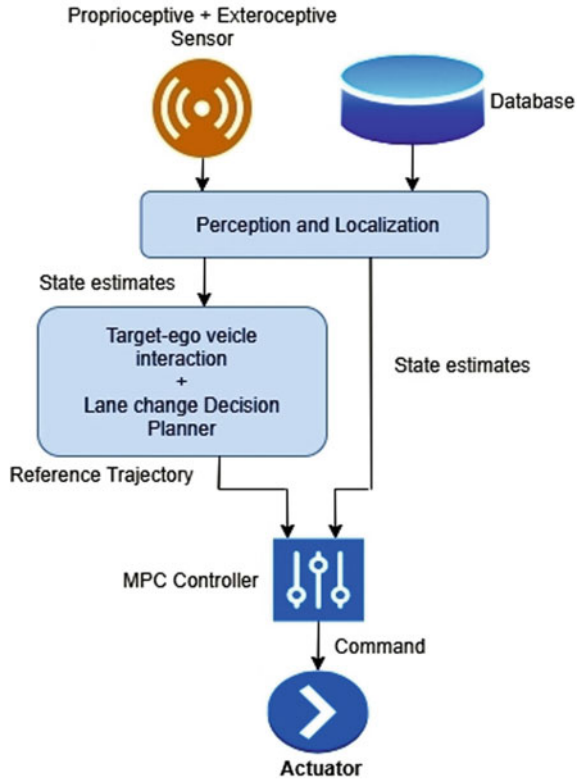
A lane navigation selection model calculates a binary mode that indicates whether the current driving environment will serve a particular motive force to hold lane retaining (mode-1) or trigger a lane change (mode-2). The mode is calculated using an SVM classifier trained on experimental lane changing data obtained from the expert drivers. This technique ensures that the AV produces lane navigation initiation behaviour close to human's natural driving, based on the which the SVM is trained. An N -sized data set with k features are modelled, and these data sets are expected to belong to either of the two modes. The working process of the proposed model in [12] is depicted in Fig. 2.

Suppose the SVM model determines that the driving force can maintain the lane, then the motion planner produces a lane-middle reference trajectory in the current lane. If, on the other hand, the model decides that lane changing should begin, the motion planner generates a reference trajectory along the centre of the adjacent lane starting at the instant when the model changes the modes. Finally, a controller is used to fine-tune the motion planner's reference trajectory while staying within the vehicle actuator's safety limits and boundaries.

Evolutionary Genetics

A Genetic algorithm (GA) is a heuristic technique used in AI and computing. It is used for locating optimised answers to look at problems primarily based on the principle of natural selection and evolutionary biology. GA is powerful for searching through large and complex information sets. It is based on Charles Darwin's theory of natural selection. Two of the algorithms that are modelled based on GA are discussed below.

Fig. 2 Process flow of SVM



Two-Chromosome GA

In [13, 14], the authors have developed a fuzzy controller which seeks the aid of GA to attain the level-5 type of AVs. A two-chromosome GA is used to meet the desired goal. The chromosomes’ populace evolves through the years via recursive mutation and competition. Controlled mutation represents a feasible candidate solution. This strategy forms the foundation of the GA. Each chromosome within the population has a related fitness to choose a new and better chromosome throughout the competition. This method is known as selection. With the aid of genetic operators along with crossover and mutation, new chromosomes are created. Fuzzy controllers are examined and optimised with GA. In this approach, initially, a part of the information that approximately imitates the human driver’s driving strategy is recorded and processed to get accurate statistics that depict the driver’s approximate mindset.

A model that returns a proper fuzzy controller based on the statistics mentioned above is created via an iterative genetic set of rules. The proposed GA method is achieved with the aid of two iterative stages. The first stage is the enhancement performed on the membership functions and the second stage is the optimisation of the fuzzy controller. In private and experimental regions, the designed controller is

tested and affirmed that the controller shows similar behaviour to the proven statistics by using human driving force.

The generated fuzzy controller takes in two inputs from the Global Positioning System (GPS) cartography. The inputs are lateral and angular errors [13]. The first step in the action plan of the algorithm includes GPS cartography. The desired direction is built mechanically by tracking the route with an automobile equipped with a GPS. Based on the GPS's recorded value, the computer picks the most precise factors to use as a reference line to measure the lateral and angular errors of the moves rendered by the human. The distance between the present and the vehicle's theoretical position is defined as the lateral error, L_e if it is on the reference trajectory. Lateral error values are defined in the interval $(-\infty, +\infty)$. The angle subtended by the reference line and the car's velocity vector is defined as the angular error, Φ . The value of angular error swings in the interval $(-180, +180)$. A pictorial representation of these errors [13] is presented in Fig. 3.

Based on the vast amount of processed data, a set of input variables is fed into the GA to deduce the output variables. The statistics set contains statistics on the vehicle's lateral and angular errors and human drivers' moves. This information is processed. The final sets of factors may be visible, used as inputs to the genetic set of rules to ensure similarity with the human behaviour and freedom to generate fuzzy controllers with a smooth floor. Thus, the AV will be able to hold the same direction without any brusque steering moves.

For modelling the controller, a Mamdani fuzzy system is used. There are two fuzzy inputs to the controller, i.e., Lateral error and Angular error. Lane selection is decided by analysing these inputs as shown in Table 3.

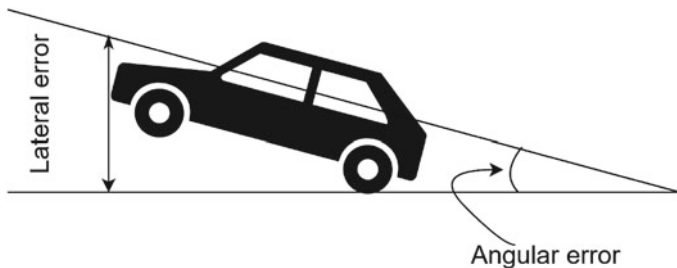


Fig. 3 Pictorial representation of the inputs to the Fuzzy controller

Table 3 Trajectory selection using the fuzzy inputs

Le (in left direction)	Φ . (in left direction)	Le (in right direction)	Φ . (in right direction)	Trajectory selection
Maximum	Maximum	NA	NA	Move to right lane
NA	NA	Maximum	Maximum	Move to left lane

The fuzzification of each input variable is achieved with the aid of four or five membership functions. There is one handy fuzzy output variable, referred to as steering, with 21 linguistic labels, whose membership functions are described via singletons. At last, GA is implemented in two exceptional stages, which are repeated in various instances and represent two GA. Thus, a relatively good controller is designed that can trace a smooth path in alignment with the reference path.

Four-Chromosome GA

A four-chromosome GA makes the collision avoidance decision more efficient and reliable, taking four factors: Speed, Brake, Angle, and Time To Avoidance (TTA). The set of rules initially computes the front, rear, left, and right distances between vehicles, then consistent with those values, the set of rules shows the best selection to keep away from the collision. It also deduces the decision parameters or initiated gene. It then calculates every gene's fitness and offers the most appropriate approach to avoid the collision.

The GA technique works as follows. Firstly, it examines the colliding object or vehicle within the horizon of the AV. In case of any obstacle detected, a pool of feasible solutions to address the given obstacle is produced. Finally, an optimised solution is selected. GA uses the idea of organic traits, such as chromosomes and genes. Functions like crossover and mutation are implemented on these chromosomes to get the subsequent populace of the solutions. There is an opportunity for the brand-new pool of decisions to be higher than those within the authentic populace or even worse than the original set of decisions. In the work proposed in [15], an initial population of 100 chromosomes is considered. The GA chooses the best offspring based on the fitness function, and the selection is made using the Roulette Wheel selection method. The probability associated with each chromosome and its fitness function is evaluated. The Roulette Wheel selection states that the higher probability chromosomes should survive for the next generation, and lower probability chromosomes should be restricted to transfer into the next generation. The next phase in the GA is crossover and mutation after selecting the higher fitness chromosomes. Thus, a collision-free and safe trajectory is determined with the aid of GA.

2.3 AI-Based Approximate Reasoning

Approximate Reasoning is the procedure or technique by which a probable vague end is deduced from a collection of imprecise premises. Fuzzy logic plays the principal position in approximate reasoning. It has the potential to cope with one-of-a-kind varieties of uncertainty. The prominent models are the Fuzzy-based and ANN-based models.

Fuzzy Inference System

Mandatory and discretionary lane changing models form the two Fuzzy Inference Systems (FIS) [16, 17]. When a car shifts from the left or middle lane to the right-most lane to exit an expressway, this is known as a forced or necessary lane shift. Mandatory lane change can also occur when a vehicle enters the parkway from an on-ramp and tries to drive to the middle or left lane to avoid a downstream exit lane. It is a microscopic manifestation of the macroscopic behaviour of route choice. Discretionary lane changing is also known as unrestricted lane changing or preferred lane changing. It can happen when a driver wants to speed up the pace or searches for more accessible surroundings, such as other lanes, before moving to the next lane. The motivations and ensuing riding behaviour for the two forms of lane alternate are distinctive. Therefore, a driving force is predicted to have one-of-a-kind choice guidelines and risk-taking behaviour for the two-lane change forms.

ANN-Based Approximate Reasoning

Artificial neurons are the set of related nodes that relatively present the structure of a biological brain. ANN is based on these artificial nodes. A connection between each node depicts the process of synapses, which is used in the biological brain to transmit signals between the neurons. The artificial neuron that is signalled may approach the other neurons to carry out the communication. ANN-based self-driving is used in [18] for driving an AV. Various driving techniques are acquired from human drivers. The motivation is twofold. The foremost one is that the AVs can get assistance from the expertise gained from human drivers' years of driving experience—secondly, a vivid perspective shared by the driver regarding the AV's behaviour on the lane.

The model comprises two main processing models, namely trajectory generator and trajectory controller. Learning-by-demonstration and a predictive control method are used as the framework for the same. A learn-by-demonstration model [18] is as shown in Fig. 4. The former generates commands that sense natural to the passengers. The latter ensures safety and balance by depending upon the decisions given out by the model-based predictions. The learning-based driver generates instructions reminiscent of a human motive force.

This model's two main peculiar features are the modification implemented on the conventional trajectory generator and the controller. A driver model is incorporated instead of using a trajectory planner. The driving force model uses the technique of learn with the aid of demonstration: it is trained using actual driving statistics shared by expert human drivers. It might generate instructions that imitate the human drivers' driving pattern on whose data the model was trained. The dependability of the reference command generated by the motion planner is inferred by deducing the confidence value. The confidence value would be high for the driving scenario that shares certain traits with the training data set.

The commands generated by the trajectory generator are fed into the trajectory controller model. The controller's position is to assure safety and trace the trajectory set by the reference command dispatched through the human driving model. When the safety conditions are met along with a high value of confidence, it can be inferred

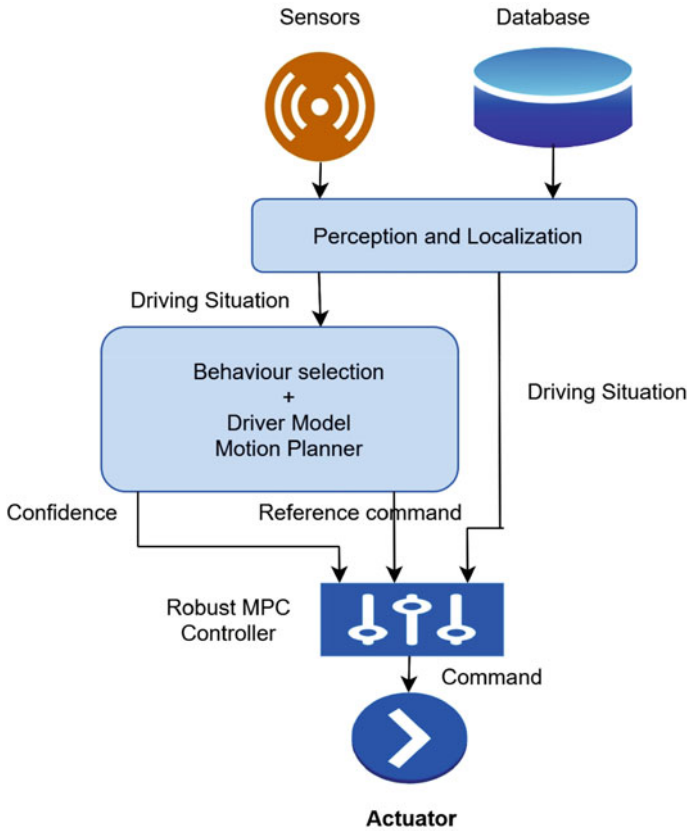


Fig. 4 A learn-by-demonstration model with ANN

that the command computed via the controller will suit the reference command. On the contrary, it can be deduced that there is a deviation in the reference command or any violation of the safety constraints for low confidence value.

A controller is designed to provide a balance to the deduced confidence value and to attain the required objectives. The controller directs the acceleration of the self-driving automobile. It aims to follow the human driver's reference acceleration while ensuring that the AV operates beneath the speed limit and no longer crashes into the preceding car. To ensure the AV is safe, a robust, MPC-based control strategy is implemented in this work. The predominant idea is to make sure the constraint is fulfilled for all possible realisations of the disturbance. Here, acceleration of the preceding automobile is considered as a bounded disturbance.

This approach can deal with normal driving conditions and unusual ones. The outcomes show that the proposed technique functions effectively and efficiently at the challenge for which it was designed, that is, to pick up the driving facts and imitate driving styles while making sure that its safety constraint is met.

Another ANN-based model is implemented in [18]. The main intention of using ANN in modelling self-driving vehicles is to develop a model to fit the driver's speed profiles under diverse driving situations. This study focuses on mastering human drivers' skills in navigating through sharp curves and turning at intersections while maintaining a velocity profile, where the speed limits cannot be determined directly from the map, and a large number of accidents occur.

Naturalistically, data on human drivers' experience and tactful driving skills in various driving situations were collected using GPS from six different locations. With 1 and 10 Hz frequencies, GPS records range, longitudes, and speed, while onboard sensor statistics such as Lateral and longitudinal acceleration and network velocity are collected. Up to eight targets in front of the vehicle can be detected using its radar sensor. A unique non-zero address is allocated for each target. After the data collection, it is to be fed into the ANN algorithm. It has the functionality of modelling complicated and ill-described relationships among entering and output variables. In model classification, clustering, forecasting, and optimisation, neural networks were widely used as they were robust and frequently used models. ANN models have the following advantages: precise fault-tolerant general performance for noisy and incomplete statistics, functionality to deal with complicated and non-linear disorders, and trained prototypes with accurate prediction and generalisation performance for huge interrelated factors.

For the variable selection, the variables ought to be defined cautiously. In this method, human drivers' driving patterns need to enhance AVs' speed control capability in curvy paths. It is impossible to include all the driver's traits and peculiar information about their driving styles in the model. Unlike prior studies, this technique examines the typical patterns of naturalistic driving records on a large scale. This system's final output no longer attempts to match the driver's mindset but imitates a driver group's typical patterns. This project's feasibility was determined by four highway parameters: curvature for each trajectory, maximum path curvature, end-state velocity, and relative longitudinal distance to the end state. Five prediction steps were added to this ANN-based model to produce five models, each of which was evaluated separately.

A three-layer ANN has been created with twenty hidden nodes [19] with the Levenberg–Marquardt learning algorithm. For the activation of the hidden layer and the output layer, a hyperbolic tangent sigmoid transfer feature and the linear transfer characteristic have been used. The suggested model can produce human-like speeds for curvilinear trajectories for a distinctive driving pattern, which can be predicted using the AV's higher level models. Therefore, the proposed model can capture human drivers' driving patterns for certain scenarios up to a few seconds, which can be explained with geometric track features, pedestrians on the avenue, directional features, and environmental conditions. A keen selection of the prediction length is crucial when implementing this model.

2.4 AI-Human-Like Convolutional Neural Network

The model used for the implementation of self-driving vehicles is intended to mimic human behaviour in the various decisions about driving that are highly crucial to make the AVs reliable and predictable. One of the most preferred algorithms among the neural network is the Convolutional Neural Network (CNN), which is best suited for image recognition and image classification. Object detections and recognition are the areas wherein CNNs are broadly used.

Due to its exceptional properties, CNN is preferred in [20, 21] to model an end-to-end learning approach for the self-driving automobile. A typical CNN model [20] is depicted in Fig. 5. Three cameras are hooked up at the back of the windshield automobile for the acquisition of data. Time-stamped video from the cameras is captured simultaneously with the steering perspective carried out through the human motive force. This steering command is acquired by tapping into the vehicle's Controller Area Network (CAN) bus. The guidance command is represented as the turning radius's reciprocal to make the system unbiased of the car geometry. CNN computes a steering command based on the images fed into the neural network. The predicted command is compared to the favoured command for that image, and the weights of the CNN are adjusted so that the predicted output from CNN converges to the desired outcome.

The weight adjustment is attained by the back-propagation technique as implemented in the Torch-7 ML package, where the training data is collected from various types of roads and diverse weather conditions. Weights of the network are trained in

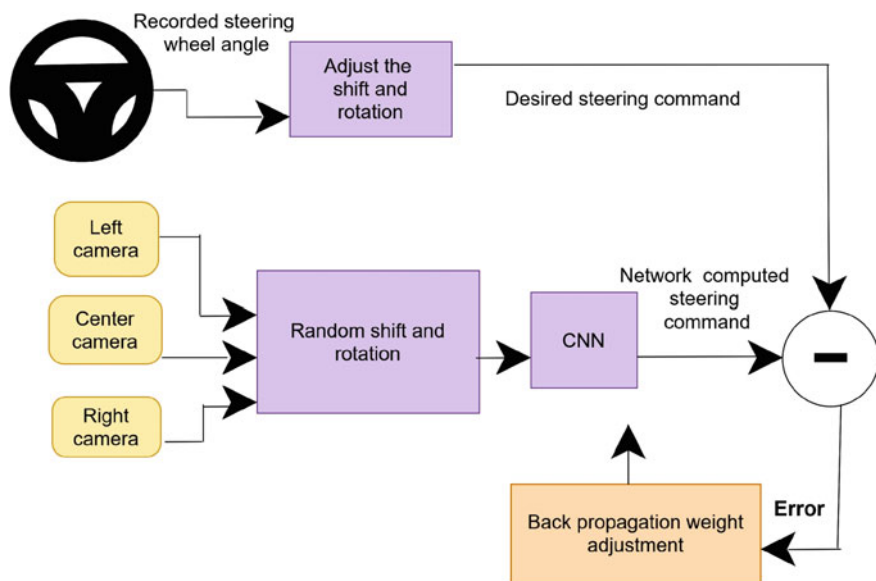


Fig. 5 Training the Neural Network-CNN model

such a way to reduce the mean square error between the network predicted steering command and the command of the human driver. In [20], the authors have designed a nine-layer network that comprises five convolutional layers, three fully connected layers, and a normalisation layer. The image normalisation is carried out in the first layer, and this layer is hardcoded and is not adopted in the learning process. Three are connected out of the five convolutional layers, determining the output control value that corresponds to the inverse turning radius. Though the fully connected layers are implemented to function as a controller to the steering command, it is barely possible to decide which subsystem of the network works as a feature extractor and operates as a controller.

During data acquisition, each collected data is labelled by considering its road conditions, driving activity, and weather. The first step in the training process is the selection of frames. The frames in which the driver occupies the central lane are considered, and the rest are discarded. After selecting the frames, the data is augmented with artificial shifts to improve poor position or orientation. To rate the simulation's efficiency performed by this CNN model, a metric called autonomy is deduced. It infers the percentage of the time the neural network could drive. Autonomy is calculated by the number of human interventions that occur during the simulation phase. It is estimated that about six seconds is required for the human to restore the control of the automobile, re-align it to the central lane, and resume the self-driving mode of operation. Without manual breakdown into road or lane marking recognition, semantic abstraction, path control and planning, CNNs can learn the entire process of lane and road following. Thus, the CNN can acquire relevant road attributes from a sparse training input. However, the robustness of the system and the visualisation of the processing steps need further improvement.

A comparative analysis between all the above-discussed algorithms is described in Table 4. The comparison is drawn w.r.t. the performance of the algorithm for highway driving.

3 Conclusion and Future Scope

The purpose of this literature review is to draw light on the prominent AI-based algorithms used for lane changing, lane following, and ensuring the safety of self-driving vehicles. This work does not claim to have collected information about all the algorithms present in this scope. Here, an effort is put to review methods that lead to the completion of modelling self-driving vehicles, which are level 4 or higher. A review of the generalised view and practical implementation of each approach is briefly discussed. It can be observed that as the model algorithm imitates human intelligence, it is more likely to acquire an AV of level 5, which would be capable of making decisions even in uncertain and extreme road/traffic conditions. Pedestrian interaction and vehicle dynamics must be considered as the critical parameters while modelling the

Table 4 Comparative analysis of the AI-ML algorithms towards lane changing ('H' = High, 'M' = Moderate, and 'L' = Low)

AI-ML algorithms	Ease of modelling	Adaptive	Real-time	Robust	Ability to handle vagueness	Computational cost and time
Rule-based [2, 3]	M	L	L	L	L	L
Decision Tree [4–9]	M	L	L	M	L	H
MDP [10, 11]	M	H	M	M	H	H
SVM [12]	H	M	M	L	L	L
Genetic Algorithm [13–15]	M	H	H	M	L	L
Fuzzy-Logic [16, 17]	L	M	M	M	H	H
ANN [18, 19]	L	H	H	H	M	H
CNN [20, 21]	L	H	H	H	H	H

lane changing algorithms. Incorporating an adaptive proportional–integral–differential controller can make the lane changing algorithm more reliable. Further evaluation of AVs' performance, practical situations, and compatibility analyses with human-driven vehicles can contribute to this area.

References

1. Claussmann L, Revilloud M, Gruyer D, Glaser S (2019 May 15) A review of motion planning for highway autonomous driving. *IEEE Trans Intell Transp Syst* 21(5):1826–1848
2. Nilsson J, Fredriksson J, Coelingh E (2015) Rule-based highway maneuver intention recognition. In: 18th IEEE international conference on intelligent transportation systems. IEEE, pp 950–955
3. Nilsson J, Silvlin J, Brannstrom M, Coelingh E, Fredriksson J (2016) If, when, and how to perform lane change maneuvers on highways. *IEEE Intell Transp Syst Mag* 8(4):68–78
4. Claussmann L, Carvalho A, Schildbach G (2015) A path planner for autonomous driving on highways using a human mimicry approach with binary decision diagrams. In: European control conference (ECC). IEEE, pp 2976–2982
5. Gray A, Gao Y, Lin T, Hedrick JK, Tseng HE, Borrelli F (2012) Predictive control for agile semi-autonomous ground vehicles using motion primitives. In: American Control Conference (ACC). IEEE, pp 4239–4244
6. Li L, Wang FY (2002) The automated lane-changing model of intelligent vehicle highway systems. In: 5th IEEE International conference on intelligent transportation systems. IEEE, pp 216–218
7. Carvalho A, Gao Y, Gray A, Tseng HE, Borrelli F (2013) Predictive control of an autonomous ground vehicle using an iterative linearisation approach. In: 16th International IEEE conference on intelligent transportation systems (ITSC 2013). IEEE, pp 2335–2340

8. Gao Y, Gray A, Frasch JV, Lin T, Tseng E, Hedrick JK, Borrelli F (2012) Spatial predictive control for agile semi-autonomous ground vehicles. In: 11th International symposium on advanced vehicle control, No. 2, pp 1–6
9. Li N, Chen H, Kolmanovsky I, Girard A (2017) An explicit decision tree approach for automated driving. In: Dynamic systems and control conference, vol 58271, pp V001T45A003. American Society of Mechanical Engineers
10. Zhou S, Wang Y, Zheng M, Tomizuka M (2017 Jul 1) A hierarchical planning and control framework for structured highway driving. *IFAC-PapersOnLine* 50(1):9101–9107
11. Lefevre S, Carvalho A, Borrelli F (2015 Nov 24) A learning-based framework for velocity control in autonomous driving. *IEEE Trans Autom Sci Eng* 13(1):32–42
12. Vallon C, Ercan Z, Carvalho A, Borrelli F (2017) A machine learning approach for personalised autonomous lane change initiation and control. In: IEEE intelligent vehicles symposium (IV). IEEE, pp 1590–1595
13. Onieva E, Naranjo JE, Milanés V, Alonso J, García R, Pérez J (2011 Jan 1) Automatic lateral control for unmanned vehicles via genetic algorithms. *Appl Soft Comput* 11(1):1303–1309
14. Nearchou AC (1999) Adaptive navigation of autonomous vehicles using evolutionary algorithms. *Artif Intell Eng* 13(2): 159–173
15. Riaz F, Niazi MA, Sajid M, Amin S, Ratyal NI, Butt F (2015) An efficient collision avoidance scheme for autonomous vehicles using genetic algorithm. *J Appl Environ Biol Sci* 5(8):70–76
16. Balal E, Cheu RL, Sarkodie-Gyan T (2016) A binary decision model for discretionary lane changing move based on fuzzy inference system. *Transp Res Part C Emerg Technol* (67): 47–61
17. Wang X, Fu M, Ma H, Yang Y (2015) Lateral control of autonomous vehicles based on fuzzy logic. *Control Eng Pract* 34:1–7
18. Ziegler J, Bender P, Schreiber M, Latégahn H, Strauss T, Stiller C, Dang T, Franke U, Appenrodt N, Keller CG, Kaus E (2014) Making bertha drive—an autonomous journey on a historic route. *IEEE Intell Transp Syst Mag* 6(2):8–20
19. Geng X, Liang H, Xu H, Yu B, Zhu M (2016) Human-driver speed profile modeling for autonomous vehicle’s velocity strategy on curvy paths. In: IEEE intelligent vehicles symposium (IV). IEEE, pp 755–760
20. End to end learning for self-driving cars. <https://arxiv.org/abs/1604.07316>. Accessed Jan 2021
21. Hu C, Wang Y, Yu G, Wang Z, Lei A, Hu Z (2018) Embedding CNN-based fast obstacles detection for autonomous vehicles. SAE Technical Paper

An Automatic Indian Traffic Signs Detection and Recognition System Using OpenCV



Chinmay Srinivas and Sharanbassappa S. Patil

Abstract The main objective of this research is to develop an automatic Indian traffic signs detection and recognition (TSDR) system which is fast and efficient for real-time implementation in autonomous vehicles. A TSDR system is an essential component of autonomous vehicles and a fast algorithm is necessary for its implementation in a real-time environment. This paper presents a TSDR system developed using Open Source Computer Vision Library (OpenCV) which includes two working stages: traffic sign detection and traffic sign recognition. A robust shape and colour-based approach is adapted for the detection of traffic signs. Image processing techniques such as image thresholding, Gaussian filter, contour detection and RGB color segmentation have been applied for traffic sign detection. The detected traffic signs are classified based on the shape and color properties of the Indian traffic signs and recognized by region of interest (ROI) segmentation based on feature matching. The developed technique is efficient in detecting and recognizing traffic signs with complex natural backgrounds under various lighting conditions and requires a low processing time of 0.30 s, allowing for real-time applications.

Keywords Traffic sign detection and recognition · Autonomous vehicles · Image processing · OpenCV

1 Introduction

Traffic sign detection and recognition (TSDR) systems can detect and recognize traffic signs from the images captured by cameras or imaging sensors. TSDR is an essential component of autonomous vehicles and advanced driver assistance systems (ADAS). In the context of autonomous vehicles, object and event detection and

C. Srinivas (✉)

PES University, Bengaluru, Karnataka 560085, India

e-mail: chinmay1567@gmail.com

S. S. Patil

Department of Mechanical Engineering, PES University, Bengaluru, Karnataka 560085, India

e-mail: sspatil@pes.edu

© The Author(s), under exclusive license to Springer Nature Singapore Pte Ltd. 2022

185

V. Krishna et al. (eds.), *Recent Advances in Hybrid and Electric Automotive*

Technologies, Lecture Notes in Mechanical Engineering,

https://doi.org/10.1007/978-981-19-2091-2_15

response (OEDR) is the ability to detect objects and events that immediately affect the driving task and to react to them appropriately. According to the SAE standard J3016 [1], driving automation of level 3 and higher requires the automated driving system (ADS) to perform the OEDR. Detection and recognition of static objects such as traffic signs is an important goal for perception, a crucial part of OEDR. Hence, a TSDR system is essential for the development of a fully autonomous vehicle.

In a traffic environment, a TSDR system is used to warn the driver and command or prohibit certain actions. An accurate TSDR system is important for ensuring the appropriate response of the vehicle to the traffic sign. For example, detection of a stop sign at an intersection is critical for stopping the vehicle at the intersection for safe maneuvering. Another response could be adjusting the vehicle's speed according to the detected speed limit. In the current era of autonomous vehicles, TSDR systems can establish strict regulation of traffic laws by following the regulatory signs and quickly responding to cautionary signs, assuring the safety of occupants as well as pedestrians.

For implementation in real-time environments, TSDR systems must have a fast algorithm and shouldn't be erroneous to avoid false sign detection. It should also be highly reliable and efficient considering the environmental constraints including lighting, weather conditions as well as additional image distortions such as motion blur. This research aims to develop an automatic Indian traffic signs detection and recognition system which is fast and efficient for real-time implementation in autonomous vehicles. The proposed TSDR system is based on shape detection, color segmentation, traffic sign classification and region of interest (ROI) segmentation developed using Open-Source Computer Vision Library (OpenCV) [2].

2 Methodology

The first work on an automatic TSDR system can be dated back to 1984 in Japan according to [3]. Following this many attempts were made by different researchers to develop an efficient TSDR system using several methods. Different shape-based approaches such as Hough Transformation [4], Similarity Detection [5] and colour-based approaches such as HSI/HSV Transformation [6] and Colour Indexing [7] are used by the researchers to detect the ROI. However, the identification of traffic signs having various complex natural backgrounds remains a challenging task in the field of image processing. OpenCV, Scikit-image, SciPy and Pillow are a few of the widely used libraries for image processing. OpenCV package for Python is used here as it includes highly optimized algorithms for real-time computer vision applications. OpenCV has over 2500 optimized algorithms which can be applied for detecting faces, identifying and tracking objects, augmented reality and more.

The developed TSDR system can be divided into mainly two stages: traffic sign detection and traffic sign recognition. Extraction of the region of interest (ROI), i.e., the region in which a traffic sign is found is the primary goal of traffic sign detection. To achieve this, the acquired image is first pre-processed by image smoothing for



Fig. 1 a Methodology b input test image, c sign detection, d sign recognition

removing noise. Then, a shape and colour-based approach is adapted to detect the traffic sign. Once a traffic sign is detected, it is classified based on the identified shape and color characteristics.

In the sign recognition stage, the detected sign is firstly classified based on its shape and color properties. Then certain ROI segments of the detected sign are compared with all possible traffic signs in the identified class. If a sign is matched and verified, the recognized traffic sign is the output of the TSDR system. Figure 1 gives an overview of the TSDR system methodology for an image taken in broad daylight containing a speed breaker-ahead sign.

3 Traffic Sign Detection

The first stage in the developed TSDR system is traffic sign detection. The algorithm implemented here for the traffic sign detection is shown in Fig. 2. Firstly, the image input or a frame from a video sequence is fed into the system. The image data is then read with OpenCV both in color and in grayscale. NumPy library in Python is used in conjunction with OpenCV to store this image data in a Numpy array which contains information on every pixel in the image. In each color-space, the pixel values range from 0 to 255. The grayscale image is the source image for shape detection and the color image is used for color segmentation. Before the images are processed, image smoothing is performed with a Gaussian filter to remove noise and enhance the image to obtain the required region. For shape detection, the grayscale image is first converted into a binary image by the binary thresholding method. The threshold is the criterion to change an image from grayscale to binary image. If the pixel value

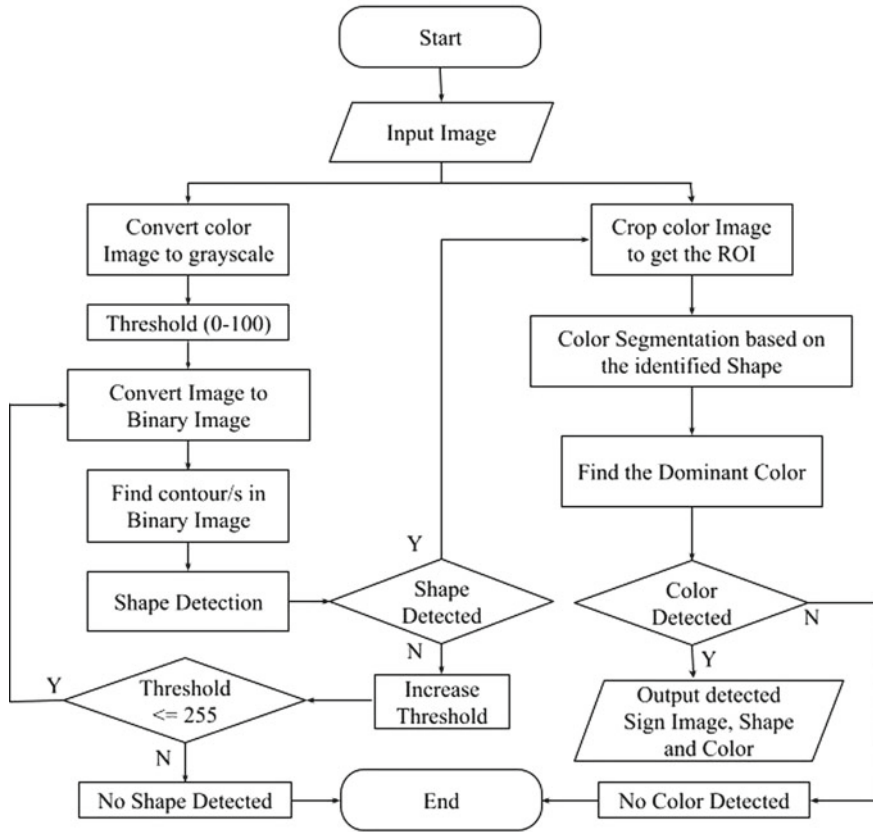


Fig. 2 The overall block diagram of the traffic sign detection system

is smaller than the threshold, it is set to 0 (black) otherwise, it is set to 255 (white). The binary image is used to find contours for shape detection.

If a sign shape is detected, the region of interest (ROI) is determined and the color segmentation process continues. However, when a sign shape is not detected, the value of the threshold is increased and the conversion of grayscale image to binary image is done using this new threshold. This process is repeated until a shape is detected or the threshold value reaches its maximum, i.e., 255 which implies that no traffic sign shape has been detected in the image. This process ensures that a sign shape is detected under different lighting conditions. Once the ROI is found, the color image is cropped and processed with color segmentation based on the identified traffic sign shape. If the shape and color of the traffic sign are identified, the traffic sign detection stage is concluded. The flow charts of the algorithm for shape detection and color segmentation are shown in Figs. 3 and 4.

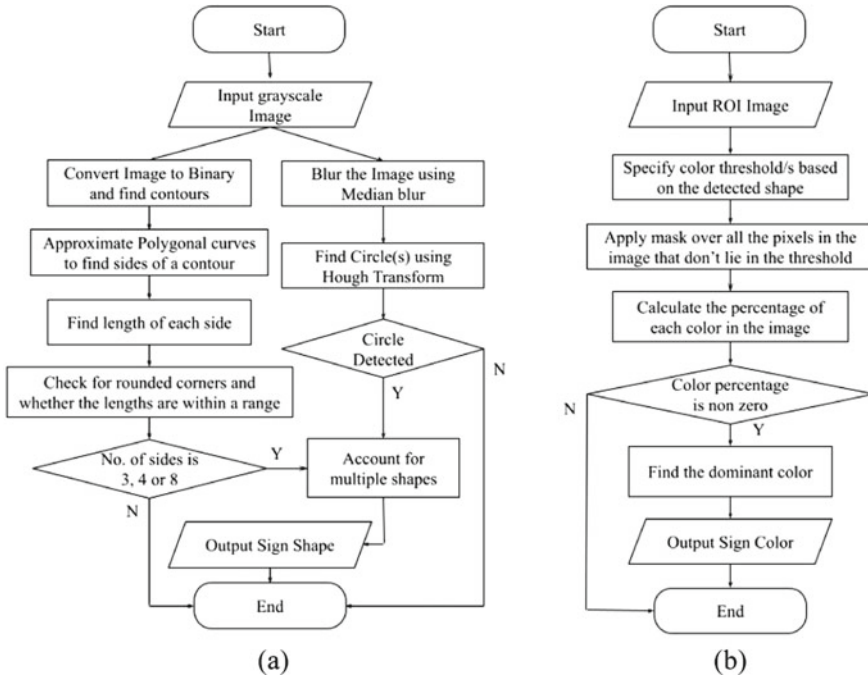


Fig. 3 Flow charts of **a** shape detection, **b** color segmentation

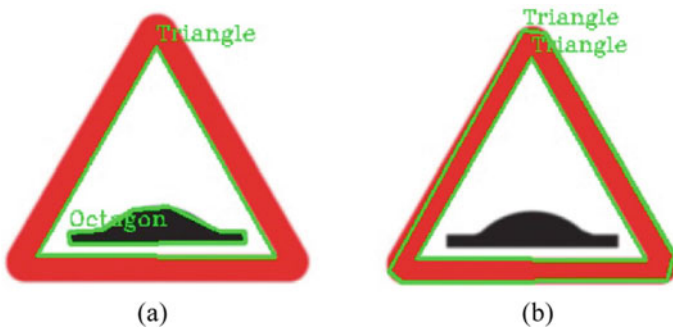


Fig. 4 Speed breaker sign shape detection **a** only according to the number of sides **b** after accounting for rounded corners and equal lengths

3.1 Shape Detection

The shape detection algorithm followed is shown in Fig. 3a. Traffic sign shapes include triangle, rectangle, octagon and circle. The traffic sign shapes triangle, rectangle and octagon can be identified by detecting the contours in an image. The contours are retrieved from the binary image as a NumPy array containing the x and

y coordinates of boundary points of each contour. The detected contours are approximated to polygonal curves which can be considered as the sides of the contour. The sign shape is determined based on the number of sides obtained. For the purpose of detecting circular sign shape, the Hough transform method is used. A median blur filter is applied to the grayscale image for accurate detection of circles.

Traffic signs have rounded corners in their outer boundary which could be falsely detected as a side. To account for this, the sides whose lengths are very much lesser compared to the average lengths of all the sides are ignored. Also, triangle and octagon sign shapes have sides of equal lengths. Hence, for more accurate shape detection, it is checked whether each of the side's length lies within a range determined by the average length of all the sides. Finally, if multiple shapes are detected in an image, the shapes whose boundaries are within the boundaries of another shape are eliminated.

3.2 Color Segmentation

Color segmentation is required to identify whether the detected sign shape contains a particular color. The algorithm used for color segmentation is shown in Fig. 3b. Based upon the identified shape, a list of boundaries is defined in the RGB color-space pertaining to the color which is to be detected. The traffic sign colors that are considered here are red, blue and yellow. A binary mask is created using the ROI image where the pixels that fall into the upper and lower limit range in the boundary are represented as white pixels (255), otherwise as black pixels (0).

In the binary mask, the white pixels represent the pixels that are of the required color. Using the binary mask, the percentage fraction of white pixels is found with respect to the total number of pixels, which is referred to here as color percentage. If there is a possibility of signs with different colors having the same detected shape, color segmentation is performed for all the individual colors and the dominant color, i.e., the color having the highest color percentage is selected as the sign color.

Figure 5 shows the combined shape detection and color segmentation process for an image of a stop sign taken during night time.

4 Traffic Sign Recognition

Traffic sign recognition is the second and final stage of TSDR. The shape and color of the detected traffic sign along with the ROI from the first stage is the input. The traffic sign recognition is based on the classification of the detected traffic sign and ROI segmentation-based matching. The proposed TSDR system is developed to recognize some of the common traffic signs found on Indian roads as listed in Table 1.

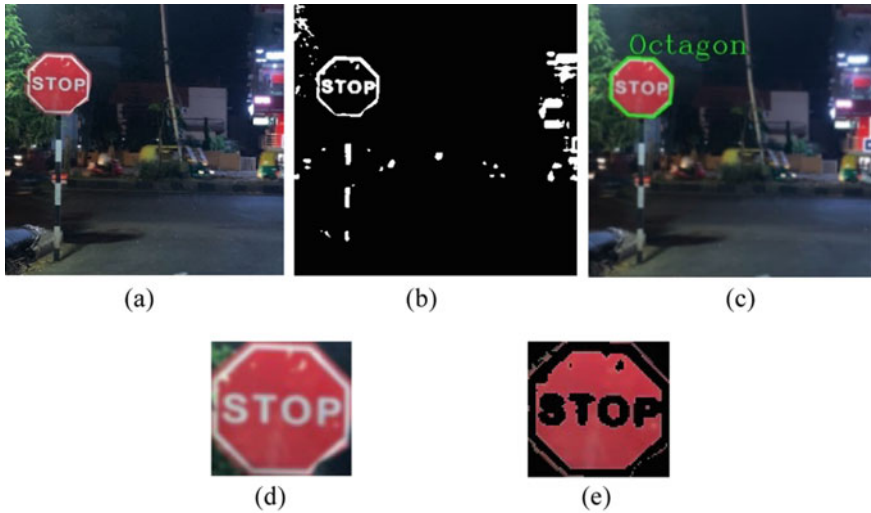


Fig. 5 Stop sign detection **a** input image, **b** binary image, **c** shape detection, **d** ROI, **e** color segmentation (red)

4.1 Indian Traffic Signs Characteristics and Classification

The detected traffic sign is categorized into different classes based on its shape and color since there could be multiple traffic signs having the same shape and color properties. These are circular and blue signs, triangular and red signs, rectangular and yellow signs having 4, 3 and 2 possible traffic sign matches as seen in Table 1.

4.2 ROI Segmentation and Matching

After the classification of the detected traffic sign, ROI segments are defined based on this identified class. The segments for each class are shown in Fig. 6. These segments are defined to extract the features of the sign in particular regions for feature matching. The ROI image is converted to a binary image by thresholding. The fraction of white pixels to the total number of pixels is found for each segment in the ROI. These fractions corresponding to each segment of the ROI are compared to the fractions of the respective segment in all possible traffic signs of the identified class. If all the segments of the ROI match with any of the possible traffic sign, then the detected traffic sign is thus recognized as the matched traffic sign.

For the recognition of speed limit signs, the numerical digits on the sign need to be read and extracted. Therefore, optical character recognition (OCR) of the detected ROI is achieved using the Pytesseract OCR library in Python. OCR is also helpful for extracting text from informative signs. Figure 7 shows the detection and recognition

Table 1 Indian traffic signs classification

Traffic sign	Name	Shape	Color	Type
	Stop	Octagon	Red	Regulatory
	Speed limit	Circle	Red	Regulatory
	Compulsory Straight Ahead	Circle	Blue	Regulatory
	Compulsory Right Turn	Circle	Blue	Regulatory
	Compulsory Left Turn	Circle	Blue	Regulatory
	Keep Left	Circle	Blue	Regulatory
	Right-Hand Curve	Triangle	Red	Cautionary
	Left-Hand Curve	Triangle	Red	Cautionary
	Speed Breaker	Triangle	Red	Cautionary
	Dangerous Right Turn	Rectangle	Yellow	Cautionary
	Dangerous Left Turn	Rectangle	Yellow	Cautionary

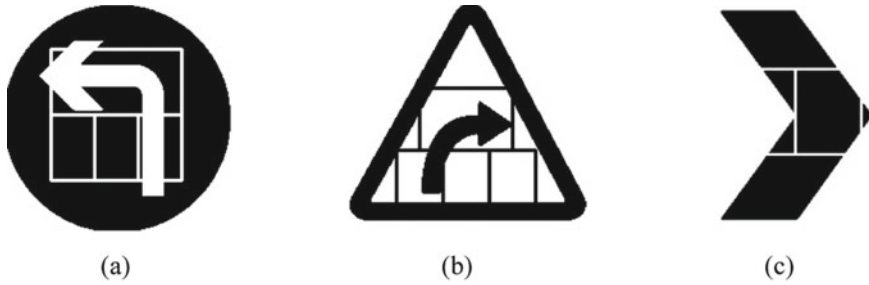


Fig. 6 Binary image ROI segments for **a** circular and blue signs, **b** triangular and red signs, **c** rectangular and yellow signs

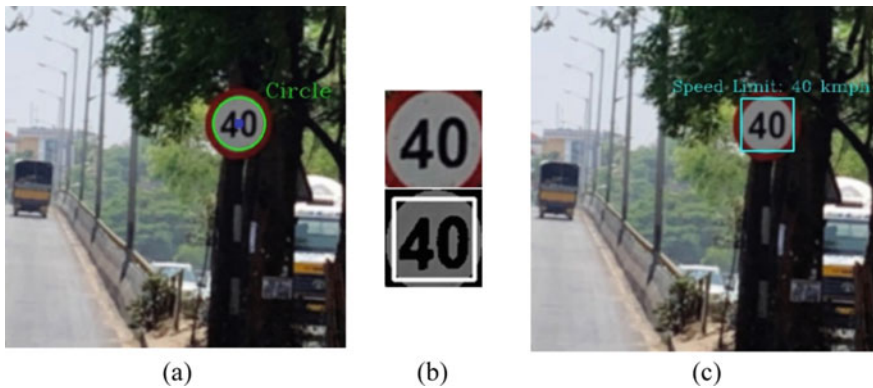


Fig. 7 Speed limit sign recognition **a** detected traffic sign of circular shape and red color, **b** ROI and ROI segment used for OCR, **c** recognized speed limit sign

of a speed limit sign situated under the shade with a complex natural background.

5 Results and Conclusion

In order to test the performance of the developed TSDR system, the images of traffic signs are resized to 150×150 pixels to reduce the computational complexity and fed to the system. The tests were performed using a 2.5 GHz Intel i5 processor. The resulting processing time required for the detection and recognition of each traffic sign is shown in Table 2.

The overall processing time of the developed TSDR system is 0.3 s. This result is compared with several existing TSDR systems in Table 3, which use different methods and detection features for traffic sign detection and recognition. A few methods that are commonly used are support vector machine (SVM) [8, 9] and

Table 2 Processing time for detection and recognition of traffic signs

Traffic sign name	Processing time (seconds)
Stop	0.1984
Speed limit	0.8927
Compulsory straight ahead	0.2656
Compulsory right turn	0.2154
Compulsory left turn	0.2235
Keep left	0.2758
Right-hand curve	0.1765
Left-hand curve	0.1260
Speed breaker	0.1645
Dangerous right turn	0.3249
Dangerous left turn	0.3156

Table 3 Comparison of TSDR systems that use different methods

References	Method	Detection feature	Processing time (s)
[8]	SVM	YCbCr and normalized cross correlation	0.2
[9]	SVM	Color segmentation and shape matching	0.43
[10]	ANN	Adaptive shape analysis	0.6
Proposed method	ROI segments matching and OCR	Shape detection and RGB color segmentation	0.3

artificial neural network (ANN) [10]. It can be observed that the processing time of the proposed method is lower than [9] and [10] and slightly higher than [8]. Hence, compared with other TSDR systems, the average processing time of 0.30 s in the proposed method is good.

This work discussed the development of an automatic Indian traffic signs detection and recognition system which is fast and efficient for real-time implementation in autonomous vehicles. A robust shape and colour-based approach is adapted for the detection of traffic signs. Image processing techniques such as image thresholding, Gaussian filter, contour detection and RGB color segmentation have been applied for traffic sign detection. The detected traffic signs are classified based on the shape and color properties of the Indian traffic signs and recognized by ROI segmentation-based feature matching. The developed TSDR system has shown promising results and is efficient in detecting and recognizing traffic signs with complex natural backgrounds and under various lighting conditions. The proposed method is fast and has a low average processing time of 0.30 s, allowing for real-time applications.

References

1. SAE Standard J3016: Taxonomy and definitions for terms related to driving automation systems for on-road motor vehicles. https://www.sae.org/standards/content/j3016_202104 (2021). Accessed 16 Oct 2021
2. OpenCV Homepage. <https://opencv.org>. Accessed 23 Oct 2021
3. Paclik P, Novovicova J, Duijn RPW (2006) Building road-sign classifiers using a trainable similarity measure. *IEEE Trans Intell Transp Syst* 7(3):309–321
4. Møgelmoose A, Trivedi MM, Moeslund TB (2012) Vision-based traffic sign detection and analysis for intelligent driver assistance systems: perspectives and survey. *IEEE Trans Intell Transp Syst* 13(4):1484–1497
5. Vitabile S, Pollaccia G, Pilato G, Sorbello E (2001) Road signs recognition using a dynamic pixel aggregation technique in the HSV color space. In: Proceedings of the 11th international conference on image analysis and processing (ICIAP '01), Palermo, Italy, pp 572–577
6. Tagunde GA, Uke NJ (2012) Detection, classification and recognition of road traffic signs using colour and shape features. *Int J Adv Technol Eng Res* 2(4):202–206
7. Swain MJ, Ballard DH (1991) Color indexing. *Int J Comput Vision* 7(1):11–32
8. Hechri A, Mtibaa A (2021) Automatic detection and recognition of road sign for driver assistance system. In: Proceedings of the 2021 16th IEEE mediterranean electrotechnical conference (MELECON), Yasmine Hammamet, Tunisia, pp 888–891
9. Wali SB, Hannan MA, Hussain A, Samad SA (2015) An automatic traffic sign detection and recognition system based on colour segmentation, shape matching, and SVM. *Math Problm Eng*
10. Fištrek T, Lončarić S (2011) Traffic sign detection and recognition using neural networks and histogram based selection of segmentation method. In: Proceedings of the 2011 ELMAR, Zadar, Croatia, pp 51–54

A Waypoint Tracking Controller for Autonomous Vehicles Using CARLA Simulator



Chinmay Srinivas and Sharanbassappa S. Patil

Abstract The main objective of this work is the development and testing of a waypoint tracking controller for autonomous vehicles. The waypoint tracking controller is developed in Python and tested using CARLA Simulator, an open-source simulator for autonomous driving research. The waypoint tracking controller is developed by implementing a PID controller for longitudinal control and a pure pursuit controller for lateral control. The PID gains are tuned to precisely track the reference speed profile. The pure pursuit controller is implemented to accurately follow the desired path. The developed controller is tested in CARLA Simulator and the simulation results indicate that the vehicle tracks 100% of the waypoints specified in the trajectory. The waypoint tracking controller also performs well in closely tracking the reference speed profile. The developed waypoint tracking controller is precise and suitable for application in autonomous vehicles for urban driving environments

Keywords Waypoint tracking controller · Autonomous vehicles · Autonomous driving simulation · CARLA simulator

Nomenclature

v	Actual speed
v_d	Desired speed
u	Acceleration
KP	Proportional gain
KI	Integral gain

C. Srinivas (✉)
PES University, Bengaluru, Karnataka 560085, India
e-mail: chinmay1567@gmail.com

S. S. Patil
Department of Mechanical Engineering, PES University, Bengaluru, Karnataka 560085, India
e-mail: sspatil@pes.edu

KD	Derivative gain
TP	Throttle position
BP	Brake position
δ	Steering angle
ld	Look-ahead distance

1 Introduction

Autonomous vehicles are the future of mobility and they are changing the way people think about travel. They can bring about a significant improvement in road safety and provide mobility for everyone while drastically reducing the cost of driving. A fully autonomous vehicle requires the automated driving system (ADS) to entirely perform the dynamic driving task (DDT) [1]. The driving task consists mainly of three sub-tasks namely perception, motion planning and vehicle control. Perception involves perceiving the driving surroundings including tracking and predicting a vehicle's motion, recognizing various elements such as road surface, road signs, vehicles and pedestrians. Motion planning contributes to defining the path or trajectory which can be tracked to reach the destination successfully. Finally, vehicle control is responsible for taking the appropriate steering, acceleration and braking decisions to control the vehicle's position, orientation and velocity.

At any point in time, the appropriate driving behaviour is decided by interpretation of the estimated vehicle pose and information on the current scene, obtained from the various on-board sensors such as GPS/IMU units, odometry, cameras and LIDARs. The driving behaviour which needs to be accomplished in the current situation is translated into a path or a trajectory, defined by a sequence of future waypoints that the vehicle should track. The generated waypoints can be tracked precisely by implementing a waypoint tracking controller. The waypoint tracking controller includes longitudinal and lateral control of the vehicle. In the developed waypoint tracking controller, a PID controller and a pure pursuit controller are implemented for longitudinal and lateral control, respectively.

A robust control system allows for safe and precise execution of the planned movements. For specified path waypoints and reference speed specifications, the vehicle should be able to track the specified path with minimum error. Vehicle dynamics, feasibility and comfort must be considered by the controller to precisely track the waypoints and follow the required trajectory. The objective of this work is to develop and simulate a waypoint tracking controller for autonomous vehicles. The developed waypoint tracking controller is programmed in Python [2] and tested using the hyper-realistic CARLA Simulator [3], an open-source simulator for autonomous driving research.

2 Controller Design

Navigating an autonomous vehicle to a specified destination requires motion planning and vehicle control. Currently, many applications such as OpenDRIVE [4] and OpenStreetMaps [5] provide the tools for the effortless creation of maps for navigation. Route planning provides a path to a specific destination that should be tracked by the path tracking controller for successfully reaching that destination. A vehicle state estimator uses a GPS-based positioning system, inertial measurement unit (IMU) and wheel odometer to estimate the current position, orientation and velocity of the vehicle. The role of the controller then is to regulate these states of the vehicle by generating appropriate actuator signals based on the desired and currently estimated states (Fig. 1).

A waypoint tracking controller obtains a set of path waypoints and reference speed specifications along with the estimated state of the vehicle as inputs and generates the vehicle control signals as outputs. The waypoint tracking controller is further comprised of two controllers, a longitudinal controller and a lateral controller. The longitudinal controller regulates the vehicle's longitudinal motion via throttle or braking whereas the lateral controller regulates the vehicle's lateral motion via steering.

Some of the basic controllers such as proportional integral and derivative (PID) controller [6] or a combination of feedback and feedforward controller [7] can be employed for longitudinal control. For lateral control, the most popular controllers are the geometric ones such as pure pursuit [8] and Stanley [9] controllers. Also, advanced applied control strategies like model predictive control (MPC) [10] can be incorporated for joint longitudinal and lateral control. In the developed waypoint tracking controller, a PID controller and a pure pursuit controller are employed for longitudinal control and lateral control, respectively.

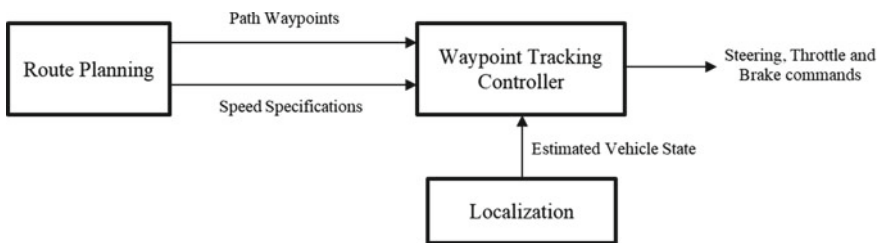


Fig. 1 General navigation architecture of an autonomous vehicle

2.1 Waypoints and Reference Speed Profile

The RaceTrack map in CARLA Simulator is chosen for the deployment of the waypoint tracking controller. A starting point and destination are selected in this track and the roadway between these two points is taken as the path that must be tracked. This path is defined by equally spaced waypoints that are stored in a sorted list. In this track, a total of 1724 waypoints are defined which are equally spaced at 1 m apart along the path. Each of the waypoints includes their positions defined by the x and y coordinates, as well as the speed which the vehicle should attain. Hence, the waypoints become the reference signal for the waypoint tracking controller and navigating through all the waypoints effectively completes the full path.

The set of waypoints is updated as the vehicle progresses on the path by finding the nearest waypoint. The controller directly uses the next waypoint in the path for implementing vehicle control. At higher speeds, the controller performs better with a continuous path. Since the waypoints are discrete, interpolating between each waypoint will reduce the spacing between each waypoint and provide a finer resolution path. The linear interpolation method is adopted to generate a smoother path and reference speed profile (Fig. 2).

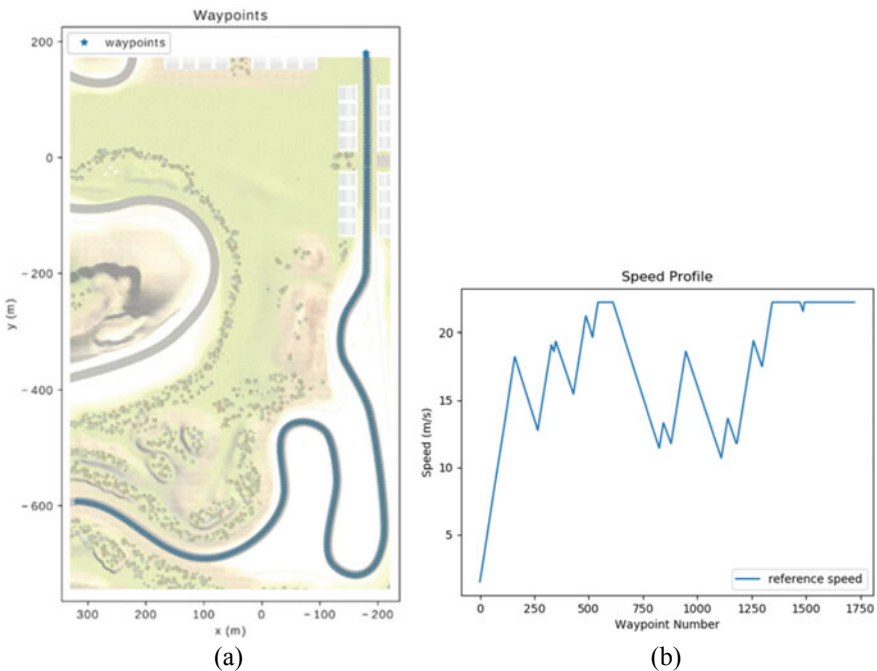


Fig. 2 Track used for simulation: a path waypoints b reference speed profile

2.2 Longitudinal Control

The longitudinal controller regulates the vehicle’s longitudinal motion by applying throttle or brake. A well-known example of longitudinal control is cruise control. A cruise control system performs the function of maintaining a fixed reference speed as well as accelerating or decelerating to a new desired speed using throttle and brake commands. A typical longitudinal controller can be split into two levels, an upper level controller and a lower level controller. Based on the speed error, i.e., the difference between the desired speed and the vehicle’s actual speed, the upper level controller determines the acceleration needed at each time step to match the desired speed. The lower level controller generates the throttle or braking actuation to track the desired acceleration (Fig. 3).

The developed waypoint tracking controller uses a PID controller for longitudinal control. The desired speed is fed to this PID controller as a reference and it outputs the throttle and brake commands for actuation. In urban environments, assuming that the desired speed is reasonably low and stable, the lower level controller is completely overridden (Fig. 4).

The PID controller includes three gain terms. First, a proportional gain term K_P multiplies the acceleration of the vehicle with a magnitude proportional to the speed error, ensuring that the vehicle accelerates in the right direction. Second, an integral gain term K_I considers the previously accumulated speed errors to make certain the steady-state errors are removed in the output. Finally, the derivative gain term K_D reduces the settling time by damping the overshoot caused by the integration term based on the rate of change of speed errors. The acceleration of the vehicle given by the PID controller output is,

$$u = K_P(v_d - v) + K_I \int_0^t (v_d - v)dt + K_D \frac{d(v_d - v)}{dt} \tag{1}$$

Proper selection of the PID gains is critical for precise tracking of the desired speed.

A good PID controller response should have minimal overshoot and steady-state error with a low rise time and settling time. The comparison between the response of a P, PD and PID controller is shown in Fig. 5. The P controller has a higher overshoot

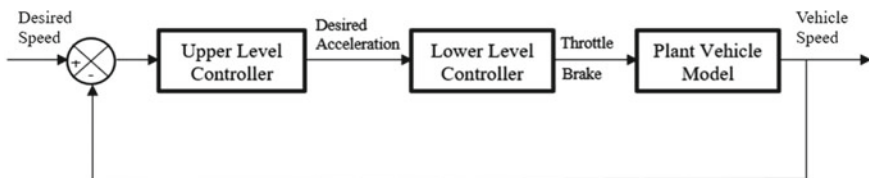


Fig. 3 Longitudinal control system

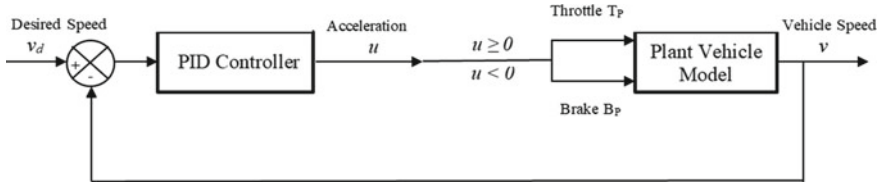


Fig. 4 Longitudinal controller implemented in the waypoint tracking controller

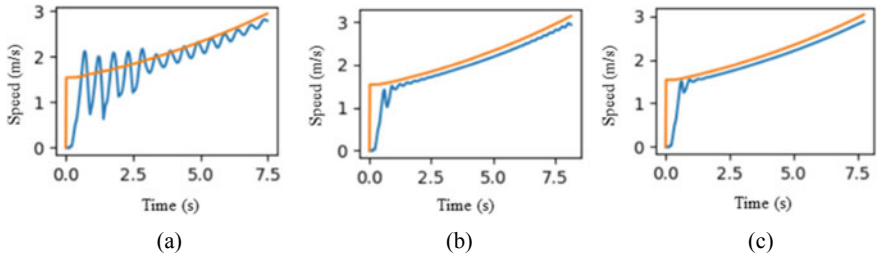


Fig. 5 Longitudinal controller response: a P controller b PD controller c PID controller

and a longer settling time than PD and PID controllers. But the PD controller has a slightly larger steady-state error than the PID controller. Hence, the PID controller performs better in precisely tracking the desired speed.

Finally in the longitudinal controller, the PID controller output, i.e. the obtained acceleration value is converted into throttle and brake commands. To generate the throttle and brake actuation signals, the throttle and brake outputs are clamped between 0 and 1. The positive acceleration outputs correspond to throttle and negative acceleration outputs correspond to brake. The throttle and brake outputs of the longitudinal controller can be written as,

$$\text{If } u \geq 0 : T_P = u, B_P = 0 \tag{2}$$

$$\text{If } u < 0 : T_P = 0, B_P = -u \tag{3}$$

2.3 Lateral Control

The lateral controller regulates the vehicle’s lateral motion via steering. A type of lateral controller is the geometric path tracking controller. Assuming the no-slip condition is true at the wheels, the geometric path tracking controller ignores dynamic forces on vehicles. This controller depends on a kinematic bicycle model to create and regulate the steering commands for path tracking. However, this approach cannot

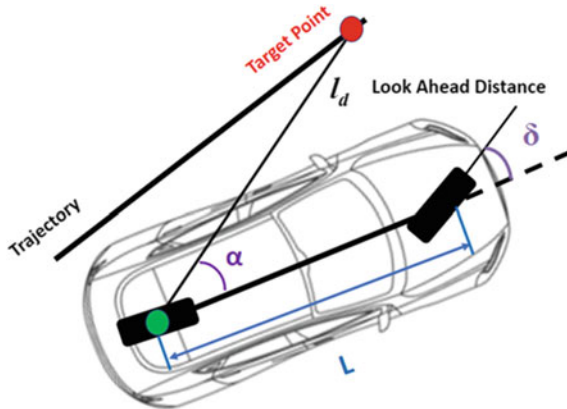


Fig. 6 Pure pursuit method for geometric path tracking

be applied for aggressive driving and manoeuvres with high lateral acceleration as its accuracy declines once the no-slip assumption doesn't hold true. Hence this controller is more suitable for driving in urban environments.

The waypoint tracking controller uses a pure pursuit controller which is a geometric path tracking controller for lateral control (Fig. 6). In the pure pursuit method, the centre of the rear axle in the vehicle is taken as the reference point and at a fixed distance from this point, a target point is determined on the path. This fixed distance is termed as the look-ahead distance (l_d). The angle between the line connecting these two points and the heading of the vehicle is called as alpha (α). Based on this the constant steering angle required to meet the target point is calculated. This steering angle is then finally converted into steering commands that must be followed by the vehicle to accurately track the path. While the vehicle heads towards the desired path, the target point also shifts ahead on the path and thus gradually reduces the steering angle. This allows for a safe and gentle manoeuvre of the vehicle towards the path that needs to be tracked.

For precise tracking of the trajectory at all vehicle speeds, the lateral controller should also take into account the forward velocity of the vehicle. Hence, the look-ahead distance (l_d) is assigned as a function of the vehicle forward speed (v_f) by adding a proportionality constant (K_{dd}) with its units in seconds. This constant can be tuned to change the stability and tracking performance of the pure pursuit controller for a particular course.

$$l_d = K_{dd}v_f \tag{4}$$

The steering angle output from the pure pursuit controller is given by Eq. 5. For practical purposes, this steering angle is limited from -1.22 rad to 1.22 rad.

$$\delta = \tan^{-1}\left(\frac{2L \sin \alpha}{l_d}\right) = \tan^{-1}\left(\frac{2L \sin \alpha}{K_{dd}v_f}\right) \tag{5}$$

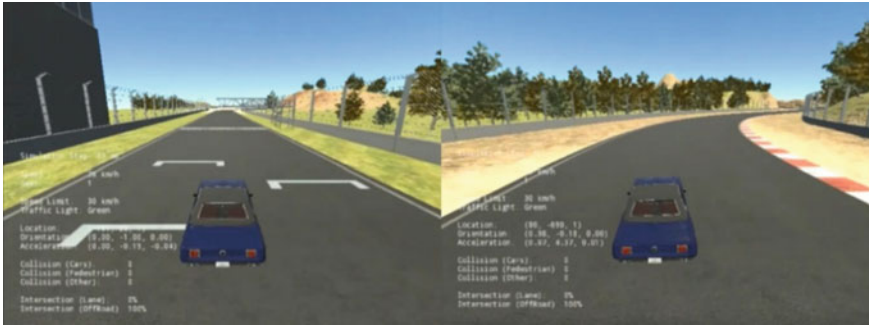


Fig. 7 Snapshots of the simulation in CARLA Simulator

Finally, in the lateral controller, the steering angle output is bound to -1 to 1 range limits to generate the steering command for steer actuation.

3 Simulation

A realistic simulation environment is essential for the development of an autonomous vehicle because it enables testing of the autonomous vehicle under various conditions and scenarios without even stepping into it. The simulation allows monitoring the vehicle's performance to ensure that the vehicle operates safely before deploying it on actual roads. One such highly realistic simulator used by a large number of researchers is CARLA Simulator. CARLA is an open-source simulator built using the Unreal game engine solely for autonomous driving research. It features highly detailed virtual worlds with vast selectable maps, numerous vehicle models, pedestrians, buildings and traffic signs including a wide range of adjustable environmental conditions (Fig. 7).

To test the accuracy and precision of the developed waypoint tracking controller, a path tracking simulation is carried out in CARLA using the specifications listed in Table 1. The PID controller is tuned to improve its performance in tracking the reference speed profile and the best resulting gain values K_P , K_I and K_D are chosen as 2.5, 1 and 0.225, respectively for the simulation. The value of K_{dd} is chosen as 1 for this path to accurately track all the waypoints in the test bench.

4 Results and Conclusion

The throttle, brake and steer outputs from the waypoint tracking controller are shown in Fig. 8. The throttle and brake outputs range from 0 to 1, corresponding to the acceleration output from the PID controller. These throttle and brake outputs function as

Table 1 Simulation specifications

Parameter	Value
Processor	Intel i5-7300HQ @ 2.5 GHz
Simulator resolution	640 × 480
Simulator Frames Per Second (FPS)	30
Proportional Gain (K_D)	2.5
Integral Gain (K_I)	1
Derivative Gain (K_D)	0.225
Proportional constant (K_{dd})	1

the actuation signals for adjusting the throttle and brake pedal position of the vehicle to accelerate accordingly. The steer output ranges from -1 to 1 , corresponding to the steering angle output from the pure pursuit controller. This steer output actuates the steering of the vehicle to turn the vehicle accordingly.

The test results indicate that the vehicle tracks 100% of the specified waypoints in the trajectory. Further, the waypoint tracking controller performs well in closely tracking the reference speed profile (Fig. 9).

This work discussed the development and simulation of a waypoint tracking controller for autonomous vehicles. The waypoint tracking controller is developed by implementing a PID controller for longitudinal control and a pure pursuit controller for lateral control. The PID gains are tuned to precisely track the reference speed profile. A pure pursuit controller is implemented for lateral control to accurately follow the desired path. The developed waypoint controller is deployed in CARLA Simulator. The simulation results indicate that the vehicle tracks 100% of the waypoints specified in the trajectory. The waypoint tracking controller also performs well in closely tracking the reference speed profile. The developed waypoint tracking controller is precise and suitable for application in autonomous vehicles for urban driving environments.

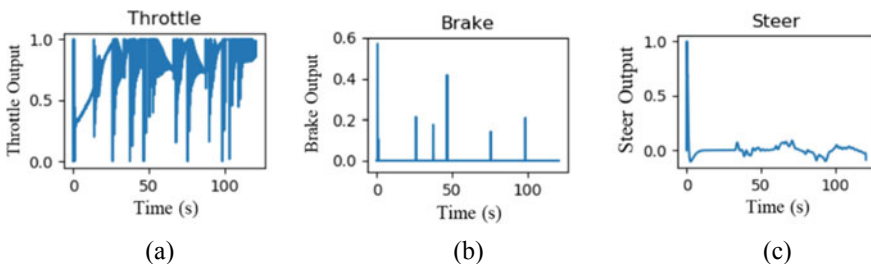


Fig. 8 Waypoint tracking controller outputs: **a** throttle **b** brake **c** steer

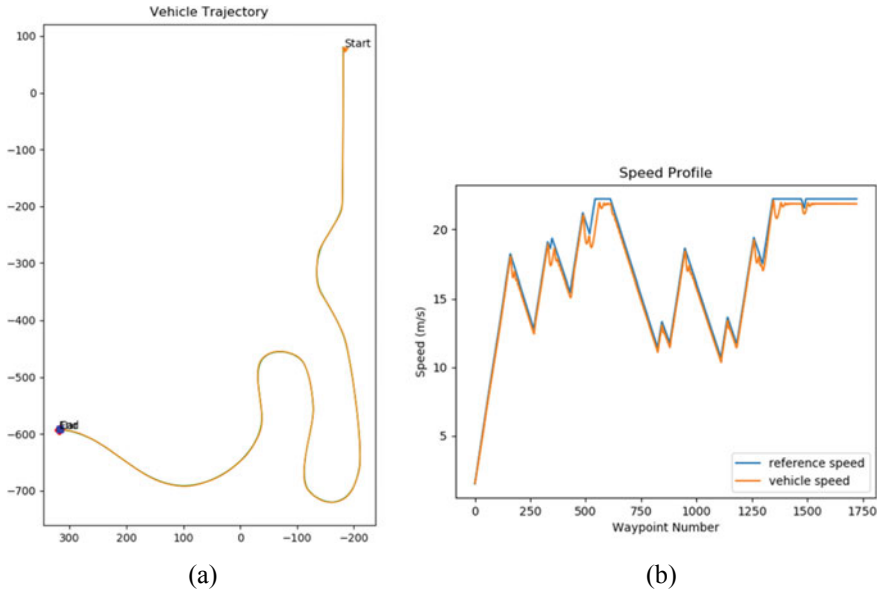


Fig. 9 Simulation results: **a** vehicle trajectory **b** vehicle speed profile

References

1. SAE Standard J3016: Taxonomy and definitions for terms related to driving automation systems for on-road motor vehicles. https://www.sae.org/standards/content/j3016_202104 (2021). Accessed 16 Oct 2021
2. Python Programming Language Homepage. <https://www.python.org>. Accessed 16 Oct 2021
3. CARLA Simulator Homepage, <https://carla.org>. Accessed 16 Oct 2021
4. OpenDRIVE, <https://www.asam.net/standards/detail/opendrive>. Accessed 16 Oct 2021
5. OpenStreetMaps, <https://www.openstreetmap.org>. Accessed 16 Oct 2021
6. Rajamani R (2012) Introduction to longitudinal control. In: Vehicle dynamics and control. 2nd edn., pp 123–150, Springer, USA
7. Sailan K, Kuhnert KD (2013) Modeling and design of cruise control system with feedforward for all terrain vehicles. In: Second International Conference on Advanced Information Technologies and Applications. Dubai, UAE
8. Samuel M, Hussein M, Mohamad MB (2016) A review of some pure-pursuit based path tracking techniques for control of autonomous vehicle. *Int J Comput Appl* 135:35–38
9. Hoffman GM, Tomlin CJ, Montemerlo M, Thrun S (2007) Autonomous automobile trajectory tracking for off-road driving: controller design, experimental validation and racing. In: Proceedings of the 2007 American control conference, pp 2296–2301, New York, NY, USA
10. Falcone P, Borrelli F, Asgari J, Tseng H, Hrovat D (2007) Predictive active steering control for autonomous vehicle systems. *IEEE Trans Control Syst Technol* 15(3):566–579

An Economic Feasibility Study of Electric Vehicle Charging Stations in India



Sajan Jerome and M. Udayakumar

Abstract To address the ever-increasing issue of greenhouse gas emissions, reduce dependence on crude oil, and increase in fuel prices in the Indian context, electric vehicles (EV) are considered a possible solution in a long run. With incentive schemes initiated by the Government of India (GoI), the adoption of EVs is happening on a large scale. A core requirement for the mass adoption of EVs is the availability of charging infrastructure at an affordable rate and without intermittency to relieve range anxiety. However, the deficiency of public charging infrastructure is considered a major hindrance to a wide-scale adoption of EVs. This paper elaborates on factors affecting the location of charging infrastructure and highlights the existing EV charging standards in India. Also, the economic feasibility of establishing an electric vehicle charging station (EVCS) as per the standards and guidelines prescribed by the government is carried out using the net present value (NPV) method. With careful planning, establishing slow as well as fast EVCSs at existing parking stations with nominal parking fees at retail spaces, workplaces, street parking areas, and along highways can encourage extensive use of EVs, leading to a profitable business opportunity.

Keywords Electric vehicle charging station · Electric vehicles · Net present value

1 Introduction

The burning of fossil fuels for transportation releases large quantities of carbon into the environment leading to air pollution and global warming. Hence, alternative energy technologies are to be introduced on a large scale [1]. The most promising method to decarbonize the transport sector is to replace conventional vehicles with EVs which are energy efficient and clean [2]. With the increasing electrification of the transportation sector, EVs represent a promising way to alleviate the pollution

S. Jerome (✉) · M. Udayakumar

Department of Mechanical Engineering, National Institute of Technology, Tiruchirappalli 620015, Tamil Nadu, India

e-mail: sajanjerome@gmail.com

and greenhouse gas emissions caused by conventional vehicles [3]. The market share of EVs is increasing globally and the GoI has also devised programs to enhance their market penetration. Economic charging solution needs to be in place to meet the rising charging requirement from transport sector. As per the infrastructure guidelines set by the GoI, in any case, one charging station must be accessible in a network of 3 km \times 3 km in cities and at every 25 km on both sides of the highways. For heavy-duty EVs, like buses and trucks, there ought to be one charging station at every 100 km on both sides of the road along highways [4]. Studies reveal that the shortage of public charging infrastructure is a major deterrent to the widespread adoption of EVs [5]. The availability of publicly accessible chargers makes people show interest in EVs. To enhance the growth of public charging infrastructure, continuous support from the government, utility grid authorities, and EV manufacturers is necessary.

The major factor hindering EV adoption is range anxiety, which is the fear of running out of battery power before it can be recharged and this concern is amplified due to limited public charging infrastructure. A lack of sufficient charging infrastructure can lead to range anxiety among the EV users, impeding their widespread acceptance [6]. Hence a wide network of public charging infrastructure is essential. Installing EVCSs at several locations can overcome range anxiety. At lower EV adoption rates, the investment in EVCSs will be hardly profitable. Hence, the EVCS investors are unsure of investing now or waiting till the critical mass of EVs is reached. The economic feasibility of establishing EVCS from an investor's point of view is not widely discussed in the literature. In the current study, we carry out an economic feasibility study on establishing an EVCS in the Indian scenario using the NPV method. Higher power rates for fast-charging stations are desired by the customers so that a time similar to the refueling time of the conventional vehicles could be obtained for EV charging [7]. Fast and ultra-fast-charging stations can reduce the charging time to a minimum level, thereby enhancing the acceptance level of EVs [8]. The study has been carried out for establishing both slow and fast-charging stations taking into account the varying amounts of incentives provided by GoI for the purchase of EV charging equipment commonly known as electric vehicle supply equipment (EVSE).

2 Methodology

EV chargers vary from 0.50 kW to as high as 500 kW, and with advances in battery chemistry, higher charging rates can be achieved in the future [9]. At lower EV adoption rates, the investment in EVCSs will be hardly profitable. Hence, the EVCS investors are unsure of investing now or waiting till the critical mass of EVs is reached. The GoI has delicensed EVCS business for EVs, whereby individuals can set up such facilities but at a regulated tariff, provided they meet the technical, safety, and performance standards as laid down by the Ministry of Power and Central Electricity Authority [10]. The government has categorized the EVCSs to provide demand incentives under the Faster Adoption and Manufacturing of Hybrid and

Table 1 Demand incentive provided for EVCS under FAME scheme

Category	Incentive	Location
I	70%	Public place for commercial purpose: Municipal parking lot Petrol stations Streets Malls Market Complexes Airports/Railway/Metro stations Bus stops
II	100%	Premises of state or central government office complexes: Government hospitals/Clinics/Dispensaries Government educational institutions Public offices for non-commercial use
III	50%	Semi-restricted premises for commercial or non-commercial purpose: Taxi aggregators for charging of taxis Co-operative housing societies

Source [11]

Electric Vehicle (FAME) Phase II scheme and the guidelines are shown in Table 1 [11]. This demand incentive is provided for the cost of EVSE excluding the upstream infrastructure including the cost of transformer required for bringing power supply to the EVCS. The economic feasibility of EVCSs is analyzed using the NPV method. The NPV is calculated using Eq. (1).

$$NPV = \sum [(C_t / (1 + r)^t)] - C_0, \tag{1}$$

where C_t represents the net cash flow for a period ‘ t ’; C_0 is the total initial investment; r is the discount rate. The discount rate considered in this study is 15%, which is higher than the usual percentage of 10% as the EVCS industry is novel in India and therefore, the associated risk involved is comparatively high [12]. The sum of the present values (PV) of all the cash inflows and outflows determines the NPV of an investment. A positive sign is assigned to cash inflows whereas the cash outflows are assigned a negative sign. The knowledge of the amount of each cash flow, as well as the time of occurrence of the cash flow, is necessary for the accurate calculation of NPV. A positive NPV means the investment makes sense financially. As explained in Table 2, when multiple options are available, an investor will select the option with maximum NPV, as it provides a maximum value addition for the firm.

The EVSE for the charging stations is selected as per the guidelines laid down by the Ministry of Power, GoI for establishing EVCSs in India [4]. In both slow- and fast-charging stations, we have assumed that the Bharat DC001 charger is provided to meet the demand of EVs currently in the Indian automobile market. The slow-charging station consists of four Bharat DC001 chargers and two Bharat AC001 chargers which can charge four and six EVs simultaneously. In the slow-charging

Table 2 NPV decision table

	Outcome	Decision
NPV > 0	The investment would add value to the firm	The project may be accepted
NPV < 0	The investment would subtract value from the firm	The project should be rejected
NPV = 0	The investment would neither gain nor lose value for the firm	The project adds no monetary value. Decision should be based on some other criteria such as strategic positioning

stations, 4W, 3W, and 2W vehicles can be charged. This is significant in a country like India, where there is a larger preference towards 2 W vehicles followed by 3Ws as a means of public transport. In case of fast-charging stations, two CCS chargers and four Bharat DC001 chargers are provided which can charge two and four EVs simultaneously. CCS charger can be used to charge 4W EVs only, whereas 4W, 3W, and 2W EVs can be charged using a Bharat DC001 charger.

The cost components for an EV charging station comprise capital as well as operational expenditures. The cost estimates for EVSE are obtained from [13] as shown in Table 3. Apart from the procurement cost of EVSE, the capital expenditure involves costs associated with new electricity connection including transformer, associated civil works, EVSE software procurement, and CCTV setup. The details are summarized in Table 4.

The safety provisions for EVCSs in India are detailed in the Measures Relating to Safety and Electric Supply (Amendment) act 2019 [14]. This specifies the general safety necessities for EVCSs which include earth protection systems, fire safety,

Table 3 Cost estimates and specifications of EVSE for EVCSs

Type of Charger	Output Power (kW)	Number of EVs that can be charged simultaneously	Charging vehicle type	Cost of equipment (Rs)
Bharat DC 001	15	1	4W, 3W, 2W	230,000
Bharat AC 001	10	3	4W, 3W, 2W	55,000
CCS	60	1	4W	1,200,000

Source [13]

Table 4 Capital expenditure associated with establishing an EVCS

Particulars	Capital expenditure (Rs)
New electricity connection	400,000
Civil works	250,000
EVSE software	40,000
CCTV setup	30,000

testing of EVSE, inspection and periodic assessment, and maintenance of records as per international standards that need to be followed. In the guidelines for establishing EVCSs in India [4], it is specified that the EVSE is to be type tested by an agency accredited by the National Accreditation Board for Testing and Calibration Laboratories (NABL) from time to time. EVSE are provided with safety measures that protect EV users from potential electric as well as fire hazards. In case of any fault, the EVSE will stop the power transfer to the EV immediately and deenergize the cable.

The annual operating expenditure consists of the salary for the EVSE technician at Rs.25000 per month and the annual maintenance cost is assumed as 10% of the total EVSE cost. Even though the procurement of land, either purchased or lease agreement involves a huge amount, depending on the location and availability of land, in this paper, it is assumed that land will be made available by the government or municipal bodies free of cost. This involves a policy decision from the government to encourage the mass adoption of EVs into the market. In course of time, as EV charging becomes a profitable business, the land can be procured by the business operators.

The following assumptions are made in the analysis:

1. The hours of charging per day are 20.
2. Capacity utilization factor for the EVCSs increases from 10 to 100% over a time span of 10 years.
3. Electricity tariff paid to the Discom by the EVCS operator is fully passed on to the consumer.
4. The existing electrical utility has spare capacity.

3 Results and Discussion

This section provides an insight into the economics of fast- and slow-charging technologies in India which may guide the investors as well as policymakers in framing policies for setting up EVCSs from a broader perspective. We first analyze the case in which a flat tariff is applied across the year and see the margin on electricity tariff to be imposed on the customer by the EVCS service provider to achieve a profitable business. We find the amount of margin on electricity to be imposed on the customers to make EVCS a successful business opportunity. The feasibility of establishing EVCSs with various amounts of demand incentives for the purchase of EVSE for Categories I, II, and III with 70%, 100%, and 50% incentives for establishing charging infrastructure at various locations as shown in Table 1 is carried out for slow as well as fast-charging stations. The analysis is carried out for various amounts of incentives being provided for the purchase of the EVSE combined with parking fees being imposed for utilizing the EVCS as shown in Figs. 1, 2, and 3. This study considers parking fees of Rs.0.00, Rs.10.00, and Rs.20.00 per hour for slow- and fast-charging stations. S/0, S/10, and S/20 represent slow-charging stations imposing Rs.0.00, Rs.10.00, and Rs.20.00 per hour, respectively, as parking

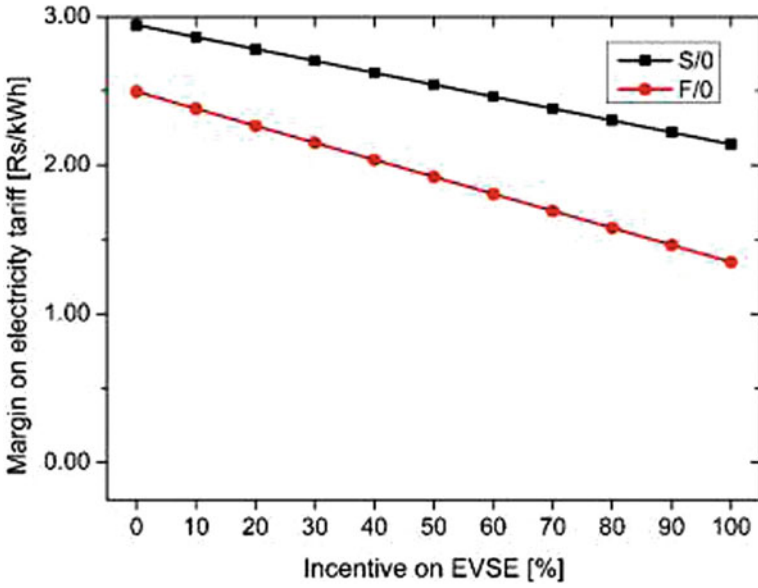


Fig. 1 Margin on electricity tariff required with various incentives on charging equipment with zero parking fee

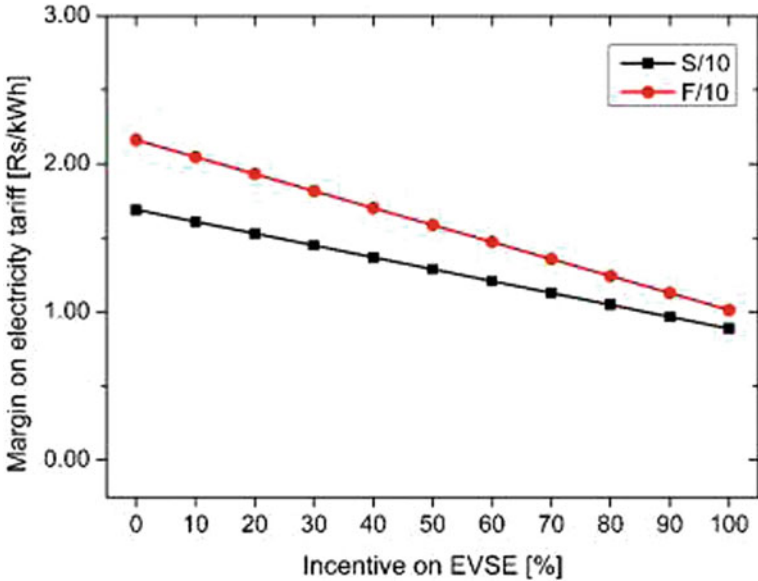


Fig. 2 Margin on electricity tariff required with various incentives on charging equipment with parking fee of Rs.10.00 per hour

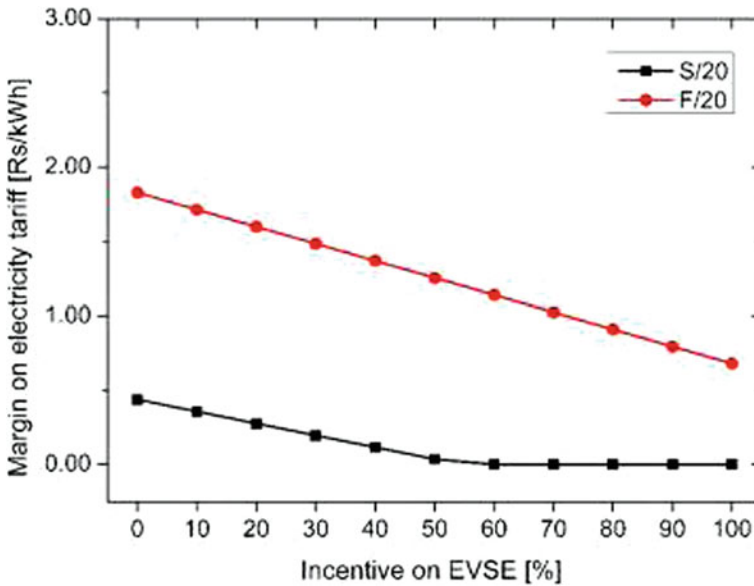


Fig. 3 Margin on electricity tariff required with various incentives on charging equipment with parking fee of Rs. 20.00 per hour

fee, whereas F/0, F/10, and F/20 represent the same for fast charging stations. To find out the breakeven for the EVCS business, when the cash flows become equal to the initial investment, we set NPV equal to zero in Eq. (1). This gives the condition required to achieve a non-profit and no-loss situation.

As seen in Fig. 1, with zero parking fees, the margin on electricity tariff required for the EV charging business to be profitable is higher for slow-charging stations when compared to fast-charging stations. Even though a higher capital expenditure is associated with a fast-charging station, the amount of electricity sold from a fast-charging station daily would be higher when compared to slow-charging stations. This makes the margin on electricity for slow-charging stations to be higher when compared to fast-charging stations with zero parking fees.

However, when a parking fee is imposed for utilizing the facility, the margin on the electricity required for fast-charging stations becomes high in comparison to slow-charging stations as seen in Figs. 2 and 3. This is because a greater number of vehicles could be charged simultaneously in slow charging stations when compared to fast-charging stations. With a parking fee of Rs. 20 per hour as shown in Fig. 3, it would be possible to forgo the margin on the electricity tariff required by slow-charging stations. This makes electricity much cheaper for charging the vehicle. In malls, parking lots, bus depots, railway stations, and airports, where the customers park the vehicle for a long duration of time, the slow-charging stations may be established which are more economically feasible, especially in India where there is a preference for low-cost vehicles in the two-, three-, and four-wheeler segments.

Also, the onboard charger used in Indian vehicles cannot take power more than 3 kW, which further limits the use of charging equipment with higher charging rates.

The minimum incentive to be provided for the purchase of EVSE to make EVCS profitable for slow- and fast-charging infrastructure for various fixed margins on electricity tariff is shown in Tables 5 and 6. As seen in Table 5, a slow-charging station imposing zero parking fee, with the margin on electricity tariff varying from Rs.0.00 to Rs. 2.00 per kWh, even with 100% incentive on EVSE, the EVCS business will be non-profitable. With an incentive above 55.23%, the EVCS can become profitable with a margin of Rs. 2.50 per kWh without imposing any parking fee, whereas with a margin of Rs. 3.00 per kWh, no incentive will be required to make the business profitable. In charging stations where a parking fee of Rs. 10 per hour is imposed, incentives above 85.94 and 23.73% for a margin of Rs. 1.00 and Rs. 1.50 per kWh, respectively, will be required for EVCS to become profitable. By imposing a margin on electricity of Rs. 2.00 per kWh and above, no incentives will be required for a profitable business opportunity. With a lower margin on electricity up to Rs. 0.50 per kWh, the charging station is not profitable even with a 100% incentive. By imposing a higher parking fee of Rs. 20 per hour, an incentive above 54.45% is required to offer zero margins on electricity to be imposed on the customers. Further, no incentive on

Table 5 Incentive required to slow charging station for profit (fixed margin on tariff)

Margin on tariff (Rs/kWh)↓	Parking fee (Rs/h)		
	S/0	S/10	S/20
0.00	NP ^a	NP	54.45%
0.50	NP	NP	0.00%
1.00	NP	85.94%	0.00%
1.50	NP	23.73%	0.00%
2.00	NP	0.00%	0.00%
2.50	55.23%	0.00%	0.00%
3.00	0.00%	0.00%	0.00%

^a Not profitable

Table 6 Incentive required to fast-charging station for profit (fixed margin on tariff)

Margin on tariff (Rs/kWh)↓	Parking fee (Rs/h)		
	F/0	F/10	F/20
0.00	NP	NP	NP
0.50	NP	NP	NP
1.00	NP	NP	72.12%
1.50	86.63%	57.60%	28.58%
2.00	43.09%	14.07%	0.00%
2.50	0.00%	0.00%	0.00%
3.00	0.00%	0.00%	0.00%

EVSE will be required for a margin on electricity greater than or equal to Rs. 0.50 per kWh for EVCS to be profitable.

As shown in Table 6, a fast-charging station imposing zero parking fee, with the margin on electricity varying from Rs.0.00 to Rs. 1.00, even with 100% incentive on EVSE, the EVCS business will be non-profitable. With incentives above 86.63% and 43.09%, the EVCS can become profitable with a margin of Rs.1.50 and Rs.2.00 per kWh, respectively, without imposing any parking fee, whereas with a margin of Rs. 2.50 per kWh and above, no incentive will be required to make the business profitable. In charging stations where a parking fee of Rs. 10 per hour is imposed, incentives above 57.60 and 14.07% for a margin of Rs. 1.50 and Rs. 2.00 per kWh respectively will be required for EVCS to become profitable. By imposing a margin on electricity of Rs. 2.50 per kWh and above, no incentives will be required for a profitable business opportunity. With a lower margin on electricity up to Rs. 1.00 per kWh, the charging station is not profitable even with a 100% incentive. By imposing a higher parking fee of Rs. 20 per hour, incentives on EVSE above 72.12 and 28.58% for a margin of Rs. 1.00 and Rs. 1.50 per kWh respectively will be required for EVCS to become profitable. By imposing a margin on electricity of Rs. 2.00 per kWh and above, no incentives on EVSE will be required for a profitable business opportunity. With a lower margin on electricity up to Rs. 0.50 per kWh, the charging station is not profitable even with a 100% incentive.

The fixed margin on electricity tariff required for EVCSs to become profitable under the categories I, II and III as shown in Table 1, for slow as well as fast-charging stations for various parking fees considered in this study are shown in Fig. 4. As seen in Fig. 4a, for slow charging stations, the highest margin on the electricity required for a profitable business is Rs. 3.00 per kWh for category III with zero parking fee. The margin on the electricity required for a profitable business for a slow-charging station is zero for categories I and II when a parking fee of Rs.20.00 per hour is imposed. As shown in Fig. 4b, for fast-charging stations the highest margin on electricity tariff required for a profitable business is Rs.2.00 per kWh for categories I and III, with zero parking fee, whereas with a parking fee of Rs. 20.00 per hour the lowest margin is Rs. 1.00 per kWh for category II.

From Fig. 4a, b, it is observed that the highest margin required on electricity tariff for a profitable charging station business is for category III whereas the lowest margin is obtained for category II for all parking fees considered in this study. The EV customers will prefer a lower margin on electricity tariff and hence a wider acceptance for using the EVCSs can be obtained by establishing them at category II locations which include the premises of state and central government office complexes as mentioned in Table 1.

We now consider the case in which there is a yearly escalation on the margin of electricity tariff with increments of Rs. 0.25, 0.30, 0.35, 0.40, 0.45, and 0.50 per kWh of electricity. The profitability for slow- and fast-charging stations with yearly increments in the margin on electricity varying from Rs. 0.25 to Rs. 0.50 per kWh for various parking fees considered are as shown in Tables 7 and 8, respectively.

As seen in Table 7, for a slow-charging station, with zero parking fees, the EVCS business will not be profitable up to annual increments in the margin of electricity up

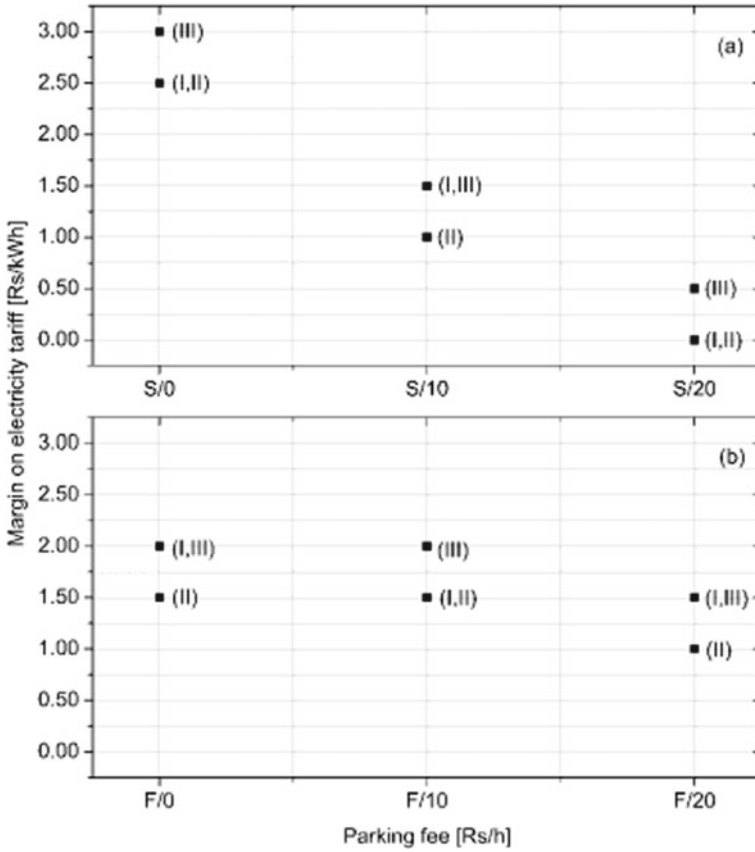


Fig. 4 Fixed margin on electricity tariff required for EVCSs to become profitable under the categories I, II, and III

Table 7 Incentive required to slow-charging stations to become profitable (incremental margin on tariff)

Annual increment (Rs/kWh)↓	Parking fee (Rs/h)		
	S/0	S/10	S/20
0.25	NP	20.84%	0.00%
0.30	NP	0.00%	0.00%
0.35	NP	0.00%	0.00%
0.40	63.03%	0.00%	0.00%
0.45	25.13%	0.00%	0.00%
0.50	0.00%	0.00%	0.00%

Table 8 Incentive required to fast-charging stations to become profitable (incremental margin on tariff)

Annual increment (Rs/kWh)↓	Parking fee (Rs/h)		
	F/0	F/10	F/20
0.25	84.60%	55.58%	26.55%
0.30	58.07%	29.05%	0.03%
0.35	31.55%	2.53%	0.00%
0.40	5.02%	0.00%	0.00%
0.45	0.00%	0.00%	0.00%
0.50	0.00%	0.00%	0.00%

to Rs. 0.35 per kWh. Incentives above 63.03 and 25.13% on EVSE will be required to support the EVCS business to become profitable with annual increments in electricity tariff of Rs.0.40 and 0.45 per kWh, respectively. With an increment of Rs.0.50 per kWh annually, no incentive on the purchase price of the EVSE is required for a profitable business. By imposing a parking fee of Rs.10 per hour, incentive above 20.84% will be required for annual increment of Rs.0.25 per kWh on the margin on electricity for a profitable business. With annual increments of Rs. 0.30 per kWh and above on margin on electricity, no incentive for EVSE is required for a profitable business. There is no requirement of incentive for EVSE on imposing a parking fee of Rs.20 per hour for all increments in the margin of electricity for a profitable EVCS business.

As seen in Table 8, for a fast-charging station, varying amounts of incentives for EVSE will be required for increments up to Rs. 0.40 per kWh for the business to become successful without imposing any parking fee. With increments above Rs. 0.45 per kW h, no incentives on EVSE will be required for a successful business proposition. With an hourly parking fee of Rs.10, there is no incentive to be provided for an annual incremental margin on electricity of Rs. 0.40 per kWh and above. The incentives required for profit with Rs.0.25, Rs. 0.30, and Rs.0.35 per kWh annual increments are above 55.58%, 29.05%, and 2.53%, respectively. With an hourly parking fee of Rs.20.00, no incentives will be required for the annual increment of Rs. 0.35 per kW h and above for the business to become viable. An incentive above 26.55% on EVSE is required for an incremental margin of Rs. 0.25 per kWh for a successful business, whereas a negligible amount of incentive may be required for tariff rise of Rs.0.30 per kWh of electricity annually.

The incremental margin on electricity tariff required for EVCSs to become profitable under the categories I, II, and III as shown in Table 1, for slow- as well as fast-charging stations for various parking fees considered in this study are shown in Fig. 5. As seen in Fig. 5a, for slow-charging stations, the highest margin on annual increment in electricity tariff required for profitable business for EVCS is Rs. 0.45 per kWh for category III with zero parking fee. The least incremental margin required is Rs.0.25 per kWh for slow-charging stations with a parking fee of Rs.10.00 and Rs.20.00 per hour. As shown in Fig. 5b, for fast-charging stations, the highest incremental margin on the electricity tariff is Rs.0.35 per kWh for category III with zero

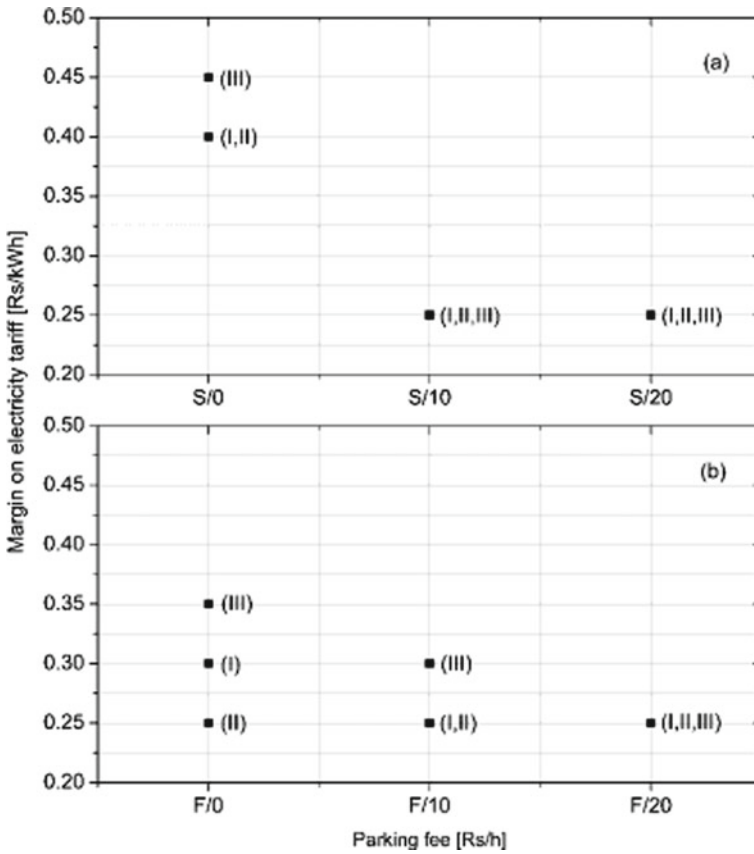


Fig. 5 Incremental margin on electricity tariff required for EVCSs to become profitable under the categories I, II, and III

parking fee, whereas the least margin required is Rs. 0.25 per kWh for all categories of charging stations with a parking fee of Rs. 20.00 per hour.

From Fig. 5a, b, it can be observed that the least incremental tariff required for a profitable charging station business is Rs. 0.25 per kWh, which is the same for all categories with S/10, S/20, and F/20 and for categories I and II for F/10. In the case of F/0, category II has the same lowest incremental tariff required for a profitable charging station business.

Thus, while establishing a slow or fast-charging station with incremental tariff, with parking fee applied, the incremental tariff to be employed is the same for all categories except for category III with F/10, for which a slightly higher incremental tariff is required for a profitable business. For fast charging stations with zero parking fees, the incremental margin required for a profitable business can be reduced to Rs.0.25 per kWh, if the incentive on the purchase of EVSE could be increased to 100% as that for category II. In doing so, the incremental margin on electricity tariff

can be reduced for category I and category III, which can attract EV users on a large scale, thereby increasing the market penetration of EVs.

In general, it is suggested that an incentive of 100% for the purchase of EVSE must be provided for category I, instead of category II, which includes municipal parking lots, petrol stations, malls, market complexes, airports, railway stations, metro stations, and bus stops, which are public places used for commercial purposes where the customer spends more amount of time. This helps the customer to utilize their time, while the vehicle is getting charged. This can help to improve the market acceptance of EVs on a large scale as they have an opportunity to charge their EVs at much lower rates. Category III, which includes the location for setting up charging stations for taxi aggregators, is provided with an incentive of only 50% on the purchase of EVSE. Under the FAME India scheme, public transportation is to be given incentives in respect of reduction in their upfront cost of the vehicle.

As shown in Figs. 4 and 5, the highest margin in electricity tariff for all parking fees is for category III and hence they have to pay a higher margin on the electricity tariff leading to a higher operating cost. Hence, it is suggested that a higher incentive on the purchase of EVSE for category III as that of category II is to be implemented to decrease the margin on electricity tariff so that it becomes beneficial for the taxi aggregators thus encouraging public transportation.

4 Conclusion

With the government's intention to provide subsidies in the range of 50, 70, and 100% on the EVSE cost, a better return can be obtained from the EVCS business thereby enabling the service providers to establish a greater number of charging infrastructure, encouraging the use of EVs by relieving the customers of the range anxiety. Currently, as per the guidelines set by the government, the incentive for the purchase of EVSE for establishing EVCSs at the premises of state and central government offices (category II) is 100%, whereas that for public places for commercial purpose (category I) is 70% and for semi-restricted premises such as taxi aggregators for charging of taxis (category III) is 50%. The following conclusions are made from this study:

- The purchase incentive on EVSE in category I locations has to be enhanced from the current rate of 70 to 100% as provided for category II locations. This can lead to a decrease in the margin on electricity required for EVCSs established in municipal parking lots, malls, market complexes as well as airport, railway, metro, and bus stations, where the EV customers are expected to park their vehicle for an adequate amount of time required to charge the EVs while completing other tasks.
- Currently, the least incentive of 50% for the purchase of EVSE is offered to category III locations. This includes semi-restricted premises used by taxi aggregators for charging their electric taxis which leads to a higher margin on electricity tariff

required for charging EV used for taxi services which include 3Ws and 4Ws. With an increase in incentive for the purchase of EVSE for establishing EVCSs in category III locations, the margin on the electricity required for a profitable charging station business can be reduced making the taxi rides more economical thereby encouraging public transportation.

With the wider establishment of EVCSs, EV user confidence can be improved, leading to their wider adoption. Hence, the government should consider enhancing the incentive on the purchase of EVSE for category I and category III locations to 100% as that of category II locations leading to greater use of EVs.

References

1. Kasim H, Ibrahim ZA, Al-Ghaili AM (2020) Reducing climate change for future transportation: roles of computing. *Comput Sci Technol*, 43–54
2. Nunes P, Figueiredo R, Brito MC (2016) The use of parking lots to solar-charge electric vehicles. *Renew Sustain Energy Rev* 66:679–693
3. Jerome S, Udayakumar M (2021) Assessment of gasoline consumption and greenhouse gas emission reduction on using battery electric two-wheeler in India. *J Braz Soc Mech Sci Eng* 43(1):1–15
4. Charging Infrastructure for Electric Vehicles (EV)-Revised Guidelines and Standards. Ministry of Power, Government of India (2019). https://powermin.gov.in/sites/default/files/uploads/Revised_MoP_Guidelines_01_10_2019.pdf
5. Berkeley N, Jarvis D, Jones A (2018) Analysing the take up of battery electric vehicles: an investigation of barriers amongst drivers in the UK. *Transp Res Part D: Transp Environ* 63:466–481
6. Kim S, Lee J, Lee C (2017) Does driving range of electric vehicles influence electric vehicle adoption? *Sustainability* 9(10):1783
7. Gnann T, Funke S, Jakobsson N, Plötz P, Sprei F, Bennehag A (2018) Fast charging infrastructure for electric vehicles: Today's situation and future needs. *Transp Res Part D: Transp Environ* 62:314–329
8. Sadeghi-Barzani P, Rajabi-Ghahnavieh A, Kazemi-Karegar H (2014) Optimal fast charging station placing and sizing. *Appl Energy* 125:289–299
9. RMI India (2020) Electric vehicle charging infrastructure: a guide for discom readiness (2019). https://rmi.org/wp-content/uploads/2020/07/EV-Readiness-Guide_Haryana_Lighthouse_Discom_Programme.pdf
10. Clarification on charging infrastructure for electric vehicles with reference to the provisions of the Electricity Act 2003, Ministry of Power, Government of India (2018). https://powermin.gov.in/sites/default/files/uploads/Clarification_EV.pdf
11. Expression of interest inviting proposals for availing incentives under FAME India scheme phase II for deployment of EV charging infrastructure within cities. Department of Heavy Industry, Ministry of Heavy Industries and Public Enterprises, Government of India (2019). <https://dhi.nic.in/writereaddata/UploadFile/EOI%20for%20EV%20charging%20in%20cities%2012%20july.pdf>
12. Rathnayake RMDIM, Jayawickrama TS, Melagoda DG (2020) Prospect of establishing electric vehicle charging stations at public hotspots. *Intell Build Int* 12(4):318–330
13. IESA (2021) India Energy Storage Alliance, Homepage. <https://indiaesa.info/products?start=0>, last accessed 2021/08/15

14. CEA (Central Electricity authority), Government of India, Measures relating to Safety and Electric Supply) (Amendment) Regulations, 2019 https://cea.nic.in/old/reports/regulation/measures_safety_2019.pdf

Liquid Cooled Battery Thermal Management System for 3S2P Li-Ion Battery Configuration



Divya D. Shetty, Aditya Nair, Rishab Agarwal, and Kshitij Gupta

Abstract Lithium-ion batteries are the future of the automotive industry. Due to their zero-emission technology, lithium-ion powered electric vehicles are hyped as the power source of the future. However, one of the main drawbacks of the cell is its high heat generation, which, in turn, affects the performance of the vehicle. Currently, research is being conducted into developing an efficient battery thermal management system (BTMS). The present study will be looking into developing a liquid battery thermal management system. To determine the efficiency of the cooling system, heat generation on a smaller battery pack was modelled with the help of the MSMD model on Ansys fluent. A smaller battery pack of a 3s2p configuration was selected to validate the results. The parameters of the cell were available on the datasheet. Materials were selected based on the data present on Ansys fluent. The simulation was conducted for two discharge rates 1C and 2C. As a result, it was observed that for the 3s2p configuration, the maximum temperatures go up to 320 K and 335 K for a discharge rate of 1C and 2C, respectively. After this, the battery pack is subjected to a liquid thermal management system. The effect of various mass flow rate on temperature are as follows at flow rate of $1e-5$ the maximum temperature decreases by 5.31%, whereas the maximum temperatures at $1e-4$ and $1e-3$ flowrate decreases by 5.93% and 6.01% respectively at 1C discharge rate. In case of 2C discharge rate, at the mass flow rate of $1e-5$, the maximum temperature decrease is by 8.65%, whereas for $1e-4$ and $1e-3$, the maximum temperature decrease is by 9.85% and 10.14%, respectively. A crossflow design is adopted and was compared with the normal flow; it is observed that there is no significant effect of flow direction on temperature.

Keywords Li-ion battery · Maximum temperature · Discharge rate

D. D. Shetty (✉) · A. Nair · R. Agarwal · K. Gupta
Department of Aeronautical and Automobile Engineering, Manipal Institute of Technology,
Manipal Academy of Higher Education, Manipal, Karnataka 576104, India
e-mail: Shetty.divya@manipal.edu

1 Introduction

Electric vehicles are the future of the automotive industry. With the rising prices of crude oil and the depleting natural resources around the world, we are forced to look for alternative ways of providing energy to the vehicle. The experts in the automobile industry thus came up with a solution to this problem by attaching and trying to power the car with a battery, motor and generator, thus giving rise to Electric Vehicles, commonly known as EVs [1]. These EVs are powered by a battery connected to a motor, which, in turn, drives the wheels. These motors act as a generator also, thus recharging the battery as the vehicle moves. Electric Vehicles are being used in passenger vehicles and motorsports with the introduction of Formula-E [2]. A Lithium-ion battery is the most popular battery used in Electric vehicles. There exist several cells with similar chemistry to that of Li-ion cells like Li-nickel-manganese-cobalt (NMC), Li-phosphate and Li manganese, with each cell being advantageous over its peers in a few sectors [3]. However, holistically, Li-ion cells have been found to be superior, chemistry-wise, to drive the powertrain of an electric vehicle for the following reasons: Higher energy density, high power density and longer cycle life [4]. In addition to high energy and power density, lithium-ion batteries have shown high life cycle, particularly when operated under shallow cycling conditions [3].

One of the major challenges is keeping the battery pack cool even after long durations of discharging and charging cycles. The solution to this problem is still in the early stages of research and development and still requires a lot of attention. This heating issue in the battery pack occurs due to the following reasons [6]: a. Thermal Runaway [7], b. Ageing, c. Gassing and d. Cost of production. In many cases, Panasonic, the supplier of cells to tesla, makes use of a Lithium cobalt aluminium configuration [8]. The need for a battery management system has increased over the years because the companies are also incorporating more and more motors in their vehicles, for example, Rimac, an electric supercar maker who has successfully developed an electric hypercar by the name of Rimac concept 1, which drives on four motors, each for one wheel. Due to this the battery heat up exponentially, thus becoming less effective in the upper region of the torque curve [7]. Another reason for a battery management system includes increasing the efficiency of the battery and the vehicle, thus increasing the range of the vehicle. Under normal use, an electric vehicle's batteries like to be in the 15 to 35 °C range [6].

1.1 Types of Battery Cooling Systems

The different types of battery thermal management systems are air-cooled, liquid-cooled, PCM-based, thermoelectric and heat pipes. The air cooled is further classified as active and passive, for active air-cooling system, some external means are required to circulate air through cooling channels. In a passive system, the atmospheric air will directly come in contact with the cell surface [9]. Aside from air, the liquid is

another heat transfer fluid that can be used to transmit heat. For thermal management systems, there are two types of liquids. Mineral oil, for example, is a direct contact liquid that can come into direct touch with the battery cells. The other is an indirect contact liquid, such as a combination of ethylene glycol and water, that can only make indirect contact with the battery cells [10]. In a direct contact system, the battery pack is directly submerged in liquid, and in an indirect contact liquid-cooled system, the fluid is circulated through a cooling jacket by some external means [11]. Heat is absorbed by PCM during melting and stored as latent heat until it reaches its maximum. The temperature is held at a melting point for a length of time, and the increase in temperature is postponed. As a result, PCM is employed in battery temperature management systems as a conductor and buffer. To manage the battery temperature, a PCM is always paired with an air-cooling system or a liquid-cooling system [7].

1.2 Innovations in Battery Solutions

Cylindrical lithium-ion batteries are preferred over their counterparts due to their high power density and ability to be produced faster. Hence, the following report summarized various literature of cooling systems for cylindrical batteries [10]. Zhao et al. [10] conducted research around a novel cooling system. The construction of the cooling system is as follows: the battery is enclosed in a cylindrical shell that consists of channels, through which liquid flows, called the liquid cooling cylinder (LCC). A liquid cooling plate (LCP) supplies the cooling liquid to the LCC and acts as a reservoir at the outlet of the LCC. The author investigated four parameters—no of channels, inlet size, mass flow rate and flow direction. The trend observed is that maximum temperature keeps decreasing with an increasing number of channels when the number of channels is greater than 4 up to 8 channels. In the case of maximum temperature difference ΔT , there is a decreasing trend found with increasing channels, but the effect of cooling decreases. In case of inlet size, it can be concluded that the capacity of heat exchange is enhanced first and then weaken along with the rising of entrance size. Flow direction also plays an important role. When the inlet and outlet were located on the same side, there was a change and a decrease in the maximum temperature. However, due to the challenges in designing a circulatory system around this, this method was not advised to be implemented.

Wang et al. [12] modified the above system by designing a transfer contact surface (TCS), which is a diamond curved shape in contact with 3 cells at a time. While investigating mass flow rate, the heat generation process was divided into three time periods: 0–100 s, 100–600 s and 600–720 s. During phase 1, the max temperature and temperature difference rise irrespective of the mass flow rate. In the second phase, the temperature can be kept constant at 1×10^{-4} kg/s. There is not a significant effect of cooling on the decrease of maximum temperature difference. Upon investigating inner diameter, it was found that decreasing inner diameter increases the velocity, which would lead to the assumption of increased heat transfer coefficient. However,

decreasing the diameter decreases the contact surface. Hence, overall, there is little effect of diameter on cooling performance. The Temperature increases gently by decreasing the height of the inlet. The optimum height is obtained when $h = 55$ mm. By increasing the contact angle, the max temperature and temperature difference reduce as the contact area increases.

Jiang et al. [13] investigated the tesla cooling system. However, a critical analysis was conducted, and a comparison was made between two different approaches adopted. In the multiple short channel approach, the U-bend is removed, and two short channels are compared with the long channel. It is observed that the short channels yield a lesser maximum temperature than the u-bend channel. This can be due to the less flow resistance caused due to the U-bend. The magnification of the contact area was also investigated. It was found that there is a decrease in the maximum temperature yield. A greater outcome of the system is the temperature uniformity of the cell obtained. Mahmud et al. [14] implemented the idea of thermoelectric cooling to cool a battery. The thermoelectric module used is connected electrically in series and thermally in parallel. There are aluminum sinks with a cooling fan and channels containing coolant to cool the hot side of the TEC module. Hence, it is a conjunction of Air and liquid cooling. The maximum temperature was investigated, and the test was first conducted without the TEC module, in the presence of water alone and then in the presence of air alone, and then with the TEC module. In comparison, the TEC module showed a drastic reduction in temperature. The cooling rate was found to be double when compared to the water and air only conditions.

Yang et al. [15] implemented a composite PCM (Composite PCM) to cool the battery pack. The C-PCM is made by first melting paraffin, and then it is melted together with expanded graphite. This is done to increase the thermal conductivity of the PCM. Low-density polyethylene is introduced. Upon discharge of the battery pack, it was found that the L-CPCM performs better cooling performance. However, during higher discharge rates above 3C, the temperature of the battery was beyond the safe limit of the lithium-ion battery. To tackle this issue, an aluminium fin was used as a heat sink to dissipate heat further away from the system. Upon experimentation, it was found that the aluminium fin has a positive effect on the cooling performance of the battery. At higher discharge rates, the maximum temperature has been found to be well within the safe limits of the lithium-ion battery. Yulong Ding et al. [16] investigated the use of metallic foam in conjunction with a PCM, and a copper pipe module containing a coolant. In this paper, A comparison is made between paraffin wax alone in the material module and copper foam/paraffin wax (C-PCM) as a material module. After discharge operation at 1800s, the outlet temperature of the copper pipe is more in case of the C-PCM, than in the standalone paraffin setup. The outlet temperature is also found to increase with increasing velocity. In case of the battery surface, the temperature of just PCM was found to rise by 16 degrees to 39 °C. However, in case of C-PCM, the temperature of the battery surface was found to be 25 °C. This is because the metallic copper foam offers greater thermal conductivity, which is less in case of paraffin wax.

From the literature, it is observed that the advantages of liquid cooling systems are as follows: (a) A liquid cooling system helps in effectively controlling the maximum

temperature and temperature difference of the cell. (b) Making use of nanofluids can help control the temperature at a velocity lesser than that used for a normal coolant, hence preventing excessive power consumption. (c) A liquid system can also be used to heat the battery pack in cold countries where ambient temperatures are below the freezing point. Disadvantages of a liquid cooling system are as follows: (a) Due to unforeseen circumstances, accidental leakage of the coolant may occur, leading to damage to the battery pack. (b) A liquid cooling system is heavier compared to other cooling systems. Hence, in order to reduce weight, a microchannel may be used. (c) A liquid cooling system consumes additional power to circulate the coolant across the battery pack. Usage of microchannels in order to reduce weight may increase the pressure drop due to which the power consumption will increase. Despite the disadvantages, the advantages outweigh them, and hence is a system preferred by many automotive companies to implement on a large scale.

2 Methodology

2.1 Modelling and Meshing

3s2p

In the present analysis, a battery pack consisting of six cells is considered. The cell used in the 3s2p configuration as shown in Fig. 1 is 18650 Li-ion cells, the diameter of the cell is 18 mm and length of the cell is 650 mm. The configuration of the battery pack is 3 in series and 2 in parallel. After naming each part of the cell, a battery connection is established by Ansys fluent. The batteries had a centre-to-centre distance of 3 mm across all directions. The cells were placed in an aluminium block. Due to its higher heat transfer coefficient, heat generated by the battery would be rapidly transferred, hence aluminium was selected as the material. Twelve channels were cut out from the aluminium block as represented in Fig. 2, which act as a channel for the coolant to flow through. The geometrical parameters of aluminium block are as follows (Fig. 3): length, breadth and height of the block are 86 mm, 64 mm and 65 mm, respectively. The diameter of the channel pierced through the aluminium block is 8 mm. Figure 1 is the 3D model of Li-ion cell with a 3s2p configuration.

Meshing

The fluid channel and body are meshed using the quad and tri elements. The cell body and cell terminals were meshed using the sweep method and the rest of the body was meshed with tetrahedral cells. The mesh element size is given as $8.49e-003$ m, 4 inflation layer was used near fluid channels in aluminium block to better simulate the effect of the boundary layer. The battery connections are setup using the dual potential Multi Scale Multi Domain (MSMD) model in Ansys. This model solves the potential across two domains: positive and negative zones of the cell. The cell

Fig. 1 Cell arrangement

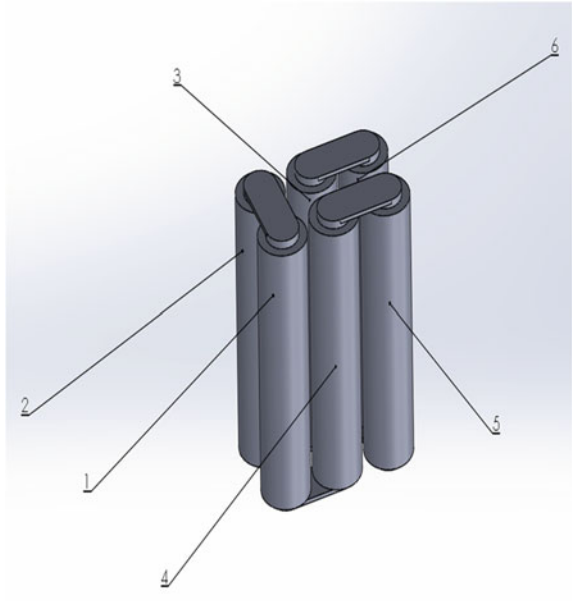
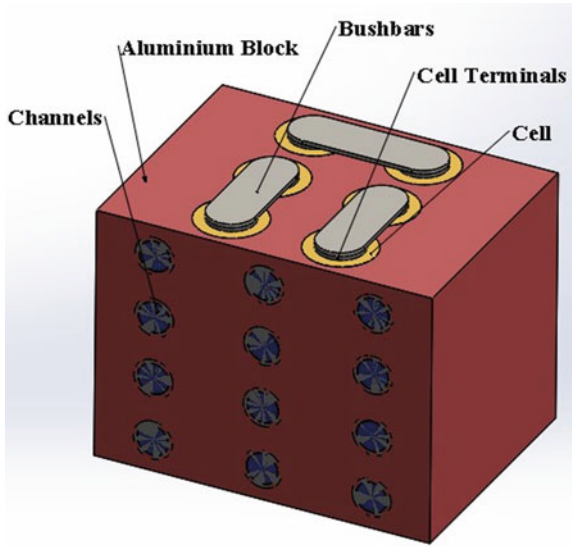
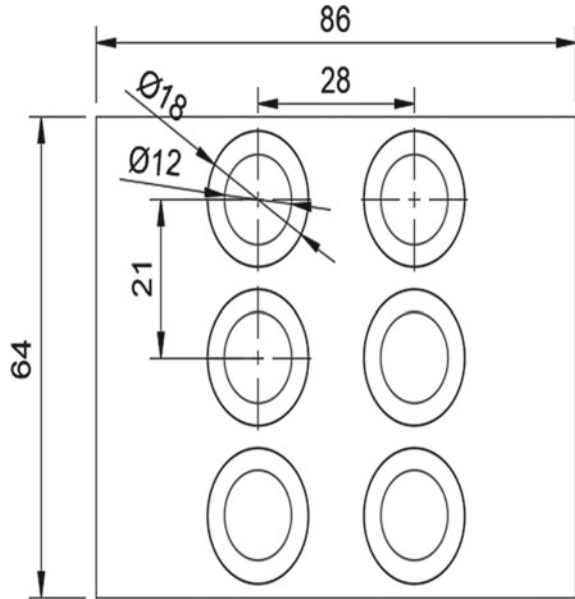


Fig. 2 Entire thermal management system



capacity of a single cell is as follows: Nominal Cell Capacity—3.5 Ah, Min Stop Voltage—2.6 V and Max Stop Voltage—4.2 V.

Fig. 3 Dimensions of thermal management system



2.2 Boundary Conditions

In the given setup, there are 12 inlets and outlets. The inlet values are mass-flow-rate for inlet condition. The inside of the channels was assigned a no-slip condition. The inlet temperature of the fluid is assumed to be at room temperature, i.e., 300 K. The battery pack parameters, as well as materials used for cell, are discussed in Table 1 and Table 2, respectively. The walls of the cell, terminals, and busbars were allotted to the material based on the data given in the Ansys fluent user guide (Table 3). The UDS diffusivity for busbars and terminals is a user-defined function in Ansys. The UDS diffusivity for the cell is $UDS-0 = 1.19e06$, $UDS-1 = 9.83e05$ [17].

2.3 Thermal Behaviour

In this case, LG 18650 cell was investigated. To obtain the thermal behaviour, the dual potential multi-scale multi-domain model is provided within Ansys fluent. In this method, governing equations are solved across two domains to simulate the current drawn, and hence heat generated by the battery is based on various discharge rates. To determine the various coefficients, a voltage versus time graph is obtained for the cells by inserting input using the TUI console. Temperature corrections are obtained using the following equations [17].

Table 1 Battery pack parameters [17]

MSMD parameters		
Parameter	Value	Unit
Cell parameters		
Nominal cell capacity	3.5	mAh
C-rate	1	
Min. stop voltage	2.6	V
Max stop voltage	4.2	V
NTGK polarization parameters		
Initial DOD	0	
Reference capacity	7	mAh
U coefficient: a1, a2, a3, a4, a5	4.19, -1.711, 8.90, -37.28, 62.418, -35.26	
Y coefficient: b1, b2, b3, b4, b5	66.196, -397.891, 2706.86, -7378.21, 8258.162, -3235.86	
Temperature corrections: C1, C2	0,0	

Table 2 Cell material [17]

Density	678	J/kg K
Specific Heat	18.4	W/m-K
Thermal Conductivity	1.19×10^6	kg/m-s
UDS-0	9.83×10^5	kg/m-s
UDS-1	3.541×10^7	Siemens/m
Electrical Conductivity	678	J/kg K

Table 3 Terminal material [17]

Density	8978	kg/m ³
Specific Heat	381	J/kg K
Thermal Conductivity	387.6	W/m-K
UDS diffusivity	Model Defined	kg/m-s
Electrical Conductivity	1×10^7	Siemens/m

$$\frac{\delta_p C_p T}{\delta T} - \nabla \cdot (k \nabla T) = q \quad (1)$$

$$\nabla \cdot (\sigma_+ \nabla \sigma_+) = -j \quad (2)$$

$$\nabla \cdot (\sigma_- \nabla \sigma_-) = j \quad (3)$$

Here, ϕ is electric potential, σ is electric conductivity, and neg and pos refer to negative and positive electrode

$$U = \left[\sum_{n=0}^3 b_n (DOD)^n \right] - C_2 (T - T_{ref}) \quad (4)$$

$$Y = \left[\sum_{n=0}^5 b_n (DOD)^n \right] \exp \left[-C_1 \left(\frac{1}{T} - \frac{1}{T_{ref}} \right) \right] \quad (5)$$

$$U = a_0 + a_1 DOD + a_2 DOD^2 + a_3 DOD^3 + a_4 DOD^4 + a_5 DOD^5 \quad (6)$$

$$Y = b_0 + b_1 DOD + b_2 DOD^2 + b_3 DOD^3 + b_4 DOD^4 + b_5 DOD^5 \quad (7)$$

Here, DOD means the depth of discharge of the cell.

C-rate is the discharge rate at which the battery discharges relative to the maximum battery capacity of the cell. C-rate is calculated using the following formula [19]:

$$C = \frac{\text{Current drawn(A)}}{\text{Capacity(Ah)}} \quad (8)$$

3 Result Analysis

3.1 Thermal Behaviour

3series2parallel configuration

After simulating the given battery pack at 1C and 2C discharge rates, an analysis of the maximum temperature of each cell in the pack was carried out as shown in Figs. 3 and 4.

After simulating the given battery pack at 1C and 2C discharge rates, the maximum temperature difference of each cell in the pack was analyzed as shown in Figs. 3 and 4. From Fig. 5, it is observed that Cell 3 has attained the highest temperature, whereas cell 1 has attained the lowest temperature. It was also observed that the temperature change for all the cells is greater than 15 K for 1C and 28 K for 2C, posing a threat of instability to the battery pack. It is noticed that the battery pack gets heated the most at the centre. Hence, while designing the thermal management system, it was important to make sure the centre of the battery pack is cooled effectively. To summarize the thermal distribution results: (a) The heat is generated due to joule heat and electrochemical heat source. (b) From Fig. 5a, c, it can be concluded that the maximum temperatures go up to 320 K and 335 K for discharge rates of 1C and 2C, respectively, for configuration of 3s2p. (c) It was also interesting to note that the temperatures across the parallel connections were the highest. These temperatures were well beyond the tolerable limit of the lithium-ion battery. Hence, to prevent

Fig. 4 Temperature distribution for 1C

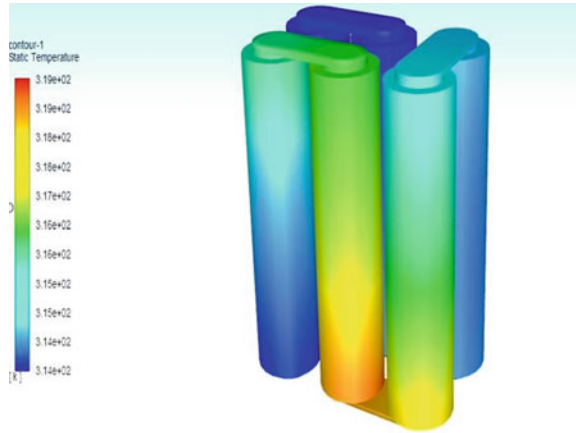
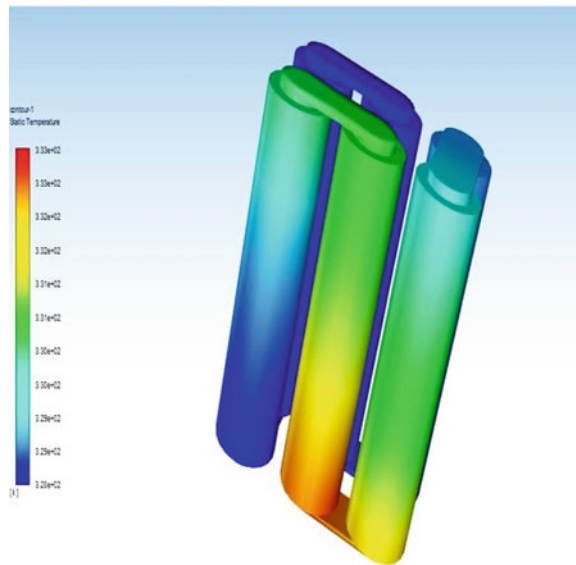


Fig. 5 Temperature distribution for 2C



thermal runaway of the battery, it is important to maintain these temperatures within the optimum operating range of a lithium-ion cell.

3.2 Cooling of 3s2p

Effect of Mass flow rate: In this section, the effect of mass flow rate was investigated. Figure 6 below depict the maximum temperature and temperature difference of the

battery pack with cooling at a discharge rate of 1C and 2C. For the first two minutes of runtime at a discharge rate of 1C, the rise in temperature is the same irrespective of the mass flow rate. This is because the temperature difference between the cell and the fluid is far lesser than the heat generation of the battery. Beyond this, the cooling effect of the mass flow rate influences the temperature of the cell as shown in Fig. 6. For the mass flow rate of $1e-5$ as shown in Fig. 6a, the maximum temperature at the end of the simulation is close to 303 K (5.31% decrease), whereas the maximum temperatures at the end of the simulation time for $1e-4$ and $1e-3$ are 301 K (5.93% decrease) and 300.75 K (6.01% decrease), respectively, for 1C discharge rate. In case of a discharge rate of 2C (Fig. 6c), the mass flow rate of $1e-5$ results in a maximum temperature of 306 K (8.65% decrease), whereas for $1e-4$ and $1e-3$, the maximum temperatures were 302 K (9.85% decrease) and 301 K (10.14% decrease). The temperature difference is defined as the difference between the maximum and minimum temperature of the cell. It is important to maintain a temperature difference as low as possible to prevent thermal runaway issues in the cell. With respect to 1C, for all mass flow rates, the temperature difference lies within 1 K as represented in Fig. 6b. For a discharge rate of 2C, the mass flow rate of $1e-3$ is the most effective, keeping it within 1 K as depicted in Fig. 6d.

Effect of direction of flow

In the following case, the direction of flow for the middle channels has been reversed and its effect has been investigated and compared with the normal flow as depicted in Fig. 7. For this case, a mass flow rate of $1e-4$ was chosen and discharge rates of 1C and 2C were applied. After the simulation, it is noticed that there is not any

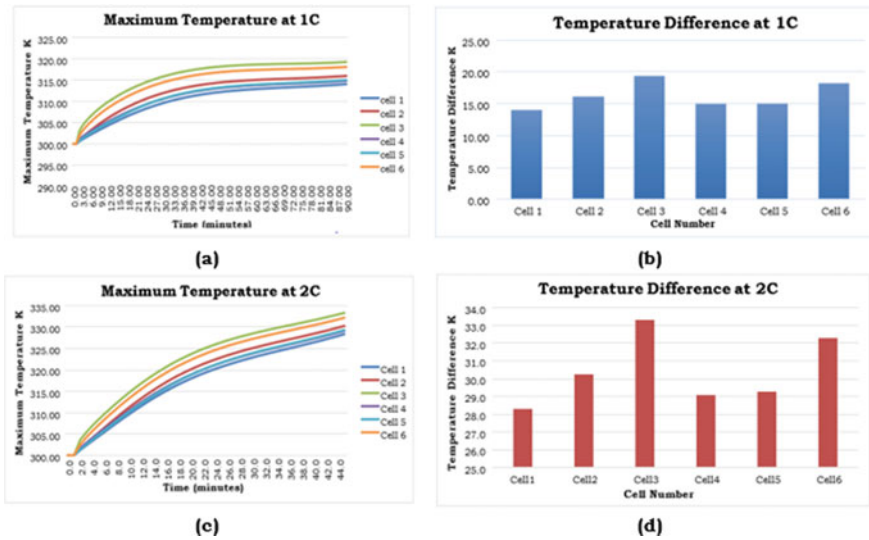


Fig. 6 Maximum temperature at (a) 1C Rate (c) 2C rate and temperature difference of the individual cell at (b) 1C (d) 2C without a thermal management system

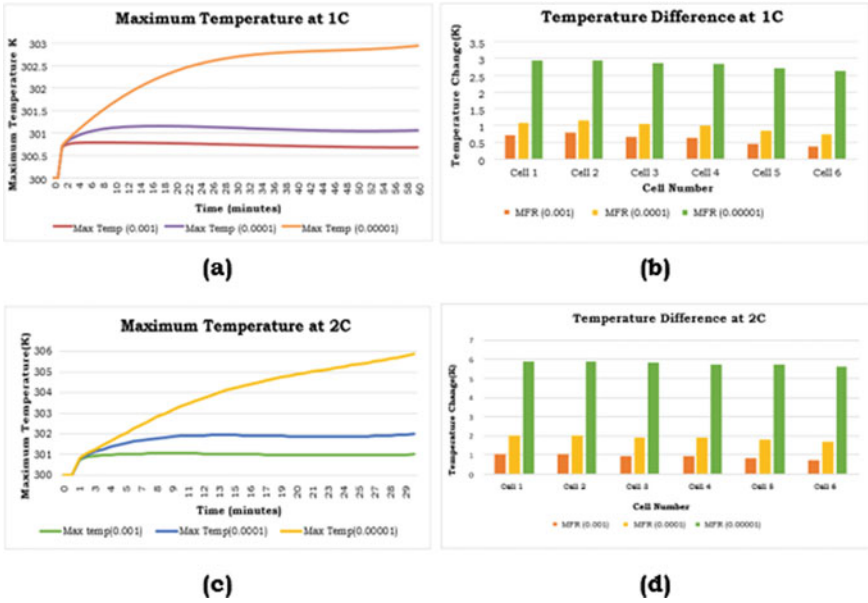


Fig. 7 Maximum temperature at (a) 1C Rate (c) 2C Rate and Temperature difference of the individual cell at (b) 1C (d) 2C with thermal management system at different mass flow rates

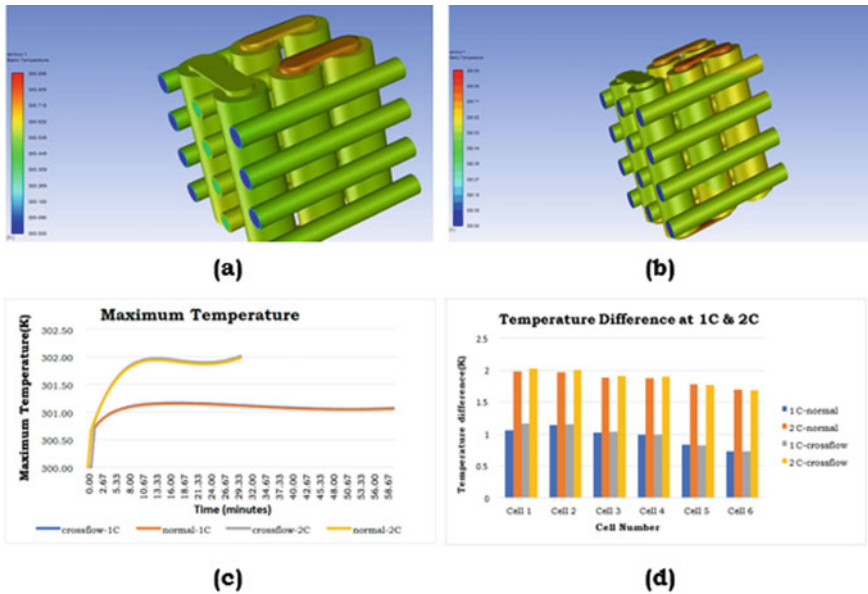


Fig. 8 Temperature distribution at (a) 1C Rate (b) 2C Rate and comparison of maximum temperature rise as well as Temperature difference at normal flow and crossflow (b) 1C (d) 2C

significant effect of the flow direction on the temperature and temperature difference of the battery pack as represented in Fig. 7.

4 Conclusion

Due to thermal issues surrounding lithium-ion batteries, the efficiency of the battery pack is reduced and the cost of the battery pack is increased. Hence, to solve these issues, a cooling system is the need of the hour. A lithium-ion cell best operates in the range of 20–35 °C. Hence, the objective of the liquid thermal management system is to maintain the temperature of these cells in a safe operating range. First, the discharge rates were chosen, in this case, 1C and 2C, and the temperatures were recorded. (a) From the results obtained, it can be concluded that the maximum temperatures go up to 320 K and 335 K for discharge rates of 1C and 2C, respectively, for configuration of 3s2p. (b) After this, the battery pack is subjected to a liquid thermal management system of various mass flow rates and recorded. For the mass flow rate of 1e-5, the maximum temperature at the end of the simulation is close to 303 K (5.31% decrease), whereas the maximum temperatures at the end of the simulation time for 1e-4 and 1e-3 are 301 K (5.93% decrease) and 300.75 K (6.01% decrease), respectively, for 1C discharge rate. In case of a discharge rate of 2C, the mass flow rate of 1e-5 results in a maximum temperature of 306 K (8.65% decrease), whereas for 1e-4 and 1e-3, the maximum temperatures were 302 K (9.85% decrease) and 301 K (10.14% decrease). (c) A crossflow design is adopted and was compared with the normal flow. It is observed that there is no significant effect of flow direction on temperature.

References

1. Khurana A, Kumar VVR, Sidhuria M (2020) A Study on the Adoption of Electric Vehicles in India: The Mediating Role of Attitude. *Vision* 24(1):23–34. <https://doi.org/10.1177/0972262919875548>
2. Gelmanova ZS et al (2018) Electric cars. Advantages and disadvantages. *J Phys Conf Ser* 1015(5). <https://doi.org/10.1088/1742-6596/1015/5/052029>.
3. Iclodean C, Varga B, Burnete N, Cimerdean D, Jurchiş B (2017) Comparison of different battery types for electric vehicles. In: *IOP Conf. Ser. Mater. Sci. Eng.*, vol 252, no 1. <https://doi.org/10.1088/1757-899X/252/1/012058>.
4. Scrosati B, Garche J (2010) Lithium batteries: Status, prospects and future. *J Power Sources* 195(9):2419–2430. <https://doi.org/10.1016/j.jpowsour.2009.11.048>
5. Miles MH (2008) Lithium batteries using molten nitrate electrolytes, 3:39–42. <https://doi.org/10.1109/bcaa.1999.795958>
6. Smith J, Singh R, Hinterberger M, Mochizuki M (2018) Battery thermal management system for electric vehicle using heat pipes. *Int J Therm Sci* 134(June 2017):517–529. <https://doi.org/10.1016/j.ijthermalsci.2018.08.022>
7. Katoch SS, Eswaramoorthy M (2020) A detailed review on electric vehicles battery thermal management system. In: *IOP Conf. Ser. Mater. Sci. Eng.*, vol 912(4). <https://doi.org/10.1088/1757899X/912/4/042005>

8. Nitta N, Wu F, Lee JT, Yushin G (2015) Li-ion battery materials: present and future. *Mater Today* 18(5):252–264. <https://doi.org/10.1016/j.mattod.2014.10.040>
9. Li J, Zhu Z, Zhu Z (2014) Battery thermal management systems of electric vehicles, 79
10. Zhao J, Rao Z, Li Y (2015) Thermal performance of mini-channel liquid cooled cylinder-based battery thermal management for cylindrical lithium-ion power battery. *Energy Convers Manag* 103:157–165. <https://doi.org/10.1016/j.enconman.2015.06.056>
11. Deng Y et al (2018) Effects of different coolants and cooling strategies on the cooling performance of the power lithium ion battery system: a review. *Appl Therm Eng* 142(April):10–29. <https://doi.org/10.1016/j.applthermaleng.2018.06.043>
12. Lai Y, Wu W, Chen K, Wang S, Xin C (2019) A compact and lightweight liquid-cooled thermal management solution for cylindrical lithium-ion power battery pack. *Int J Heat Mass Transf* 144:118581. <https://doi.org/10.1016/j.ijheatmasstransfer.2019.118581>
13. Zhao C, Sousa ACM, Jiang F (2019) Minimization of thermal non-uniformity in lithium-ion battery pack cooled by channeled liquid flow. *Int J Heat Mass Transf* 129:660–670. <https://doi.org/10.1016/j.ijheatmasstransfer.2018.10.017>
14. Lyu Y, Siddique ARM, Majid SH, Biglarbegian M, Gadsden SA, Mahmud S (2019) Electric vehicle battery thermal management system with thermoelectric cooling. *Energy Rep* 5:822–827. <https://doi.org/10.1016/j.egy.2019.06.016>
15. Lv Y, Yang X, Li X, Zhang G, Wang Z, Yang C (2016) Experimental study on a novel battery thermal management technology based on low density polyethylene-enhanced composite phase change materials coupled with low fins. *Appl Energy* 178:376–382. <https://doi.org/10.1016/j.apenergy.2016.06.058>
16. Zhao Y, Zou B, Li C, Ding Y (2019) Active cooling-based battery thermal management using composite phase change materials. *Energy Procedia* 158:4933–4940. <https://doi.org/10.1016/j.egypro.2019.01.697>
17. Gümüŝsu E, Ekici Ö, Köksal M (2017) 3-D CFD modeling and experimental testing of thermal behavior of a Li-Ion battery. *Appl Therm Eng* 120:484–495. <https://doi.org/10.1016/j.applthermaleng.2017.04.017>
18. Ravnik J, Kerget L, Hriberek M (2010) Analysis of three-dimensional natural convection of nanofluids by BEM. *Eng Anal Bound Elem* 34(12):1018–1030. <https://doi.org/10.1016/j.enganabound.2010.06.019>
19. Zhang H, Li C, Zhang R, Lin Y, Fang H (2020) Thermal analysis of a 6s4p Lithium-ion battery pack cooled by cold plates based on a multi-domain modeling framework. *Appl Therm Eng* 173(December 2019):115216. <https://doi.org/10.1016/j.applthermaleng.2020.115216>

Implementation of Multi-carrier Modulation Techniques to Increase Image Quality for Underwater Sonar Image Transmission



Rishav Kumar Kedia, Aditi Goyal, Rohan Vashishtha, and G. Swetha

Abstract Sonar image transmission is very important for undersea expeditions as it has many applications in real world but it is very tough due to the limited bandwidth and multi-path fading. Therefore, to improve the quality of multi-carrier modulation for the purpose of sonar image transmission, various techniques are implemented. Dual-tree complex wavelet transform-based OFDM (Orthogonal Frequency Division Multiplexing), discrete wavelet transform-based OFDM, and conventional OFDM are implemented. The results show that DTCWT-OWDM and DWT-OFDM perform much better than conventional OFDM with improved Peak Signal-to-Noise Ratio (PSNR) and Peak-to-Average Power Ratio(PAPR).

Index Terms OFDM · OWDM · AWGN channel · DTCWT

1 Introduction

Sonar image transmission is considered very important for undersea expeditions as it has many applications in real world such as ocean rescue and locating underwater debris. Image quality that has many applications in various fields such as medical imaging, underwater debris, and many others is taken as the main parameter. This also finds application in underwater communication in times of medical emergency, war threats, and other such conditions where the quality and clarity of the image play an important role. It is essential in such conditions that the image transmission be prompt and the received image be as limitedly distorted as can be. Another important parameter is PAPR which stands for peak power to average power ratio. Large PAPR causes nonlinear distortions of signals and nonorthogonality of signal of sub-carrier and produce peak power value of signal so the performance of OFDM system will

R. K. Kedia (✉) · A. Goyal · R. Vashishtha
B. Tech ECE Department, PES University, Bangalore, India
e-mail: rishav267@gmail.com

G. Swetha
Department of ECE, PES University, Bangalore, India

decrease. It also causes difficulty in the implementation of power amplifiers and high cost of implementation.

To overcome these points, new techniques are implemented and compared with OFDM. Underwater acoustic channel is most preferably used for underwater communication as electromagnetic waves get attenuated at a very fast pace in underwater condition.

2 Single-carrier FDMA

FDMA stands for frequency division multiple access systems. It is also called linear pre-coded OFDMA (LP-OFDMA). It usually deals in shared communication resource in which multiple users are assigned. SC-FDMA can also be taken as linearly pre-coded OFDMA scheme which means additional DFT processing step is added when compared to conventional OFDMA processing.

SC-FDMA is considered an alternate to OFDMA as it has lower peak to average power which is very useful for mobile terminals when we talk about transmit power efficiency. SC-FDMA utilizes frequency domain quantization at receiver and single-carrier modulation at transmitter and it has same overall structure as OFDMA.

In a single-carrier modulation system, the symbol period must be greater than the delay time to avoid ISI. Since the data rate is inversely proportional to the symbol period, it means having a long symbol period is low data rate and communication inefficiency. ISI which stands for inter-symbol interference is desired to be avoided, therefore symbol period must be greater than delay time in single-carrier modulation system. Long symbol period is inversely proportional to data rate which indicates that long symbol period leads to system inefficiency as low data will be there.

3 Multi-carrier Modulation

MCM or multi-carrier modulation system is very useful in sending data more efficiently with less corruption of data. The principle used in MCM is division of stream into multiple sub-stream to transmit data at a lower rate and uses these sub-streams to modulate several carriers. First, such a system was developed by military in the 1950s–1960s. Earlier conducted experiments indicate that the selection of modulation technique is critical for wireless data transmission.

Carriers are placed closely in spectrum to achieve a high overall data rate. This sometimes leads to interference between them which is known as ICI which stands for inter-carrier interference. To avoid this condition, guard bands are placed between adjacent sub-carriers.

OFDM is a key technology used in multi-carrier digital communication scheme to address both the issues. The orthogonal nature of sub-carriers gives reason for closely

spaced sub-carriers and even overlapped without ICI. OFDM usually combines a large number of low data rate carriers to composite communication system.

4 Orthogonal Frequency Division Multiplexing

OFDM is the most used multi-carrier modulation technique and it is a type of digital transmission and method of putting into code the digital data on multiple carrier frequencies. Wideband or frequency selective is tough channel and OFDM has emerged as a key technology in recent times and famous strategy for these types of channel sand is used in applications like television (digital) and for audio broadcasting, 4G mobile communications, and wireless networks. The principle by which OFDM works is by dividing or splitting the signal into multiple sub-signals that are transmitted to receiver at different frequencies simultaneously. OFDM provides a high degree of spectral efficiency and is very buoyant to selective fading, interference, and multi-path effects as OFDM uses a huge number of carriers with each carrier having low bit rate data. OFDM has various advantages and one such advantage is its ability to cope with severe channel conditions without complex equalization filters over a single-carrier scheme. In case of OFDM, channel equalization simplifies as it may be viewed as using many slowly modulated narrowband signals instead of one rapidly modulated wideband signal. However, OFDM requires strict synchronization between the receiver and transmitter because sub-carriers lose orthogonality between them due to frequency deviation which leads to inter-carrier interference. The main cause of frequency offsets are mismatched transmitter and receiver oscillators or even by Doppler shift due to movement.

High-rate serial data stream is split up into many low rate sub-streams in parallel transmission technique (OFDM) and each sub-stream is modulated on a separate sub-carrier. When the sub-carriers have enough spacing to satisfy orthogonality, their spectra will overlap. Sub-carrier spectra overlap when sub-carriers have enough spacing and satisfy orthogonality. The main aspect of OFDM is maintaining the orthogonality of the sub-carriers. The equation for orthogonality is

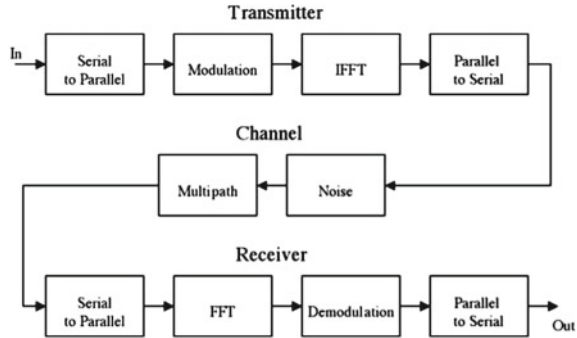
$$\int_0^{n/2} \cos(2\pi f m t) \cos(2\pi f n t) dt = 0 \quad m \neq n \quad (1)$$

OFDM system removes Intersymbol Interference (ISI) by allocating sub-carrier frequencies such that they are integer multiples of the symbol rate. By dividing the total available bandwidth into independent sub-channels, multiple access is achieved by distributing sub-channels between users (Fig. 1).

Some important techniques used throughout the OFDM system are explained below.

- (1) **FFT**: It stands for fast Fourier transform. It is an algorithm that computes the discrete Fourier transform of a sequence or its inverse. An FFT rapidly

Fig. 1 Block Diagram for OFDM



computes transformations by factorizing the DFT matrix into a product of sparse factors. It takes time domain input data and converts it into frequency domain data.

- (2) *IFFT*: It stands for inverse fast Fourier transform. It takes frequency domain input data and converts it into time domain data. The IFFT block provides a simple way to modulate data on to N orthogonal sub-carrier. It is also known as backward Fourier transform.
- (3) *Orthogonality*: If the integral of the product of two signals is zero, the signals are said to be orthogonal. The equation we are using here is:

$$\int_0^{n/2} \cos(2\pi f_0 mt) \cdot \cos(2\pi f_0 nt) dt = 0 \quad m \neq n \quad (2)$$

- (4) *Constellation Mapping*: It is a procedure to map the number of bits to symbols after converting them into parallel blocks (bits) from serial bits. Symbols are present in the IQ plane (frequency domain). After using IFFT, each group of symbols is moved from the IQ plane to time domain. Some examples are BPSK, QAM, etc. (Fig. 2).
- (5) *Modulation*: Modulation means imposing the input signal which has low frequency on carrier wave of high frequency, so it can travel through the channel efficiently.
- (6) *QAM*: It stands for quadrature amplitude modulation. It's a name of a family of digital modulation methods and related family of analog modulation method (Figs. 3 and 4).

Various modulation techniques used:

- (6.1) *4-QAM*: 4 QAM stands for 4 quadrature amplitude modulation. In this type of modulation, 2 bits are present per symbol yielded by 2 in-phase values and 2 quadrature values. 4 QAM takes more time to transmit data than any other QAM technique but it has the best BER when compared with every other technique.
- (6.2) *16-QAM*: 16 QAM stands for 16 quadrature amplitude modulation. In 16 QAM, 4 bits per symbol are presently yielded by four I values and

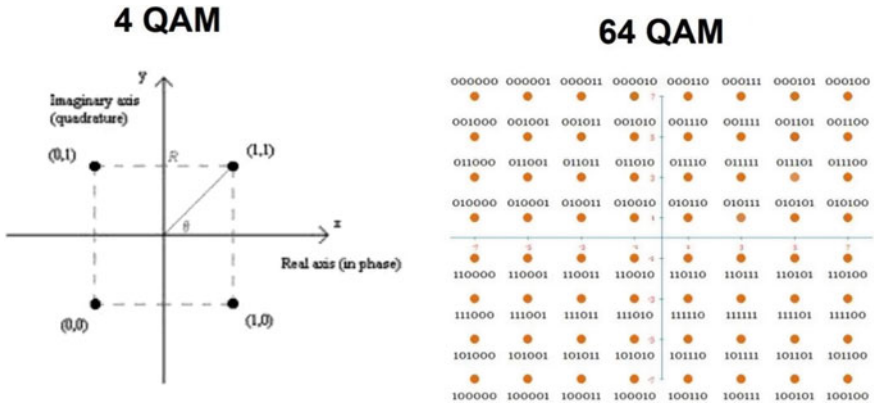


Fig. 2 Constellation mapping

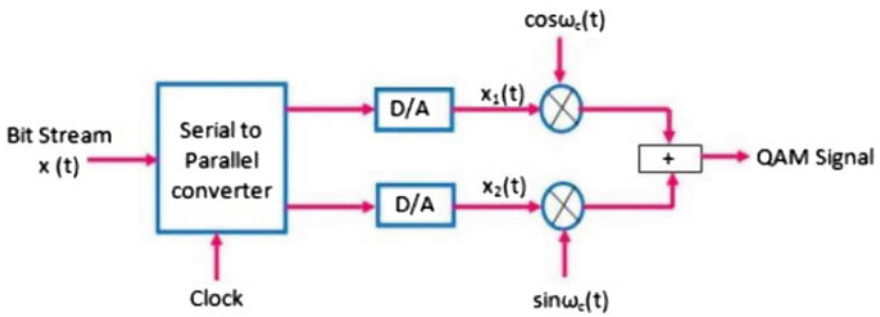


Fig. 3 QAM modulation

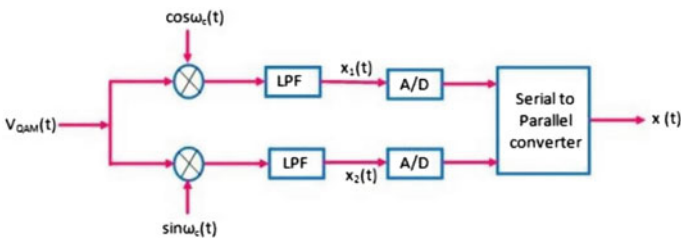
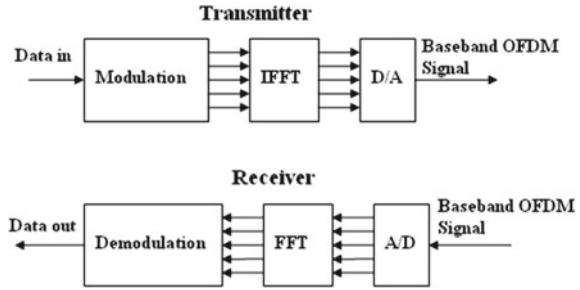


Fig. 4 QAM demodulation

four Q values where I stands for in-phase and Q stands for quadrature. 4bits/second/Hz is the theoretical bandwidth efficiency for 16 QAM. 16 QAM has 4-bits symbols, so to encode our 12 bits, we break them into three groups of four, thereby using three symbols. It takes less time but the bit error rate is more than 4 QAM.

Fig. 5 Uncoded OFDM block diagram



- (6.3) *64-QAM*: 64 QAM is another quadrature modulation scheme which gives 64 signal combinations and has 6 bits per symbol. Transmission rate is six times the signal rate in this type of complex modulation scheme. To encode 12 bits in 64 QAM, we break 12 bits strings into two symbols each having 6 bits as it has dense symbols. It is used for high data rate transmission at the expense of a more bit error rate as constellation diagram has closely packed symbols which is more prone to noise.
- (6.4) *256-QAM*: 256 QAM is the scheme which has 8 bits per symbol. This scheme provides the highest data rate and it is very fast but due to the closely compact constellation diagram, it is more prone to error and has the highest BER when compared to above-mentioned schemes. To encode 8 bits data, it uses only one symbol whereas schemes like 4 QAM and 16 QAM use 4 symbols and 2 symbols, respectively.

The OFDM system is one among the modern techniques which are most abundantly used in next-generation wireless communication networks for transmitting many forms of digital data in an efficient manner.

5 Uncoded OFDM

This is a basic type of OFDM which consist of the following transmitter and receiver (Fig. 5).

6 Proposed System

Our project is split into three main sub-tasks:

- (a) Many different modulation schemes based on OFDM, namely, 4QAM, 16 QAM, 64QAM, and 256 QAM separately. Each of these schemes is explained above.
- (b) AWGN/UWA channel.

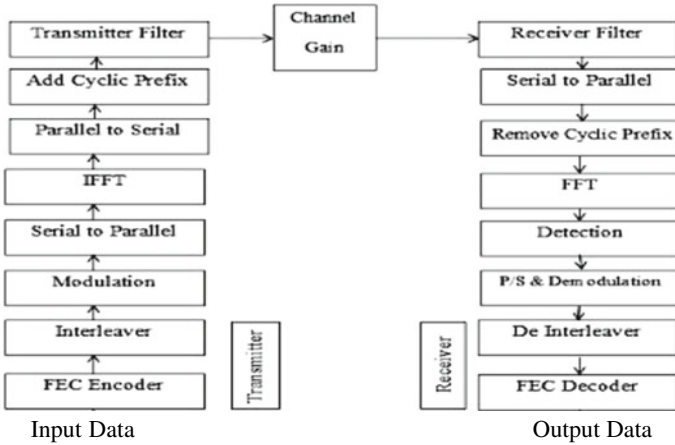


Fig. 6 Coded OFDM Block Diagram

(c) Calculation of PSNR BER and PAPR.

(A) *Coded OFDM:*

This is the type of OFDM which we are using in our project.

In this scheme, data is taken as input bits and divided into multiple packets and encoded convolutionally. After that interleaving of data is done using matrix interleaver and pilot insertion is used for channel estimation. It also includes cyclic prefix which is responsible for synchronization of sub-carriers between receiver and transmitter to overcome the effect of ISI and to maintain orthogonality (Fig. 6).

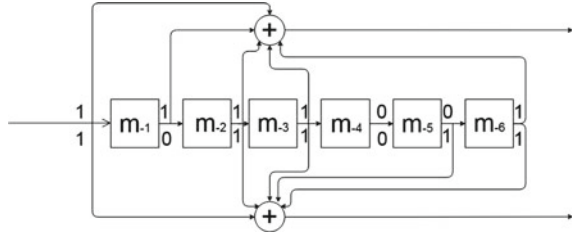
(B) *Convolutional Encoding:*

Convolutional encoding is used as error-correcting code. Convolution encoding uses sliding operation feature of a Boolean polynomial function to generate parity symbols to a data stream. “Convolutional encoding” term is used as the sliding application represents encoder convolution with data. Convolution codes’ sliding nature facilitates trellis decoding by using time-invariant trellis. With reasonable complexity, convolutional codes are to be maximum likelihood softdecision decoded which is allowed by time-invariant trellis decoding.

The major benefit of convolutional codes is their ability to perform economical maximum likelihood soft decision decoding. Base code rate and the depth of the encoder are characteristics of convolutional codes. The base rate is defined as n/k , where k is the output symbol rate and n is the input data rate. Depth or memory of encoder is also called “constraint length” where output is a function of previous and current inputs.

Reliable data transfer is achieved using convolutional codes.

Fig. 7 Shift register for the (7,[171 133]) convolutional code polynomial



Some of the most used convolutional codes are given below:

- (1) Constant length = 5 Polynomials = [35 23]
- (2) Constant length = 6 Polynomials = [51 73]
- (3) Constant length = 7 Polynomials = [171 133]
- (4) Constant length = 8 Polynomials = [371 247]
- (5) Constant length = 9 Polynomials = [753 561]

As we increase constant length, the BER of system decreases but the complexity of system increases exponentially. So basically, there is the trade-off between BER and complexity of system.

In our project, we have used constant length = 7 with polynomials [171 133] to get the best result with respect to both BER and complexity of system (Fig. 7).

(C) Trellis:

Trellis is a vertical representation of nodes in slices(time) where each node is connected to at least two nodes. One node represents the earlier time and the other represents the later time. Trellis can be used as encoder and decoder for encryption and communication theory. The data symbol in each node will be the combination of 0s and 1s (00,01,10,11) (Fig. 8).

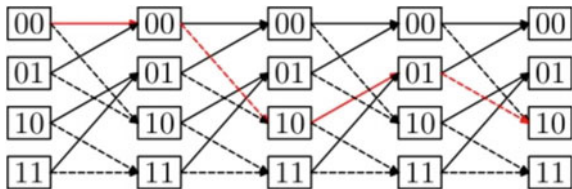
(D) Interleaver:

A technique which is used to convert a transmission channel into memory-less channel. Interleaving process is used as coded data is passed through this process to increase the performance of forward error correction in presence of burst errors.

Alteration of input symbol sequence at transmitter is the main function of interleaver. At the receiving side, input to de-interleaver is altered to get the original signal.

(E) Pilot Insertion:

Fig. 8 Convolutional code trellis diagram



Pilot insertion is used for channel estimation.

In our project, we are using 256 sub-carriers out of which 192 are payload sub-carriers and 8 are used as pilot insertion. Therefore, we are using 1 pilot sub-carriers at every 25th position.

(F) Cyclic Prefix:

Cyclic prefixes are used as guard band to reduce ISI. Cyclic prefix makes channel estimation easy by combating multipath effects. Usage of cyclic prefix is a key element in enabling the OFDM signal to operate reliably. In our project, we have taken 1/4 of the total sub-carriers as cyclic prefix.

7 Channel

AWGN Channel stands for “Additive White Gaussian Noise. It is one of the most basic noise models used in Information Theory and communication systems to replicate the results of many random processes in real world that occur naturally. The terms refer to the specific features of the noise”:

“**Additive**” as it just gets numerically added to any other noise that might be present in the communication system.

“**White**” as it has uniform power across all the frequency bands of the communication system.

“**Gaussian**” as the channel has a normal distribution in the time domain. It has a mean equal to zero.

AWGN is very frequently used as a channel in various real-world models for various experiments. The only difficulty it introduces is a linear addition of white noise. It has a Gaussian distribution of amplitude.

UWA Channel: UWA channel stands for Underwater Acoustic channel and it is considered as the toughest means of communication. Signal is propagated through the means of sound as the speed of sound underwater is 1500m/s. UWA channel has various noises such as thermal noise, wave noise, turbulence noise, and shipping noise. In our project, we have considered a calm water body with only the effect of thermal noise.

Thermal noise varies with temperature and distance of the link. Transmission of data is very tough underwater and leads to a higher bit error rate and distortion of signal, therefore, we have used 4 QAM in our project which uses 2 bits per symbol and provides the least BER among all techniques applied in our project.

Underwater channel has the following parameters:

- (1) *Multipath:* Multipath arises from either wave reflection from the surface, bottom, and other objects, or wave refraction caused by sound speed variations with depth. Acoustic waves always bend towards regions where the propagation speed is lower. Multipath propagation can severely deteriorate the acoustic signal as it generates ISI.

Table 1 Parameters for UWA channel

Channel parameters	Specifications
Speed of sound (m/s)	1500
Total subcarriers	256
Bandwidth (KHz)	10
Channel length (m)	1000
Modulation scheme	4QAM

- (2) *Propagation loss*: UWA channel propagation loss is affected by three parameters characterizing the geometrical spreading, attenuation, and the abnormality of spreading.
- (3) *Ambient noise*: The significant factors on the level of the UWA channel ambient noises are shipping, turbulence, wind waves, and thermal noise.
- (4) *Doppler shift*: A Doppler shift in the UWA channel is very challenging and it is relevant to the frequency shift and low propagation speed (Table 1).

8 Peak Signal-to-Noise Ratio (PSNR)

PSNR stands for Peak signal-to-noise ratio. It is a metric that compares the luminance value of pixel coefficients of test and reference images and shows the difference between them. The difference is computed as an assessment of image quality. The PSNR is calculated by the following equation with mean square error (MSE):

$$\text{PSNR}(I, \bar{I}) = 10 \times \log_{10} 255^2 / \text{MSE}(I, \bar{I}) (\text{dB}), \quad (3)$$

where I and \bar{I} represent the pixel values of test image and reference image, respectively.

The term PSNR is an expression for the ratio between the maximum possible value (power) of a signal and the power of distorting noise that affects the quality of its representation.

9 Bit error rate (BER)

Bit error rate is used as an assessment of data transmitted and received. When we send bits through channel, noise is added to some bits causing distortion and corruption of data. The more the BER, the more is the corruption of signal. Bit error ratio is a unitless performance measure.

BER is given by

BER = Number of errors in received bits/total number of bits sent

10 Results

(A) *Input and Output Images*

Performance comparison between uncoded and coded OFDM (Figs. 9, 10, 11, 12, and 13).

(1) Baboon

Observations: Coded OFDM is outperforming uncoded OFDM in MSE

OBSERVATION: Coded OFDM is outperforming uncoded OFDM (Figs. 14, 15, 16, and 17)

Observations: Coded OFDM outperforms uncoded OFDM

Fig. 9 BABOON



Fig. 10 Uncoded OFDM
output image

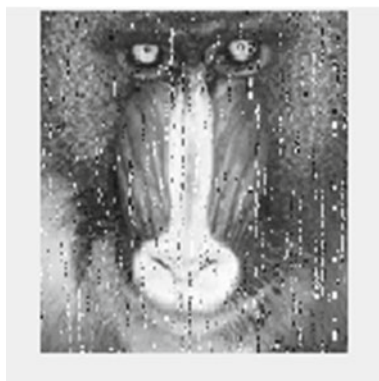




Fig. 11 Coded OFDM output image

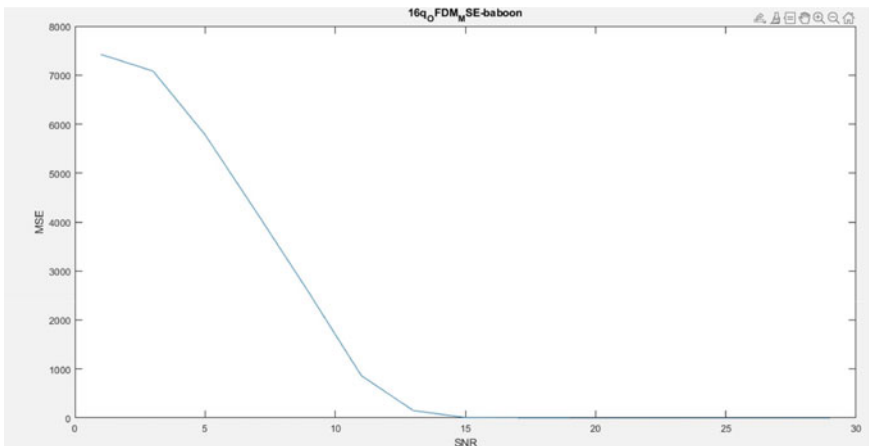


Fig. 12 Coded OFDM MSE

11 Results

By seeing the above observations, we can conclude that coded OFDM outperforms uncoded OFDM in all three parameters which are PSNR, BER, and MSE.

Coded OFDM with various modulation techniques.

Input and Output Images

(1) Baboon

Observation: AT SNR = 14 Db, best image quality is of 4 QAM when SNR is lower and as we increase SNR value 16 QAM is best with less time and high-quality image (Figs. 18, 19, 20, 21, and 22).

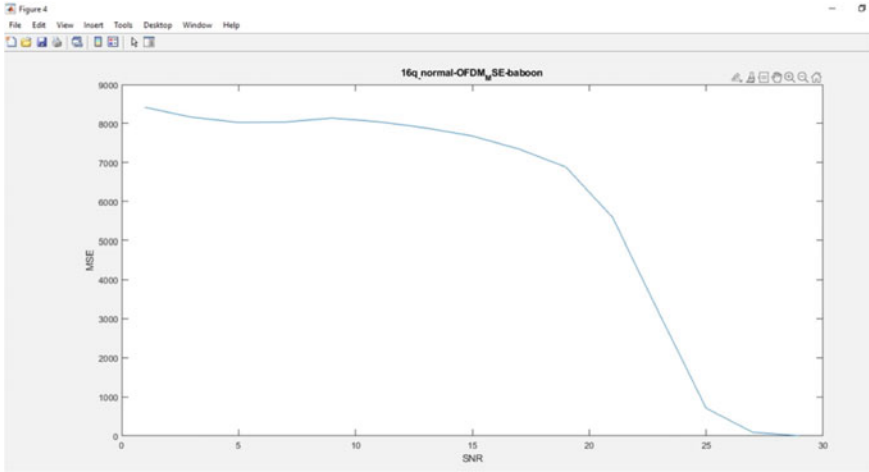


Fig. 13 Uncoded OFDM MSE

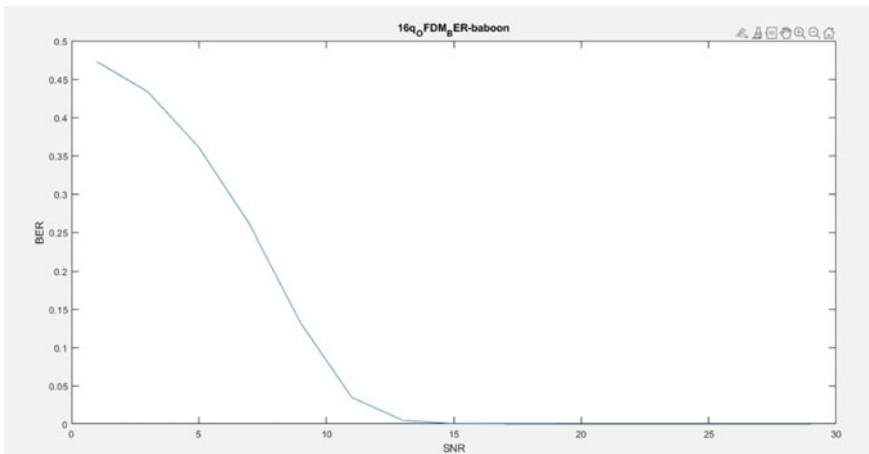


Fig. 14 Coded OFDM BER

Observations: 4 QAM outperforms every other modulation technique in terms of BER when the SNR value is low (Figs. 23, 24, 25, and 26).

Observations: 4 QAM outperforms every other modulation technique in terms of MSE when the SNR value is low (Figs. 27, 28, 29, and 30).

Observations: 4 QAM outperforms every other modulation technique in terms of PSNR when the SNR value is low (Figs. 31, 32, 33, and 34).

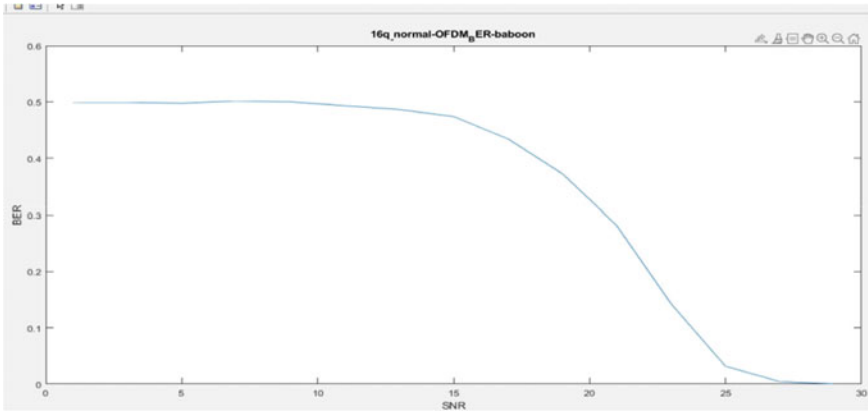


Fig. 15 Uncoded OFDM BER

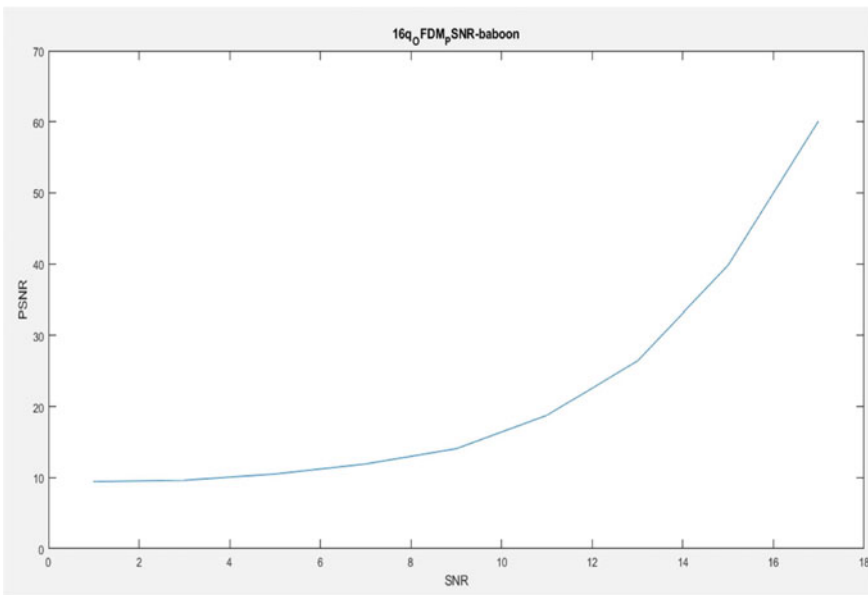


Fig. 16 Coded OFDM PSNR

12 Peak-to-Average Power Ratio (PAPR)

The ratio of peak power of the signal to average power of the signal is known as PAPR. It is desired to reduce the PAPR for better efficiency and use lesser power for transmission (Table 2).

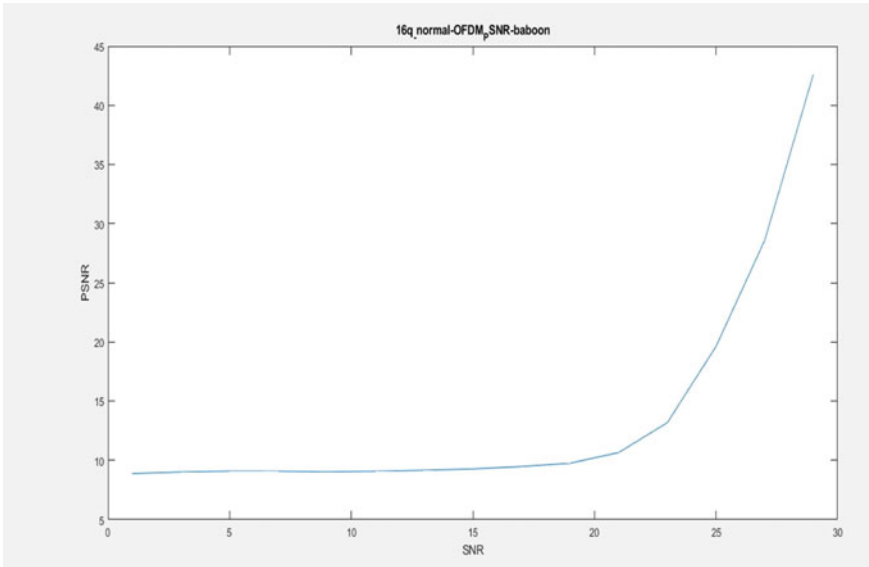
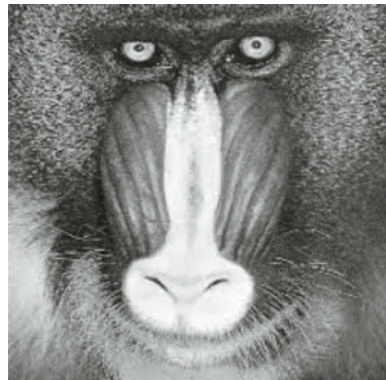


Fig. 17 Unencoded OFDM PSNR

Fig. 18 Input image



$$\text{PAPR}(x(t)) = \max(|x(t)|^2) / E\{|x(t)|^2\} \tag{4}$$

13 Results

4 QAM outperforms other modulation techniques in terms of BER, PSNR, and PAPR when SNR is lower but the time taken is too long. So, there is a trade-off between throughput and quality of signals. As we increase the modulation value, the symbols

Fig. 19 4-QAM SNR = infinity



Fig. 20 16 QAM PSNR = 60.5

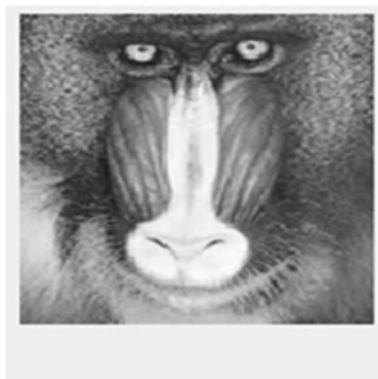


Fig. 21 64 QAM, PSNR = 37.5





Fig. 22 256 QAM PSNR = 19.6

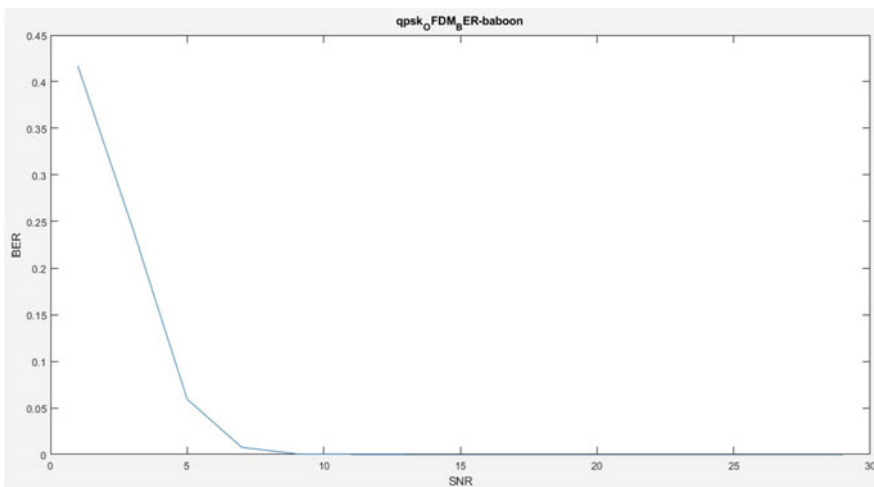


Fig. 23 4-QAM BER

come closer to each other which leads to more noise errors. Therefore, we conclude for higher SNR 16 QAM is best for AWGN. But BER is the highest in UWA channel and noise is very prominent, and sending more bits per symbol will lead to higher distortion and BER, therefore, we choose 4 QAM.

UWA CHANNEL OUTPUT (4 QAM AND 256 SUBCARRIERS) (Figs. 35, 36, 37, and 38):

Observations: By Observing the above values and graphs, we can conclude that distortion is very high in underwater channels and it is very tough to communicate and transmit images underwater as PSNR for 4 QAM is 10.6 and image quality is not good as in case of AWGN. 4 QAM is the best technique for underwater communication as

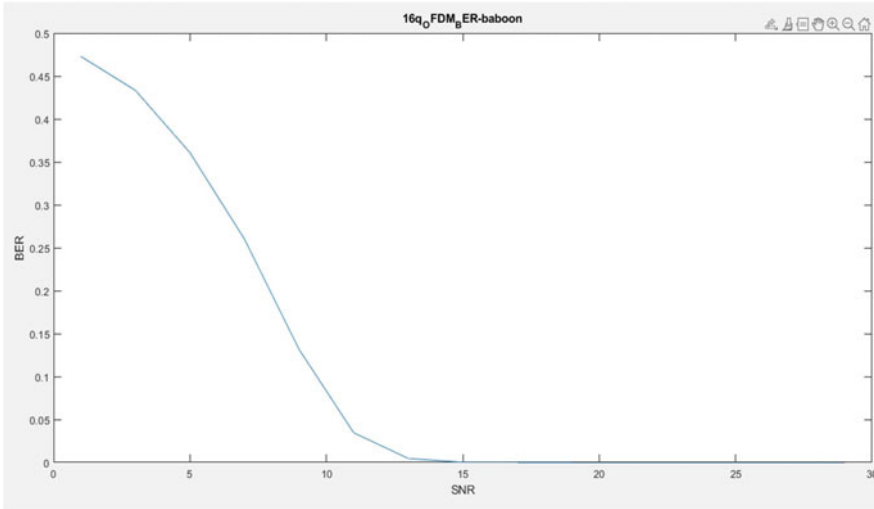


Fig. 24 16-QAM BER

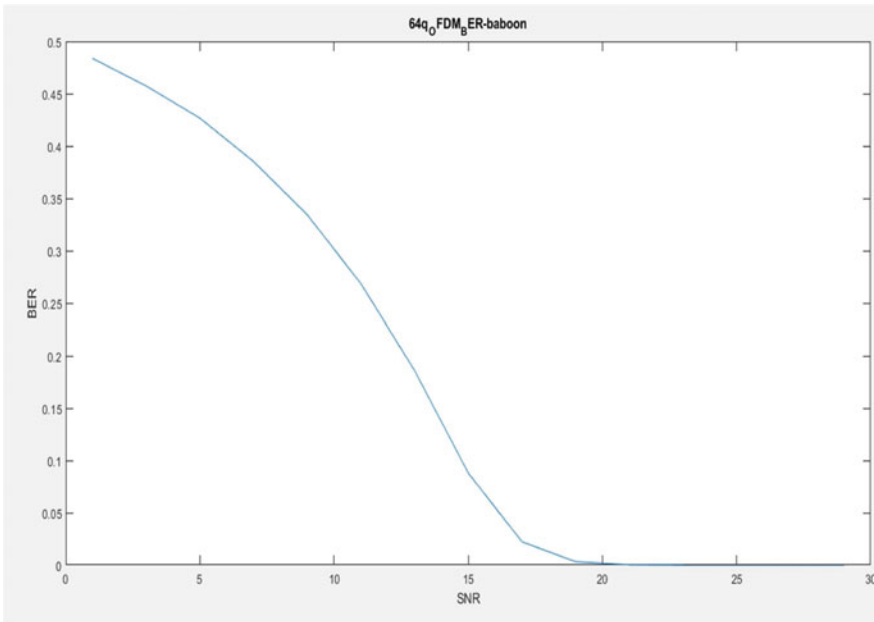


Fig. 25 64 QAM

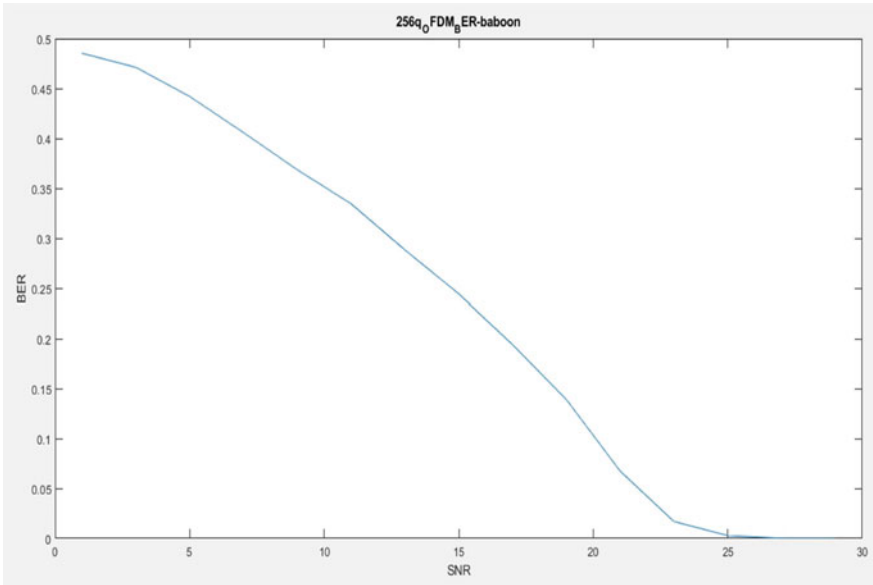


Fig. 26 256 QAM BER

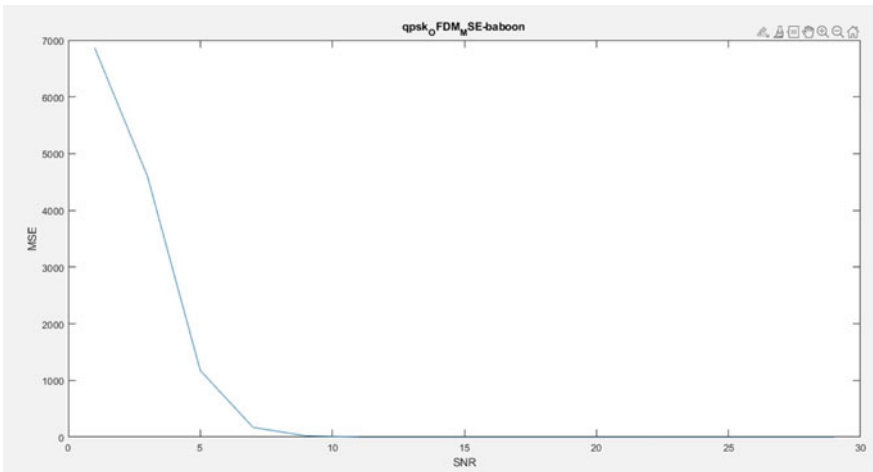


Fig. 27 4-QAM MSE

higher modulation schemes gives very distorted and corrupt images because of the noise present in underwater communication.

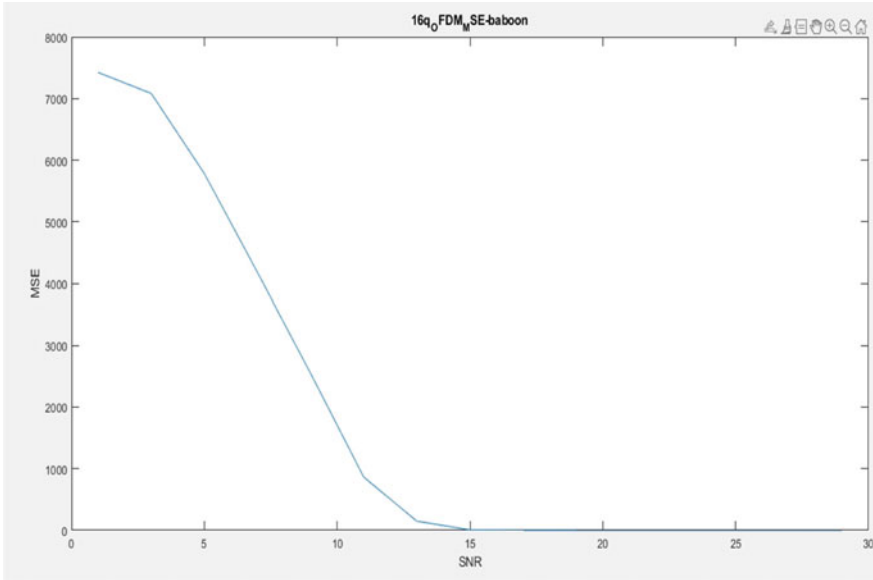


Fig. 28 16 QAM MSE

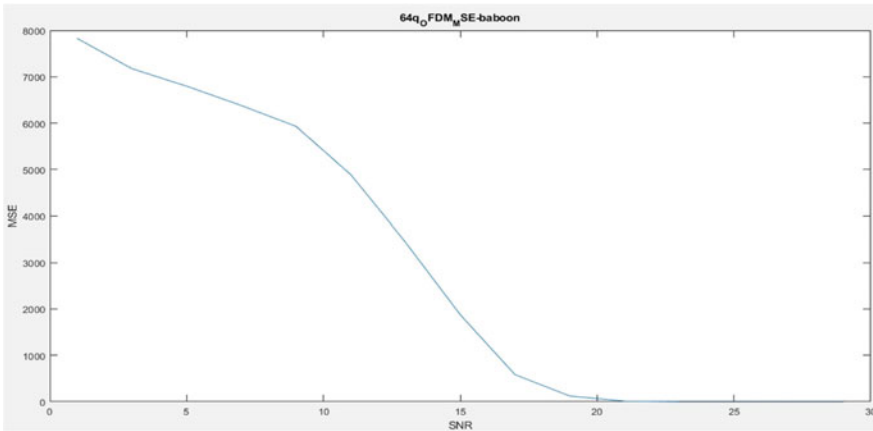


Fig. 29 64 QAM MSE

14 Applications

We have successfully proposed and implemented FFT-based coded OFDM. We have also seen the improvement in PAPR with 4 QAM and as the modulation scheme increases, PAPR also increases, and with 4 QAM improved PSNR value which has many applications in various fields such as medical imaging, underwater debris, and

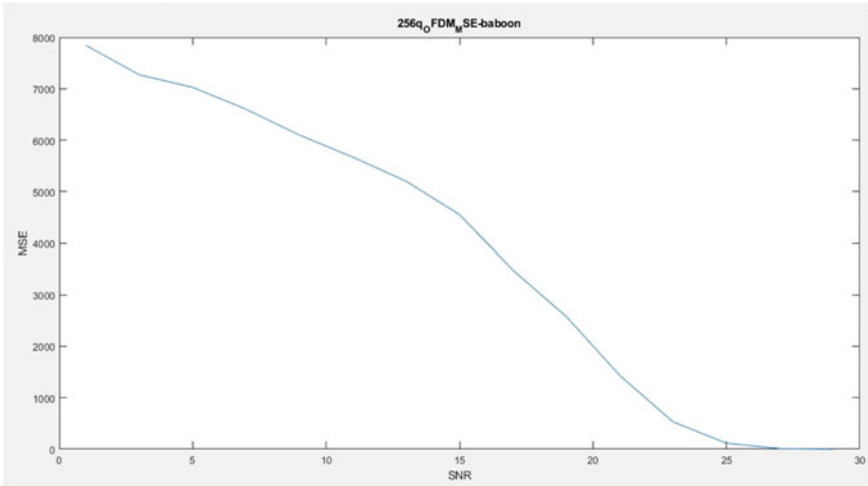


Fig. 30 256 QAM MSE

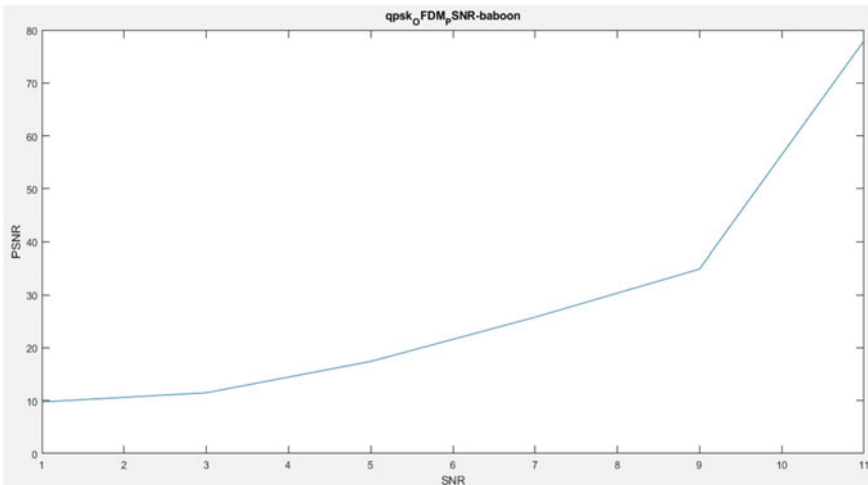


Fig. 31 4-QAM PSNR

many others where noise is very prominently present. This also finds application in underwater communication in times of medical emergency, war threats, and other such conditions where the quality and clarity of the image play an important role. It is essential in such conditions that the image transmission be prompt and the received image be as limitedly distorted as can be.

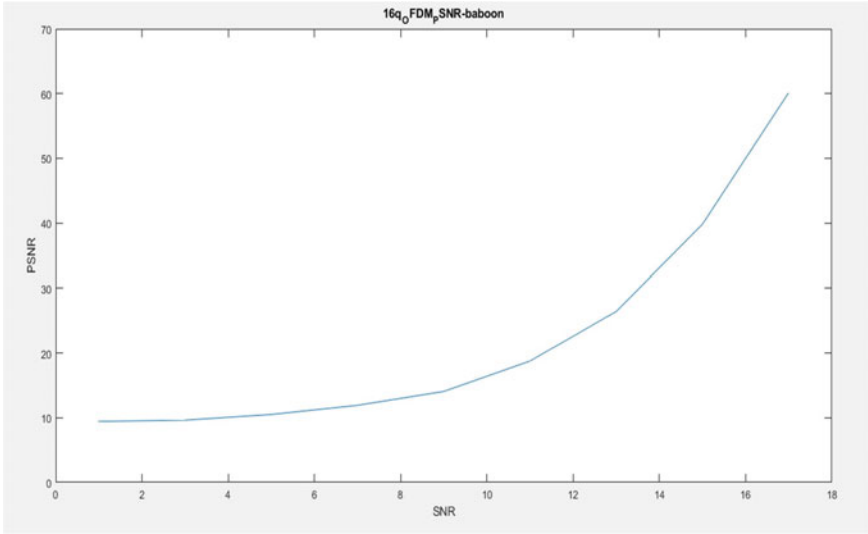


Fig. 32 16 QAM PSNR

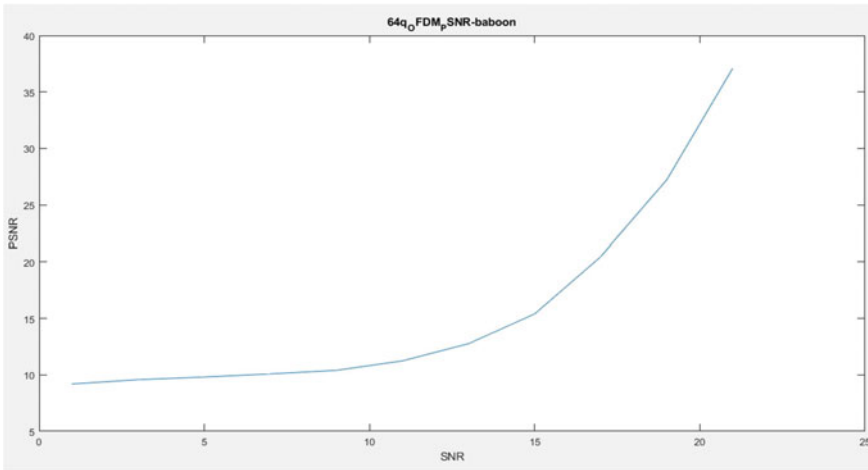


Fig. 33 64 QAM PSNR

15 Conclusion

The scheme based on coded OFDM was successfully implemented and results were compared with uncoded OFDM and coded OFDM outperforms the latter. Coded OFDM based on multiple modulation schemes, namely, 4 QAM, 16 QAM, 64 QAM, and 256 QAM was also implemented successfully. By observing the results, we

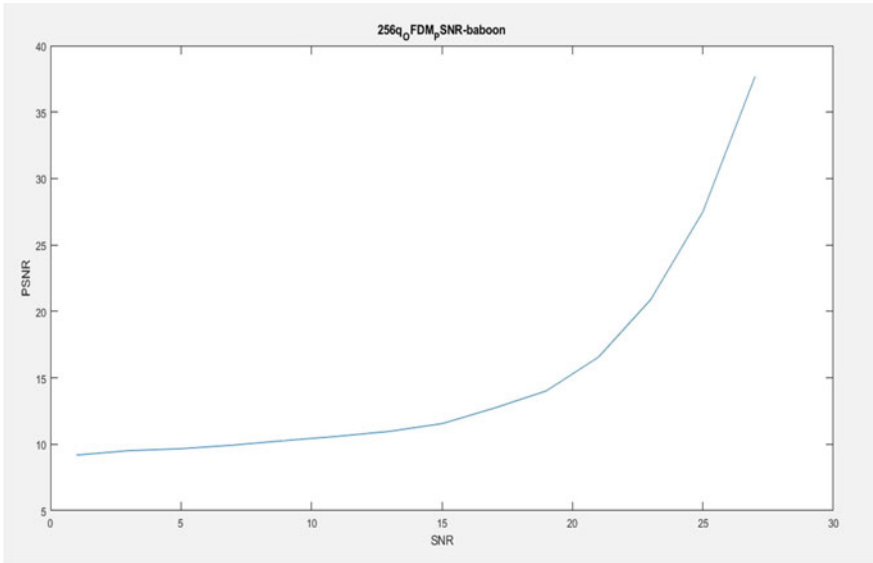


Fig. 34 256 QAM PSNR

Table 2 PAPR and time elapsed comparison for different modulation schemes in coded OFDM with 256 sub-carriers

Technique	PAPR	Time taken (s)
4 QAM	10.3364	36.729036 s
16 QAM	18.0112	26.290217 s
64 QAM	24.3959	19.410710 s
256 QAM	30.6103	13.579218 s

Fig. 35 QAM, PSNR = 10.6



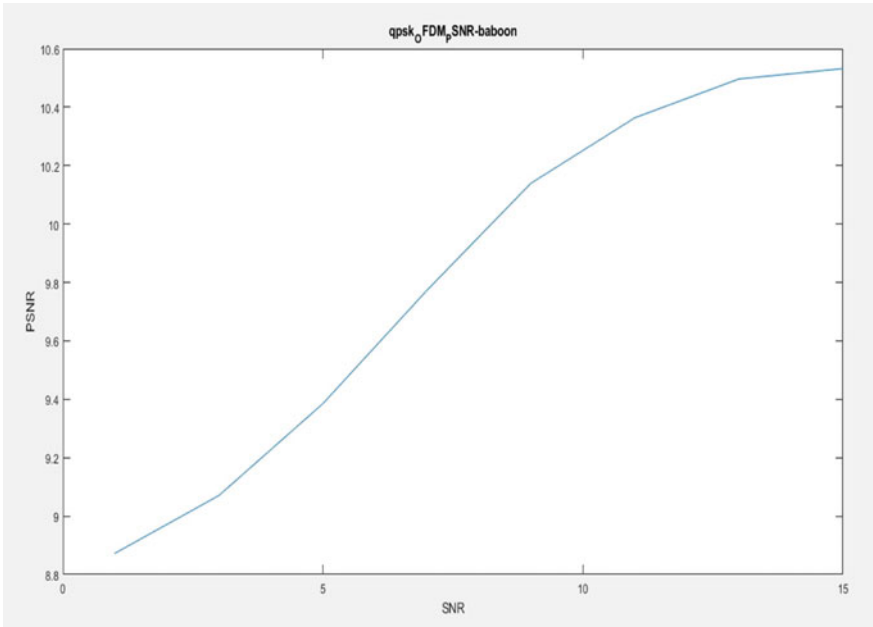


Fig. 36 PSNR in UWA (4-QAM)

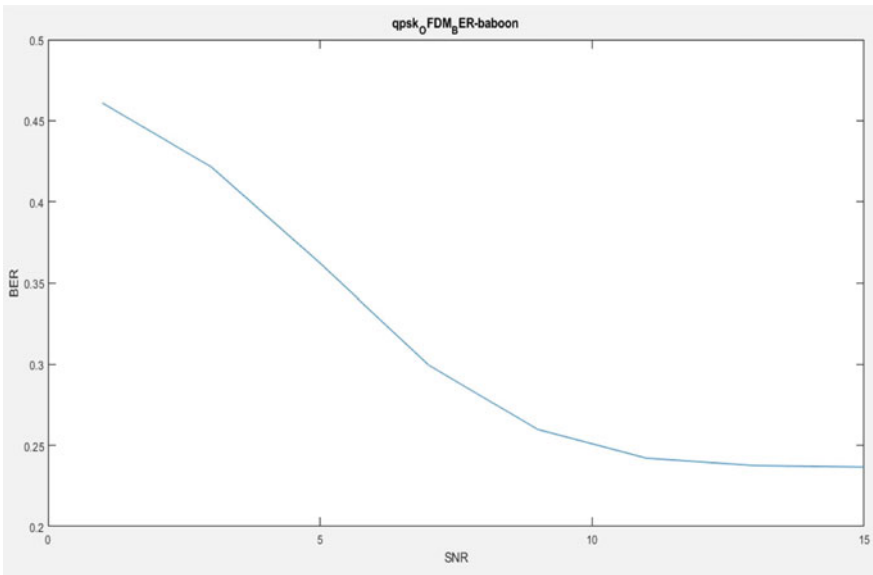


Fig. 37 BER in UWA

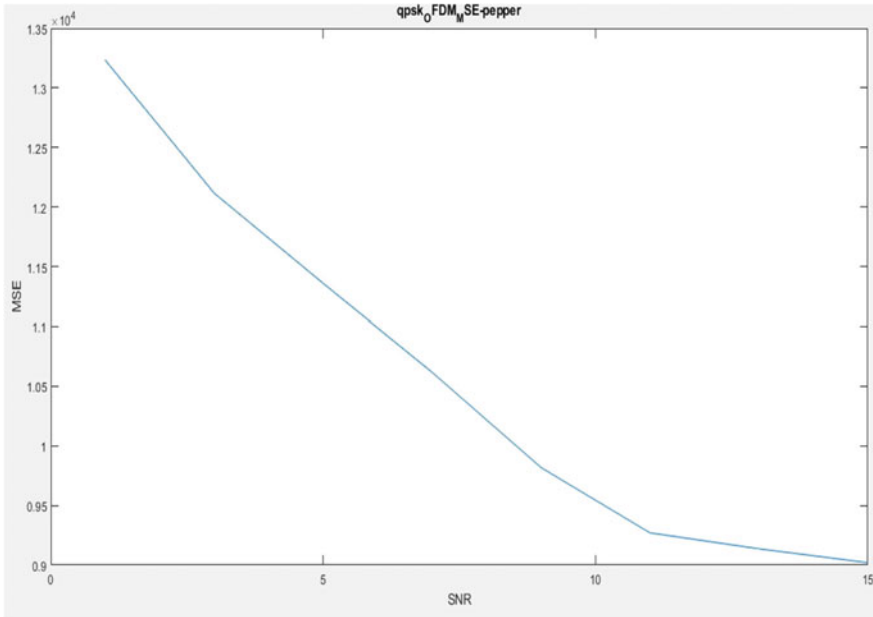


Fig. 38 MSE in UWA

can conclude that (4 QAM) PSNR and PAPR of Coded OFDM are better than the traditional OFDM for lower SNR values when noise is present very prominently and the best option (4 QAM) for underwater image transmission where noise is a very serious concern.

Bibliography

1. Ahmed N (2000) Joint detection strategies for orthogonal division multiplexing. Thesis Master of Science. Texas
2. www.MathWorks.Com
3. Y. V. Zakharov and A. K. Morozov, "Ofdm transmission without guard interval in fast-varying underwater acoustic channels," IEEE Journal of Oceanic Engineering, Jan 2015.
4. Ebihara T, Leus G (2016) Doppler-resilient orthogonal signal-division multiplexing for underwater acoustic communication. IEEE J Ocean Eng
5. Image transmission through OFDM system under the influence of AWGN channel
6. AUTHORS: Dharavathu Krishna and M.S. Anuradha,
7. AUCE, India
8. Underwater Communications: Recent Advances. Mohammad Furqan Ali, NRTPU, Russia Tharindu D., LMNIT, India

Design and Analysis of Skateboard Chassis



N. Sharath Chandra and R. Vikas

Abstract Due to rising fuel prices and pollution, the focus of this research is on electric vehicles. The Tata Ace engine chassis is being used as a model for the skateboard chassis that will be created. The main aim of this work is to design a skateboard chassis for the Tata Ace that is lighter than the current Tata Ace engine chassis. The skateboard chassis will be created with CATIA V5, and the structural analysis will be completed with Ansys software. The modal analysis is used to examine the mode shapes of the skateboard at the chassis at various frequencies ranging from 18.34 to 84.98 Hz, as well as the tradeoff between deformation rate and mode shape. Finally, the findings are compared to the engine chassis based on total deformation, geometric mass, and stress intensity, indicating a weight reduction of 15.72%, which will reduce the vehicle's weight, resulting in lower energy consumption and manufacturing costs.

Keywords Electric vehicle · CATIA V5 · Vehicle's weight

1 Introduction

India and other Western countries, which were early connectors for the zap of transportation, are seeing an increase in demand for electric automobiles. Nations with large cities and dense populations have begun to consider electric vehicles as a solution to air pollution problems in their major cities. A vehicle's chassis is an important component. It serves as the vehicle's backbone, supporting all of the vehicle's components. The chassis of a vehicle consists of the frame, transmission system, and suspension system, among other things. The automotive chassis is designed to keep all components together while driving and to distribute loads to various parts, which are created by acceleration and loads on the chassis via the suspension and wheels.

N. Sharath Chandra (✉)
CTAT, National Institute of Engineering, Mysore, India
e-mail: sharath.chandra@nie.ac.in

R. Vikas
M. Tech in Machine Design, National Institute of Engineering, Mysore, India

It also covered the steering, braking, and suspension systems. India is also one of the world's largest vehicle manufacturer [1, 2].

Backbone, ladder, spaceframe, monocoque, and skateboard are the most common chassis types. A static analysis combines steady inertia loads and time-varying loads which will be approximated as static equivalent hundreds. Strength, stiffness, and vibrational behavior are all significant parts of structural analysis [3, 4]. According to research, a 4mm thickness is safe enough to carry a 15-ton load on truck chassis [5]. Finite element techniques may be used to easily examine structural systems such as the chassis. As a result, an appropriate chassis finite element model must be built. In ANSYS, the chassis is modelled [6]. Natural frequencies and mode shapes can be determined using modal analysis and the Finite Element Method (FEM) [7]. The alloy steel material used to make the chassis has a design stress of 500 MPa [8].

The traditional chassis design technique is based on the chassis' strength and stiffness, and if the chassis' weight is reduced, which reduces power usage and lowers the material's overall cost. The design of a vehicle chassis is critical to the overall performance of the vehicle. The stress investigation is crucial because it will help us determine the maximum load that can be applied to the vehicle. The load point is consequently critical in order to resolve and optimize the mounting of segments such as motors/batteries, suspension, gearbox, and others.

This project focuses on vehicle chassis, which is the backbone of autos, making chassis design one of the most important and difficult tasks in the automotive industry. CATIA is the software that is utilized to model the chassis in this project. It is CAD/CAM/CAE software that is advanced, and ANSYS is the software that is utilized for finite element analysis. The major features of this study are stress analysis and weight loss. The location of high stress zones and load capabilities are identified during the design and study of chassis. The skateboard chassis is the chassis design employed in this work.

2 Design Consideration for Skateboard Chassis

Designing is a multi-stage, integrated process that must be adaptable to allow for changes in response to unique challenges and requirements that develop along the process. Integrated Product and Process Development (IPPD) is one of the design management techniques.

2.1 CATIA V5 R20

Computer Aided Three-dimensional Interactive Application (CATIA) is a multi-platform software package developed by Dassault Systems for Computer Aided Design (CAD), Computer Aided Manufacturing (CAM), Computer Aided Engineering (CAE), PLM, and 3D.

2.2 Design Concepts

Weight, stress, and deformation are the parameters used to choose the best design. This method generates a 3×3 matrix of design approaches for determining the best answer to the problem statement (Fig. 1).

Design Concept 1:

The above design in Fig. 2 is created using the FAE chassis as a reference, and this form was created to see if the weight of this skateboard chassis is less than the current Tata ace engine chassis, which was verified using the Catia V5 software. The weight of structural steel with a thickness of 3mm is calculated, and the results are displayed in Fig. 3. The weight of this design is 155kg, which is significantly more than the current Tata ace engine chassis. The stress value for this concept is 126.7MPa, which

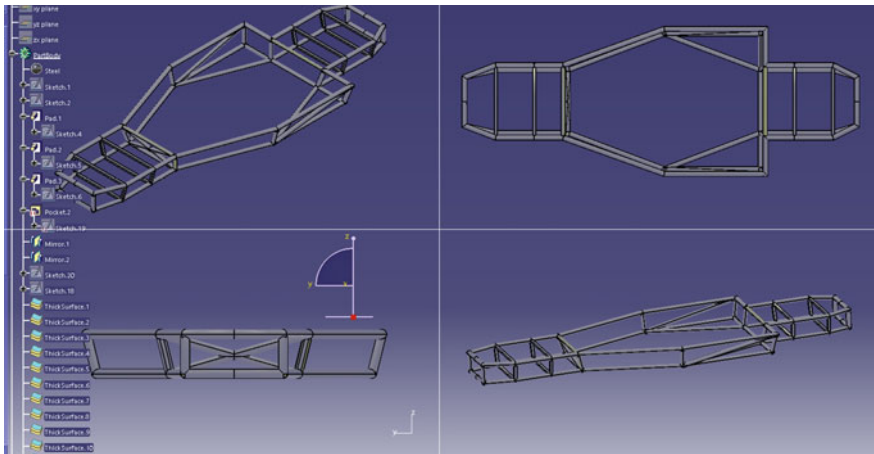


Fig. 1 Design concept 1

Characteristics		Center Of Gravity (G)	
Volume	1.978e+007mm3	Gx	2130.23mm
Area	5.784m2	Gy	0.149mm
Mass	155.465kg	Gz	-87.637mm
Density	7860kg_m3		

Fig. 2 Mass of design concept 1

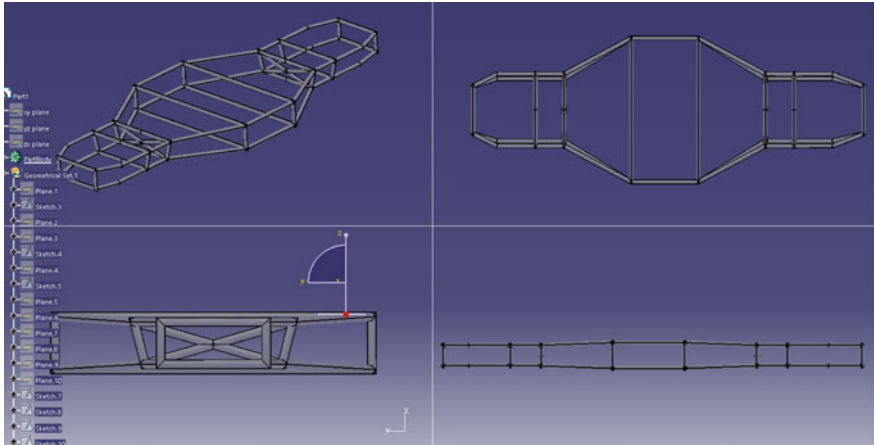


Fig. 3 Design concept 2

is less than the yield strength, and the deformation is 8.51mm, indicating that it is safe to proceed.

Design Concept 2:

The chassis weight is calculated for structural steel with a thickness of 3mm as shown in Figs. 4 and 5 displays the weight derived from this notion. The weight of this design is 157 kg, which is significantly more than the current Tata ace engine chassis. The stress value for this concept is 125.23 MPa, which is less than the yield strength, and the deformation is 7.92 mm, indicating that it is safe to proceed.

Design Concept 3:

Similarly in design concept 3 as shown in Fig. 6 the chassis' weight was determined by using structural steel with a thickness of 3mm, resulting in a weight of 99.3 kg. The stress and deformation values are 130.22MPa and 9.08mm, respectively. Electric

Result	
Calculation mode: Exact	
Type: Volume	
Characteristics	Center Of Gravity (G)
Volume	Gx
Area	Gy
Mass	Gz
Density	

2.008e+007mm3	-2056.265mm
4.38m2	-0.005mm
157.805kg	0.996mm
7860kg_m3	

Fig. 4 Mass of design concept 2

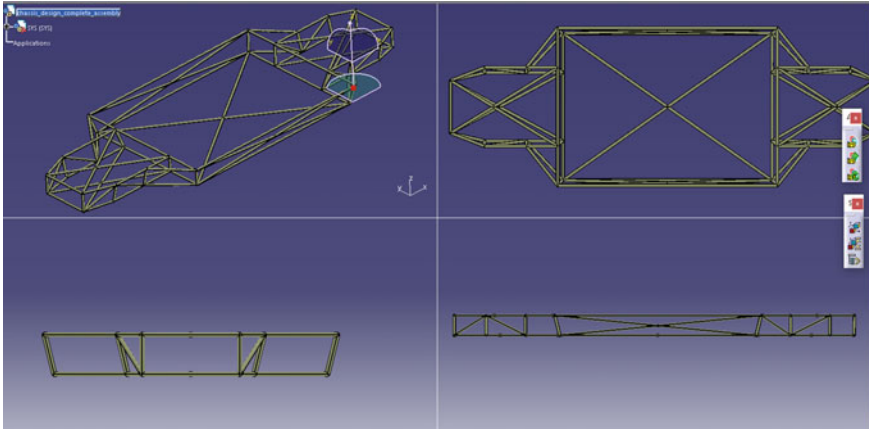


Fig. 5 Design concept 3

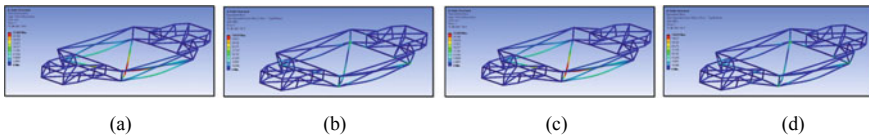


Fig. 6 a Displacement for aluminum tube (3 mm Thickness), b stress intensity for aluminum tube (3 mm Thickness), c displacement for grey cast iron tube (3 mm thickness), and d stress intensity for grey cast iron tube (3 mm thickness)

vehicle chassis design uses the rectangular cross section in the middle portion so that more space will be available for the vehicle components.

2.3 Parameters Comparison

The major goal of this work is to minimize chassis weight while reducing stress and deformation. The characteristics in design concept 3 satisfy our requirements. Although the stress and deformation values in concepts 2 and 3 are slightly lower than in idea 3, the weight of these concepts 1 and 2 exceeds that of the existing chassis. When comparing the weights of the three concepts for structural steel 3mm thickness, the concept 3 skateboard chassis is lighter than the design concepts 1 and 2, with better stress and deformation values as indicated in Table 1.

Table 1 Comparison of parameters

Parameters	Concept 1	Concept 2	Concept 3
Weight (kg)	155.465	157.805	99.3
Stress (Mpa)	126.7	125.32	130.22
Deformation (mm)	8.51	7.92	9.08

3 Structural and Modal Analysis of Skateboard Chassis

Finite element techniques may be used to easily examine structural systems such as the chassis. For weight loss, a sensitivity analysis is performed. As a result, an appropriate chassis finite element model must be built. CATIA V5 was used to model the chassis. The ANSYS Workbench is used to perform FEA on the simulated chassis.

ANSYS Software:

ANSYS is a general-purpose programme that engineers can use to simulate interactions across several disciplines of physics, including as structural, vibration, fluid dynamics, heat transfer, and electromagnetics.

Materials used in ANSYS:

The materials are chosen based on considerations such as cost and material strength. Materials which are considered are

- a. Aluminum
- b. Grey Cast Iron
- c. Structural Steel.

Dimensions and Assumptions made from the present Tata Ace:

The Tata Ace pickup truck for this analysis.

Model—TATA Ace

Length of the chassis—4072 mm

Width of the chassis—1500 mm

Wheel base—2100

Tube Outer Diameter—25 mm

Kerb weight—950 kg

Payload Capacity—750 kg

Total Load to be applied = $(950 + 750) \times 9.81 = 16,677 \text{ N}$

4 Structural Analysis on Different Materials

A structural analysis is done using weights derived theoretically by the preceding chassis and applied to various materials [10]. For this work purposes, structural steel, aluminum, and grey cast iron are chosen for better pricing efficiency and because they are the most widely utilized, and then an analysis is performed.

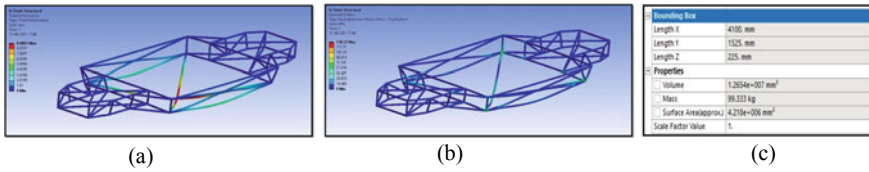


Fig. 7 a Displacement for structural steel tube (3 mm thickness), b stress intensity for structural steel tube (3 mm thickness), and c material properties of structural steel for 3 mm thickness

When all of the data were compared, it was discovered that structural steel with a thickness of 3 mm produced better results in terms of weight and capacity. As a consequence, structural steel with a thickness of 3 mm is the ideal configuration for conducting the impact test.

The stress and displacement chart for the 3 mm aluminum tube is shown in Fig. 6a, b. After applying 16677N force to the 6 rods and fixing the differential position, we obtained a deformation value of 25.609mm and a stress value of 130.91 MPa. Both stress and displacement are high, despite being better than the 1.5 mm thickness configuration. The stress and displacement chart for the 3 mm aluminum tube is shown in Fig. 6c, d. After applying 16,677 N force to the 6 rods and fixing the differential position, we obtained a deformation value of 25.609 mm and a stress value of 130.91 MPa. Both stress and displacement are high, despite being better than the 1.5 mm thickness configuration.

The above image in figure (a) and figure (b) shows the stress and displacement chart for the 3 mm structural tube, after applying 16,677 N force to the 6 rods by fixing the differential position we got the deformation value as 9.0897 mm and stress value as 130.22 MPa, as it can be noticed in the above images there is a huge improvement in the value of displacement here, and also the stress is falling under permissible range. The chassis is analyzed for 3 mm thickness using material properties which are listed in Fig. 7c. The weight reference comes from TATA Ace’s Structural Analysis of Automotive Chassis and Optimization, and Material Properties of aluminum for 1.5 mm, 3 mm, and 4.5 mm thickness are examined in ANSYS programme is given in Table 2 (Figs. 8, 9, and 10).

5 Modal Analysis

The most fundamental and significant aspect of dynamic character analysis is modal analysis. The inherent frequency and mode forms of the structures were discovered using this current technology. It was possible to analyze the stiffness and avoid resonance vibrations. For example: In the 1st mode the frequency observed is 18.34 Hz and behavior of the structure at this particular natural frequency is shown in Fig. 11 at this mode displacement of the chassis is 11.198 mm and it is occurring at the center of the skateboard chassis. The behavior of the at the skateboard chassis at

Table 2 Comparison of structural analysis results

Material	Thickness (mm)	Stress (MPa)	Deformation (mm)
Aluminum	1.5	300	48.84
	3	130	25.6
	4.5	83.5	18.6
Grey cast iron	1.5	297.78	31.532
	3	129.78	16.524
	4.5	82.301	12.185
Structural steel	1.5	298.95	17.342
	3	130.22	9.089
	4.5	82.642	6.7038

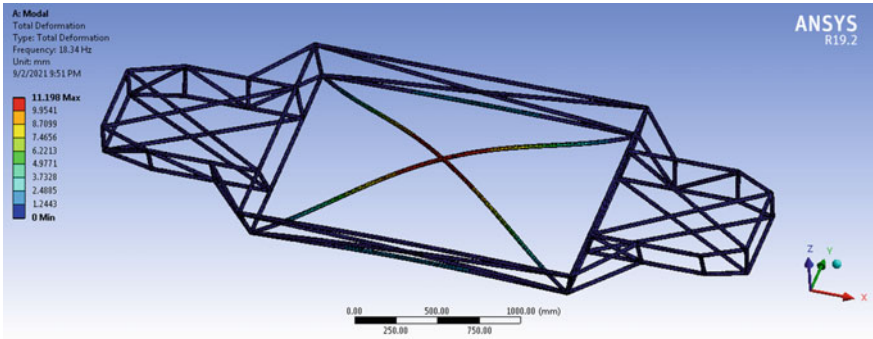


Fig. 8 1st mode shape

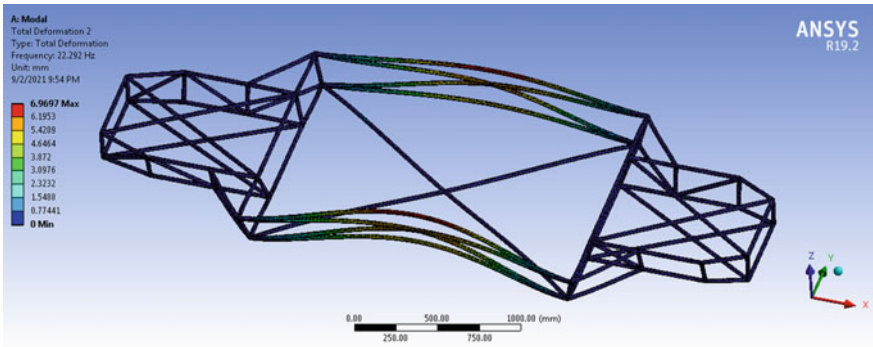


Fig. 9 2nd mode shape

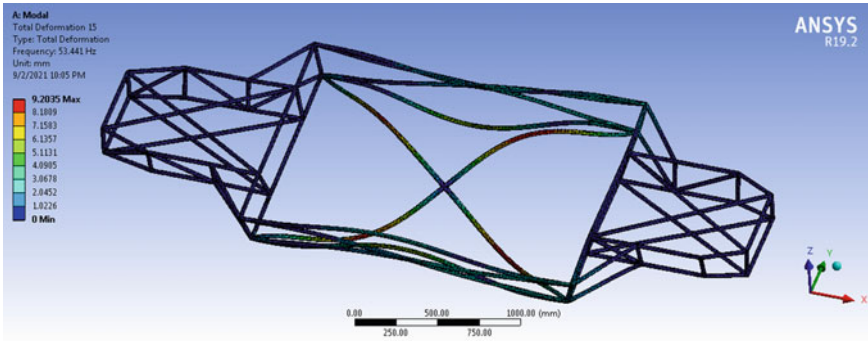


Fig. 10 15th mode shape

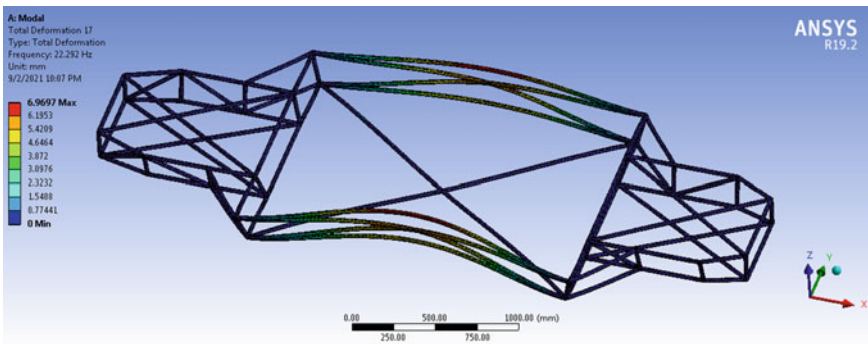


Fig. 11 17th mode shape

the 2nd mode shape is shown in Fig. 12 and the deformation is causing in the side member of the chassis the frequency and deformation at this node is observed as 22.292 Hz and 6.9697 mm. Similarly at the 15th mode the deformation is occurring at both the side and center members, and it is shown in Fig. 13 the frequency and deformation value is observed as 53.441 Hz and 9.2035 mm. The structural behavior at the 17th mode is shown in Fig. 14 the frequency is observed as 59.765 Hz and at this mode deformation is observed as 6.9697 mm occurring at side members of the chassis.

The behavior of the at the skateboard chassis at the 20th mode shape is shown in Fig. 15, and the deformation is causing in the side member of the chassis the frequency and deformation at this node is observed as 65.325 Hz and 10.619 mm. In the 25th mode the frequency observed is 76.558 Hz and behavior of the structure at this particular natural frequency is shown in Fig. 16 at this mode displacement of the chassis is 12.386mm, and it is occurring at the side member of the skateboard chassis. The deformation at 28th mode is occurring at side and center members of the skateboard chassis, and it is shown in Fig. 16. At the 30th mode, deformation of

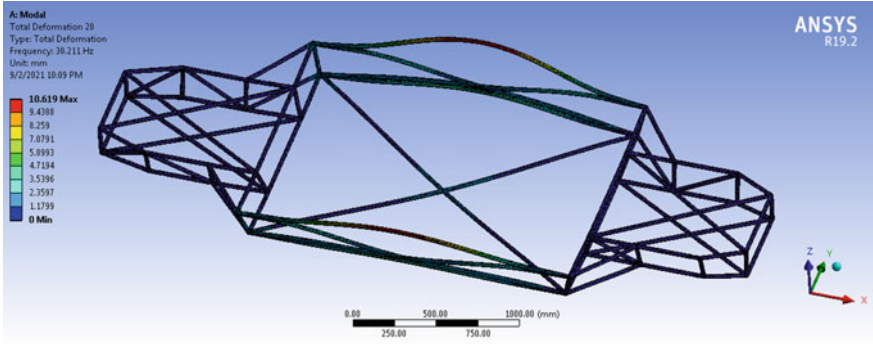


Fig. 12 20th mode shape

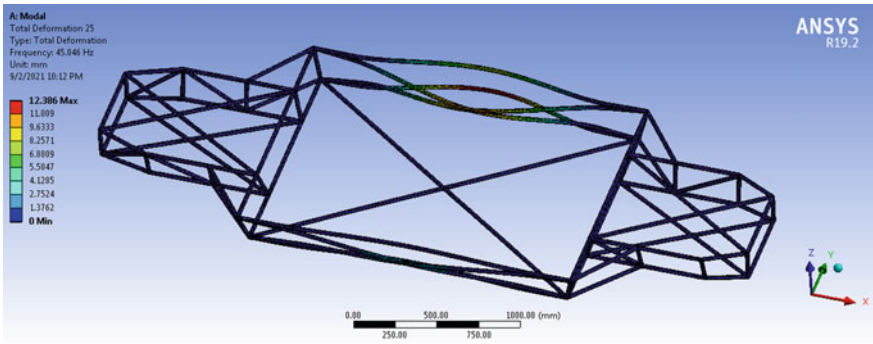


Fig. 13 25th mode shape

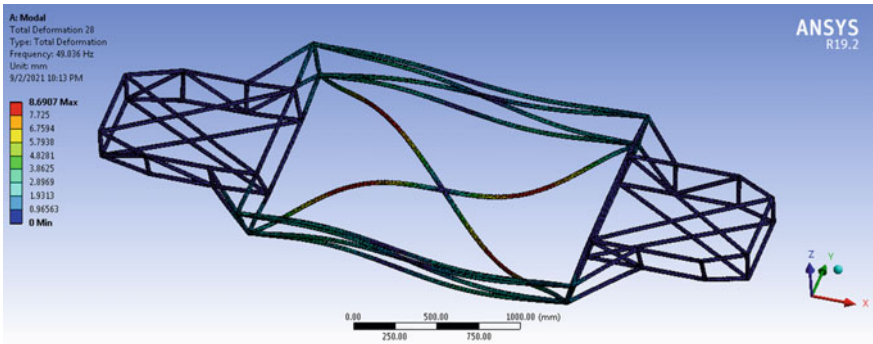


Fig. 14 28th mode shape

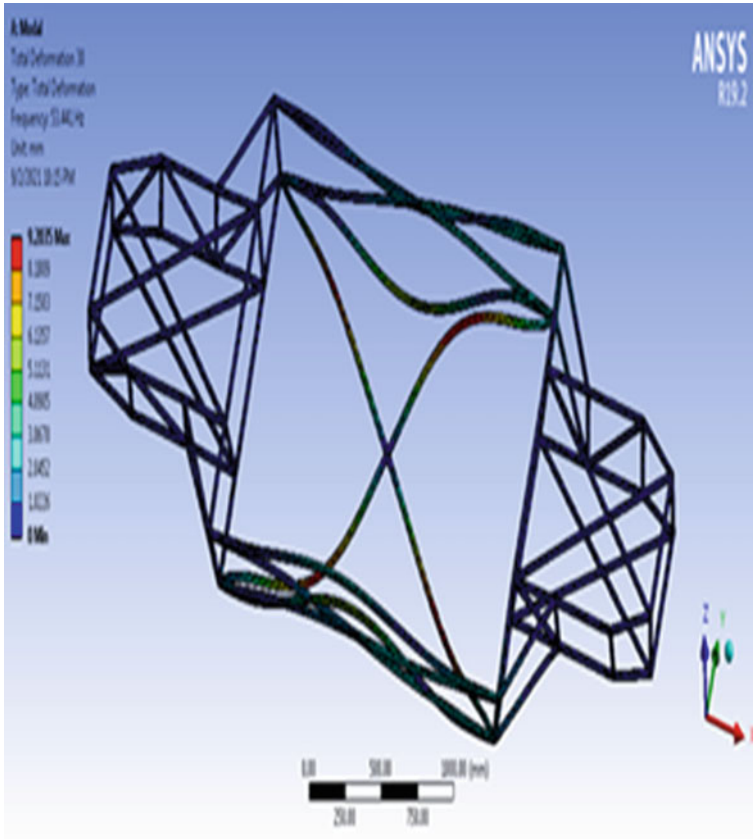


Fig. 15 30th mode shape

9.2035 mm occurs at the side and center members at a frequency of 84.981 Hz, as illustrated in Fig. 16.

This analysis is performed to study the dynamic behavior of the skateboard chassis at different modes FE analysis is carried out in ANSYS workbench for the 30 mode shapes each natural frequencies with respective mode shape the resulting frequencies are shown in Table 3.

6 Results and Discussions

Aluminum, grey cast iron, and structural steel are the most often used and efficient materials, according to the literature review. The Tata Ace pickup truck for this analysis. To analyze the dynamic behavior of the skateboard chassis, modal analysis was performed for 30 possible mode shapes and all frequencies. When comparing the

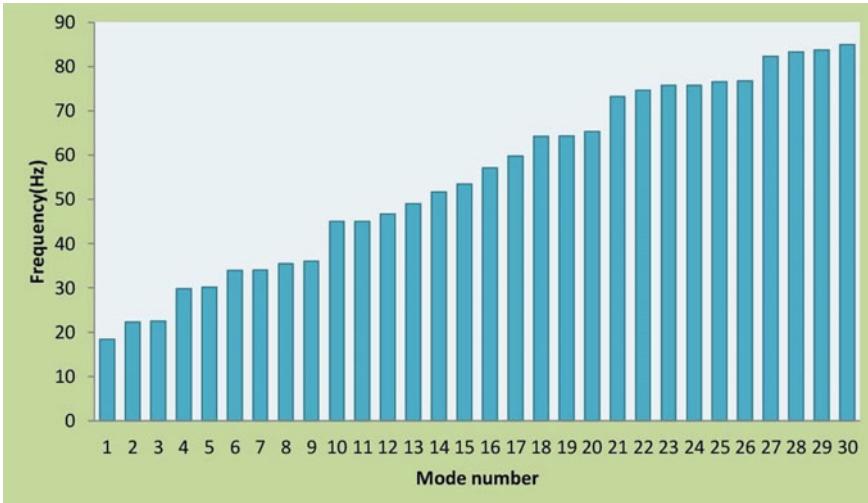


Fig. 16 Frequency versus mode number graph

Table 3 Natural frequencies and deformation

Mode shape	Frequencies (Hz)	Deformation (mm)	Mode shape	Frequencies (Hz)	Deformation (mm)
1	18.34	11.198	16	57.145	11.198
2	22.292	6.9697	17	59.765	6.9697
3	22.448	6.9866	18	64.176	6.9866
4	29.818	10.077	19	64.373	10.047
5	30.211	10.619	20	65.325	10.619
6	33.972	9.9092	21	73.24	9.9092
7	37.053	9.9154	22	74.62	9.9148
8	35.515	10.326	23	75.764	10.326
9	36.088	11.137	24	75.829	11.134
10	45.046	12.386	25	76.558	12.386
11	45.066	12.398	26	76.803	12.398
12	46.648	4.953	27	82.319	4.983
13	49.036	8.6907	28	83.271	8.6907
14	51.657	10.418	29	83.803	10.418
15	53.441	9.2035	30	84.98	9.2035

Table 4 Comparison of chassis [3]

Sl. No.	Parameter	Original chassis	Skateboard chassis	Percentage difference
1	Total deformation	4.51 mm	9.08 mm	-101.33%
2	Geometric mass	117.83	99.3 kg	15.72%
3	Stress intensity	113.62	130.22	-15.04%

structural analysis results to the original chassis, it was discovered that structural steel with a thickness of 4.5 mm has the lowest deformation value and stress value when compared to 3 mm thickness, but the weight of the 4.5 mm thickness structural steel material is 149 kg, which is heavier than the original chassis. The maximal deformations and stresses, as well as their location on the chassis, are determined using the finite element analysis technique in the static analysis study. We had successfully assessed the chassis' resistance to a front-end impact. On the basis of total deformation, geometric mass, and stress intensity, the newly developed Skateboard chassis was compared to the original TATA Ace IC engine chassis. The outcomes are listed in Table 4.

The comparison between the two chassis is shown in the table above. It can be observed that a weight reduction of 15.72% has been accomplished, which will reduce the weight of the vehicle, resulting in lower energy consumption and manufacturing costs. The purpose of this analysis is to investigate the dynamic behavior of the skateboard chassis in various modes. For each of the 30 mode forms, FE analysis is performed in ansys workbench, and the resulting frequencies are shown in the corresponding graph in Fig. 19.

The goal of this work was to create a skateboard chassis for a pickup truck based on the Tata Ace. Lightweight, running period, safety factor, flexibility, hazardous emission, design quality, and reduced chassis weight are all elements to consider while designing a chassis that can handle 1.5 tonnes of cargo. To examine the behavior of the skateboard chassis under various conditions, a modal analysis is done for 30 different frequencies.

7 Conclusion

The current study looked at a variety of sources. Various sorts of electric vehicle chassis designs have been investigated, and certain changes have been included into the new model. Reverse engineering of the new model was completed successfully, and design changes were made. To evaluate the design, a detailed finite element analysis with bump analysis was done. The chassis' weight has been reduced significantly, and the design has been confirmed using FE analysis. Different mode forms were evaluated using modal analysis. The entire load, which includes the products and vehicle body, is used to construct the supporting structure. As a result, the

components can be fine-tuned and optimized with updated mass, saving materials and making them more cost effective.

References

1. Rathod, HH, Kumar S, Goel V (2018) A review on analysis and design of vehicle chassis and its materials. *Int J Sci & Eng Res* 9(3), ISSN 2229-5518
2. Rajpal J, Thorat SG et al (2014) Design considerations for automobile chassis for prevention of rolling over of a vehicle. *Appl Mech Mater* 612:41–49. <https://doi.org/10.4028/www.scientific.net/AMM.612.41>
3. Godse S, Prof. Patel DA, Static load analysis of Tata ace ex chassis and stress optimisation using reinforcement technique. *Int J Eng Sci & Res Technol*. 0.5281/zenodo.155097.
4. Hidaitulla Mangole, “Cross- section and material optimization of an automotive chassis using FEA” *WSN* 69 (2017) 98–110 EISSN 2392–2192.
5. Begum SN, Bhanu Murthy SP (2016) Modelling and structural analysis of vehicle chassis frame made of polymeric composite material. *Int Res J Eng Technol (IRJET)* 3(8)
6. Ali RD (2020) Design and development of a chassis concept for an autonomous airport shuttle. In: Degree project in Vehicle Engineering, Stockholm, Sweden
7. Rao S, Bhattu A, Dynamic analysis and design modification of a ladder chassis frame using finite element method. *Amity J Comput Sci (AJCS)* 1(2). ISSN: 2456-6616
8. Ganga Rao G, Suresh M (2015) Design, static and dynamic analysis of automobile chassis. *Int J Res Adv Eng Technol* 1(3). , ISSN: 2455 0876
9. Rajappan R, Vivekanandhan M (2013) Static and modal analysis of chassis by using Fea. *Int J Eng Sci* 2(2), ISSN: 2319-1813, ISBN: 2319-1805, 2013
10. Garud RY, Tamboli SC, Pandey A (2018) Structural analysis of automotive chassis, design modification and optimization. *Int J Appl Eng Res* 13(11):9887–9892. ISSN 0973-4562

Electro-Thermal Model for Field Effective Transistors



Allen Denny, Neelkanth Kirloskar, Babu Rao Ponangi, Rex Joseph, and V. Krishna

Abstract This paper describes an electro-thermal model, which gives the real-time junction temperature of the MOSFET. The thermal model is obtained from the thermal impedance curve given in the datasheet of the selected MOSFET (IAUT260N10S5N019). The RC network models are obtained from the thermal impedance curve given in the MOSFET datasheet. The resistance and capacitance values for the thermal network are obtained after curve fitting the thermal impedance curve. The obtained thermal network model is then validated on MATLAB Simulink. The simulations are carried out on MATLAB Simulink, the software results were validated using NEXPERIA application note experiments, and the results conclude the validity of the Simulink model. The simulations were run by constructing a thermal network from the obtained resistance and capacitance values and supplying power of a predetermined value through the thermal network to obtain the thermal impedance. This is then compared with the thermal impedance curve in the datasheet of the MOSFET. The comparison shows that the results obtained from the thermal network are similar to the thermal impedance curve of the MOSFET.

Keywords Thermal model · Thermal network model · Foster model · Cauer model · Thermal impedance · Thermal resistance · Thermal capacitance · RC network

A. Denny · N. Kirloskar · B. R. Ponangi (✉) · V. Krishna
Department of Mechanical Engineering, PES University, Bangalore 560085, India
e-mail: baburaoponangi@pes.edu

B. R. Ponangi · V. Krishna
PMR Lab, Department of Mechanical Engineering, PES University, Bangalore 560085, India

R. Joseph
Department of Electrical and Electronics Engineering, PES University, Bangalore 560085, India

1 Introduction

A metal-oxide semiconductor field-effect transistor (MOSFET) is a field-effect transistor where the gate voltage determines the conductivity of the device. It is widely used in power electronics applications. MOSFETs generate a lot of heat due to their switching operation and this heat has to be carried away from the component for its long life and smooth operation. Over the years, the power density of power electronics components has exponentially increased. This means that the heat dissipated per unit area of the power electronics components is very high and will go on increasing over the coming years. Hence, a good understanding of the heating of the MOSFETs is necessary and this is done through the thermal analysis of the MOSFET. The MOSFETs used in the automotive sector have varying input powers and hence a transient thermal model is needed to analyze the heating of the MOSFET during its operation. The thermal behavior of power MOSFETs is done using RC thermal models.

Qian et al. [1] review the various thermal management methods available for thermal management of power electronic devices. It talks about the different thermal failures in power electronic components and the current studies on the subject.

Kojima et al. [2] describe a compact electro-thermal model for a hybrid vehicle. The paper describes the method to calculate the parameters for the RC—thermal model while considering lateral heat dissipation and Si-chip interference. Kojima et al. [3] describe an efficient method to create multi-chip thermal models. The model depicts thermal interference between each chip and model. The effects of Thermal interference are considered in the model.

Luo et al. [4] describe the methodology to calculate the thermal impedance between junction and ambient for an IGBT power module.

Igic et al. [5] describe the generation of a compact electro-thermal model. The thermal model is generated based on prior simulation using FEM. The thermal impedance calculated is then used to create the thermal network model. The electrical model is generated in SPICE based on the different MOSFETs. The results and model are validated against the experimental results.

Zhou et al. [6] describe the generation of a compact electro-thermal model for variable speed drivers. The thermal model is generated based on the FEM simulation results. The thermal impedance was used to calculate the thermal resistance and capacitance of the thermal model. The electrical model is created to depict the working of the power module while connected to the motor. The model is validated experimentally by supplying a constant three-phase load to the module and the simulation results are in good agreement with experimental results.

In this work, a thermal model was developed for the Infineon power transistor, IAUT260N10S5N019 [8]. This paper describes the methodology to calculate the RC values of the Foster model using the thermal impedance curve and the conversion of the Foster model to the Cauer model. The models and simulations are run on MATLAB Simulink, and the software is validated based on experiments depicted in Nexperia application note [9].

2 Methodology

The thermal modeling of power MOSFETs is done using RC thermal-network models. The two models considered in this paper are the Foster and Cauer thermal network model.

Foster models are derived by semi-empirically fitting a curve to the Thermal Impedance (Z_{th}), the result of which is a one-dimensional RC network, as shown in Fig. 1. The resistance and capacitance values in the Foster model do not correspond to geometrical locations on the physical device, therefore these values cannot be calculated from a device material constant. The Foster models have the benefit of ease of expression and are calculated using the following expressions [7].

$$Z_{th(t)} = \sum_{i=1}^n R_i * \left[1 - e^{-\frac{t}{\tau_i}} \right] \tag{1}$$

$$T_i = R_i * C_i \tag{2}$$

The Cauer model consists of an RC network but the thermal capacitances are all connected to the thermal ground (ambient temperature) as shown in Fig. 1. The nodes of the Cauer model can have physical meaning and allow access to the temperature of the internal layers of the semiconductor structure. The Foster model is generated by curve fitting the Thermal Impedance curve.

From the curve-fit equation, the R-C values are calculated. The Cauer model is calculated by mathematical equations to calculate the R-C values for the Cauer model. The thermal network models are generated and simulated for the power MOSFET, IAUT260N10S5N019.

2.1 Mathematical Model

Foster Model of the IAUT260N10S5N09 MOSFET was created using the steps mentioned in [7]. The thermal impedance vs time curve of the IAUT260N10S5N09

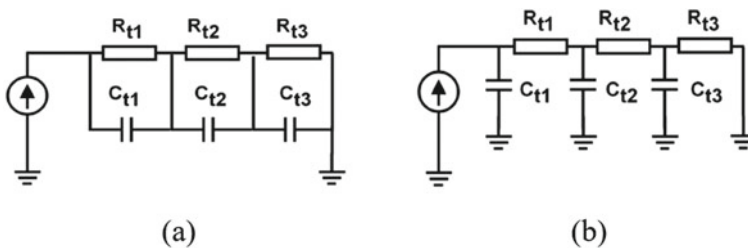


Fig. 1 a Foster and b Cauer RC Model [6]

MOSFET was obtained from the datasheet of the MOSFET [8], and the values were extracted for the single pulse case of the IAUT260N10S5N09 MOSFET given in the thermal impedance vs time graph in [8].

The extracted data were fed to MATLAB and using the curve fitting app available on MATLAB. The data were curve fit using a custom equation depicted below:

$$R_{Th} = R_1(t)\left(1 - e^{1-\frac{t}{\tau_1}}\right) + R_2(t)\left(1 - e^{1-\frac{t}{\tau_2}}\right) + R_3(t)\left(1 - e^{1-\frac{t}{\tau_3}}\right) + R_4(t)\left(1 - e^{1-\frac{t}{\tau_4}}\right) \quad (3)$$

where R_1, R_2, R_3, R_4 are the resistances of the Foster model, and $\tau_1, \tau_2, \tau_3, \tau_4$ are the thermal time constants, the capacitance values for the Foster model are obtained from Eq. 4,

$$C_x = \frac{T_x}{R_x} \quad (4)$$

where C_x is the capacitance of the Foster model, τ_x is the thermal time constant, and R_x is the resistance of the Foster model. These values of resistances and capacitance for the Foster model are obtained from the curve fitting app in MATLAB. The values are shown in the table below.

Cauer Model was generated by converting the Foster model obtained in the previous section. The algorithm for conversion was obtained from [10], and the MATLAB code is used for calculation using [11]. The thermal impedance vs time curve of the Cauer model was validated against the single pulse case curve of IAUT260N10S5N09 MOSFET [8] and Simulink Foster model of the MOSFET. The process of converting the Foster model to the Cauer model involves the calculation of Thermal impedance Z_n for the Foster model. The thermal impedance is given in Eq. 5.

$$Z_n(s) = \frac{N_n(s)}{D_n(s)} = \sum_{s=1}^m \frac{R_s}{1 + ST_s} = \frac{1}{sC_n + \frac{1}{R_n + Z_{n-1}(s)}} \quad (5)$$

where n is the index of RC node of Foster model, Z is thermal impedance, N is the numerator, D the denominator, R_s is the resistance of the Foster model, τ_s , is the product of resistance and capacitance of the Foster model, C_n and R_n are capacitance and resistance of the Cauer model, respectively.

The Foster model RC values are used as input in Eq. 5 and simplified to get the RC values for the Cauer model. Table 2 depicts the calculated Cauer RC values.

2.2 Simulation Setup

Foster Model Using the values in Table 1, a Foster model was created in MATLAB Simulink for the IAUT260N10S5N09 MOSFET. The Foster model generated for the IAUT260N10S5N09 MOSFET is depicted in Fig. 2. The power dissipated is fixed as 1 W, and the simulation was run for 1 s. In the model, the power dissipated by the MOSFET is represented as current, the temperature is represented as voltage, the thermal resistances are represented as electrical resistors, and the thermal mass is represented as electrical capacitors. A voltage sensor was used to get the transient junction temperature of the MOSFET during the simulation. The ambient temperature was assumed to be 25 °C [8]. The thermal impedance of the MOSFET is obtained from the junction temperature using the following Eq. 6.

Table 1 Resistance and capacitance values for Foster model of IAUT260N10S5N09 MOSFET

Capacitance (C)	Resistance (R)
0.1068	0.0455
0.0038	0.1549
0.1061	0.2954
739.2596	4.376e-05

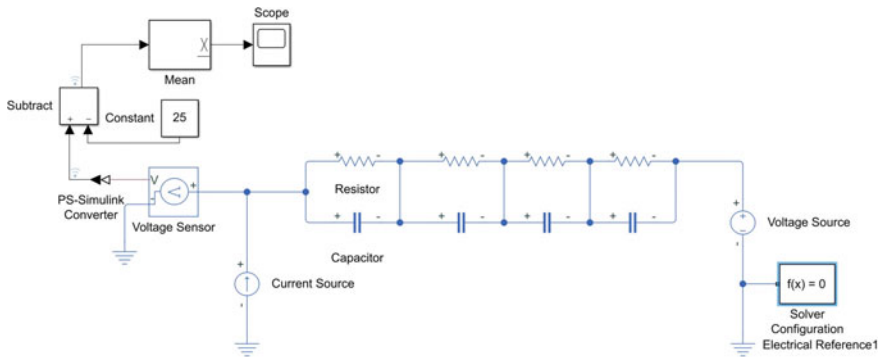


Fig. 2 Foster model of IAUT260N10S5N09 MOSFET

Table 2 Resistance and Capacitance values for Caue model of IAUT260N10S5N09 MOSFET

Capacitance (C)	Resistance (R)
0.0036	0.177
0.0578	0.1487
0.0976	0.1701
1.0498E + 06	3.0842E-08

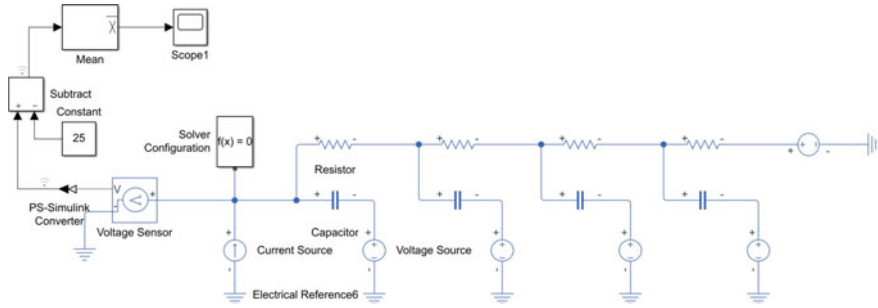


Fig. 3 Caer model of IAUT260N10S5N09 MOSFET

$$Z_{Th} = T_J - T_{amb} * P \tag{6}$$

where T_J is the junction temperature, T_{amb} is the ambient temperature, and P is the power dissipated by the MOSFET. Since the power dissipated is 1 W, and the ambient temperature was assumed to be 25 °C, the values from the voltage sensor were reduced by 25 to get the thermal impedance of the MOSFET. These data were logged for validation.

Caer Model RC Values on the four Caer nodes as depicted in Fig. 3 are taken from Table 2. The voltage source, current source, power, ambient temperature and simulation time are kept the same as the Foster model. The junction temperature is calculated using Eq. 6, and the results of the study were recorded for validation.

3 Results and Discussion

3.1 Validation

The software was validated using [9]. Nexperia Application note describes the experimental setup and results of the thermal network model. The experimental setup was recreated in MATLAB Simulink, and the results were validated.

Generating Thermal Impedance Curve The simulation setup is as depicted in [8]. On running the simulation, the thermal behavior of the curve was plotted in the scope. Figure 4 shows the comparison of the thermal behavior as plotted in [8] and those plotted by our simulations in Simulink. The curve displays the junction temperature at each instance of time. The thermal behavior of the Simulink plot is in good agreement. The error is less than 1%.

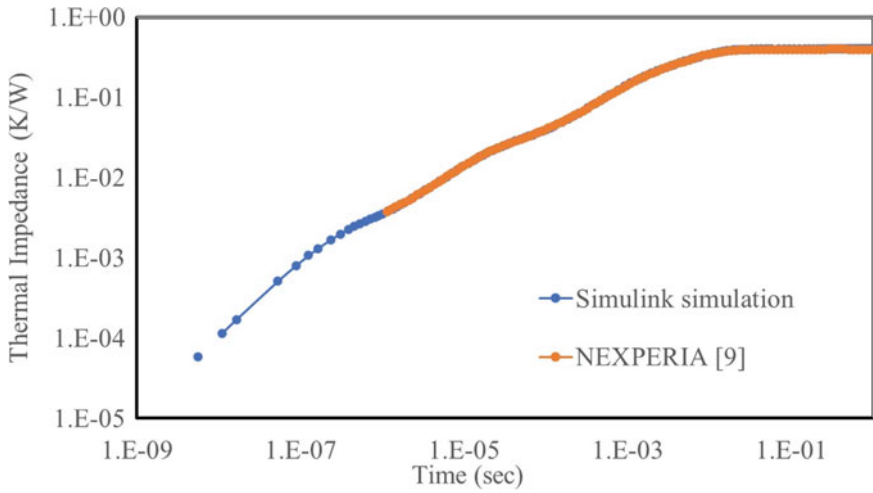


Fig. 4 Thermal behavior curve Nexperia Document [9] and Simulink simulations

3.2 Results

The Foster and Cauer model thermal impedances were plotted in logarithmic axis and compared with the values of thermal impedance obtained from the datasheet [8]. Fig. 5 compares the three values.

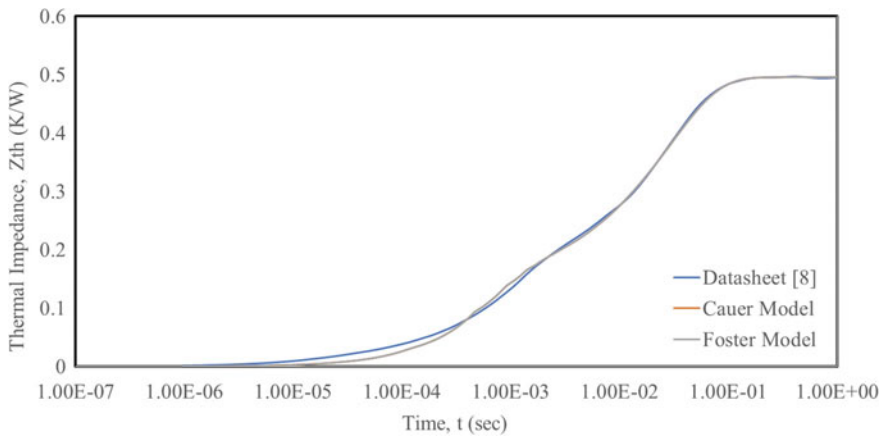


Fig. 5 Comparison of thermal impedance versus time graphs obtained from IAUT260N10S5N09 MOSFET datasheet [8] and the Simulink Foster and Cauer model simulation

4 Conclusions

The comparison shows that the values obtained from the Foster and Cauer model created in Simulink and those obtained from the datasheet of the IAUT260N10S5N09 MOSFET [8] are in good agreement with error less than 1%. This shows that the Foster and Cauer model can accurately predict the transient junction temperature of the MOSFET for different values of power dissipated.

The Cauer and Foster model curves completely overlap one another showing the complete conversion of the Foster model to the Cauer model.

Acknowledgements The authors acknowledge the financial support from M/s Garrett—Advancing Motion for conducting the present study.

References

1. Qian C, Gheitaghy AM, Fan J, Tang H, Sun B, Ye H, Zhang G (2018) Thermal management on IGBT power electronic devices and modules. *IEEE Access* 2(6):12868–12884
2. Kojima T, Yamada Y, Nishibe Y, Torii K (2007) Novel rc compact thermal model of hv inverter module for electro-thermal coupling simulation. In: 2007 Power conversion conference-Nagoya, pp 1025–1029. *IEEE* (2007) <https://doi.org/10.1109/PCCON.2007.373092>
3. Kojima T, Yamada Y, Ciappa M, Chiavarini M, Fichtner W (2004) A novel electro-thermal simulation approach of power igbt modules for automotive traction applications. *R&D Rev Toyota CRDL* 39(4):27–32
4. Luo Z, Ahn H, Nokali M (2004) A thermal model for insulated gate bipolar transistor module. *IEEE Trans Power Electron* 19(4):902–907
5. Igic P, Mawby P, Towers M, Batcup S (2001) Dynamic electro-thermal physically based compact models of the power devices for device and circuit simulations. In: Seventeenth annual IEEE semiconductor thermal measurement and management symposium (Cat. No. 01CH37189), pp 35–42. *IEEE* (2001) <https://doi.org/10.1109/STHERM.2001.915142>
6. Zhou Z, Holland P, Igic P (2008) Compact thermal model of a three-phase igbt inverter power module. In: 2008 26th international conference on microelectronics, pp 167–170. *IEEE* (2008) <https://doi.org/10.1109/ICMEL.2008.4559249>
7. Pandya K, McDaniel W (2002) A simplified method of generating thermal models for power mosfets. In: Eighteenth annual IEEE semiconductor thermal measurement and management symposium. Proceedings 2002 (Cat. No. 02CH37311), pp 83–87. *IEEE* (2002) <https://doi.org/10.1109/STHERM.2002.991350>
8. Infineon Datasheet, <https://www.infineon.com/cms/en/product/power/mosfet/20v-800v-automotive-mosfet/75v-100v-n-channel-automotive-mosfet/iaut260n10s5n019/#!?fileId=5546d4625ee5d4cd015f2460488e3241>. Accessed 9 Oct 2020
9. Nexperia Application note, <https://assets.nexperia.com/documents/application-note/AN11261.pdf>. Accessed 9 Sept 2020
10. System-Level Thermal Simulation FTF-SDS-F0027, <https://www.nxp.com/files-static/training/doc/ftf/2014/FTF-SDS-F0027.pdf>. Accessed 20 Oct 2020
11. Foster and Cauer equivalent networks <https://in.mathworks.com/matlabcentral/fileexchange/48042-foster-and-cauer-equivalent-networks>. Accessed 22 Oct 2020

A Parametric CFD Study on the Cooling Capability of a Rectangular Channel Heat Sink



Akhilesh Danesh Jatti, Mayur Chetan Shanbhag, D. S. Shashwath, Babu Rao Ponangi, and V. Krishna

Abstract This paper is focused on the study to determine an effective method for the thermal management and cooling of power electronic packages used in Hybrid Electric Vehicles (HEVs). It has been carried out with the help of Computational Fluid Dynamics (CFD). After extensive study, one such method chosen for the cooling application is the use of fluid-cooled heat sinks. Modeling and simulation have been carried out using COMSOL Multiphysics. Validation of the CFD results from the research paper by Quadir et al. was performed. Building upon the validation, a simple rectangular channeled heat sink was built for analysis. Furthermore, a parametric analysis was carried out by varying the channel height and channel width of the heat sink to study their effects on cooling. It was determined that an increase in the height and width together leads to a decrease in the outlet temperature and also a decrease in heat transfer coefficient.

Keywords Hybrid electric vehicles · Microchannel heat sink · Electronics cooling · Computational fluid dynamics · Parametric sweep

1 Introduction

Due to the depletion of natural and non-renewable energy resources such as crude oil, the need for alternative and clean energy resources has become an impending necessity. One such advancement is the invention and use of HEVs, which make use of both, an internal combustion engine as well as an electrical power pack. These HEVs make use of various electronic packages to run the vehicle. With technological advancement in electronic packages possessing greater computing ability, there is an increase in power requirement to run them. With increasing power requirement, there is a proportionate increase in heat dissipation, which necessitates the need for thermal management of these electronic packages.

A. D. Jatti (✉) · M. C. Shanbhag · D. S. Shashwath · B. R. Ponangi · V. Krishna
PES University, 100 Feet Ring Road, Banashankari Stage III, Bengaluru, Karnataka 560085, India
e-mail: akhileshjatti1@gmail.com

1.1 Literature Review

The following points were summarized from the literature that was reviewed pertaining to the subject of study:

- Wu et al. [5] created and studied a setup for an immersed jet array impingement cooling device. In this setup, the integrated circuit is submerged in the coolant, and it is sprayed onto all the surface of the electronic package with the help of jets as well.
- Turek et al. [4] summarized the evaporative spray cooling to remove heat using the phase change process by using the latent heat of vaporization. The cooling is done by integrating a spray cooling mechanism, which cools the bottom of the boards of the inverters with specified coolant.
- Pease et al. [3] first proposed the idea of a microchannel heat sink in 1981. Their work explained the physics of a microchannel heat sink setting the foundation for further studies in this topic.
- Khan et al. [1] studied the effects of various shapes for the microchannel heat sink and evaluated them and presented them via this paper. Along with shapes, they evaluated the effect of Reynolds number on the thermal resistance.
- Quadir et al. [2] talk about the improvement of a finite element formulation using Galerkin method to study the performance of a microchannel heat sink that is utilized in thermal management of electronic packages. The outcomes were contrasted with CFD results, and it was resolved that the strategy utilized could be an alternative to massive CFD calculations.

From the literature reviewed, several cooling techniques such as immersed jet array impingement cooling, microchannel heat sink, evaporative spray cooling, etc. have been explored. Microchannel heat sinks are especially suited to our needs as they can be etched/bonded onto the surface of a control package and are thus not counterproductive to the proposed miniaturization. Parallel microchannel heat sinks were proposed by the original proposers of this method.

2 Methodology

2.1 Validation of Paper by Quadir et al. [2]

The data obtained from this paper are validated with CFD analysis performed. This comparison of the results obtained in the paper along with CFD results proves that this model built can predict surface temperature and fluid temperature. The geometry used in the setup is taken up from [2], and the dimensions are mentioned in Table 1.

The coolant chosen is water. The general properties of conduction and flow are shown in Table 2.

Table 1 Dimensions used to build the geometry

Parameter	Value
Channel height	200 μm
Channel width	56 μm
Fin half-thickness	12 μm
Channel length	0.5 cm
Base thickness	2 μm

Table 2 Properties of conduction and fluid

Parameter	Value
Fluid velocity	1.973 m/s
Coolant inlet temperature	10 $^{\circ}\text{C}$
Channel thermal conductivity (Silicon)	125 W/mK
Coolant thermal conductivity	0.609 W/mK
Coolant absolute viscosity	$9.8 \times 10^{-4} \text{Ns/m}^2$
Coolant specific heat capacity	4180 J/kgK
Coolant density	1000 kg/m^3

Geometric Modeling. The geometry (Fig. 1) was modeled based on the details from Table 1 in COMSOL Multiphysics.

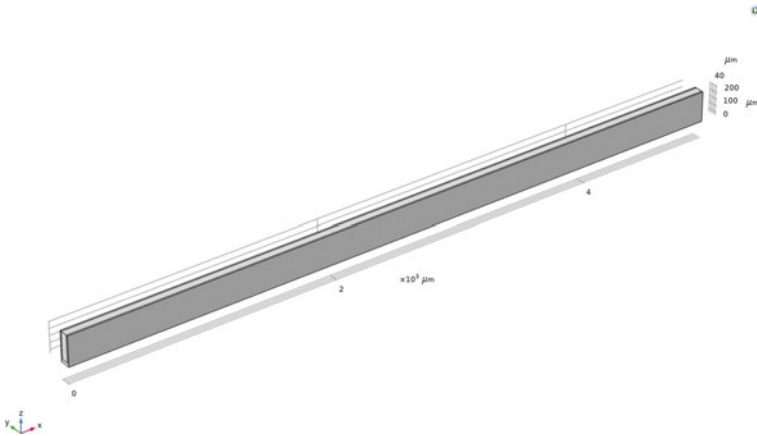


Fig. 1 Geometry on COMSOL

2.2 Heat Sink with Rectangular Channels

A circuit board houses several parts such as the resistors, transistors, capacitors, inductors, diodes, etc. however, one of the most important parts of a circuit board is the control unit, which performs the function as the brain of the board. As such, the tasks conducted by the controller are complicated and thus power intensive. This power requirement is accompanied by the need for a method to cool the controller. One such method that has been applied in this paper is the use of a simple rectangular channel heat sink.

Geometric Modeling. A heat sink as shown in Fig. 2 was modeled with the following dimensions:

Length: 60 mm Width: 50 mm Base thickness: 2 mm.

Initial Channel height: 10 mm Initial Channel width: 3.67 mm.

As seen in Fig. 2, the grey portion is the heat sink, and the blue portion is the channels containing the coolant.

Parametric Sweep is the study of a model for varying parameters, which can be used to optimize the model. This function was used from COMSOL Multiphysics. In this study, a parametric sweep was conducted to analyze the variation of cooling effect of the heat sink by varying the channel height and width.

Using parametric sweep, the height and width of the channel were varied to study the heat sink behavior. This process was carried out in three steps, i.e., variation of height alone, variation of width alone, finally varying both the parameters together.

Varied Parameter values are as follows:

Channel Height: 1. 11 mm 2. 12 mm 3. 13 mm 4. 14 mm.

Channel Width: 1. 3.80 mm 2. 3.85 mm 3. 3.90 mm 4. 3.95 mm.

Meshing. The model was meshed with the following mesh statistics (Table 3) with the mesh in Fig. 3.

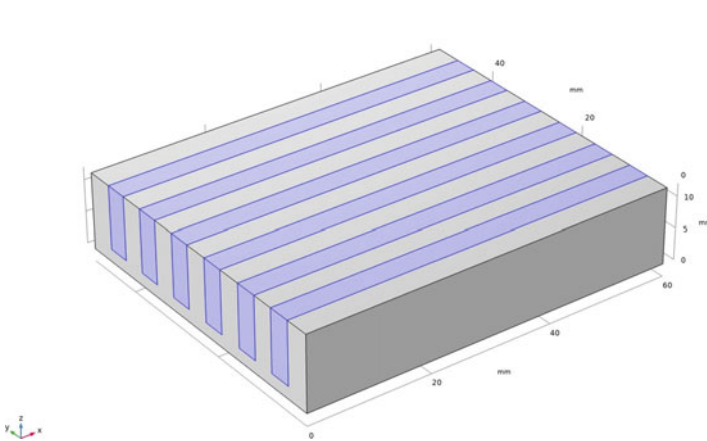


Fig. 2 Geometry of the heat sink analyzed

Table 3 Mesh statistics of the parametric sweep model

Parameter	Value
Number of elements	1,544,742
Average element quality	0.677

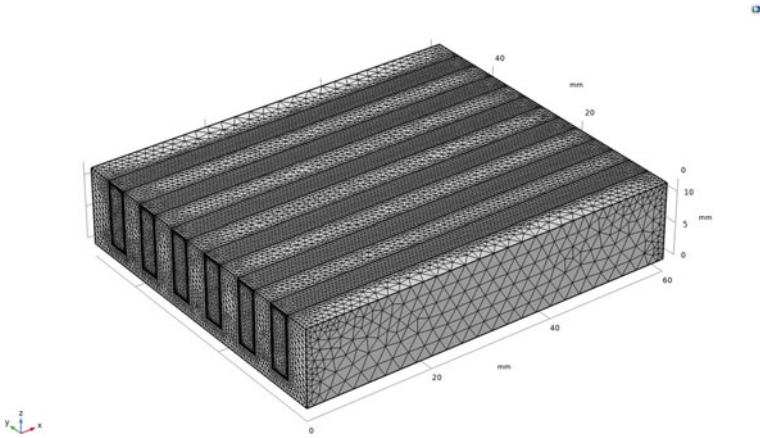


Fig. 3 Mesh of the geometry used in the study of parametric sweep

Table 4 Boundary conditions in the analysis of parametric sweep model

Parameter	Value
Physics	Turbulent flow k-ε model
Velocity inlet	1.973 m/s
Pressure outlet	0 Pa (Gauge pressure)
Heat flux	10^6 W/m ² given at base of heat sink
Coolant (density, viscosity)	Water (1000 kg/m ³ , 9.8×10^{-4} Ns/m ²)

Reynolds number from calculations was found to be 10,811.23 and was observed to be greater than 2300. Thus, a Turbulent Flow model was used. The boundary conditions used for the simulation are given in Table 4.

3 Results and Discussions

3.1 Validation of Research Paper by Quadir et al. [2]

The results of a newly developed methodology must be validated against previously known results, ideally against experimental results or results from other numerical or analytical methods, in order to establish its credibility. This paper has been validated against CFD results reported and used by Quadir et al. [2]

The single microchannel model that was studied was simulated on two softwares, i.e., COMSOL Multiphysics (Fig. 4a) and ANSYS Fluent (Fig. 4b). For the given

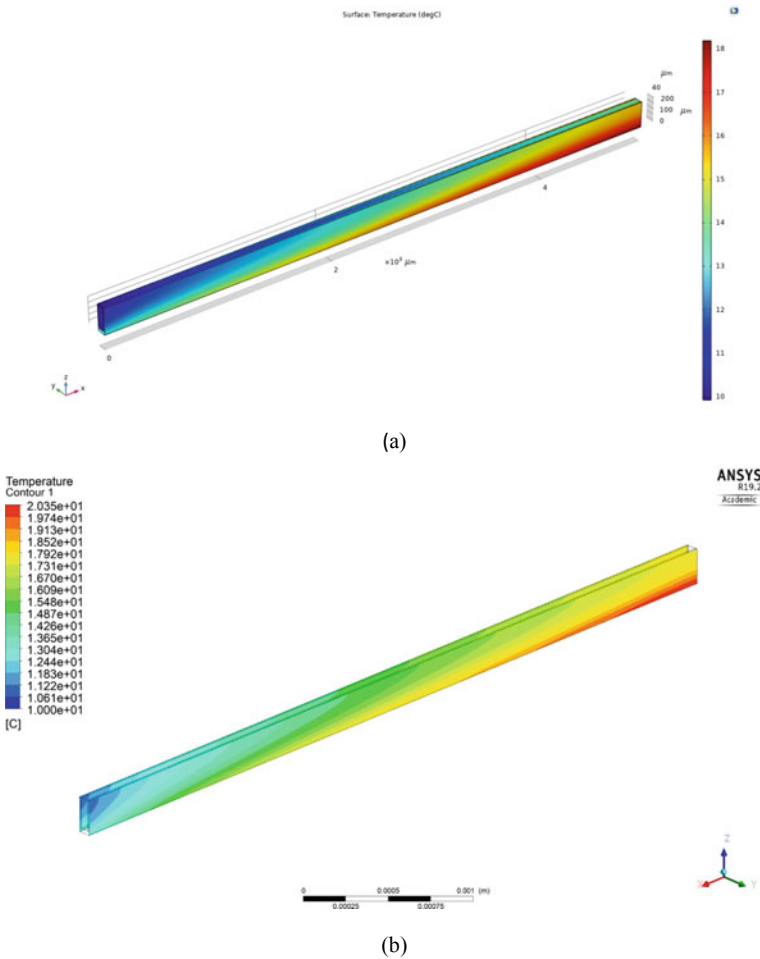


Fig. 4 Temperature plot on COMSOL (a) and Ansys (b) in °C

boundary conditions, the outlet temperature of the single microchannel was found to be 14.612 °C. The temperature at the outlet mentioned in the paper [2] was 15.16 °C. Thus, an error of 3.61% was seen. Similarly, the maximum temperature observed at the surface of the microchannel was 18.197 °C. However, the paper [2] mentioned a value of 20.006 °C. Thus an error of 9.04% was seen.

These error percentage values were greater than 2.5% and thus due to unsatisfactory results, the same model was analyzed on Fluent. For the same boundary conditions, the maximum surface temperature and the outlet temperature values are found to be 20.3512 °C and 15.1053 °C, respectively. Thus, error values of 1.69% and 0.36% were found for the maximum surface temperature and outlet temperatures, respectively. Since these values are within the acceptable limit, the CFD part of the paper [2] has been validated.

3.2 Parametric Sweep

The CFD analysis was carried out for three different combinations of the varying parameters. From the graph in Fig. 5a, where only channel height is varied, it is observed that increasing height decreased the outlet temperatures. From Fig. 5b, where channel width is varied, it is seen that increasing width decreased the outlet temperature. From Fig. 6, as expected, for the combination of the highest values of width and height, the outlet temperature was minimum. Figure 7 gives us the variation in the heat transfer coefficient as observed in the model.

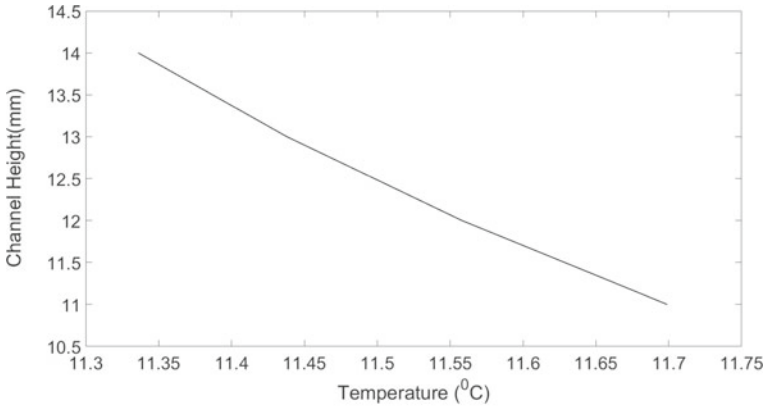
4 Conclusions

The analysis was carried out on the microchannel heat sink proposed in the paper [2]. We were able to validate the paper with an error of 1.36% and 0.35% in the values of the outlet temperature and maximum surface temperature by using the Ansys Fluent software as done by the paper.

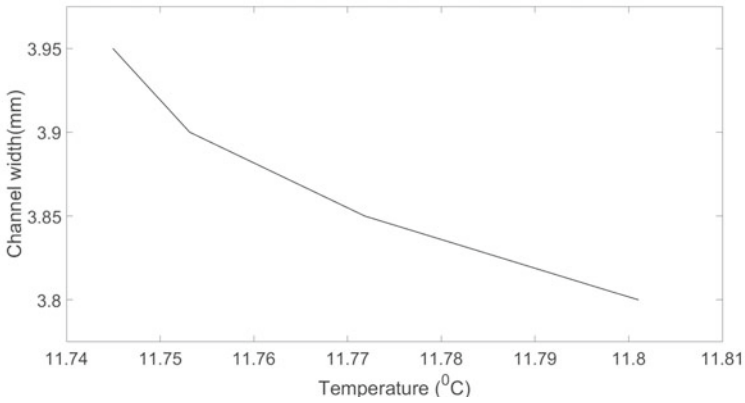
The next analysis was a parametric sweep done in COMSOL Multiphysics for different values of height and width in order to understand the variation and sensitivity of these parameters. In this study, it was found out that, increasing in height alone and width alone decreases the temperature of the fluid at the outlet.

More importantly, when both the variations in height and width are combined, we find that the results from the previous models are held true. An increase in the height and width together leads to a decrease in the outlet temperature.

Another important finding from these studies happens to be the massive reduction in pressure between the inlet and the outlet. As seen from Fig. 8, the pressure drop in the parametric sweep model was as high as 0.33 kPa for a mere channel length of 60 mm. From this, we can conclude that the pumping power needed to push the



(a)



(b)

Fig. 5 Outlet temperature graph for increasing (a) channel height (b) channel width

coolant through the channel is going to be relatively high; thus making the pressure drop a very significant factor while designing any microchannel heat sink.

After taking into the consideration, several determining constraints such as pressure drop, surface temperature and heat transfer coefficient, the critical factors which determined the optimum cooling capability of the heat sink corresponded to the maximum channel height and minimum channel width.

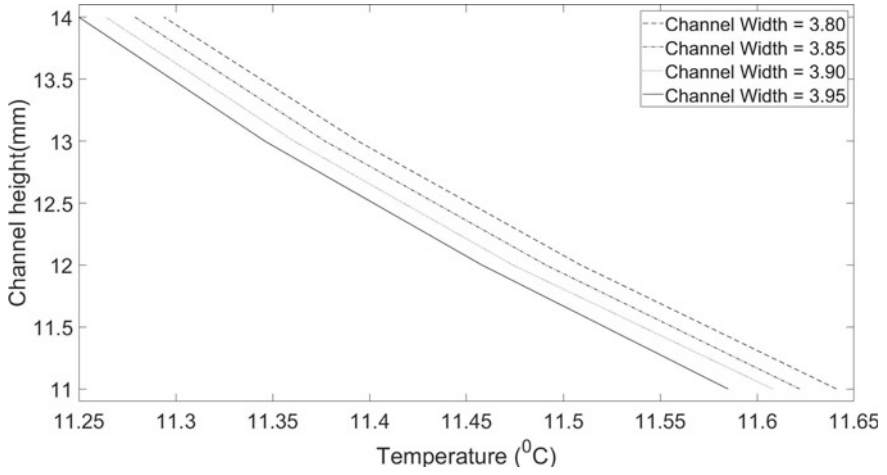


Fig. 6 Variation of outlet temperature with channel height for different channel width

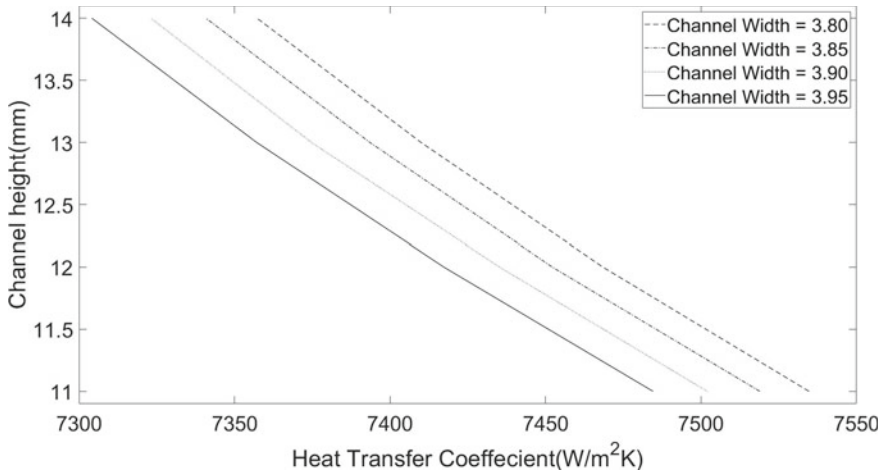


Fig. 7 Variation of heat transfer coefficient with channel height for different channel width

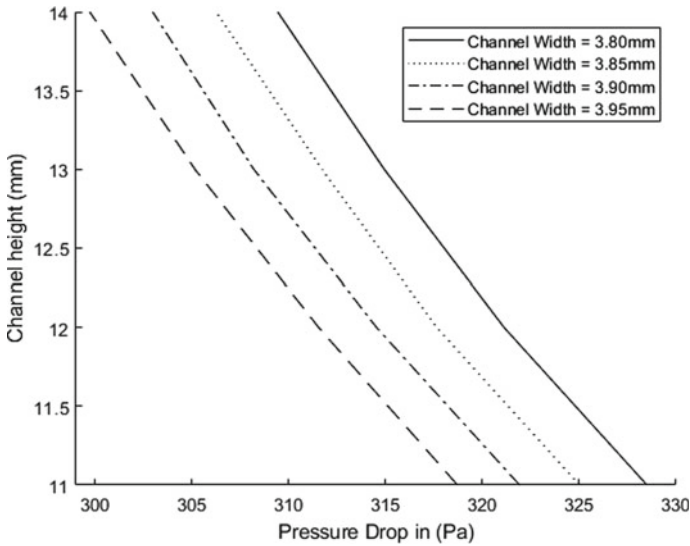


Fig. 8 Variation of pressure drop with channel height for different channel width

Acknowledgements The authors acknowledge the financial support from M/s Garrett—Advancing Motion for conducting the present study.

References

1. Khan AA, Kim KY (2016) Evaluation of various channel shapes of a microchannel heat sink. *Int J Air-Condition Refrigeration* 24(03):1650018
2. Quadir G, Mydin A, Seetharamu K (2001) Analysis of microchannel heat exchangers using FEM. *Int J Numerical Methods Heat Fluid Flow*
3. Tuckerman, D., Pease, R.: High-performance heat sinking for VLSI. *Electron Device Letters, IEEE* 2, 126 – 129 (06 1981). <https://doi.org/10.1109/EDL.1981.25367>
4. Turek, L.J., Rini, D.P., Saarloos, B.A., Chow, L.C.: Evaporative spray cooling of power electronics using high temperature coolant. In: 2008 11th Intersociety Conference on Thermal and Thermomechanical Phenomena in Electronic Systems. pp. 346–351. IEEE (2008)
5. Wu, R., Yiwen, F., Hong, T., Zou, H., Hu, R., Luo, X.: An immersed jet array impingement cooling device with distributed returns for direct body liquid cooling of high power electronics. *Applied Thermal Engineering* 162, 114259 (08 2019). <https://doi.org/10.1016/j.applthermaleng.2019.114259>

Estimation of Tire Scaling Coefficients and Simulation of On-Road Vehicle Behaviour



Nandish H S, Prajwal P, and Patil S S

Abstract The paper aims at estimating the tire scaling coefficients to predict the on-road handling behaviour of a car. The effect of amplified tire forces due to the constant deposition of tire rubber on the tire testing belt can be compensated by the tire scaling coefficient. Scaling coefficients along with the tire force coefficients can be helpful in estimating the on-road tire forces and moments. The tire's lateral scaling coefficients were evaluated using the data from tire testing and the on-road tests. A full car model was developed using VI-CarRealTime considering parameters from different subsystems like vehicle body/frame, power-train, suspension, steering, tires, brakes and wheels. Skid-pad simulations were followed by skid-pad tests to validate the full car model.

Keywords Tire scaling coefficient · Data acquisition system · Vehicle testing · Skid-pad · MMM diagram · MF tire model

Nomenclature

F_x	Tire Longitudinal Force, in N,
F_y	Tire Lateral Force, in N
F_z	Tire Normal Load, in N
SA	Tire Slip angle, in deg
F_y/F_z	Coefficient of friction of the tire in lateral direction
DOF	Degrees of Freedom
MMM	MRA Moment Method
TTC	Tire Testing Consortium

Nandish H S (✉) · Prajwal P
PES University, Bengaluru, Karnataka 560085, India
e-mail: nandish.hs.shetty@gmail.com

Patil S S
Prof. Department of Mechanical Engineering, PES University, Bengaluru 560085, India
e-mail: sspatil@pes.edu

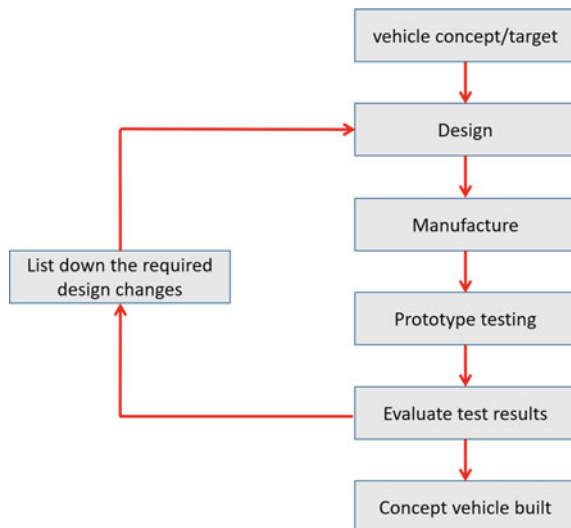
GPS	Global Positioning System
GLONASS	Global Navigation Satellite System
MF Tire Model	Magic Formula Tire Model
IMU	Inertial Measurement Unit
RPM	Revolutions per minute
C_g	Centre of gravity
VI-Car RealTime	A software used for building full vehicle simulation model
Lotus Suspension Analysis	A software used to design the kinematics of a car

1 Introduction

A good handling response of a car gives the driver much-needed confidence to drive. The car’s response to driver’s input is crucial when the car is operating at its limits. Hence, it is important to optimize the parameters influencing the handling. Testing the car at its limits and optimizing the parameters imposes life risk. Hence a simulation model can be used as a substitute to reduce iteration in real-time testing to optimize the limiting parameters. This can also be helpful in educating the driver about car’s expected behavior under various maneuvering conditions.

The importance of simulations in vehicle development can be understood by comparing the old school approach to the current approach. The conventional or old school approach as shown in Fig. 1, requires incorporating changes or rebuilding a prototype for iterative optimization of vehicle parameters. This method of building

Fig. 1 Conventional method of vehicle development



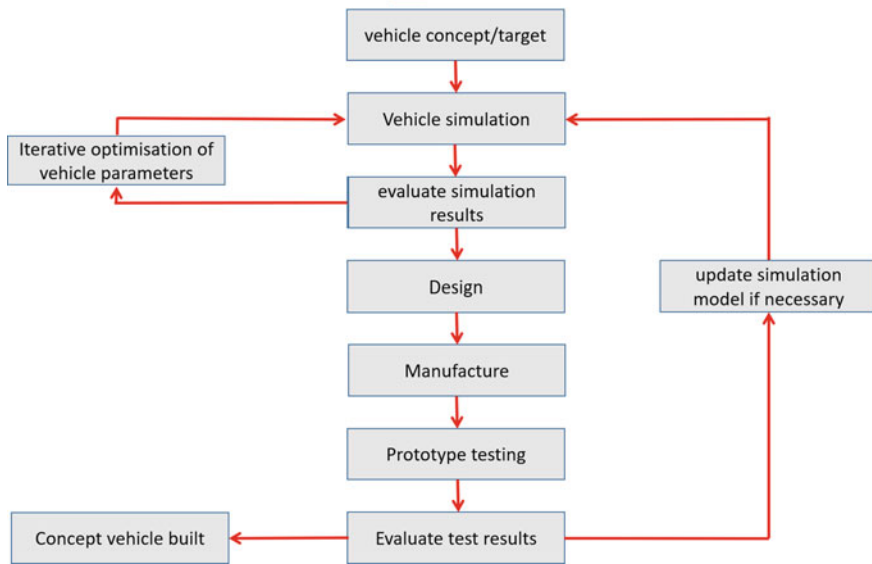


Fig. 2 Simulation driven vehicle development

prototypes for every iteration is both time-consuming and is not cost-intensive. The steps involved in conventional method of vehicle development coupled with system level simulation are shown in Fig. 2.

A full car model which can predict the limits of the car helps cut down the overall development time. Tires are the most critical components of simulations especially if the vehicles limits must be estimated. Hence, accurate modelling of tires gives a good platform for vehicle simulations. The approach to tune the vehicle platform and the tires can be understood from references [1, 2] respectively. A formula student car was considered for this research. Formula student events are engineering design competition in which students design, build and test formula style open wheeled race cars.

Testing was carried out on the said car post instrumentation. The normalized tire forces were calculated from testing to estimate the scaling coefficients for the MF tire model. The estimated coefficients were fed into the full car simulation model build using VI-CarRealTime software. The model was further validated with the on-road test data.

2 Testing of Formula Student Car

The formula student car was rigged up with VBOX 3i data logging system which had sensors like GPS, IMU, steering angle sensor and so on. Racelogic VBOX 3i data

logger recorded data such as lateral, longitudinal accelerations, longitudinal speed, yaw-rate, heading angle, steering wheel angle, etc.

2.1 Instrumentation

A potentiometer of 10 kΩ max resistance was used to measure the angular deflection of the steering wheel. VBOX 3i uses a GPS/GLONASS receiver to log data at a rate of 100 Hz to achieve high accuracy. Velocity and heading data are calculated by Doppler Shift method in the GPS signal. The logger has the ability to utilize data from the IMU and uses a Kalman Filter to improve all parameters measured in real time. IMU integration ensures accurate test results in areas of unreliable satellite reception, typically caused by trees, buildings and bridges [3].

Inertia measurement unit (IMU), GPS and power connections were made to the logger using the allocated ports. The logger has a 4-channel analog input and necessary voltage output for any extra sensors. The potentiometer used to measure the steering wheel angle was connected to the logger using a D-sub connector. The connections are depicted in the schematic in Fig. 3. The actual connections are shown in Fig. 4.

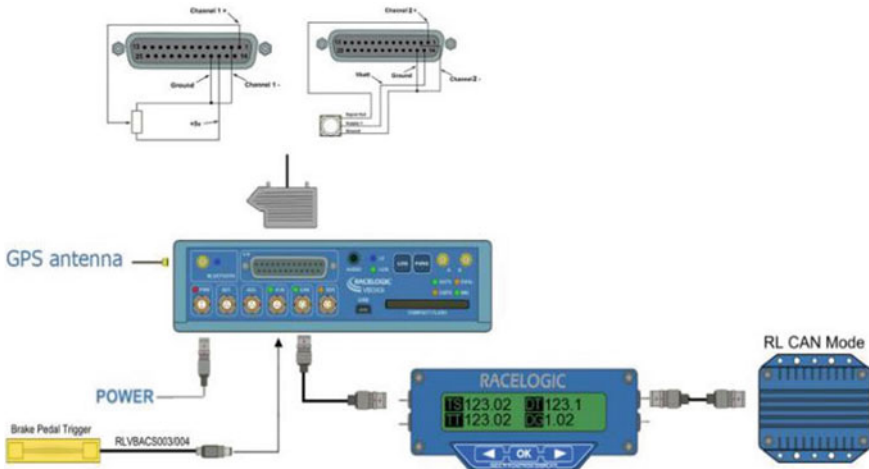


Fig. 3 Indicative diagram of the data logger connection



Fig. 4 Data logger connections

2.2 Testing and Data Logging

The design of a car involves a trade-off in certain aspects to improve upon the performance. Vehicle testing is done to validate the design and understand the design flaws involved.

Skid-pad testing was done to evaluate the steady state parameters of the vehicle. Skid-pad testing involves running the car around a circular track mainly to evaluate the forces and moments acting on the vehicle at steady state. The track was setup for a turning radius of 5 m and the target vehicle speed was 21 kmph.

Human error is inevitable and hence there are small corrections induced by the driver. The data logged during skid-pad testing after applying Kalman filter is shown in Fig. 5. The figure shows the variation of speed, lateral acceleration, and yaw-rate. Figure 6 represents the latitude and longitudinal track map obtained using the GPS data. This figure indicates the path that the vehicle took during the test.

Tire forces were estimated using bicycle model. The tire forces were then normalized with respect to the normal load (F_z) on each wheel in order to overcome the effect of wheel normal load. The equations for the same can be found in [4].

3 Data Processing

The raw data obtained from tire testing at the Calspan tire research facility needs to be converted to a format supported by simulation software. MF tire model is one of the commonly supported models by simulation software. The raw data is converted to MF Tire model coefficients by a method of regression as explained in the Fig. 7.

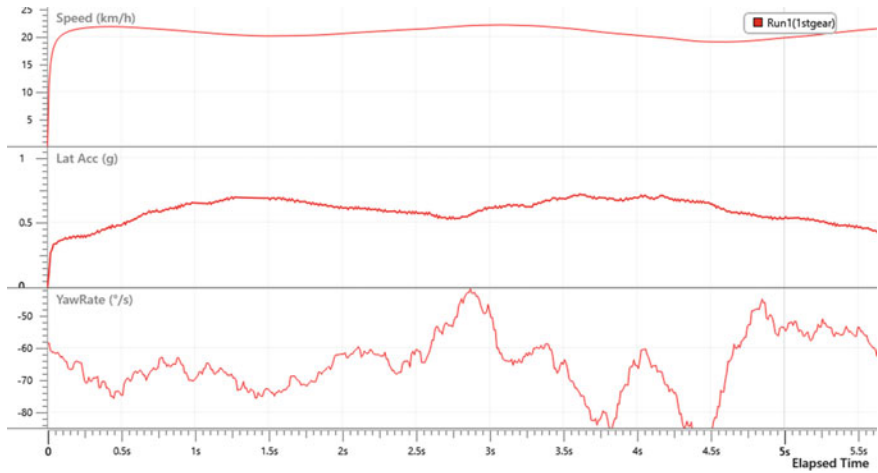
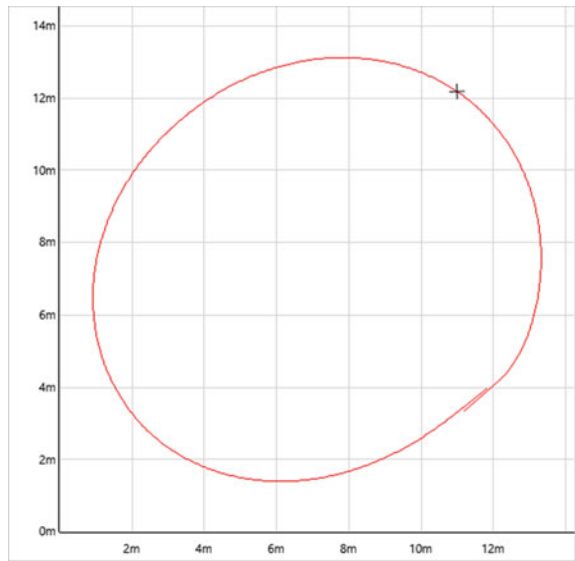


Fig. 5 Test data obtained from VBOX

Fig. 6 GPS data of the vehicle path using latitude and longitude



Raw data is compared with the coefficient value. The error so estimated is minimized using Fmin search in MATLAB.

The data collected from testing was processed and the corresponding lateral forces, slip angles at the front and the rear wheels were evaluated. These lateral forces are normalized with respect to the instantaneous wheel normal load as different tires of the vehicle are operating at different wheel normal loads. A regression method similar to that used in estimation of MF tire coefficients was used to arrive at the

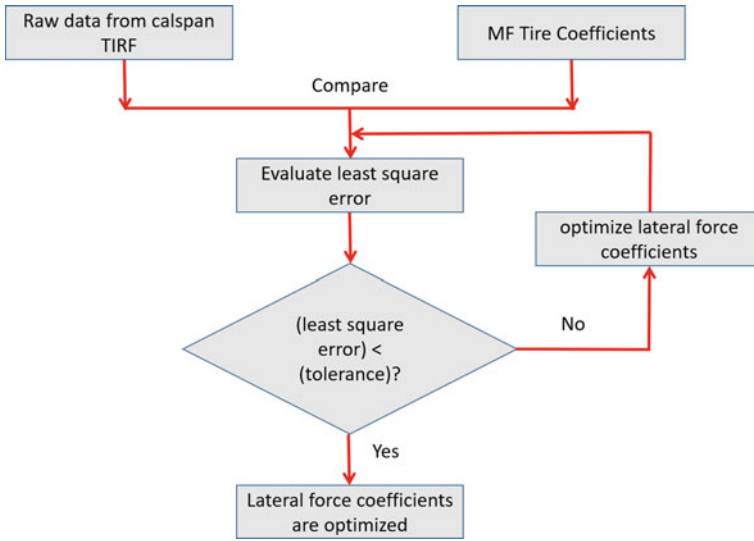


Fig. 7 Estimation of MF tire coefficients

scaling factors. The error obtained by the sum of test data, MF tire coefficients and scaling factors has been minimized using Fmin search in MATLAB. Thus estimating the scaling factors. The flowchart for this process can be found in Fig. 8.

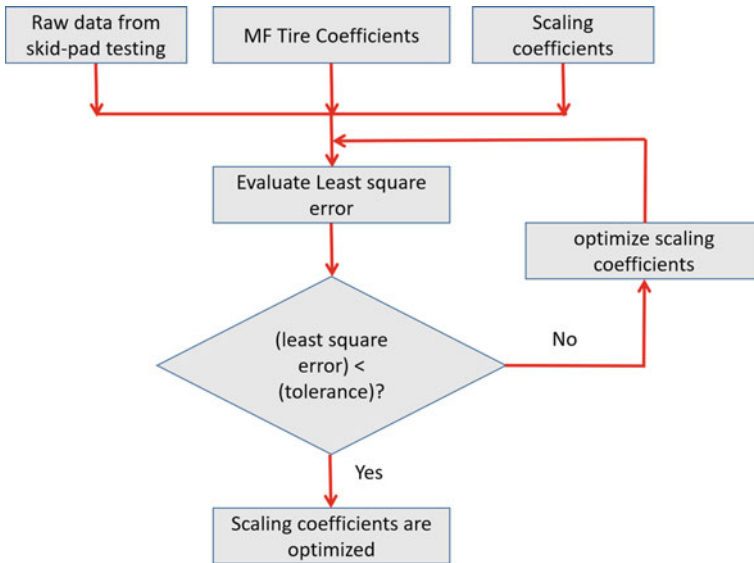


Fig. 8 Estimation of scaling coefficients

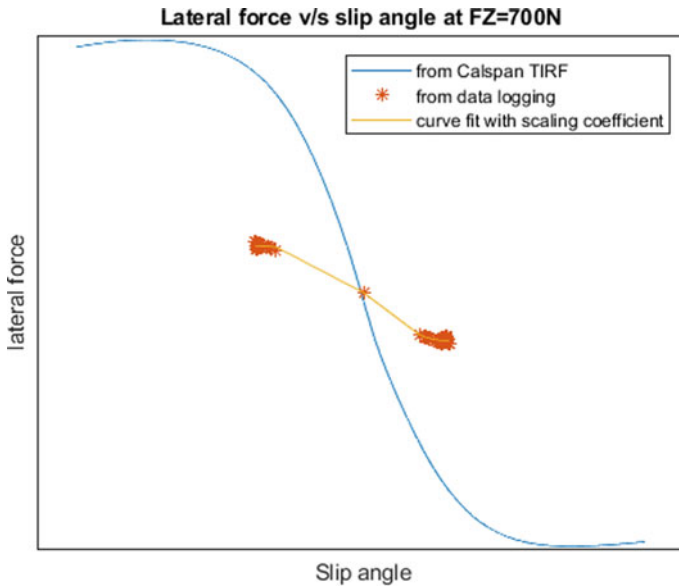


Fig. 9 Normalized lateral force from tire testing versus data from testing

Figure 9 shows difference in the normalized lateral forces between test data obtained from Calspan and that from testing. Clearly the test was performed at lower friction surface compared to that seen on the test belt of the tire testing facility. The difference between the curves before and after using the tire scaling coefficients can be seen in Fig. 10.

4 Building Simulation Model

Vehicle simulation (according to Chap. 9 of [5]) can be defined as a set of equations, typically solved by a computer program, which calculates the response of the entire vehicle to a set of operating conditions. VI-CarRealTime provides the platform to build the car model and run the required simulations.

VI-CarRealTime, a virtual modelling and simulation environment is used to build a simplified 4 wheels vehicle model. Its functionality includes the ability to assemble vehicle system by collecting its fundamental subsystems, specifying dynamic maneuver, schedules, launching standalone or MATLAB/SIMULINK embedded simulations, post processing the obtained results as explained in [6].

The parameters that define the vehicle subsystems control the vehicle behavior in different maneuvering conditions. The parameters input from various subsystems are explained in the following sections.

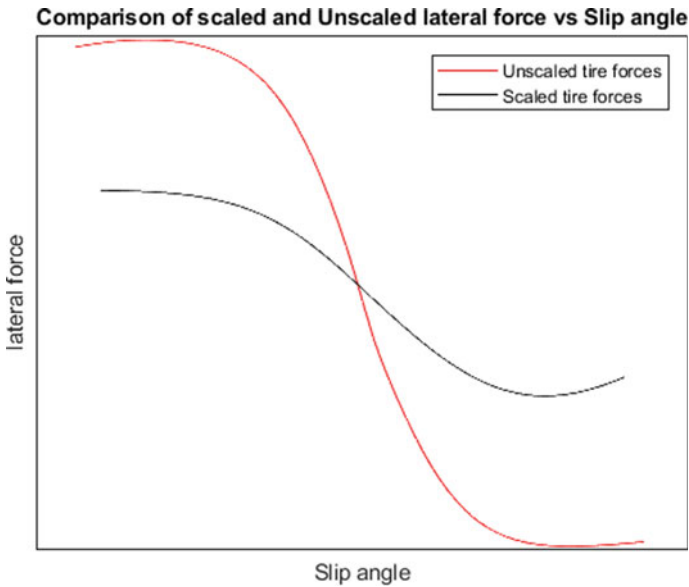


Fig. 10 Lateral tire force versus slip angle with and without scaling coefficients

4.1 Brake Parameters

Brake parameters like master cylinder pressure gain, effective piston area, brake bias, etc. were calculated with data available on the master cylinder and calliper dimensions. A 2 g braking scenario was assumed to calculate the front brake bias. Parameters like the coefficient of friction between the disc and the brake pad had to be taken from spec sheets.

4.2 Suspension Parameters

The suspension system was initially designed using Lotus Suspension Analysis, a simulation model used for designing the kinematics of a suspension system. The hard points were imported to VI-SuspensionGen, which is a part of the Vi-grade software package. VI-SuspensionGen runs kinematic and elasto-kinematic analysis and the results are exported to VI-CarRealTime as an input to the full car model.

The front suspension system is a pull rod suspension to reduce the centre of gravity and for better packaging. A spring stiffness value of 25 N/mm was designed for the front suspension. The modelling of the rear suspension system follows the same steps as the front suspension system. A push-rod suspension was designed for the rear due to packaging constraints and ease of tuning the rear spring. A spring stiffness value of 35 N/mm was designed for the rear suspension to account for the required roll

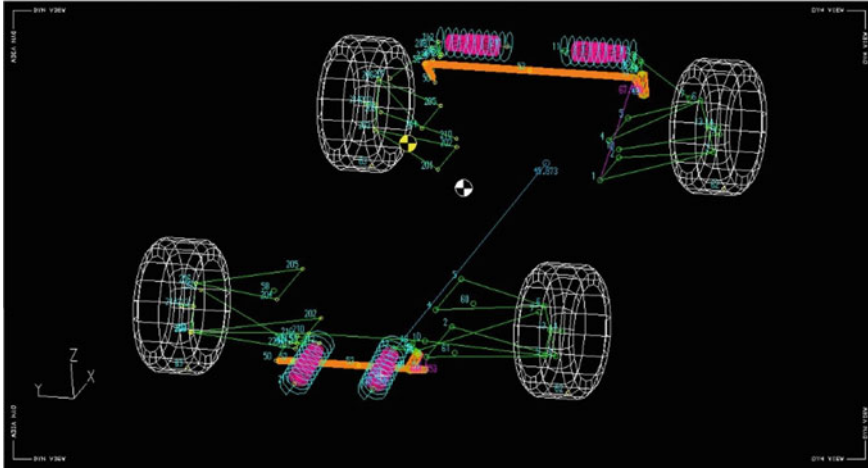


Fig. 11 Suspension design of the car

couple distribution. The said stiffness of the springs were estimated based on ride frequency and flat ride analysis. The front and rear suspension systems are as shown in the Fig. 11.

Dampers act like dynamic springs and controls the rate of change of load transfer. Custom-made shocks were provided by Gabriel India limited. The damping coefficients were calculated considering a 7 DOF suspension model. Equation in Chap. 7 of [5] was helpful in estimating the ride frequencies and damping ratios required for the calculations. The damper force vs velocity curve of the front and rear dampers are as shown in Fig. 12. The said data was obtained from damper testing at Gabriel's test facility.

4.3 Powertrain Parameters

The car uses a single cylinder, liquid-cooled KTM 390 engine. The choice of the engine is with respect to the convenience of handling and servicing. Also, the light weight single cylinder engine decreases the polar moment of inertia compared to its multi-cylinder counterparts. The torque curve is a graph of engine output torque v/s different operating speeds of the engine. The car was tested on a chassis dynamometer and the torque curve was evaluated. The peak torque was obtained close to 6500 rpm. The parameters input to the model includes transmission ratio, torque curve as shown in Fig. 13, transmission ratio, idle RPM, rev limit, stall RPM, shift RPM, etc.

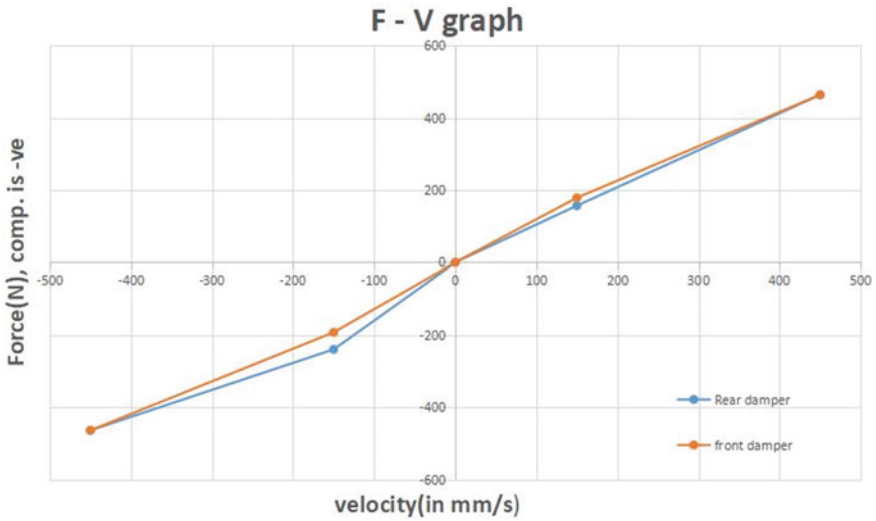


Fig. 12 Front and rear damper test data

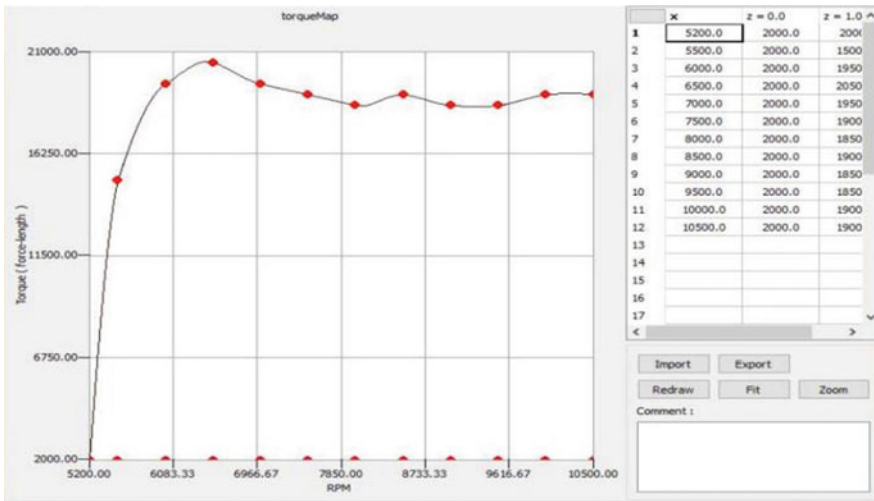


Fig. 13 Front and rear damper test data

4.4 Vehicle Body Parameters

Vehicle body parameters such as the x, y and z positions of the Cg, the mass, and inertias of the body are the required inputs. The inertia properties were estimated based on the CAD design of the full car assembly. The Cg of the car with the driver was measured by applying force equilibrium equations which are depicted in [7] and

Fig. 14 Vehicle on weighing scale during Cg measurement



the position of the Cg in the x, y and z directions were estimated. The measurement of Cg is shown in Fig. 14.

The Cg positions and the inputs to the vehicle body model are depicted in Fig. 15. The inertias were taken by CAD upon assigning material properties to each of the components.

4.5 Tire Parameters

The simulation model requires a tire property file which defines the tire's ability to generate forces and moments. The tire parameters were input based on the MF tire model (Refs. [5, 8]). The lateral coefficients of the tire were evaluated using the method of least squares and as explained in Fig. 15. Curve fitting was done to the data obtained from FSAE TTC [9] and the plot of lateral force v/s slip angle for different normal loads under combined slip conditions [5, 8, 10] are as shown in Fig. 16.

Mass and Inertia	
	Full
CG longitudinal front wheel distance	683.14
CG lateral position	2.17
CG height	215.18
Mass	219.5
Ixx	21240000.0
Iyy	60760000.0
Izz	73610000.0
Ixy	-680000.0
Ixz	-1460000.0
Iyz	-270000.0

Fig. 15 Vehicle body parameters input to VI-CarRealTime

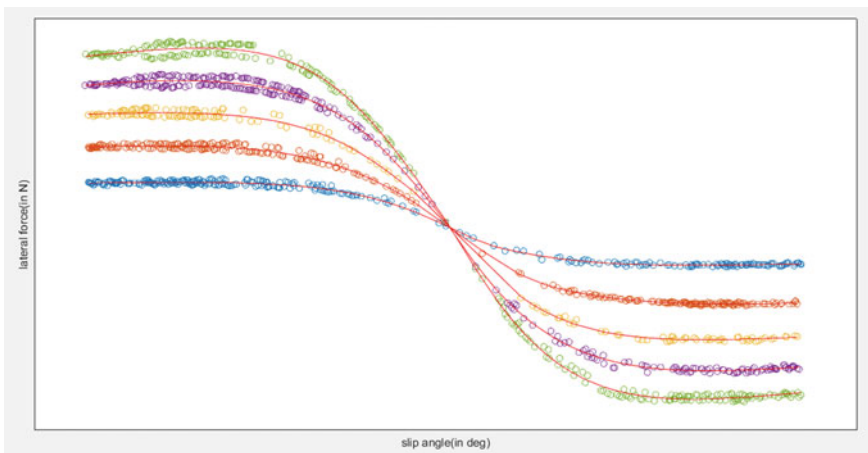


Fig. 16 Vehicle body parameters input to VI-CarRealTime

System was initially designed using Lotus Suspension Analysis, a simulation model used for designing the kinematics of a suspension system. The hard points were imported to VI-SuspensionGen, which is a part of the Vi-grade software package. VI-SuspensionGen runs kinematic and elasto-kinematic analysis and the results are exported to VI-CarRealTime as an input to the full car model.

Table 1 Cross-weight distribution of the simulated model and the actual car

	Simulation corner weights (in N)		Actual vehicle corner weights (in N)	
	Left	Right	Left	Right
Front	697.6 (71.11 kg)	669.23 (68.2 kg)	706.32 (72 kg)	676.89 (69 kg)
Rear	615.95 (62.78 kg)	615.98 (62.8 kg)	568.98 (58 kg)	608.22 (62 kg)

4.6 Static Equilibrium Test

The accuracy of the simulation model's vehicle inertia properties can be verified by running a static equilibrium test. The normal loads on the tires are compared with the actual vehicle corner weights. The total vehicle weight with the driver was found to be 262 kg. The total weight obtained from the simulation was 264.9 kg. The detailed cross-weights table is shown in Table 1.

4.7 Skid-Pad Simulation

Skid-pad simulation as described in Chap. 11 of [4], is a way to measure the steady state vehicle characteristics. The balance of the vehicle at peak lateral accelerations, the under-steer gradient, etc. can be evaluated using skid-pad simulations or testing. Skid-pad simulations were run on VI-CarRealTime for a turning radius of 5 m and a constant speed of 21 kmph.

4.8 MMM Diagram for Steady State Simulation

As presented in Chap. 8 of [4], the MMM, also called Cn-Ay diagrams or Yaw-moment diagrams are specialized plots representing the measured or computed forces and moments from a constrained test or simulated test. In principle, the diagrams are similar to those from wind tunnel tests which portray the variation of vehicle aerodynamic forces and moments as a function of attitude (angles of attack or yaw) and control positions. The calculation of the tire forces using the scaling coefficients helps in predicting the on-road behaviour of the car.

The MMM diagram uses the scaling coefficients along with the lateral forces coefficients for evaluating the tire lateral forces. Hence, the diagram so obtained depicts the steady state behaviour of the vehicle on-road. The procedure of plotting the yaw moment diagram is shown in Fig. 17.

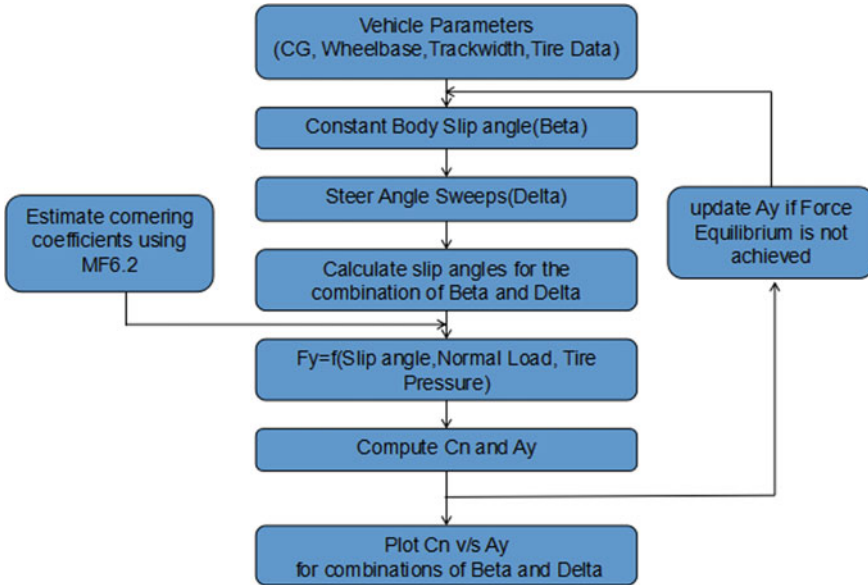


Fig. 17 Method of estimation of MMM diagrams

5 Results

The estimated tire scaling coefficients against the test data obtained from tire testing as shown in figure-10 in the earlier section were used for the simulation model built using VI-CarRealtime. The scaling coefficients thus estimated are shown in Table 2.

For an average percentage deviation of 1% in the longitudinal speed, the percentage deviation in the lateral accelerations and yaw-rates were found to be 7.27% and 15.7% respectively. The comparison for longitudinal velocity, lateral acceleration, and yaw-rate for VI-CarRealTime simulation and the test data from skid-pad testing are shown in Figs. 18, 19 and 20 respectively.

Table 2 Scaling coefficients obtained from regression analysis

LKYG	2.2461
LCY	2.0901
LVY	0.6940
LMUY	0.3717
LKYA	-0.3465
LHY	1.0364
LEY	1.7790
LVYK	-0.0138
LYK	2.2239

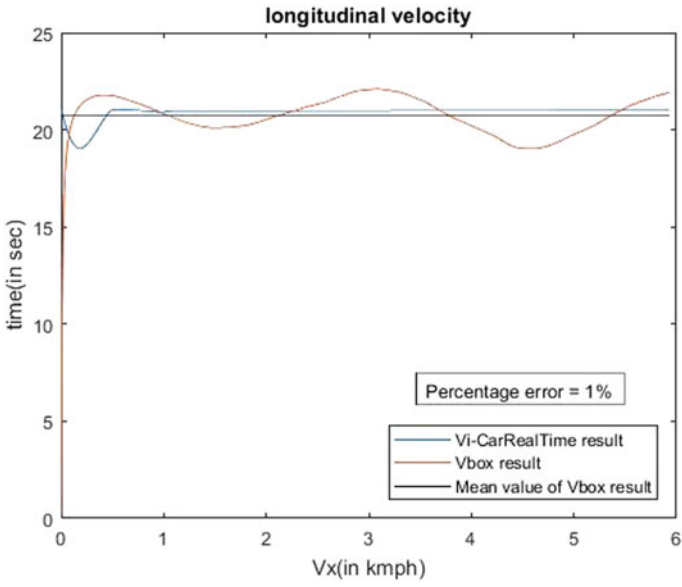


Fig. 18 Comparison of longitudinal velocity

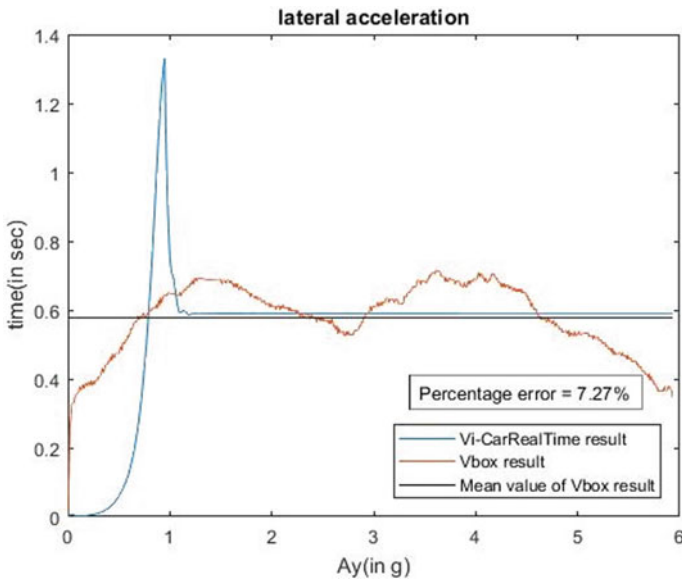


Fig. 19 Comparison of lateral acceleration

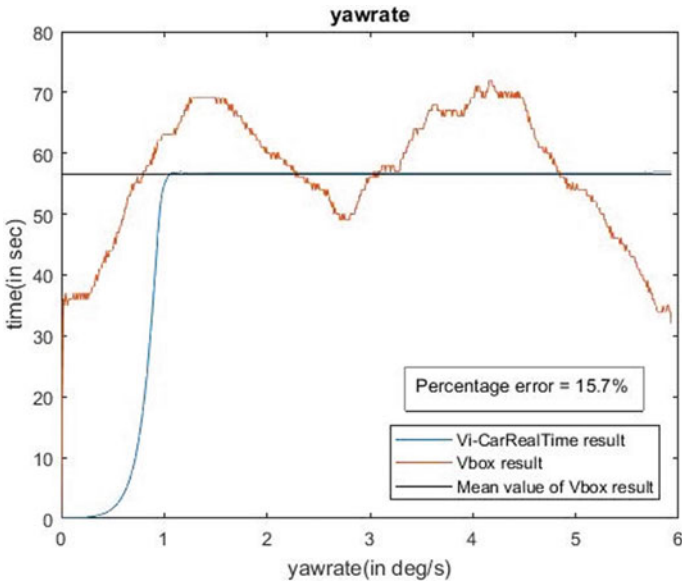


Fig. 20 Comparison of yaw-rates

The MMM diagram for the car at speeds of 60 and 75 kmph is as shown in Figs. 20 and 21.

The inference that can be drawn from the MMM diagrams are:

- The vehicle under-steers at peak lateral acceleration. Hence the vehicle points away from the corner at its lateral limit.
- The maximum possible lateral acceleration under zero yaw condition is 1.3 g.
- The slope of the constant beta lines gives the aligning effect induced with the changing steering wheel angle. For example, the $\beta = 0$ line passing through the origin represents the state of the vehicle at corner entry. The slope of the line gives the aligning effect of the car at corner entry.
- The increase in the slope of the constant beta lines with increase in the speed of the vehicle indicate that the aligning effect increases with speed.

The Steer angle and under-steer gradients v/s lateral acceleration is as shown in Figs. 23 and 24, respectively. It can be seen that the maximum possible steering angle at 60 kmph is 20 degrees. Beyond this value of steering input the vehicle under-steers as it goes beyond its peak operating conditions. This kind of information is key to any driver who is trying to push the car to its limits.

The corresponding under-steer gradient which is the change in steering wheel angle to the change in lateral acceleration is as shown in Figs. 22, 23 and 24.

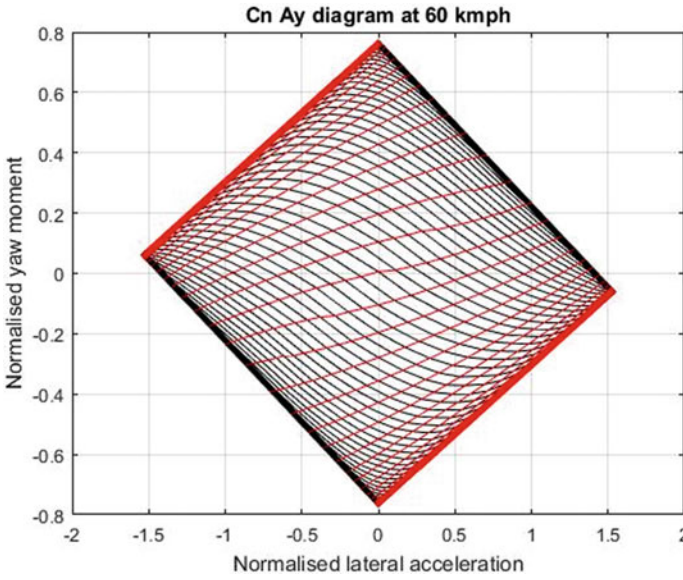


Fig. 21 MMM diagram at 60 kmph

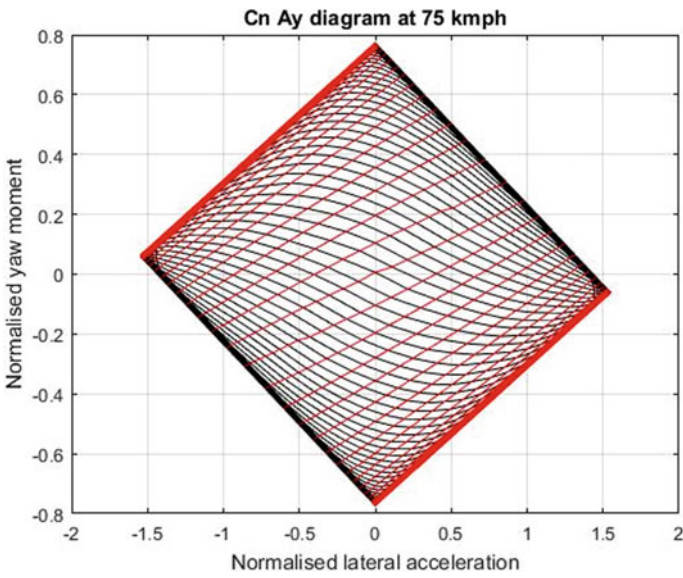


Fig. 22 MMM diagram at 75 kmph The MMM Skid-pad

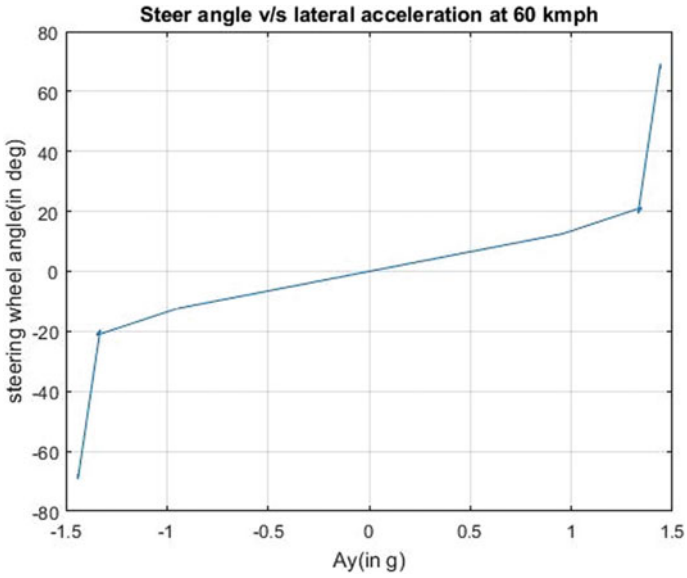


Fig. 23 Steer angle v/s lateral acceleration at 60 kmph

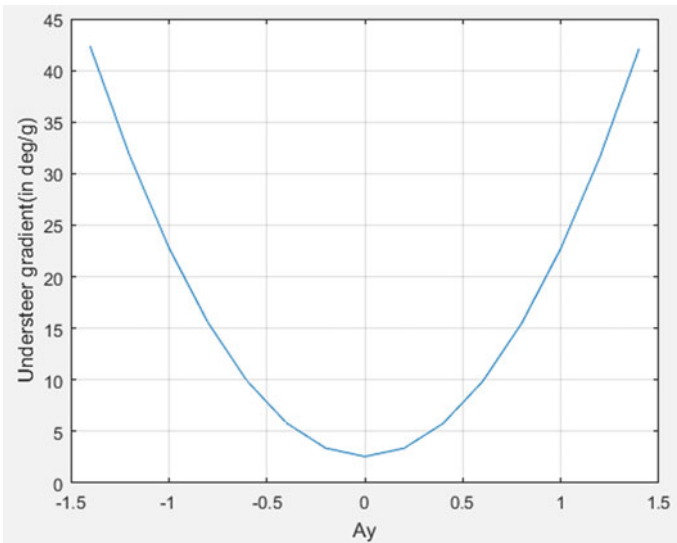


Fig. 24 Understeer gradient v/s lateral acceleration at 60 kmph

Acknowledgements We would like to thank Prof. D Jawahar, CEO, PES Institute of Technology for financial and moral support during the course of the project. We extend our gratitude to Dr. K.S. Shridhar, Prof. & Head, Department of Mechanical Engineering, PES Institute of Technology for all his help and support. We express our regards to Dr. N. Rajesh Mathivanan and Prof. Ajay Nayar, faculty advisors, Team Haya Racing for their support throughout the course of the project.

We would like to thank all members of Team Haya Racing for their unconditional love and support towards achieving the objective of this project. We express our sincere gratitude to FSAE TTC and Calspan Tire Research Facility for providing Tire test data. Special thanks to MathWorks and VI-grade for providing software support to Team Haya Racing.

References

1. Smith C (1978) *Tune To win, the art and science of race car development and tuning*. Aero Publishers, Fallbrook, CA 92028
2. Pacejka H (2006) *Tire and vehicle dynamics*, 2nd edn. Butterworth-Heinemann, Oxford, United Kingdom
3. Racelogic Logic Support Center. <https://racelogic.support>
4. Milliken WF, Milliken DL (1995) *Race car vehicle dynamics*. Society of Automobile Engineering, Inc. Warrendale, Pa
5. Michael R, Suzanne R (2012) *Learn and compete, a primer for formula SAE, formula student and formula hybrid teams*. Racecar Graphic Limited, London
6. Vi-CarRealTime printable document. Vi-CarRealTime 18.1 Documentation. Vi-grade GmbH, Germany
7. Determination of Vehicle CG position. Informal document No. 11 79th GRSG, 16–20 October 2000 agenda item 4. Regulation 66.
8. MSC software. Using PAC2002 Tire model http://mech.unibg.it/~lorenzi/VD&S/Matlab/Tire/tire_models_pac2002.pdf
9. Formula SAE tire test consortium, <http://www.fsaettc.org>
10. Besselink IJM, Schemitz AJC, Pacejka HB (2017) An improved magic formula/swift tyre model that can handle inflation pressure changes. Eindhoven University of Technology, P.O.Box 513, 5600 MB Eindhoven, The Netherlands

Multivariable Load Prediction Using LSTM



G. Satya Rohan, V. Sailaja, K. Deepa, and Abhijith Prakash

Abstract Power supply regulation and load forecast are important factors in electric power distribution systems. The advent and ever-expanding adoption of renewables and distributed energy resources in the energy sector have introduced a lot of complexity into the day-to-day operations and maintenance of a wide-area power grid. Implementation of big data analysis and deep learning tools in power distribution systems has enabled predictive maintenance, grid health monitoring, demand forecasting, and reliability analysis, and also provided a host of other features for overall improvement of grid operations. A thorough analysis reflecting presents and future patterns can aid in critical decisions regarding generation capacity, transmission, and distribution systems for a successful load flow system planning. The focus of this paper is on ways to estimate load using the deep learning technique Long short-term memory (implemented by Python programming language).

Keywords LSTM · RNN · Time series

1 Introduction

Load forecasting strategy is used by the electric power industry to predict power production and satisfy load requirements. Forecasting accuracy is significantly important in operational and administrative stacking for a service organization. It is critical for different people in the electric power industries, like distribution, transmission and markets, power providers, International Organization for Standardization (IOS), and other related establishments. The most determining techniques utilize numerical methods or algorithms that involve artificial intelligence such as down-turn, fuzzy, genetic algorithm, neural systems, and undefined rationale for load forecasting and other energy-saving applications [1–5]. Load forecast could be done for the present circumstances (a couple of hours), medium-term (half a month as long as

G. S. Rohan · V. Sailaja (✉) · K. Deepa · A. Prakash
Department of Electrical and Electronics Engineering, Amrita School of Engineering, Amrita
Vishwa Vidyapeetham, Bengaluru, India
e-mail: v_sailaja@blr.amrita.edu

a year), or long haul (longer than a year) [6]. Contingent upon time-series estimating, outcomes are classified as seasonal, trend, and random.

Power systems extension planning begins with forecasts of future load prerequisites [7–11]. The estimation of both demand and load is pivotal to compelling system planning. Forecasts are utilized for deciding the age limit, transmission, and distribution systems parameters.

This topic has been examined as a fundamental research for quite a while. Numerous researchers have made a lot of examinations on forecast theories and techniques, and have set forward a few prediction techniques [12, 13]. It requires the analysis of the attributes related to the load and also considers the demand factor relationship between the actual demand imposed on the systems and the loads that have been connected.

In short, forecasting the demand is the main parameter for operations and celerity in the distribution system to avoid unforeseen outcomes like power failure, etc. [6, 14]. It is essential for the monetary activity, planning load dispatch, and generation in automatic control [15]. It not only assists the clients with picking a progressive and proper power utilization scheme but also lessens the electricity intake and improves equipment usage, subsequently decreasing the manufacturing cost thus adding to the financial advantage. Distribution and transmission sector has advanced two-fold in the present scenario; hence, the level of power marketization is additionally improved, so theories on how to rapidly and precisely anticipate transient power loads have made this field the current topic of research importance This paper focuses on forecasting the load demand using Long short-term memory (LSTM).

2 Conception

Load estimation is a complex multi-variable and multidimensional problem where determining techniques, such as numerical analysis-based curve fitting technique fails to produce precise outcomes; something that deep learning algorithms are better at [15–17]. Some of the common deep learning algorithms are detailed below.

(A) Recurrent Neural Network (RNN)

In neural systems, outputs are independent of inputs. However, there are cases like word or phrase prediction, most conventional where the initial set of words or phrases is necessary to predict the probable expressions that may follow in a sentence. Consequently, the RNN algorithm was developed to handle such issues with the assistance of a hidden layer. This lowers the multifaceted nature of parameters and simplifies the problem to a large extent, in contrast to other neural systems.

A deeper network, for example, may have single input and output with three hidden layers with its own set of weights and biases in each hidden layer. In such cases, RNN transforms independent actuations into dependent initiations by assigning all layers with the same weights and biases. This decreases complications due to a large number of parameters. Each output of a layer is memorized and fed to the succeeding layer.

The three hidden layers are combined into a single intermittent layer so that the same weights can be assigned to all neurons. This process can be simplified using an algorithm as explained below:

1. A single input is given to RNN for each sampling time.
2. The network ascertains its present status utilizing the current and past data.
3. Present hidden state h_t turn out to be h_{t+1} in the next sampling time instant.
4. After completion of all inputs, the last state is utilized to compute the final output.
5. Computed output is compared with the authentic value, for example, objective output, and if any deviation then the error is identified.
6. This error is assimilated into the system for weight updation and, subsequently, RNN is updated.

RNN's advantage is that it has the ability to recollect information over a time span.

(B) Long Short-Term Memory (LSTM)

The LSTM system is a distinctive case of RNN, used for long-term learning. They are well suited for many applications and explicitly intended to avoid the long-term dependency issue. RNNs have repeating blocks of \tanh layer, as appeared in Fig. 1 and Eq. 1.

$$\hat{C}_t = h_t = \tanh(W_c \cdot [h_{t-1}, x_t] + b_c) \tag{1}$$

LSTMs also have a structure resembling a chain, but rather than a single layer, it has four layers that interact as described in Fig. 2.

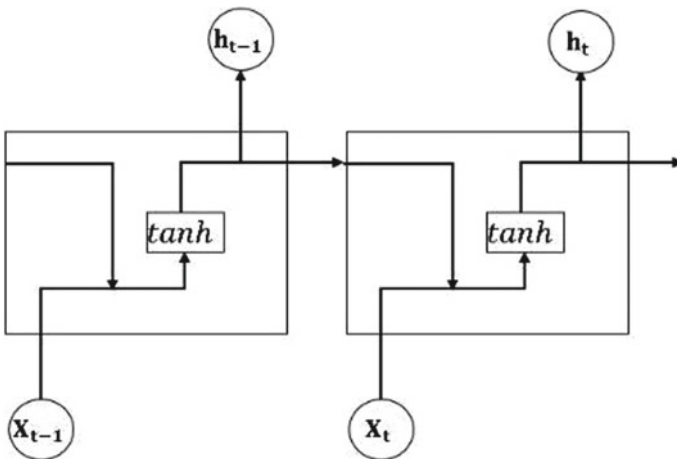


Fig. 1 Structure of the repeating module of RNN

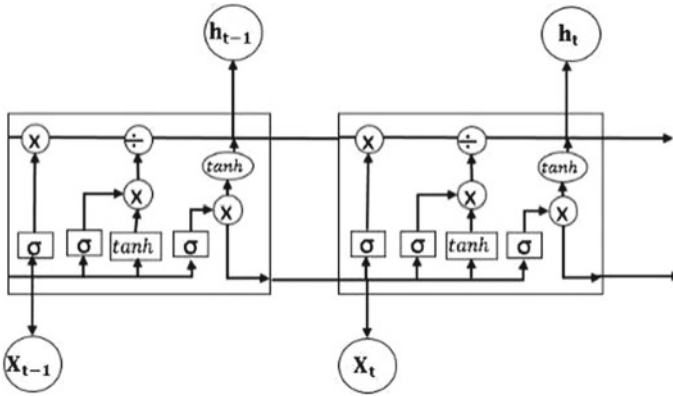


Fig. 2 Structure of an LSTM module

In Fig. 2, each line conveys a whole vector, from the output of one node to the input of other nodes. Each circle denotes point-wise tasks of summation and the final output h is obtained as per the mathematical function of each block.

(i) **Step-by-Step working of LSTM**

Sigmoid layer, the first step named “forget gate layer” decides on the data to be discarded from this state. It takes a look at h_{t-1} ; the output will be a number in the range of 0 and 1. For each number in the state C_{t-1} , “1” means “to totally keep this” and a “0” means “to totally dispose of this.” Necessary calculations are made from Eq. 2.

$$f_t = \sigma(W_f.[h_{t-1}, x_t] + b_f) \tag{2}$$

where f_t —forget gates activation vector, σ —sigmoid function, W_f —weight matrices, h_{t-1} —hidden state vector, x_t —input vector, b_f —bias vector parameters.

The next step is to select the kind of new data to be put into the cell state. It involves two sections: (i) “Input gate layer” to update the appropriate value and (ii) tanh layer. These two sections are joined to update the state, and necessary calculations are made from Eqs. 3 and 4.

$$i_t = \sigma(W_i.[h_{t-1}, x_t] + b_i) \tag{3}$$

$$\hat{C}_t = \tanh(W_c.[h_{t-1}, x_t] + b_c) \tag{4}$$

where i_t —input gates activation vector, \hat{C}_t —cell input activation vector, b_i, W_i, b_c, W_c —bias vector and weight matrices for the input and the cell state, respectively.

The previous cell state is refreshed into the new cell state as Eq. 5. The old state is multiplied by f_t , and summed with $i_t * C_t$. This new value is scaled by the amount chosen to refresh each state value.

$$C_t = f_t * C_{t-1} + i_t * \hat{C}_t \tag{5}$$

C_t, C_{t-1} —present and previous cell state vectors, respectively.

Finally, the yield is picked. This yield is a filtered version established based on the cell state. Initially, “sigmoid layer” is run which picks the cells that are going to be yielded. Cell state is put through tanh so that the value toggles in between -1 and 1 and incremented by the yield of the sigmoid layer, with the objective that only the final yield is achieved. Necessary calculations are made from equation Eq. 3.

(C) Time Series (TS)

TS analysis is a statistical technique that manages time series data or pattern examination [18]. It implies that data is in a progression of specific time spans or spans. It is a kind of panel data which is a “multidimensional data set”, whereas TS is a “one-dimensional panel, which is similar to a cross-sectional data set.” Data set has characteristics of panel and TS data. One approach is to find the difference between the recordings of one data with other recordings. If the appropriate response is in the time data field, it represents a TS data set, whereas, if the non-time identifier responds, then the data set index is a cross-sectional or panel data set.

3 Working and Output

LSTM is implemented with the Python programming language in this work. Libraries such as TensorFlow, Keras, and NumPy are used as deep learning algorithms. The program is written in a Jupyter notebook and divided into 39 blocks. And also, output graphs and other visual information are generated during execution. The flow of the algorithm implementation is explained in detail below:

Blocks 1–12

The data used in this paper is from Kaggle data sets named Household Electric Power Consumption [19]. This data consists of global active power, global reactive power, voltage, and global intensity which is recorded by minute. These data are downsampled from minutes to hours. For evaluating the performance, 2-year data with 17520 samples are considered for training and 17039 samples are used for validation. The libraries from Python, namely, NumPy, scikit-learn, and pandas are imported for the algorithm. A plain text file that contains values like date, time, etc., is loaded as the index for the algorithms. The mean of each of the values provided, i.e., date, time, etc., is identified and resampled. The values are then sorted into a list. This is essential for fast value search operations as lists consume less memory and are immensely helpful for visualizing forecasting. The values found

are assigned to variables named as `Global_active_power`, `Global_reactive_power`, `Voltage`, `Global_intensity`, `Sub_metering_1`, `Sub_metering_2`, and `Sub_metering_3`. The series data is converted to supervised data, where the present values are used to predict future values. The input sequence is found for “n” number of values and then used for forecasting. The values are then collated into a file. The algorithmic sequence of steps is shown in Fig. 3a.

Blocks 13–24

Thirty timestamps are considered, with each hour being one timestamp. “n” features of data are predicted. This corresponds to a multi-parallel time series forecasting problem. The frame is then reframed for supervised learning. The columns that should not predict are then dropped, using `reframed.drop(reframed.columns[-6:], axis = 1, inplace = True)`. This is used to predict only 1 column (which is variable 1, i.e., global active power). The algorithm is trained with a 2-year span of data so that it generates an output $y(0)$ for an input $x(0)$. These values are then projected into three dimensions: samples, time steps, and features, which is an important procedure in LSTM training. The input shape must be the time steps; here, it is `n_features`. That way, it takes one list item of (`n_in`) time steps of (`n_features`) columns to predict one future time step. Some other libraries, like TensorFlow and Keras are imported. The algorithm is now trying to make a prediction. Since (`yhat`) has a shape with seven columns, it can perform properly. If the prediction is made with only one column, then it is needed to get it concatenated with six other random columns (usual convention: `test_X`, last six columns are used to concatenate), obtain the inverse transform, and remove the first column, i.e., the required output. Now, the operation `inv_yhat = np.concatenate((yhat, test_X[:, -6:]), axis = 1)` is performed and `inv_yhat[0]` is used for output. Then mean squared error is used to optimize the model by using the Adam optimizer. The corresponding algorithm for these steps is shown in Fig. 3b. The 4-year data considered is from 16 December 2006 to 26 November 2010, roughly 8500 data are being taken. After training the model, the last 200 samples of predicted validation samples are plotted. Forecasting is performed for the next 20 h data using the last 30 samples of available data.

The global active, reactive power, voltage, and metering reading obtained at each step of the algorithm are presented in Figs. 4 and 5 shows the number of epochs taken to forecast the data with time and losses. Figure 6a shows the plot of trained and test data, it is observed that the training was successful since the test data also follows the trained data with a very small error of 1×10^{-3} which is in the acceptable range. The same is further validated in Fig. 6b–h which has the plot of active, reactive, voltage, global intensity, and all three sub-metering readings. These figures have the plot of actual and forecasted values and they both follow the same trace for all the parameters confirming that the forecasted values are accurate.

Blocks 25–39

The main forecasting begins here. The entire data is scaled again. To hold the forecasts, `test_predictions = []` is carried out. Then, the forecasted values are appended to our `test_predictions`. In the last step, the first time step in the batch used to predict

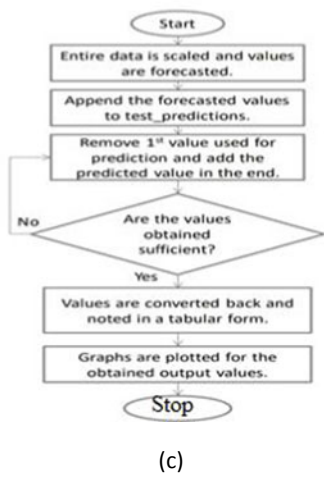
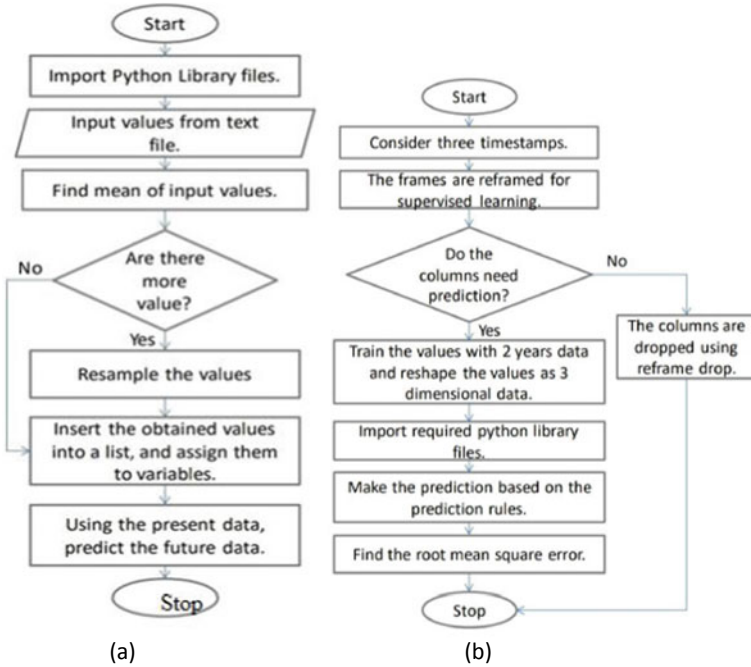


Fig. 3 a Algorithm for the blocks 1-12 b Algorithm for the blocks 13-24 c Algorithm for the blocks 25-39

dt	Global_active_power	Global_reactive_power	Voltage	Global_intensity	Sub_metering_1	Sub_metering_2	Sub_metering_3
2006-12-16 17:24:00	4.216	0.418	234.84	18.4	0.0	1.0	17.0
2006-12-16 17:25:00	5.360	0.436	233.63	23.0	0.0	1.0	16.0
2006-12-16 17:26:00	5.374	0.498	233.29	23.0	0.0	2.0	17.0
2006-12-16 17:27:00	5.388	0.502	233.74	23.0	0.0	1.0	17.0
2006-12-16 17:28:00	3.666	0.528	235.68	15.8	0.0	1.0	17.0

(a)

dt	Global_active_power	Global_reactive_power	Voltage	Global_intensity	Sub_metering_1	Sub_metering_2	Sub_metering_3
2006-12-16 17:00:00	4.222889	0.229000	234.643889	18.100000	0.0	0.527778	16.861111
2006-12-16 18:00:00	3.632200	0.080033	234.580167	15.600000	0.0	6.716667	16.866667
2006-12-16 19:00:00	3.400233	0.085233	233.232500	14.503333	0.0	1.433333	16.683333
2006-12-16 20:00:00	3.268567	0.075100	234.071500	13.916667	0.0	0.000000	16.783333
2006-12-16 21:00:00	3.056467	0.076667	237.158667	13.046667	0.0	0.416667	17.216667

(b)

```

Global_active_power      421  Global_active_power      0
Global_reactive_power    421  Global_reactive_power    0
Voltage                  421  Voltage                  0
Global_intensity         421  Global_intensity         0
Sub_metering_1          421  Sub_metering_1          0
Sub_metering_2          421  Sub_metering_2          0
Sub_metering_3          421  Sub_metering_3          0
dtype: int64             dtype: int64
    
```

(c)

(d)

Fig. 4 **a** Loaded txt file **b** Line output **c** Line 7 output **d** Line 9 output

is removed and the predicted values are added to the last. Thus, making it, again, time steps the amount of data to predict one more. This goes on a loop. The time steps are then forecasted. Now, the values are converted back. For establishing a periodicity, a table is made with date and time as columns and the variables in the rows. Then the forecasted values are filled accordingly. The table, which contains the forecasted values, is being printed. Graphs for each variable are plotted against time. From the graphs obtained, it looks like the predicted values seem to be almost equal to the actual values, thereby making a successful forecast. This step can be made into an algorithm, as depicted in Fig. 3c.

$$RMSE = \sqrt{\frac{\sum_{i=1}^N (x_i - \hat{x}_i)^2}{N}} \tag{6}$$


```

Train on 17520 samples, validate on 17039 samples
Epoch 1/20
17520/17520 [=====] - 25s 1ms/sample - loss: 0.0210 - val_loss: 0.0152
Epoch 2/20
17520/17520 [=====] - 25s 1ms/sample - loss: 0.0157 - val_loss: 0.0143
Epoch 3/20
17520/17520 [=====] - 25s 1ms/sample - loss: 0.0147 - val_loss: 0.0137
Epoch 4/20
17520/17520 [=====] - 28s 2ms/sample - loss: 0.0142 - val_loss: 0.0134
Epoch 5/20
17520/17520 [=====] - 26s 1ms/sample - loss: 0.0139 - val_loss: 0.0134
Epoch 6/20
17520/17520 [=====] - 26s 1ms/sample - loss: 0.0136 - val_loss: 0.0134
Epoch 7/20
17520/17520 [=====] - 25s 1ms/sample - loss: 0.0134 - val_loss: 0.0131
Epoch 8/20
17520/17520 [=====] - 26s 1ms/sample - loss: 0.0132 - val_loss: 0.0129
Epoch 9/20
17520/17520 [=====] - 26s 2ms/sample - loss: 0.0130 - val_loss: 0.0128
Epoch 10/20
17520/17520 [=====] - 27s 2ms/sample - loss: 0.0128 - val_loss: 0.0127
Epoch 11/20
17520/17520 [=====] - 26s 1ms/sample - loss: 0.0127 - val_loss: 0.0127
Epoch 12/20
17520/17520 [=====] - 26s 1ms/sample - loss: 0.0125 - val_loss: 0.0126
Epoch 13/20
17520/17520 [=====] - 27s 2ms/sample - loss: 0.0124 - val_loss: 0.0126
Epoch 14/20
17520/17520 [=====] - 27s 2ms/sample - loss: 0.0123 - val_loss: 0.0125
Epoch 15/20
17520/17520 [=====] - 29s 2ms/sample - loss: 0.0122 - val_loss: 0.0125
Epoch 16/20
17520/17520 [=====] - 27s 2ms/sample - loss: 0.0121 - val_loss: 0.0124
Epoch 17/20
17520/17520 [=====] - 27s 2ms/sample - loss: 0.0119 - val_loss: 0.0125
Epoch 18/20
17520/17520 [=====] - 28s 2ms/sample - loss: 0.0119 - val_loss: 0.0126
Epoch 19/20
17520/17520 [=====] - 33s 2ms/sample - loss: 0.0117 - val_loss: 0.0125
Epoch 20/20
17520/17520 [=====] - 28s 2ms/sample - loss: 0.0117 - val_loss: 0.0125
    
```

Fig. 5 Epoch value

$$MAE = \frac{\sum_{i=1}^n |y_i - x_i|}{n} \tag{7}$$

$$MSE = \frac{1}{n} \sum_{i=1}^n (x_i - \hat{x}_i)^2 \tag{8}$$

where $x_i, \hat{x}_i, y_i \in \mathbb{N}$ are the actual, estimated, predicted, and missing data, respectively.

The forecasting results for 1 day before and after sampling are presented in Fig. 7, while the same is plotted for active, reactive, voltage, global intensity, and all three sub-metering readings in Fig. 8a–g. The predicted values are for 20 h from 26 November 2010, 22:00 to 27 November 2010, 17:00. The testing data RMSE, MAE, and MSE are calculated using Eqs. 6, 7, and 8, respectively, and are found to be RMSE: 0.128, MAE: 0.077, MSE: 0.016. These less values clearly indicate the exact prediction efforts of the LSTM model.

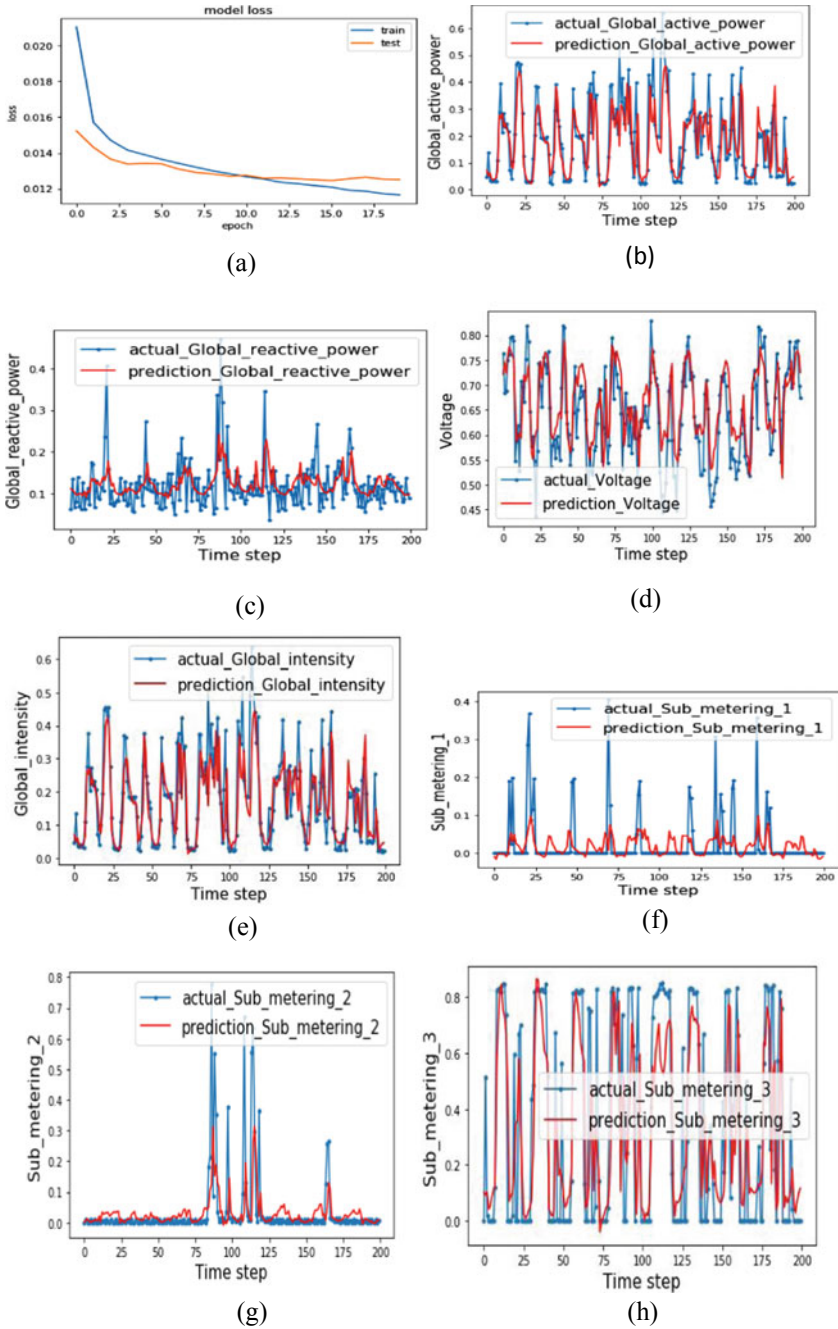


Fig. 6 a-i Line outputs from lines 20, 22-28

	Global_active_power	Global_reactive_power	Voltage	Global_intensity	Sub_metering_1	Sub_metering_2	Sub_metering_3
2010-11-26 22:00:00	1.004956	0.088226	242.604434	4.207523	0.292974	0.709638	4.338490
2010-11-26 23:00:00	0.730664	0.086966	244.046052	3.050386	0.029975	0.592670	3.481152
2010-11-27 00:00:00	0.535695	0.083014	244.558288	2.247131	-0.109740	0.557405	2.209750
2010-11-27 01:00:00	0.427485	0.079188	245.042789	1.801110	-0.182404	0.335722	1.583200
2010-11-27 02:00:00	0.378344	0.078776	245.413756	1.599384	-0.150065	0.138340	1.383057
2010-11-27 03:00:00	0.351663	0.075843	245.602677	1.491254	-0.105145	0.039719	1.432754
2010-11-27 04:00:00	0.334858	0.074991	245.547987	1.422351	-0.113449	0.074636	1.592537
2010-11-27 05:00:00	0.362156	0.072864	245.420174	1.524410	-0.265445	0.202119	1.598101
2010-11-27 06:00:00	0.788717	0.073306	244.903958	3.275470	-0.548782	0.348564	3.670717
2010-11-27 07:00:00	1.861343	0.082134	242.408885	7.739853	0.155391	0.738931	12.062154
2010-11-27 08:00:00	1.909045	0.079502	241.270258	7.915304	1.685400	1.095913	15.148912
2010-11-27 09:00:00	1.697145	0.088164	241.188341	7.033667	1.529030	1.474505	15.243663
2010-11-27 10:00:00	1.646876	0.102733	241.414580	6.831239	1.963497	2.285100	14.182523
2010-11-27 11:00:00	1.626228	0.116885	241.888292	6.760518	2.101371	3.337375	12.209010
2010-11-27 12:00:00	1.611779	0.126859	242.524813	6.715193	2.328216	4.319807	9.989075
2010-11-27 13:00:00	1.588306	0.130055	243.162152	6.624777	2.442384	4.879583	8.282734
2010-11-27 14:00:00	1.532026	0.127650	243.435776	6.388683	2.326555	4.844779	6.913376
2010-11-27 15:00:00	1.493099	0.124249	243.073137	6.254131	2.083239	4.439753	5.734144
2010-11-27 16:00:00	1.558665	0.124015	242.110759	6.551225	1.900768	3.907733	4.927482
2010-11-27 17:00:00	1.781206	0.127636	240.958275	7.417469	1.901276	3.374799	4.670576

(a)

dt	Global_active_power	Global_reactive_power	Voltage	Global_intensity	Sub_metering_1	Sub_metering_2	Sub_metering_3
2006-12-16 17:00:00	4.222889	0.229000	234.643889	18.100000	0.0	0.527778	16.861111
2006-12-16 18:00:00	3.632200	0.080033	234.580167	15.600000	0.0	6.716667	16.866667
2006-12-16 19:00:00	3.400233	0.085233	233.232500	14.503333	0.0	1.433333	16.883333
2006-12-16 20:00:00	3.269567	0.075100	234.071500	13.916667	0.0	0.000000	16.783333
2006-12-16 21:00:00	3.056467	0.076667	237.158667	13.046667	0.0	0.416667	17.216667
...
2010-11-26 17:00:00	1.725900	0.061400	237.069667	7.216667	0.0	0.000000	12.866667
2010-11-26 18:00:00	1.573467	0.053700	237.531833	6.620000	0.0	0.000000	0.000000
2010-11-26 19:00:00	1.659333	0.060033	236.741000	7.056667	0.0	0.066667	0.000000
2010-11-26 20:00:00	1.163700	0.061167	239.399000	4.913333	0.0	1.066667	0.000000
2010-11-26 21:00:00	0.934667	0.000000	239.890000	3.800000	0.0	0.000000	0.000000

(b)

Fig. 7 a & b Forecasted values before and after resampling

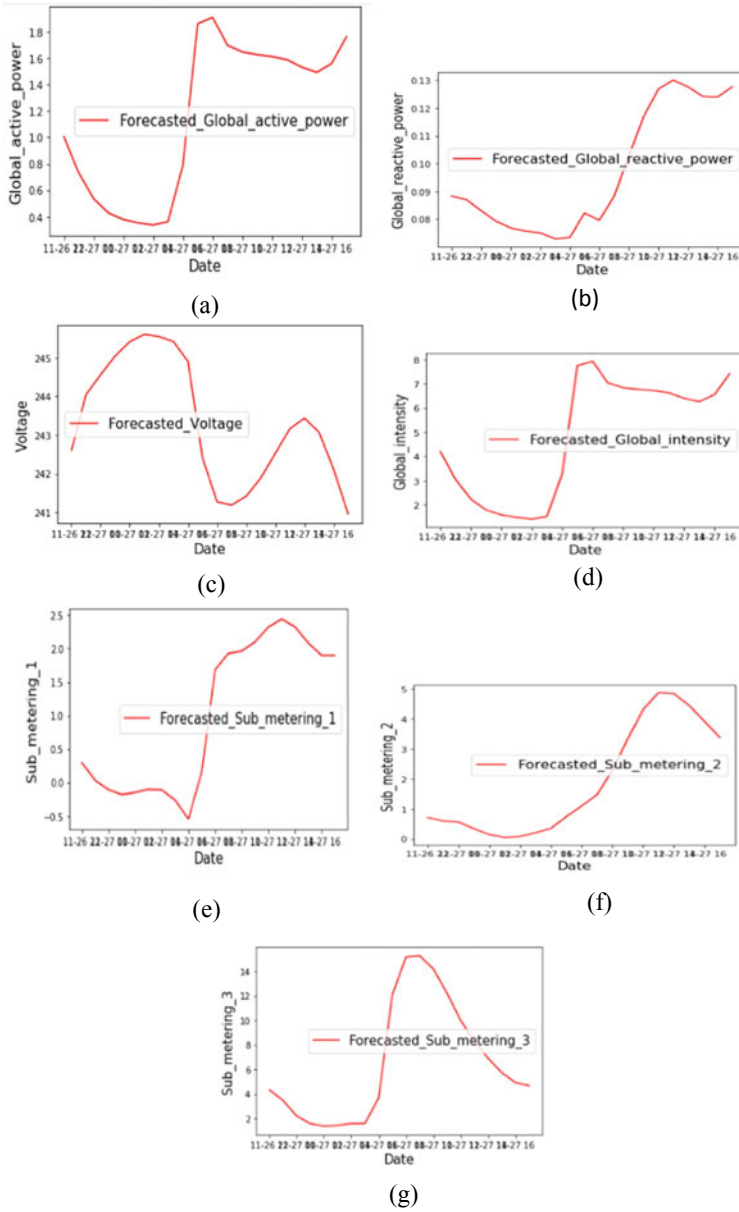


Fig. 8 a–g Outputs at line 39.1–39.6

4 Conclusion

Load forecasting is the establishment for utility planning and it is a basic business issue in the utility industry. Numerous components impact the load forecasting precision, for example, geographic good variety, data quality, gauge skyline, figure source, and client division. A similar model that functions admirably in one utility may not be the best model for another utility. Indeed, even inside a similar utility, a model that estimates well in 1 year may not produce a good gauge for one more year. So as to set up the validity in load determining, utilities need to follow forecasting standards to build up a steady load estimating approach. Organization of brilliant systems advancements has made high granular data accessible for load determining. While redoing the models for each sub-locale or utility would improve the determining precision at the sub-provincial level or utility level, the exactness picked up at a lower level can be regularly meant by the upgraded gauges at the amassed levels as proven by the results of LSTM in this work.

References

1. Bathala P, Srivasthav BS, Reddy YSS, Deepa K (2020) Estimation of regenerative braking force in electric vehicles for maximum energy recovery. In: IEEE 17th India council international conference (INDICON 2020)
2. Rahul GP, Teja ON, Shivani PG, Deepa K, Manitha P, Sailaja V (2020) Long distance power transmission system with ZVS ultra-lift Luo converter from large photovoltaic generation. In: 2020 Third international conference on smart systems and inventive technology (ICSSIT), Tirunelveli, India
3. Prasanth B, Surya GS, Vinay GS, Deepa K, Manitha PV, Sailaja V (2021) Placement of distribution generators in IEEE 14 bus system with consumer benefit maximization. Lecture Notes in Electrical Engineering
4. Sravya ASL, Yoshita LN, Reddy BDD, Sailaja V, Manitha PV, Deepa K (2020) Impedance bus matrix formation using bus building algorithm for power system analysis. In: Proceedings of 2020 IEEE international women in engineering (WIE) conference on electrical and computer engineering, WIECON-ECE 2020, pp 200–205
5. Shabarish PR, Krishna RP, Prasanth B, Deepa K, Manitha PV, Sailaja V (2020) Fuzzy based approach to enhance the wireless charging system in electric vehicles. In: 2020 4th international conference on electronics, communication and aerospace technology (ICECA), Coimbatore, India, pp 176–181
6. Mi J, Fan L, Duan X, Qiu Y (2018) Short-term power load forecasting method based on improved exponential smoothing grey model. *Math Probl Eng Hindawi* 1–11
7. Fazil G, Filiz F (2018) Deep learning for renewable power forecasting: an approach using LSTM neural networks. *World Acad Sci Eng Technol Int J Energy Power Eng* 12(6)
8. Anwar T, Sharma B, Chakraborty K, Sirohi H (2018) Introduction to load forecasting. *Int J Pure Appl Math* 119(15):1527–1538
9. Gupta V, Pal S (2017) An overview of different types of load forecasting methods and the factors affecting the load forecasting. *Int J Res Appl Sci Eng Technol (IJRASET)* 5(IV):729–733
10. Soliman SA, Al-Kandari AM (2010) Electrical load forecasting : modelling and model construction. Elsevier publications

11. Pengwei S, Tian X, Wang Y, Deng S, Zhao J, An Q, Wang Y (2017) Recent trends in load forecasting technology for the operation optimization of distributed energy system. *Energies* 10(9):1–13
12. Fayaz M, Kim D (2018) A prediction methodology of energy consumption based on deep extreme learning machine and comparative analysis in residential buildings. *Electronics* 7:222
13. Hayes B, Prodanovic M (2014) State estimation techniques for electric power distribution systems. In: UKSim-AMSS 8th european modelling symposium. IMDEA Energy Institute, Madrid, Spain, pp 303–308
14. Feinberg EA, Genethliou D et al (2005) Load forecasting. In: *Power electronics and power systems. Applied Mathematics for Restructured Electric Power Systems*. Springer, Boston, MA
15. Gajowniczek K, Zabkowski T (2017) Two-stage electricity demand modeling using deep learning algorithms. *Energies* 10:1547
16. Somarajan S, Shankar M, Sharma T, Jeyanthi R (2019) Modelling and analysis of volatility in time series data. In: Wang J, Reddy G, Prasad V, Reddy V (eds) *Soft computing and signal processing. Advances in Intelligent Systems and Computing*, vol 898. Springer, Singapore
17. Harivigneshwar CJ, Dharmavenkatesan KB, Ajith R, Jeyanthi R (2019) Modeling of multivariate systems using vector autoregression (VAR). In: *2019 Innovations in power and advanced computing technologies (i-PACT)*, pp 1–6
18. Elsworth S, Güttel S (2003) Time series forecasting using LSTM networks: a symbolic approach, pp 1–12
19. <https://www.kaggle.com/uciml/electric-power-consumption-data-set>